

---

This item was submitted to [Loughborough's Research Repository](#) by the author.  
Items in Figshare are protected by copyright, with all rights reserved, unless otherwise indicated.

## **A hybrid approach to tyre modelling based on modal testing and non-linear tyre-wheel motion**

PLEASE CITE THE PUBLISHED VERSION

PUBLISHER

© Vasileios Ch. Tsinias

PUBLISHER STATEMENT

This work is made available according to the conditions of the Creative Commons Attribution-NonCommercial-NoDerivatives 4.0 International (CC BY-NC-ND 4.0) licence. Full details of this licence are available at: <https://creativecommons.org/licenses/by-nc-nd/4.0/>

LICENCE

CC BY-NC-ND 4.0

REPOSITORY RECORD

Tsinias, Vasileios. 2015. "A Hybrid Approach to Tyre Modelling Based on Modal Testing and Non-linear Tyre-wheel Motion". figshare. <https://hdl.handle.net/2134/17852>.

**A hybrid approach to tyre modelling based on modal testing  
and non-linear tyre-wheel motion**

by

Vasileios Ch. Tsinias

Dipl.-Ing

**A Doctoral Thesis**

*Submitted in partial fulfilment of the requirements  
for the award of  
Doctor of Philosophy of Loughborough University*

November 2014

LOUGHBOROUGH UNIVERSITY

© by Vasileios Ch. Tsinias 2014

## **Certificate of Originality**

### **Thesis Access Conditions and Deposit Agreement**

Students should consult the guidance notes on the electronic thesis deposit and the access conditions in the University's Code of Practice on Research Degree Programmes

**Author** VASILEIOS TSINIAS

**Title** A hybrid approach to tyre modelling based on modal testing and non-linear tyre-wheel motion

I, VASILEIOS TSINIAS, 73 Kent Crescent, Wigston, LE18 4XR, UK, "the Depositor", would like to deposit "*A hybrid approach to tyre modelling based on modal testing and non-linear tyre-wheel motion*", hereafter referred to as the "Work", once it has successfully been examined in Loughborough University Institutional Repository

**Status of access** OPEN

**Moratorium Period**.....years, ending...../.....20.....

**Status of access approved by (CAPITALS)**.....

**Supervisor (Signature)**.....

**School of** Aeronautical, Automotive, Chemical and Materials Engineering

**Author's Declaration** *I confirm the following :*

#### CERTIFICATE OF ORIGINALITY

This is to certify that I am responsible for the work submitted in this thesis, that the original work is my own except as specified in acknowledgements or in footnotes, and that neither the thesis nor the original work therein has been submitted to this or any other institution for a degree

#### NON-EXCLUSIVE RIGHTS

The licence rights granted to Loughborough University Institutional Repository through this agreement are entirely non-exclusive and royalty free. I am free to publish the Work in its present version or future versions elsewhere. I agree that Loughborough University Institutional Repository administrators or any third party with whom Loughborough University Institutional Repository has an agreement to do so may, without changing content, convert the Work to any medium or format for the purpose of future preservation and accessibility.

#### DEPOSIT IN LOUGHBOROUGH UNIVERSITY INSTITUTIONAL REPOSITORY

I understand that open access work deposited in Loughborough University Institutional Repository will be accessible to a wide variety of people and institutions - including automated agents - via the World Wide Web. An electronic copy of my thesis may also be included in the British Library Electronic Theses On-line System (EThOS).

I understand that once the Work is deposited, a citation to the Work will always remain visible. Removal of the Work can be made after discussion with Loughborough University Institutional Repository, who shall make best efforts to ensure removal of the Work from any third party with whom Loughborough University Institutional Repository has an agreement. Restricted or Confidential access material will not be available on the World Wide Web until the moratorium period has expired.

- That I am the author of the Work and have the authority to make this agreement and to hereby give Loughborough University Institutional Repository administrators the right to make available the Work in the way described above.

- That I have exercised reasonable care to ensure that the Work is original, and does not to the best of my knowledge break any UK law or infringe any third party's copyright or other

Intellectual Property Right. I have read the University's guidance on third party copyright material in theses.

- The administrators of Loughborough University Institutional Repository do not hold any obligation to take legal action on behalf of the Depositor, or other rights holders, in the event of breach of Intellectual Property Rights, or any other right, in the material deposited.

*The statement below shall apply to **ALL** copies:*

**This copy has been supplied on the understanding that it is copyright material and that no quotation from the thesis may be published without proper acknowledgement.**

**Restricted/confidential work:** All access and any copying shall be strictly subject to written permission from the University Dean of School and any external sponsor, if any.

**Author's signature**.....**Date**.....

<b>user's declaration:</b> for signature during any Moratorium period (Not Open work):			
<b><i>I undertake to uphold the above conditions:</i></b>			
Date	Name (CAPITALS)	Signature	Address

*This thesis is wholeheartedly dedicated to the three most important people in my life:*

*My mother Eirini, my father Charalampos and my partner Katerina*

## Abstract

The current state-of-the-art tyre models tend to be demanding in parameterisation terms, typically requiring extensive and expensive testing, and computational power. Consequently, an alternative parameterisation approach, which also allows for the separation of model fidelity from computational demand, is essential.

Based on the above, a tyre model is introduced in this work. Tyre motion is separated into two components, the first being the non-linear global motion of the tyre as a rigid body and the second being the linear local deformation of each node. The resulting system of differential equations of motion consists of a reduced number of equations, depending on the number of rigid and elastic modes considered rather than the degrees of freedom. These equations are populated by the eigenvectors and the eigenvalues of the elastic tyre modes, the eigenvectors corresponding to the rigid tyre modes and the inertia properties of the tyre. The contact sub-model consists of bristles attached to each belt node. Shear forces generated in the contact area are calculated by a distributed LuGre friction model while vertical tread dynamics are obtained by the vertical motion of the contact nodes and the corresponding bristle stiffness and damping characteristics.

To populate the abovementioned system of differential equations, the modal properties of the rigid and the elastic belt modes are required. In the context of the present work, rigid belt modes are calculated analytically, while in-plane and out-of-plane elastic belt modes are identified experimentally by performing modal testing on the physical tyre. To this end, the eigenvalue of any particular mode is obtained by fitting a rational fraction polynomial expression to frequency response data surrounding that mode. The eigenvector calculation requires a different approach as typically modes located in the vicinity of the examined mode have an effect on the apparent residue. Consequently, an alternative method has been developed which takes into account the out-of-band modes leading to identified residues representing only the modes of interest.

The validation of the proposed modelling approach is performed by comparing simulation results to experimental data and trends found in the literature. In terms of vertical stiffness, correlation with experimental data is achieved for a limited vertical load range, due to the nature of the identified modal properties. Moreover, the tyre model response to transient lateral slip is investigated for a range of longitudinal speeds and vertical loads, and the resulting relaxation length trends are compared with the relevant literature.

**Keywords:** tyre modelling, tyre modal testing, flexible tyre belt, tyre response, tyre belt eigenvalues, tyre belt eigenvectors

## List of Publications

### Journal Articles / Conference Proceedings

1. V. Tsiniias, G. Mavros, *Efficient In-Plane Tyre Mode Identification By Radial-Tangential Eigenvector Compounding*, Tire Science and Technology, v. 43(1), p. 71-84, 2015
2. V. Tsiniias, G. Mavros, *Efficient experimental identification of three dimensional tyre structural properties*, submitted for publication in Mechanical Systems and Signal Processing
3. V. Tsiniias, G. Mavros, *Tyre modelling by combination of modal testing and non-linear tyre-wheel motion*, Proceedings of the 4th International Tyre Colloquium, p. 342-351, 2015

### Conference Presentations

1. V. Tsiniias, G. Mavros, *Efficient In-Plane Tyre Mode Identification By Radial-Tangential Eigenvector Compounding*, presented at the 32<sup>nd</sup> Annual Meeting and Conference on Tire Science and Technology, 10 – 11 September 2013, Akron, Ohio, USA
2. V. Tsiniias, G. Mavros, *Tyre modelling by combination of modal testing and non-linear tyre-wheel motion*, presented at the 4<sup>th</sup> International Tyre Colloquium, 20 – 21 April 2015, University of Surrey, Guildford, UK



## Acknowledgments

I would like to express my sincere gratitude to the Department of Aeronautical and Automotive Engineering, Loughborough University for the life-changing opportunity to undertake this research, for offering generous studentship and for providing all the means necessary for this work.

Also, I would like to thank everyone at SIMPACK UK, and Managing Director Dr Suresh Gupta in particular, for providing all the time necessary to finish this Thesis and for showing a genuine interest in my research.

This work would not be anywhere near completion without the continuous – way beyond the call of duty – guidance of my supervisor, Dr George Mavros. It has been truly a privilege to study under his supervision and I will always remember his invaluable advice.

I would like to extend a special ‘thank you’ to all the new friends I made in Loughborough, and in particular my fellow researchers from the Department of Aeronautical and Automotive Engineering, Shuo, Wasim, Agis and Chris, and the Department of Chemical Engineering, Kostas and Dinos, and also my friend and colleague Matthew. These past four years would not have been the same without you. I would also like to thank my valuable friends back in Greece, Vassilis, Kostas and Paschalis. I miss you all!

Last, but definitely not least, I would like to thank my parents, Eirini and Charalampos, for their unconditional love and support. A ‘thank you’ is not enough and I feel very privileged to have been raised by those two exceptional people. Also, I would like to thank my partner Katerina for the continuous love, care and support, especially during the highly stressful closing stages of this work. All three of you have always been there for me and I will never forget it.

Vasilis Tsinias  
November 2014

## Contents

Abstract.....	6
List of Publications .....	7
Acknowledgments.....	8
Contents .....	9
1. Introduction .....	12
1.1 Background, motivation and broad aim .....	12
1.2 Structure of the present work.....	13
2. Previously conducted research on dynamic tyre modelling.....	17
2.1 Introduction.....	17
2.2 Magic Formula .....	18
2.3 Brush model.....	20
2.3.1 Pure lateral slip.....	21
2.3.2 Pure longitudinal slip .....	23
2.3.3 Combined slip .....	23
2.4 Short Wavelength Intermediate Frequency Tyre model (SWIFT model) .....	25
2.5 LuGre tyre model .....	28
2.6 Models based on the macroscopic physical description of tyres .....	34
2.6.1 Introduction.....	34
2.6.2 Flexible structure tire model (FTire) .....	35
2.6.3 CDTire.....	38
2.7 Finite element tyre models.....	42
2.8 Analytical tyre models.....	44
2.9 A modal approach towards the simulation of tyre deformation .....	50
2.10 Assessment of the presented tyre models .....	53
2.11 Alternative tyre modelling approach .....	56
3. Tyre model formulation.....	58
3.1 Introduction.....	58
3.2 Model overview .....	59
3.2.1 Model formulation.....	59
3.2.2 Frames of reference and transformations.....	60
3.3 Tyre belt modelling .....	67
3.3.1 Overview .....	67

3.3.2	Linear dynamics of the deformable belt .....	77
3.3.3	Non-linear dynamics of the non-deformable belt .....	78
3.3.4	Nodal motion expressed with respect to the global frame of reference .....	81
3.3.5	External force vector .....	84
3.4	Estimation of contact forces .....	94
3.4.1	Vertical tread modelling.....	94
3.4.2	Force generation in the contact area .....	98
3.4.3	Implementation of drum surface instead of even road .....	102
3.5	Remarks on Chapter 3 .....	103
4.	Identification of tyre modal parameters .....	106
4.1	Previously conducted research on modal parameter identification of pneumatic tyres .....	106
4.2	Theoretical approach.....	122
4.3	Experimental set-up .....	127
4.3.1	Overview .....	127
4.3.2	Boundary conditions .....	129
4.4	Modal parameter identification procedures and results.....	132
4.4.1	Identification of eigenvalues and eigenvectors .....	132
4.4.2	Identified properties .....	139
4.4.3	Complex to real normal modes .....	145
4.4.4	Digital filtering .....	151
4.4.5	From radial/tangential to wheel-fixed coordinates.....	158
4.4.6	Apparent repeated mode shapes .....	163
4.4.7	Multiple modes.....	165
5.	Tyre model validation .....	169
5.1	Introduction .....	169
5.2	Experimental layout .....	170
5.3	Vertical stiffness.....	171
5.3.1	Theoretical and experimental background .....	171
5.3.2	Vertical stiffness dependency on tyre belt fidelity .....	173
5.3.3	Data acquisition.....	177
5.3.4	Simulation results and comparison to experimental data .....	184
5.4	Transient lateral slip.....	190
5.4.1	Introduction.....	190
5.4.2	Slip angle frequency sweep – Longitudinal velocity variation .....	195
5.4.3	Slip angle frequency sweep – Vertical load variation .....	199

5.5	Remarks on chapter 5.....	206
6.	Conclusions, contribution to knowledge and suggestions for future work.....	208
6.1	Conclusions.....	208
6.1.1	Objective 1 .....	208
6.1.2	Objective 2a.....	210
6.1.3	Objective 2b .....	211
6.1.4	Objective 3 .....	214
6.2	Contribution to knowledge.....	215
6.3	Suggestions for future work.....	216
	References.....	219
	Appendix A – Table of Figures.....	227
	Appendix B – Tables .....	234

# **1. Introduction**

## **1.1 Background, motivation and broad aim**

Tyre modelling has been a challenging engineering field for at least three decades. Starting from simple steady-state empirical tyre models, the engineering community has currently reached a point where high-fidelity physical tyre models are available, capable of capturing various phenomena, such as dynamic contact forces and moments or tyre NVH characteristics. These advances, introduced between the first tyre modelling attempts and the current state-of-the-art, are presented in Chapter 2 of the present work. However, in order to achieve a certain level of accuracy and fidelity, the most recent tyre models are quite complex in structure, expensive in terms of computational power, and require extensive parameterisation procedures.

Specifically, after examining the current state-of-the-art regarding the established tyre models, it has been noticed that each one of these – from the analytical to the empirical ones – required some sort of experimental procedure to identify a, model-specific, variety of tyre properties. In many cases, this parameter identification may introduce extensive technical difficulties which, in addition to the unavoidable assumptions which follow the structure of any model, could jeopardise its results. This particular observation led to the concept presented in this work, which includes the development of an efficient tyre model, reconstructed directly from – feasible to obtain – modal testing data.

The tyre modal model presented in this work has been designed to couple the structural dynamics of the tyre belt, derived directly from modal testing, with the non-linearities associated with the motion of the pneumatic tyre. This feature is of interest in several automotive applications, particularly in cases where the mass of the tyre is comparable to the mass of the vehicle and, consequently, excitation arisen by the rigid body motion of the wheel could influence the vehicle to a great extent.

Consequently, the first critical objective of the present work is the development of a three-dimensional high-fidelity tyre model requiring data obtained either by simple static measurements, such as the tyre mass or tyre dimensions, or directly by modal testing on the physical tyre. This is a rather challenging task as the starting point is the typical second order

system of differential equations of motion. It follows that the next fundamental objective is the identification of those modal quantities required to populate the system matrices of the abovementioned tyre model. This particular objective is divided into two sub-objectives: the first being the experimental acquisition of the digital signals representing the transfer functions relating the force applied on the tyre to the respective acceleration of each tyre belt node – that is the actual modal testing performed on the physical tyre; the second being the post-processing of the aforementioned set of data to identify the eigenvalues and eigenvectors corresponding to the elastic modes of the tyre belt. The third objective is the validation of the proposed modelling approach and, in particular, the effect of belt deformation on tyre response.

The generic broad aim of the research work presented in this Thesis is to demonstrate the requirement for a shift in the way that tyre models are formulated and consequently in the way that tyre modelling parameters are obtained. In this work, a balance between the two is sought. The proposed tyre model is formulated having in mind the experimental procedure required to identify the necessary model parameters and, additionally, the experimental procedure is designed and executed in order to derive these parameters, so that the combination of these two actions – model formulation and parameter identification – is efficient and streamlined. Moreover, this combination is designed to require the minimum possible workload – the proposed tyre model is designed to directly exploit the experimentally acquired data, and the experimental procedure consists of typical modal testing performed on the physical tyre, instead of intricate tasks, for example measuring material properties for the tyre sidewall or the tyre belt layers.

## **1.2 Structure of the present work**

Initially, a broad range of tyre models is presented in Chapter 2, so as to expose the reader to the current state-of-the-art in tyre modelling and tyre model parameter identification and the potential benefits of the suggested approach, which is the development of a tyre model directly from modal testing. Also, Chapter 2 is demonstrating a number of useful modelling techniques and approaches that are implemented or could potentially be implemented in the suggested model, in particular ways to model contact between the tyre and the ground.

The approach adopted in this work demonstrates that parameter identification for dynamic tyre modelling does not necessarily have to be an experimentally intensive procedure. To this end, the system of second order differential equations capturing the tyre motion is further developed in Chapter 3, so that it may be populated by feasible to obtain quantities, namely the experimentally obtained eigenvalues and eigenvectors of the tyre belt, instead of the laborious to identify and typically-used inertia, stiffness and damping matrices. In addition, the macroscopic rigid-body motion of the tyre and the local deformation of the tyre belt are solved separately, the only interconnection being that a change in the tyre rigid-body states will excite the respective elastic structural modes. To complete the tyre modelling suite, an elastic boundary between the tyre and the ground and a distributed LuGre contact model<sup>[113]</sup> are embedded, having as input the global motion of each belt node – rigid-body motion coupled with local deformation – and calculating contact forces as outputs. It should be noted that, in the context of the present work, the tyre is examined macroscopically. Contrary to previous FEM studies where the structure of the examined tyre is modelled in detail, i.e. modelling of the specific elements formulating the real-world tyre structure (steel cords, rubber layers, etc), in this work the virtual tyre is represented as follows:

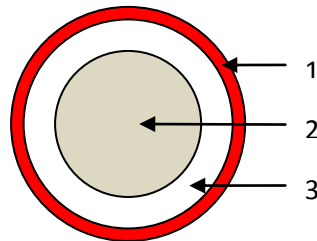


*Figure 1.1 – Tyre formulation (1: tyre tread, 2: rim, 3: tyre belt, sidewall and air cavity)*

The next step in formulating the complete tyre model, which – in addition – is one of the vital elements of the presented work demonstrating the effectiveness of the proposed approach, is the required modal testing. This particular procedure has been designed and executed having in mind the necessity to identify the modal quantities required to populate the structural component of the tyre model developed in Chapter 3. The quality of the obtained modal data is critical as it defines the accuracy of any performed simulation using this particular tyre model. In the context of the present formulation, that is the adopted floating physical tyre modelling approach where a change in the tyre motion will excite the respective elastic structural modes, the identified eigenvalues and eigenvectors need to be derived from the modal set containing also the contribution of rigid-body modes. This requirement, along with

other practical reasons described in Chapter 4, dictated the boundary condition of the performed modal testing. In particular, the tyre has been freely suspended from elastic cords, so that the measured acceleration of each node contains the contribution of both rigid-body and elastic modes.

In terms of modal parameter identification, also presented in Chapter 4, two distinct procedures have been applied to the measured transfer functions. Initially, the eigenvalues of the system have been identified by fitting a predefined expression in the frequency band surrounding each elastic mode, taking into account the effect of adjacent elastic modes. With regard to eigenvector identification, a new approach has been developed and implemented. Similarly to the eigenvalue identification procedure, each elastic mode is considered and treated separately. To enhance the accuracy of the identified eigenvector component, the adopted approach isolates the mode under investigation from all the out-of-band modes and therefore it results in identified properties corresponding exclusively to the mode of interest. Because of the experimental origin of the obtained structural properties corresponding to the frequency band of interest, it has been noted that the eigenvectors contain a certain level of spatial noise. Since the purpose of these eigenvectors is to be exploited in a tyre modelling environment, this spatial noise has been eliminated by applying a digital spatial filter to every identified eigenvector. This process enhanced the accuracy of the proposed tyre model as it resulted in noise-free eigenvectors, without any loss of fundamental information with respect to the waveform of each mode shape.

Having developed the theoretical background of the proposed tyre model in Chapter 3 and identified the structural properties of the tyre in Chapter 4, Chapter 5 is dedicated to demonstrating the respective validation process. Initially, the vertical deflection of the virtual tyre under the application of vertical load is examined for different levels of modal reduction, followed by a comparison between the virtual tyre and experimentally obtained data in terms of vertical stiffness. These processes revealed several interesting features and limitations of the proposed modelling approach with regards to the relation between model fidelity and applied vertical load. Additionally, the virtual tyre has been validated in terms of response to dynamic lateral slip. Two distinct scenarios have been examined, namely tyre response for varying longitudinal speed and for varying level of applied vertical force. The tyre response, or more precisely the time delay occurring between an imposed variation of a model input and the respective response of the tyre model, has been quantified by adopting the relaxation



length concept. For the particular case examined in the present work, the abovementioned model input and output are a predefined variation in the user-defined steering angle and the resulting contact lateral force, respectively. The relaxation length trends obtained by the virtual tyre for the two examined cases described above are found in accordance with similar trends found in the literature.

## **2. Previously conducted research on dynamic tyre modelling**

### **2.1 Introduction**

Tyre modelling has been one of the most popular and expanding topics in automotive research and industry for at least the past thirty years. A tyre is a highly non-linear and complex structure<sup>[37]</sup> and as a result the respective simulation requires a significant amount of computational power, a resource which was not widely available for the majority of the 20<sup>th</sup> century. During these early stages, tyre modelling was performed by fitting a polynomial expression in experimental data, a procedure which is demonstrated by J. R. Ellis in [29]. Without the current computing facilities available, this procedure was extremely work-intensive and time-consuming.

The rapidly evolving field of computer science, along with our constantly developing understanding of tyre dynamics, led to a new generation of more complex and more accurate tyre models. This new era started when H. B. Pacejka et al. in [81] presented an alternative modelling method (“Magic Formula”) which would revolutionise the way tyres are simulated. Since the introduction of the Magic Formula, which is capable of simulating a limited amount of steady state phenomena, tyre models have been evolving in an attempt to improve their accuracy and their ability to predict tyre behaviour as a response to various inputs. Although this evolution has been highly important, as it provided a broad insight into tyre dynamics, it led to the current situation in which tyre models are extremely demanding in terms of computational power and parameter identification. In particular, this new tyre modelling generation is divided into three major categories; namely, the analytical, the empirical and the high-fidelity discretised models. The fundamental difference between these three approaches is the way in which each model is formulated. The analytical models are based on currently established theoretical knowledge and, through various assumptions, simulate the tyre structure as a significantly less complex body. On the other hand, the empirical tyre models require numerous experimentally obtained data so as predict the response of the tyre. The high-fidelity discretised models exploit recent advances in computer science and the investigated tyre is modelled as the sum of simpler elements. Typical representatives of the last category are tyre models developed in an FEM environment.

Without any doubt, the current state-of-the art in tyre modelling, which is demonstrated in the following sections, represents a significant leap in simulating tyre-related phenomena. In spite of that, it is also demonstrated that each one of these models imposes the requirement for a variety of intensive experimental procedures in order to identify numerous parameters associated with its structure. Apart from the time-inefficiency of this approach, current models tend to become extremely parameter-sensitive and as a result a minor, experimentally induced, parameterisation error could compromise the validity of the simulation output. After all, one could state that *“a tyre model is as accurate as its identified parameters”* and one may wonder whether the current tendency in tyre modelling is on the right path or an alternative approach is required.

The objective of this chapter is to present the tyre models which have made a significant contribution in this particular research field. This presentation is aimed at demonstrating the requirement, mentioned above, for acquisition of a significant amount of intricate experimental data and, in addition, the identification of several parameters, along with complexities arising from the formulation of each model.

## 2.2 Magic Formula

H. B. Pacejka’s Magic Formula (MF) has been the starting point of significant advances in tyre modelling. It has altered the way in which tyres had been modelled for decades, it is used even today for steady-state studies and it can be implemented as the essential friction model in more advanced high-fidelity tyre models.

In [9], [10], [80] and [81], H. B. Pacejka et al. used a modelling method similar to the tyre modelling approach widely spread during that era – fitting of a polynomial expression to experimentally obtained data<sup>[29]</sup>. By examining the tyre shear force and moment characteristics, as a function of longitudinal or lateral slip, it became apparent that the adoption of a polynomial, as a way to express these curves using an analytical form, may not be the optimum method. An alternative equation, with a basic form which is similar to the force and moment versus slip curves, was required and the outcome of that investigation is the following expression:

$$y = D \cdot \sin[C \cdot \arctan[Bx - E(Bx - \arctan(Bx))]] \quad 2.2-1$$

in which

$$y(x) = Y(x) - S_V \quad 2.2-2$$

$$x = X + S_H \quad 2.2-3$$

and

B: stiffness factor

C: shape factor

D: peak value

E: curvature factor

$S_H$ : horizontal shift

$S_V$ : vertical shift

The above quantities correspond to the force versus slip or moment versus slip curves, see Figure 2.1.

Also:

Y: longitudinal force, lateral force or aligning moment generated in the contact area between the tyre and the ground

X: slip angle ( $\alpha$ ) or slip ratio ( $\kappa$ ) as defined by the following two expressions:

$$\alpha = \arctan \left( -\frac{V_{sy}}{V_x} \right) \quad 2.2-4$$

$$\kappa = -\frac{V_x - V_x \frac{\Omega}{\Omega_0}}{V_x} \quad 2.2-5$$

where  $V_x$  is the longitudinal speed of the wheel centre,  $V_{sy}$  is the lateral component of the slip velocity,  $\Omega_0$  is the lateral component of the rotational velocity of the wheel corresponding to  $V_x$  and  $\Omega$  is the actual lateral component of the rotational velocity of the wheel.

Depending on the range of the experimental data, this formulation of the MF can produce reliable results, for steady-state studies, using minimum computational resources. The above

constants are identified using a set of experimental data points and they are influenced by tyre parameters, such as vertical load and camber angle. As it is obvious, more data points give more accurate constant values. The way in which these constants affect the shape of the MF curves is displayed in the following figure:

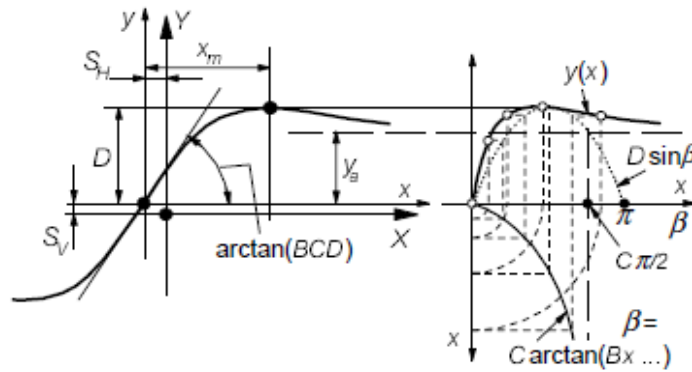


Figure 2.1 – Magic Formula curves and influence of constant terms ([80])

Advanced versions of the MF have been developed in order to reproduce more complex phenomena, such as combined slip, turn slip, and combination of ply-steer and conicity or even dynamic input and inflation pressure variations<sup>[16][78]</sup>. The main difference between Equations 2.2–1 to 2.2–3 and these versions is the interpretation of constants and inputs, which are modified to include the parameters that affect the abovementioned phenomena.

A comparison between MF results and experimental data can be found in [80]. The correlation between simulation and reality is accurate for pure lateral or pure longitudinal slip for a broad range of vertical loads. On the other hand, for combined slip, the deviation between MF and experimental data is significant, especially in the case of the aligning torque. As it can be seen from Equation 2.2–1, tyre deformation is not taken into account and consequently first order tyre behaviour cannot be captured using MF. Nevertheless, MF has successfully been introduced as the friction sub-model of higher fidelity models which take into account tyre belt dynamics, see Section 2.4.

## 2.3 Brush model

A thorough description of the tyre brush model can be found in [80]. The structure of this model consists of a number of elastic bristles connected to a rigid wheel. Some of these bristles are in contact to the ground and their deflection produces the horizontal contact

forces of the tyre. In the most fundamental form of the brush model, there are three distinct sets of equations, depending on the slip direction.

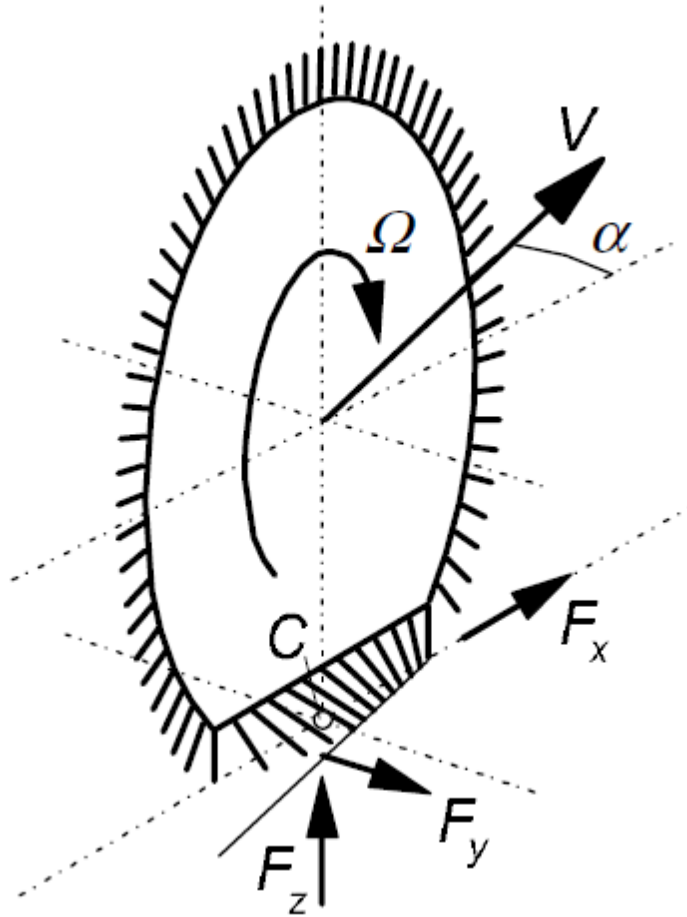


Figure 2.2 – The brush tyre model; view of the driven and side-slipping tyre ([80])

### 2.3.1 Pure lateral slip

In this case, the bristles in contact to the ground are deflected only in the lateral direction and as a result, the force vector has only a lateral component. A significant parameter of this model is the slip angle in which the tread is sliding, experiencing no adhesion regions. This angle is given by the following expression<sup>[80]</sup>:

$$\tan(\alpha_{sl}) = \frac{1}{\theta_y} \quad 2.3-1$$

where

$$\theta_y = \frac{2c_{py}a^2}{3\mu F_z} \quad 2.3-2$$

and  $c_{py}$  is the lateral stiffness of the bristle,  $a$  is half of the length of the contact area,  $\mu$  is the coefficient of friction and  $F_z$  is the normal force acting on the contact area. For additional information on the derivation of  $\theta_y$ , the reader may refer to equations 3.1 to 3.5 of [80].

The magnitude of the lateral force and the aligning moment depend on the relation between the actual slip angle and the  $\alpha_{sl}$  defined above. If  $|\alpha| \leq \alpha_{sl}$ , then:

$$F_y = \mu F_z (1 - \lambda^3) \text{sgn}(\alpha) \quad 2.3-3$$

and

$$M_z = -\mu F_z \lambda^3 \alpha (1 - \lambda) \text{sgn}(\alpha) \quad 2.3-4$$

where

$$\lambda = 1 - \theta_y |\tan(\alpha)| \quad 2.3-5$$

while if  $|\alpha| \geq \alpha_{sl}$ , then:

$$F_y = \mu F_z \text{sgn}(\alpha) \quad 2.3-6$$

and

$$M_z = 0 \quad 2.3-7$$

It should be noted that quantity  $\lambda$  in the above equations, expresses the distribution of sliding and adhesion regions. Another important quantity is the pneumatic trail, which is the distance between the contact centre and the point at which the resultant lateral force acts. If the magnitude of the slip angle is lower than  $\alpha_{sl}$ , then the pneumatic trail is:

$$t = -\frac{M_z}{F_y} \quad 2.3-8$$

In any other case, the pneumatic trail is equal to zero.

### 2.3.2 Pure longitudinal slip

The equations describing the pure longitudinal slip situation are similar to those presented above. If a particular study is focused only on the linear area of the tyre, then the resulting longitudinal force is given by the following expression<sup>[80]</sup>:

$$F_x = C_{F\kappa}\kappa \quad 2.3-9$$

in which the term  $\kappa$  is the slip ratio and the term  $C_{F\kappa}$  is the longitudinal slip stiffness.

An analytical expression for the longitudinal slip stiffness is the following:

$$C_{F\kappa} = \left. \frac{\partial F_x}{\partial \kappa} \right|_{\kappa=0} = 2c_{px}a^2 \quad 2.3-10$$

### 2.3.3 Combined slip

This section requires the introduction of the alternative slip, which is presented in the following equation, in vectorial form:

$$\boldsymbol{\sigma} = \begin{bmatrix} \sigma_x \\ \sigma_y \end{bmatrix} \Rightarrow$$

$$\boldsymbol{\sigma} = -\frac{\mathbf{V}_s}{V_r} \Rightarrow$$

$$\boldsymbol{\sigma} = -\frac{1}{V_r} \begin{bmatrix} V_{sx} \\ V_{sy} \end{bmatrix} \quad 2.3-11$$

where  $\mathbf{V}_s$  is the slip speed vector, and  $V_r$  is the rolling speed (see figure below).



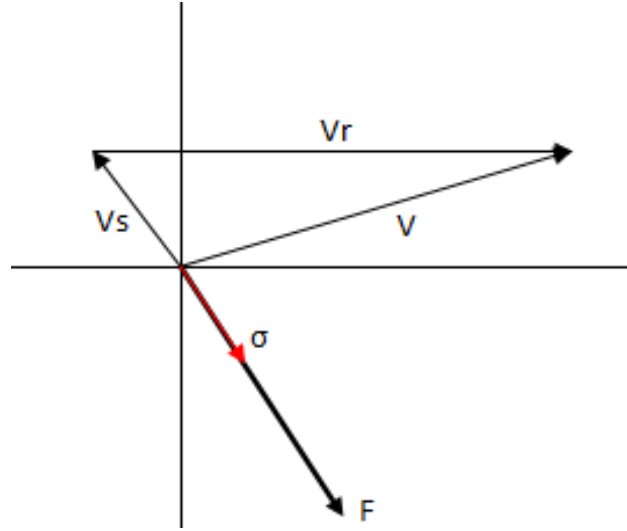


Figure 2.3 – Vectorial form of total slip

The method presented in the lateral force subsection is applied for the calculation of the total combined force. Initially, the slip, at which the total contact area is sliding, is obtained as follows:

$$\sigma_{sl} = \frac{1}{\theta} \quad 2.3-12$$

where parameter  $\theta$  is given by the following relation, assuming an isotropic material:

$$\theta = \theta_x = \theta_y = \frac{2 c_p a^2}{3 \mu F_z} \quad 2.3-13$$

The general form for the resulting force is the following:

$$\mathbf{F} = \begin{bmatrix} F_x \\ F_y \end{bmatrix} = F \frac{\boldsymbol{\sigma}}{\sigma} \quad 2.3-14$$

If  $\sigma \geq \sigma_{sl}$ , the magnitude  $F$  of the force  $\mathbf{F}$  is simply a function of the vertical load and the coefficient of friction:

$$F = \mu F_z \quad 2.3-15$$

If  $\sigma \leq \sigma_{sl}$ , the effect of partial slip regarding the contact area should be included in the expression for the magnitude  $F$ :

$$F = \mu F_z (1 - \lambda^3) \quad 2.3-16$$

where

$$\lambda = 1 - \theta \alpha \quad 2.3-17$$

The calculation of the aligning moment requires a modified expression of the pneumatic trail in order to adapt to the case of combined slip. An alternative form of the equation of the pneumatic trail, derived in the subsection of the pure lateral slip, is used by substituting the term  $\theta_y \cdot \sigma_y$  by  $\theta \cdot \sigma$ . By doing so, it is possible to obtain the pneumatic trail for the combined slip case (parameter  $\theta$  and slip  $\sigma$  are functions of  $x$  and  $y$ ) and, as a result, the aligning moment is:

$$M_z = -t(\sigma) \cdot F_y \quad 2.3-18$$

Similarly to the Magic Formula tyre model, presented in the preceding section, the brush model is capable of simulating the steady-steady shear force generation of a tyre in contact to the ground, but once again tyre belt dynamics are not taken into account.

## 2.4 Short Wavelength Intermediate Frequency Tyre model (SWIFT model)

The SWIFT model is described thoroughly in [80] and [93] and it is an extension of H. B. Pacejka's Magic Formula. As it was stated in Section 2.2, the MF can only be applied in steady-state studies. When the excitation of a wheel is not performed by a constant – in the time domain – input, there is significant deviation between the results of the MF and experimental data, because of the frequency dependency between an input variation and the respective tyre response<sup>[93]</sup>. The research group led by H. B. Pacejka has made several attempts to implement the MF into a more generic and dynamic tyre model. These preliminary steps include the relaxation length concept<sup>[50][72]</sup>, the introduction of a contact patch sub-model along with the MF<sup>[78]</sup>, or even the combination of these two elements with an elastically founded rigid ring which represents the – non-deformable in that context – tyre belt<sup>[71][118]</sup>.

On the relaxation length concept, its primary role is to accommodate for the phase lag between a dynamic tyre input (slip angle or slip ratio variation) and the resulting contact force

or moment. It is defined as the travelling distance of the tyre required so as the force generated in the contact area reaches the 63% of the respective steady-state value. The first dominant factor which dictates the relaxation length value is the compliance of the tyre structure, as most of the phase lag derives from the deformation of the tyre belt and the tyre sidewall<sup>[93]</sup>. The second effect, which is taken into account via this particular concept, is the mechanism which governs friction generation in viscoelastic materials. From a mathematical point of view, it is used as a 'distance' constant in the differential equations which describe the contact force development<sup>[71]</sup>. In the same study, it is demonstrated that a MF/relaxation length combination is capable of generating valid results for cases in which the excitation frequency does not exceed 8Hz. With reference to the present work, the relaxation length concept has been exploited for the validation of the proposed tyre model, see Chapter 5.

In cases where the investigation is focused on higher-fidelity tyre modelling, then a rigid ring representing the tyre belt should be included in the formulation of the model. Although the rigid ring implementation allows for a simple way to broaden the fidelity band of the tyre model, it imposes a significant limitation, i.e. an upper frequency limit which is located in the area between 60Hz and 100Hz<sup>[93]</sup>, depending on the tyre. In typical passenger car tyres, a higher excitation frequency results in triggering of tyre flexible modes and, consequently, the phenomena associated with these modes cannot be neglected, thus it is not valid to describe the tyre belt as a rigid ring<sup>[118]</sup>.

The basic structure of the SWIFT model is presented extensively in [92] and [93] and consists of the following 4 parts:

- Magic Formula
- Contact patch slip model
- Rigid ring
- Obstacle enveloping model

The theory describing the Magic Formula has been presented in Section 2.2. In the context of the SWIFT model, the MF is used to define the forces and moments which act on the contact patch. These forces and moments are used as an input to the contact patch slip model to excite the rigid ring.

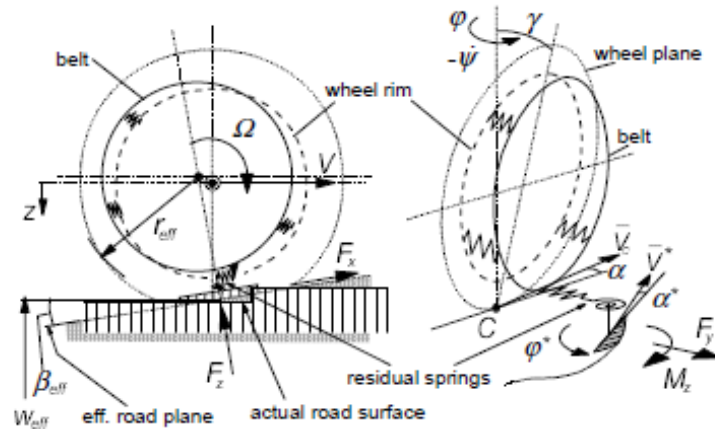


Figure 2.4 – SWIFT model formulation ([93])

As has been stated above, for an excitation frequency of up to circa 100Hz, the tyre belt can be simulated as a rigid ring<sup>[51][93]</sup> with moderate loss of information, as the contribution of tyre belt flexible modes is not dominant in that frequency band. In the SWIFT model, the rigid ring is constrained to the rim in all spatial six degrees of freedom by a number of elastic elements. Also, the residual elements presented in Figure 2.4 connect the ring to the contact patch. The influence of the rigid ring dynamics on the whole model is presented in [93], where a comparison between the MF model, the SWIFT model and experimental data is carried out. It is clear that the inclusion of the rigid ring is important for any cases where the excitation frequency is higher than circa 5Hz.

The final element of the SWIFT model is the obstacle enveloping feature, which allows for the simulation of road irregularities by using an effective road surface. This surface is produced by a number of elliptical cams and it is defined by three parameters. The first parameter is the vertical position of the effective road surface which is the average result of the vertical position of each cam across the width of the contact patch. The second one is the slope of the effective road, which is calculated by the same method as the vertical position. The third parameter is the road camber, which represents the slope of the road in the lateral direction.

An investigation of particular interest, which demonstrates the strong and the weak points of the SWIFT model and follows the previous work of P. W. A. Zegelaar et al. ([118]), is conducted by J. P. Pauwelussen et al. in [83]. In that study, the SWIFT model is compared to a sum of experimental data, in an attempt to simulate the challenging case of ABS-aided braking on uneven road. As it has been expected, in the lower frequency range (up to a critical point which is located between 60Hz and 70Hz where the first flexible tyre mode is triggered) the simulation results almost coincide with measurements. Beyond that critical point, the

deviation becomes non-negligible and consequently the results produced by the SWIFT model may not be trusted. Furthermore, in [51], the SWIFT model has been used to simulate a complicated parking manoeuvre and the respective results are compared to experimental data in terms of aligning torque. Some fine-tuning regarding the parameters of the model eliminates the deviation between the simulation and the experimental data, demonstrating that this particular model is capable of generating valid results for the abovementioned limited excitation frequency range.

Since the fundamental formulation and structure of the SWIFT model has been established, there have been various improved versions attempting to evolve it into a more generic model. H. B. Pacejka in [79] has developed an extended version to accommodate for the forces generated by the spin of the tyre, which is defined as *“the component of the rotational velocity of a body which is normal to the contacting surface”*. The same research group has investigated the possibility to include the tyre inflation pressure as a parameter of the SWIFT model in [16].

In the context of the present work, a tyre model formulation similar to the one found in SWIFT is adopted, as the contact sub-model output is used to excite the tyre structure. The fundamental difference between the proposed tyre model and the SWIFT model is that in the former case tyre deformation is taken into account.

## 2.5 LuGre tyre model

As it is stated in [17], the LuGre tyre model derives from the Dahl friction model. Consequently, a brief description of the latter is required before proceeding to the presentation of the former. The main expression of the Dahl model, regarding the friction force  $F$  between two bodies, is the following:

$$\frac{dF}{dx_r} = \sigma \left( 1 - \frac{F}{F_c} \operatorname{sgn}(v_r) \right)^\beta \quad 2.5-1$$

where  $x_r$  is the relative displacement,  $\sigma$  is the stiffness coefficient,  $F_c$  is the maximal friction force,  $v_r = dx_r/dt$  is the relative speed and  $\beta$  is a parameter which depends on the stress-strain curve. The shape of the friction force  $F$ , as it is derived by the above equation, is

different from the one obtained by the Magic Formula. The Dahl friction force increases for increasing relative displacement while the force from the Magic Formula reaches a maximum and then decreases.

The derivative of the friction force with respect to time is obtained by using the chain rule:

$$\frac{dF}{dt} = \frac{dF}{dx_r} \frac{dx_r}{dt} = \frac{dF}{dx_r} v_r = \sigma \left( 1 - \frac{F}{F_c} \operatorname{sgn}(v_r) \right)^\beta v_r \quad 2.5-2$$

If  $\beta=1$  the time derivative of the friction force is:

$$\frac{dF}{dt} = \sigma \left( v_r - \frac{F}{F_c} |v_r| \right) \quad 2.5-3$$

or in state model description:

$$\frac{dz}{dt} = v_r - \sigma \frac{z}{F_c} |v_r| \quad 2.5-4$$

where  $z$  is a relative displacement given by the following equation:

$$z = \frac{F}{\sigma} \quad 2.5-5$$

The relative length distance is defined as:

$$\eta_r(t) = \int_0^t |v_r(\tau)| d\tau \quad 2.5-6$$

The final expression for the Dahl model is obtained by implementation of the above equation in Equation 2.5-4:

$$\frac{1}{\sigma} \frac{dF}{d\eta_r} = -\frac{1}{F_c} F + \operatorname{sgn}(v_r) \quad 2.5-7$$

As it was mentioned above, the LuGre model is a tyre-specific application of the Dahl model. Its most fundamental version (“lumped model”) is presented in [17] and [26] and consists of the following 3 equations:

$$\dot{z} = v_r - \frac{\sigma_0 |v_r|}{g(v_r)} z \quad 2.5-8$$

$$g(v_r) = \mu_c + (\mu_s - \mu_c) e^{-|v_r/v_s|^\alpha} \quad 2.5-9$$

$$F = (\sigma_0 z + \sigma_1 \dot{z} + \sigma_2 v_r) F_n \quad 2.5-10$$

where  $\sigma_0$  and  $\sigma_1$  are the lumped stiffness and damping in the longitudinal direction,  $\sigma_2$  is the viscous relative damping,  $\mu_s$  and  $\mu_c$  are the normalized static and Coulomb friction,  $F_n$  is the normal force,  $v_r = r \cdot \omega - v$  and  $v_s$  are the relative and the Stribeck relative velocity,  $z$  is the internal friction state and parameter  $\alpha$  is used to adapt the expression of  $F$  to the steady state friction/slip curve.

A more complex version of the LuGre model can be found in [17]. The main difference between the lumped version and this, more advanced, model (“distributed model”) is that the latter evaluates the friction force for different points along the contact patch. If  $\zeta$  is the position of a point at the contact patch, the time rate of the deflection distribution is given by the following expression:

$$\frac{dz(\zeta, t)}{dt} = v_r - \frac{\sigma_0 |v_r|}{g(v_r)} z \quad 2.5-11$$

and the respective friction force:

$$F = \int_0^L dF(\zeta, t) \quad 2.5-12$$

The integration term of Equation 2.5-12, can be derived from Equation 2.5-13:

$$dF(\zeta, t) = \left( \sigma_0 \cdot z(\zeta, t) + \sigma_1 \frac{\partial z(\zeta, t)}{\partial t} + \sigma_2 \cdot v_r \right) dF_n(\zeta, t) \quad 2.5-13$$

In steady-state condition, the normal force distribution is only a function of space:

$$dF_n(\zeta, t)|_{s-s} = dF_n(\zeta) \quad 2.5-14$$

thus it can be expressed, by using the force per unit length function  $f_n(\zeta)$ , as follows:

$$dF_n(\zeta) = f_n(\zeta)d\zeta \quad 2.5-15$$

Combination of Equations 2.5–13 and 2.5–15, yields the expression of the total friction force:

$$F = \int_0^L \left( \sigma_0 \cdot z(\zeta, t) + \sigma_1 \frac{\partial z(\zeta, t)}{\partial t} + \sigma_2 \cdot v_r \right) f_n(\zeta) d\zeta \quad 2.5-16$$

Finally, the time derivative of variable  $z$  may be written in the following form:

$$\frac{dz(\zeta, t)}{dt} = \frac{\partial z}{\partial \zeta} \frac{\partial \zeta}{\partial t} + \frac{\partial z}{\partial t} \quad 2.5-17$$

Substitution of 2.5–17 into 2.5–11 produces a partial differential equation of  $z$  in space and time, which can be used to calculate the total friction force:

$$\begin{aligned} \frac{\partial z}{\partial \zeta} \frac{\partial \zeta}{\partial t} + \frac{\partial z}{\partial t} &= v_r - \frac{\sigma_0 |v_r|}{g(v_r)} z \xrightarrow{\frac{\partial \zeta}{\partial t} = |r\omega|} \\ \frac{\partial z}{\partial \zeta} |r\omega| + \frac{\partial z}{\partial t} &= v_r - \frac{\sigma_0 |v_r|}{g(v_r)} z \end{aligned} \quad 2.5-18$$

A two dimensional version of the LuGre model is developed in [112]. The force along axis  $x$  and  $y$  is calculated using the following equation:

$$F_i(t) = \int_0^L \mu_i(t, \zeta) \cdot f_n(\zeta) d\zeta, \quad i = x, y \quad 2.5-19$$

and the aligning torque is:



$$M_z(t) = - \int_0^L \mu_y(t, \zeta) \cdot f_n(\zeta) \cdot \left( \frac{L}{2} - \zeta \right) d\zeta \quad 2.5-20$$

In order to derive the term  $\mu_i$  of Equations 2.5–19 and 2.5–20, a friction model needs to be defined. This friction model consists of an expression regarding the deflection distribution and another one regarding the friction coefficient:

$$\dot{z} = \dot{u} - \lambda(u, \dot{u}, z) M_k^{-2} \frac{K}{F_n} z \quad 2.5-21$$

$$\mu = \begin{bmatrix} \sigma_{0x} & 0 \\ 0 & \sigma_{0y} \end{bmatrix} z - \begin{bmatrix} \sigma_{1x} & 0 \\ 0 & \sigma_{1y} \end{bmatrix} \dot{z} - \begin{bmatrix} \sigma_{2x} & 0 \\ 0 & \sigma_{2y} \end{bmatrix} \dot{u} \quad 2.5-22$$

Function  $\lambda(u, \dot{u}, z)$ , may be calculated by the following equation:

$$\lambda(u, \dot{u}, z) = \frac{\|M_k^2 \dot{u}\|}{g(\dot{u})} \quad 2.5-23$$

where function  $g(\dot{u})$  is defined as:

$$g(\dot{u}) = \frac{\|M_k^2 \dot{u}\|}{\|M_k \dot{u}\|} + \left( \frac{\|M_s^2 \dot{u}\|}{\|M_s \dot{u}\|} - \frac{\|M_k^2 \dot{u}\|}{\|M_k \dot{u}\|} \right) e^{-\left( \frac{\|\dot{u}\|}{v_s} \right)^y} \quad 2.5-24$$

If  $\mu_k$  is the kinetic coefficient of friction, the matrix  $M_k$  is:

$$M_k = \begin{bmatrix} \mu_{kx} & 0 \\ 0 & \mu_{ky} \end{bmatrix} \quad 2.5-25$$

and if  $\mu_s$  is the static coefficient of friction, the respective matrix is:

$$M_s = \begin{bmatrix} \mu_{sx} & 0 \\ 0 & \mu_{sy} \end{bmatrix} \quad 2.5-26$$

The matrix  $K$ , found in Equation 2.5–21, consists of the bristle stiffness in each direction:

$$K = F_n \begin{bmatrix} \sigma_{0x} & 0 \\ 0 & \sigma_{0y} \end{bmatrix} \quad 2.5-27$$

Finally,  $\dot{u}$  is the relative velocity between the bristles and the ground.

Having established the above friction model, a more suitable form for this particular application can be derived. The first quantity that needs to be defined is the matrix of the relative velocity between the contact area and the ground:

$$v_r = \begin{bmatrix} v_{rx} \\ v_{ry} \end{bmatrix} = \begin{bmatrix} \omega r - v \cdot \cos(\alpha) \\ -v \cdot \sin(\alpha) \end{bmatrix} \quad 2.5-28$$

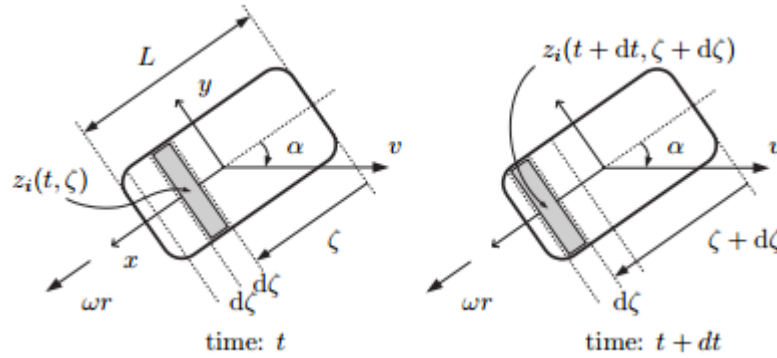


Figure 2.5 – Frame of reference and velocities at the contact patch. Derivation of the distributed tire model ([107])

The two-dimensional LuGre friction model consists of the following equations:

$$\frac{dz_i(t, \zeta)}{dt} = \frac{\partial z_i(t, \zeta)}{\partial t} + \frac{\partial z_i(t, \zeta)}{\partial \zeta} |\omega r| = v_{ri} - C_{0i}(v_r) \cdot z_i(t, \zeta), \quad i = x, y \quad 2.5-29$$

$$\mu_i(t, \zeta) = -\sigma_{0i} z_i(t, \zeta) - \sigma_{1i} \frac{\partial z_i(t, \zeta)}{\partial t} - \sigma_{2i} v_{ri}, \quad i = x, y \quad 2.5-30$$

Substitution of equation 2.5–30 into equations 2.5–19 and 2.5–20, produces the longitudinal and lateral friction forces and the aligning moment of the two-dimensional LuGre model, as presented in [112]. In that work, the abovementioned model is compared to a number of simulation data which can be found in [31] and the results coincide to a great extent.

Throughout the LuGre tyre model presented above, it is assumed that the tyre is a rigid body, see longitudinal and lateral speed calculation in equation 2.5–28, and consequently tyre flexible modes are not taken into account. With reference to the tyre model presented in this work, a modified version of the LuGre model presented above is embedded as the friction sub-

model exciting the flexible belt, see Section 3.4.2. The key element of this modified model, which was inspired by the work of J. Deur et al. in [26], is that sliding longitudinal and lateral speeds depend on tyre belt deformation.

## **2.6 Models based on the macroscopic physical description of tyres**

### **2.6.1 Introduction**

This category of tyre models is located between the empirical models, such as the Magic Formula or the SWIFT model, and the finite element models. One major issue of the empirical models is that, depending on the initial experimental data set, their valid simulation range is limited<sup>[34]</sup>. On the other hand, the finite element models tend to be accurate but demanding in computational power and, as a result, time-inefficient.

The following sections demonstrate the two dominant representatives of an alternative approach in tyre modelling, according to which the tyre is modelled as a whole structure, hence the term ‘macroscopic’, and not by identifying the physical properties of each tyre sub-component, such as the cord layers. Although this formulation allows for rapidly generated and accurate results for a wide range of simulation scenarios, it leads to the necessity to identify numerous tyre properties which, in the vast majority of tyre studies, represents a significant drawback.

During the writing of this thesis, the software entities developing the tyre models presented in the following two sections have released real-time versions of the respective models. Because of the commercial nature of these tyre models, no particular details have been published but it is to the author’s understanding that these real-time versions have been possible based on recent advances in solver algorithms in addition to significantly simplifying the virtual tyre representation by eliminating degrees of freedom and/or by adopting an extensive modal reduction approach. Nevertheless, although the economy of these models is enhanced in these latest releases, the fundamental drawback highlighted in this work, namely the extensive requirements in terms of parameter identification, is still confining the efficiency of the overall tyre modelling process.

### 2.6.2 Flexible structure tire model (FTire)

FTire is a commercially available tyre model which is presented in [39] and [40]. It is a highly non-linear model and it is able to cope with high-frequency inputs. The main structure of this particular model consists of two components. The first one is the structural part, which simulates the stiffness and damping phenomena within the tyre, while the second part describes the interaction between the tyre and the road.

The structural part is represented by a number of distributed nodes along the circumference of the tyre. Each one of these nodes is connected to the adjacent ones by stiffness elements as it can be seen in Figure 2.6.

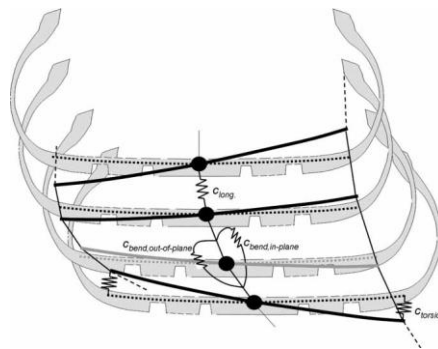


Figure 2.6 – Some force elements between adjacent belt elements and rim ([40])

The connection between the nodes and the rim is achieved by the model shown in the following figure:

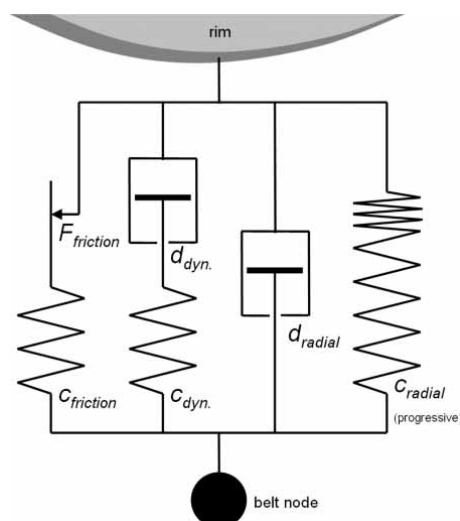


Figure 2.7 – Force elements between single belt node and rim (only those in radial direction shown) ([40])

It should be noted that the above spring and damping elements depend on the inflation pressure of the tyre.

The contact model consists of several stiffness elements located between two neighbouring nodes. The forces generated by these elements affect the nodes and, as a consequence, the structural model is excited. The shear force acting on an element of the contact model is a function of the normal load and the coefficient of friction:

$$|F_{\text{friction}}| = \mu(v_{\text{slide}}, p_{\text{ground}}, T_{\text{tread}}) \cdot F_{\text{normal}} \quad 2.6-1$$

The above description refers to the most basic version of the FTire model. There are several additional features which could be combined with this basic version. In [39] a temperature and a wear model can be found.

Since this model is commercially available, literature references regarding the respective solver algorithm are limited. A brief presentation is included in [40] but it is quite insufficient in describing the solver. Nevertheless, as it has been stated above, a significant disadvantage of the FTire model is the necessity to identify numerous parameters, a requirement which, depending on the available equipment, is not always effective and it introduces a substantial workload. These parameters may be found on the FTire official website and the complete list is presented below:

*‘The actual version of FTire needs as input:*

- *rolling circumference*
- *rim diameter*
- *tread width*
- *tyre overall mass*
- *portion of tyre mass that ‘moves’ with belt or tire radial stiffness at very low loads*
- *increase of overall radial stiffness at high speed, compared to radial stiffness during stand-still, and wheel speed, at which this dynamic stiffening reaches half of the final value*
- *percentage of rolling circumference growth at a running speed of 200km/h, compared to low speed*
- *natural frequencies and respective damping moduli of first, second and fourth vibration mode of inflated, but unloaded tyre with fixed rim*

- *natural frequency of the in-plane bending mode or belt in-plane bending stiffness of inflated but unloaded tyre*
- *natural frequency of the out-of-plane bending mode or belt out-of-plane bending stiffness of inflated but unloaded tyre*

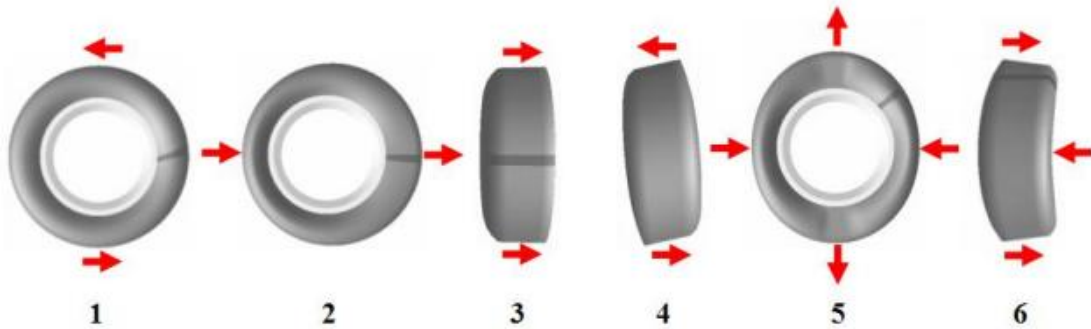


Figure 2.8 – First unloaded vibration modes for use in FTire parameterization and validation ([39])

- *profile height, i.e. mean groove depth in tread,*
- *rubber height over steel belt for zero profile height, i.e. distance between steel belt and grooves*
- *stiffness of tread rubber*
- *percentage of contact area with respect to overall footprint area*
- *quotient of tread rubber damping and elasticity moduli*
- *sum of the moments of inertia of rim and other rotating parts with respect to the wheel spin axis*
- *coefficients of maximum friction and sliding friction that occur between tread rubber and road, both at very low and at very high ground pressure values'*

From this extensive list, it is obvious that, although FTire is a powerful tyre model widely used in research and industry, the identification of each one of these parameters imposes a significant challenge to every tyre modelling study which incorporates the FTire model. Additionally, a non-accurate estimation or identification of a parameter could jeopardise the quality of the simulation results.

### 2.6.3 CDTire

Similarly to the FTire model, CDTire is a commercially available tyre model and, consequently, the related published material is quite limited. Nevertheless, an overview of the various versions can be found in [34].

The three different version of this particular model vary in terms of complexity, fidelity and capabilities:

- Model 20

Structural: Rigid ring with viscous-elastic sidewall

Frictional: Geometric normal contact and shear contact derived by a partial differential equation (no more information is provided)

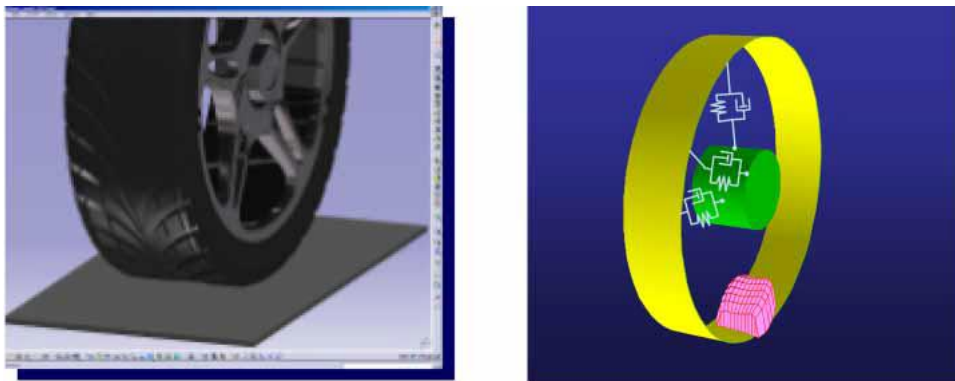


Figure 2.9 – CDTire model family (Model 20) ([34])

- Model 30

Structural: In-plane flexible tyre belt with viscous-elastic sidewall

Frictional: Brush type contact

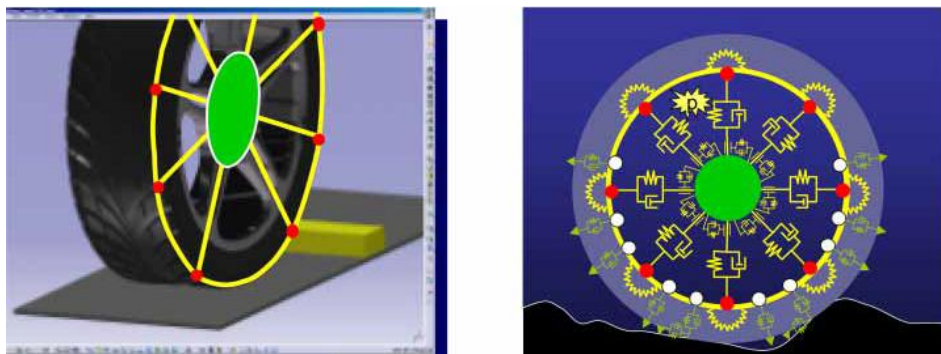


Figure 2.10 – CDTire model family (Model 30) ([34])

- Model 40  
Structural: 3D flexible tyre belt with viscous-elastic sidewall  
Frictional: Brush type contact

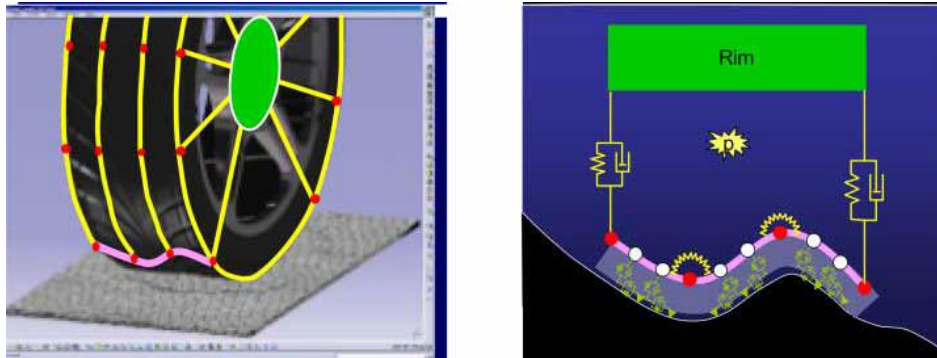


Figure 2.11 – CDTire model family (Model 40) ([34])

Each one of these versions dictates the identification of several parameters. The procedure according to which these parameters are identified is demonstrated in [34] and [35]. Initially, a tyre test rig is required in order to perform a series of static and dynamic measurements. These measurements include the estimation of the modal properties of the tyre, its capability for shear force generation and phenomena which affect the interaction between the tyre contact area and the (level or not) ground. Each set of measurements, which represents a significantly intensive and time-consuming workload, has to be repeated several times for different values of inflation pressure, preload and tyre speed<sup>[35]</sup>. Having obtained these experimental data, the next step is their exploitation so as to estimate the optimum set of parameters for the CDTire model via the implementation of an optimization algorithm. This algorithm minimizes an objective function, i.e. the deviation between the actual measurement and the outcome of the CDTire model for each set of parameters. After what seems like a computationally demanding process, described in [35], the abovementioned objective function is minimized. Consequently, the set of parameters which has generated these results is the optimum representation of the measured tyre.



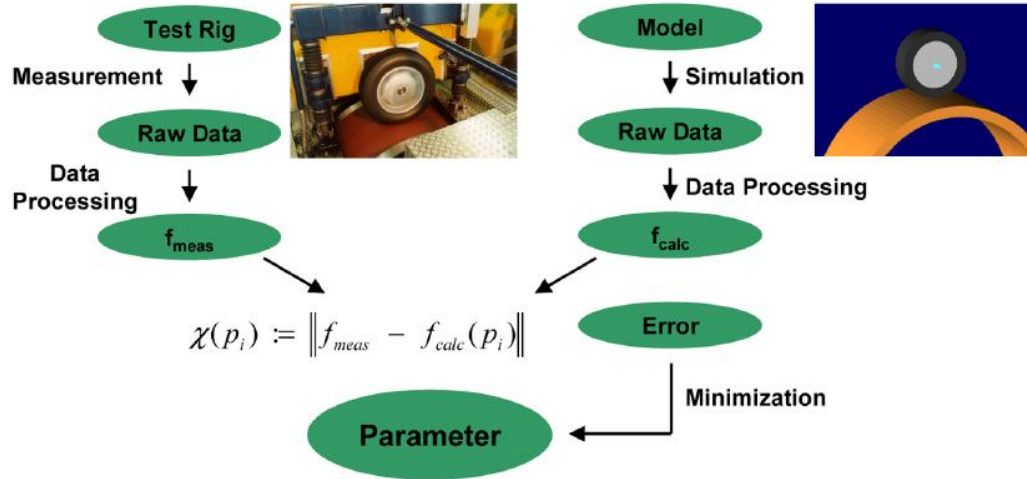


Figure 2.12 – Generic description of CDTire parameter identification procedure ([34])

A detailed comparison between the FTire and the CDTire models, in terms of tyre response to a cleat, is conducted in [48]. In that study, these two models are compared to a series of experimentally obtained results, which have been acquired using a unique tyre testing rig consisting of a double drum, a rigid frame mounted on the ground and an automotive suspension attached to the frame. Additionally, that rig has the feature to introduce several cleats attached along the circumference of the double drum.

The comparison between these two models and the experimental data is divided into two distinct cases. In the first case the investigation examines whether the simulation results are capable of matching the force generation of a ‘tyre without suspension on a drum’, while the second case explores the potential to simulate a ‘tyre-suspension assembly on a drum’.

The first investigation, which is of major interest in the context of the present work, has proved that either one of these two models is capable of generating valid results for the situation in which a tyre meets one or even several cleats, one of the most intriguing challenges for every tyre modelling attempt.

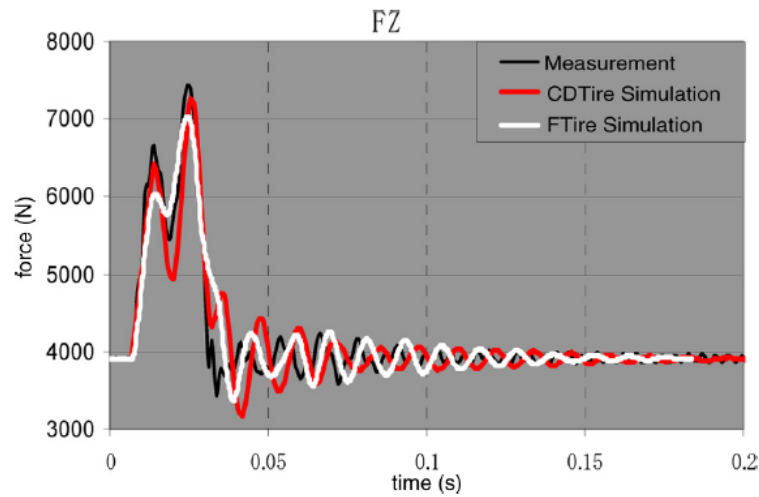


Figure 2.13 – Vertical force for a trapezoid cleat 20 mm high (without a suspension; drum surface speed, 40 km h<sup>-1</sup>) ([48])

In the second case, the experimental data are obtained from the suspension members of the rig, a situation which exceeds the purpose of the present work and it is closer to the immediate interests of the automotive industry. An additional sub-model representing the suspension has to be implemented in both models. According to H. Haga in [48], the suspension sub-models, which have been developed by the research groups developing these two tyre models, are responsible to a great extent for the deviation between simulation results and experimental data (see Figure 2.14 and Figure 2.15). In particular, the reason which causes this deviation is considered to be the bushing sub-model formulation and the non-linearity associated with that particular suspension component.

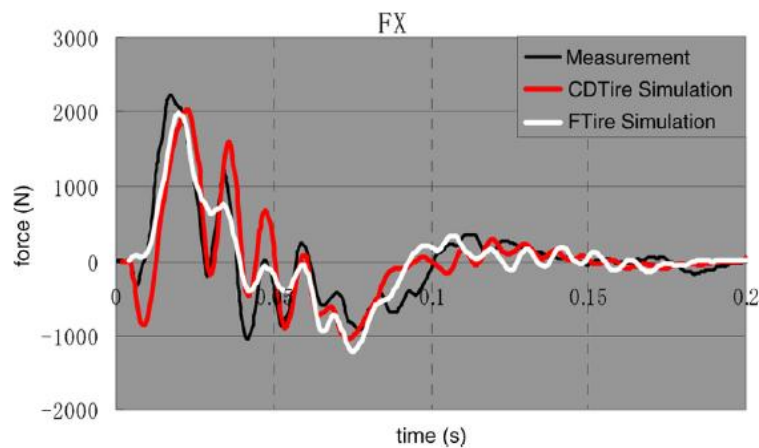


Figure 2.14 – Longitudinal force for a variant cleat 36 mm high (drum surface speed, 40 km h<sup>-1</sup>) ([48])

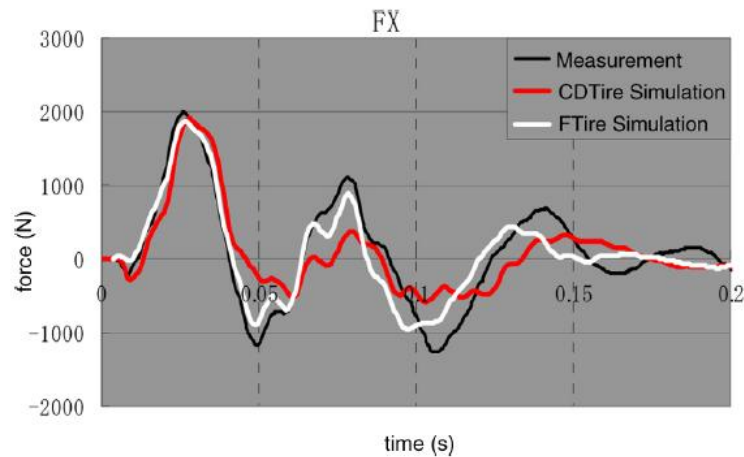


Figure 2.15 – Longitudinal force for a variant cleat 36 mm high (drum surface speed, 20 km h<sup>-1</sup>) ([48])

## 2.7 Finite element tyre models

The recent significant advances in computer science enabled the development of tyre models based on the finite element theory, a formulation which allows for dynamic and highly accurate simulation of tyre related phenomena as the tyre belt is represented by a deformable body. In general, the finite element theory, which is presented thoroughly in [47], [53] and [89], investigates the behaviour of simple elastic elements so as to generate analytical expressions for various quantities of interest, such as the deformation or the stress distribution along each element.

Having obtained the abovementioned analytical expressions, it is possible to simulate more complex geometries by combining a number of individual finite elements. Initially, it is necessary to generate a distribution of nodes along the original geometry of the body of interest, a procedure which is usually called *meshing*. These nodes define the edges of each element and, consequently, the initial body is divided into a number of basic elements.

Moreover, the location and the orientation of each element allow for the transformation and the combination of the local system matrices of each element into global stiffness, mass and damping matrices. These global matrices are used to simulate the dynamic response of the tyre as they formulate a system of second order differential equations, the input of which is the external force vector.

The current state-of-the-art in finite element tyre models varies in terms of complexity and some of the most typical cases are presented below. The simpler formulation of this category

of tyre models consists of an isolated two or a three-dimensional tyre belt. In this case, the input force vector depends on the air pressure, the sidewall forces acting on the inner edge or surface of the belt, and the distribution of contact forces. One representative model of this category has been formulated by H. Sugiyama and Y. Suda in [104]. In that work, the authors used their own purpose-developed curved beam element (see [102]), which is based on the theory of absolute nodal coordinate formulation developed by A. A. Shabana et al. in [13], [94], [95] and [103]. Some typical examples of the implementation of this formulation into beam-like elements, similar to the ones that could model the belt of a tyre, may be found in [14] and [96].

At this point, it is necessary to mention the RMOD-K tyre model. This is another commercial model, so literature resources are limited. However, C. Oertel and A. Fandre in [75] provide an insight into the structure and the expected results of this particular model. The main structure of the most advanced version of RMOD-K consists of a flexible belt and a rigid rim.

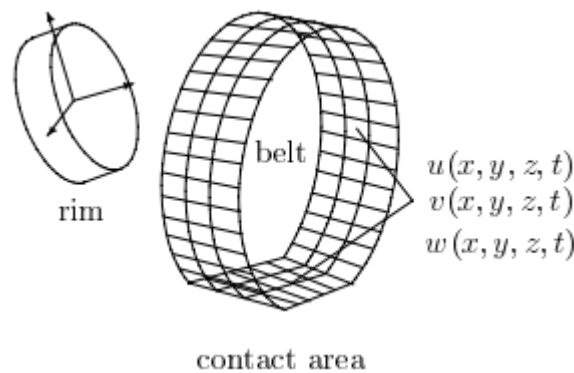


Figure 2.16 – Illustration of flexible belt and rigid rim ([75])

The following figure is derived from a 2D version of the flexible model and it represents the first five mode shapes, which are in accordance with results from theoretical models<sup>[60][110]</sup>.

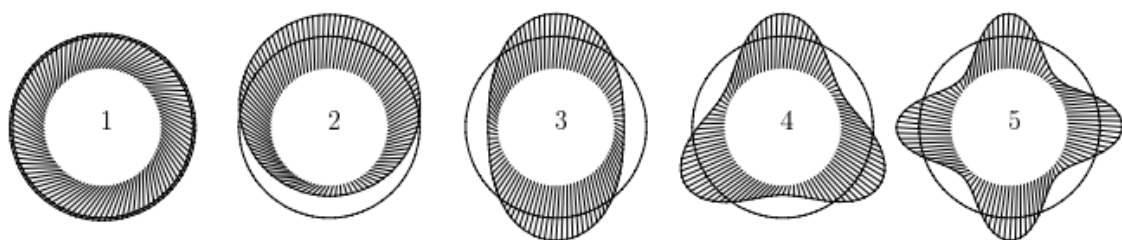


Figure 2.17 – Calculated mode shapes ([75])

In the same paper, there is an extensive comparison between the results of RMOD-K and measured data for various scenarios. The lack of deviation between simulation and experiment is remarkable for almost every case.

Furthermore, in the general case of tyre models consisting of finite elements, the next step is to include the sidewall structure in the mesh geometry. A typical example of this case has been the outcome of the research conducted by J. R. Cho et al. in [22]. The more advanced formulations include the air cavity in the mesh and describe the wheel as a deformable body as well. These models are too complex for regular handling studies and their use is focused on research associated with NVH phenomena. Such an investigation may be found in [58].

Currently, the most advanced finite element models are able to represent in detail various physical tyre properties, such as the tread pattern (see [21]). Due to the computational demands, imposed by such level of detail, the use and development of these models is usually oriented towards industrial exploitation. Another requirement for this type of models is the identification of material properties for each body represented by finite elements. In the present study, an attempt has been made to address these two elements – computational demands and identification of material properties – by introducing the proposed tyre model.

## **2.8 Analytical tyre models**

The analytical – vibrational tyre models represent an extensive field of research. Although there is no intention to explore these methods in the context of the present work, they offer a useful insight in the structural behaviour of pneumatic tyres. The fundamental formulation of such a model includes an analytical expression which describes tyre deformation. Several different approaches may be found in the literature and an extensive comparison has been conducted by A. Tsotras and G. Mavros in [111]. In particular, the analytical tyre models are divided into two distinct categories:

- In the first category the tyre belt is simulated using a one-dimensional linear element, such as a string or a beam, or a two-dimensional level element, such as a membrane element.
- In the second category the belt is modelled by a circular analytical element.

With regard to the first case, one may refer to the work of J. Perisse et al. in [84]. In that study, an orthotropic thin plate under tension is used to model the dynamic behaviour of an unloaded tyre. This plate is divided into three regions, along its longitudinal axis. The two external regions represent the sidewall of the tyre while the central one describes the belt:

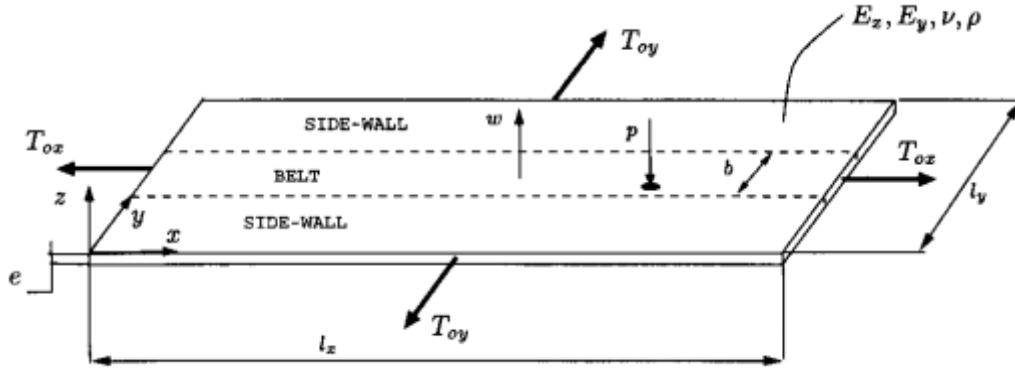


Figure 2.18 – Tire model: orthotropic thin plate under tension ([84])

According to Kirchhoff's hypothesis of thin plates, the governing equation of the vertical motion of such a plate is as follows:

$$\begin{aligned}
 & -T_{ox} \frac{\partial^2 w}{\partial x^2} - T_{oy} \frac{\partial^2 w}{\partial y^2} + B_x \frac{\partial^4 w}{\partial x^4} + B_y \frac{\partial^4 w}{\partial y^4} + \\
 & 2B_{xy} \frac{\partial^4 w}{\partial x^2 \partial y^2} + s + m'' \frac{\partial^2 w}{\partial t^2} = p(x_0, y_0, t)
 \end{aligned}
 \tag{2.8-1}$$

The tension of the membrane, which depends on the inflation pressure of the tyre, is denoted by  $T_{ox}$  and  $T_{oy}$ , along axes  $x$  and  $y$  respectively, while  $B_x$ ,  $B_y$  and  $B_{xy}$  represent the stiffness of the tyre in each direction.

The motivation of the investigation presented in [84] is to demonstrate the capability of such a plate to simulate the modal behaviour of a smooth tyre, for a given frequency range. Towards that aim, a series of measurements has been conducted in order to investigate the response of a freely suspended tyre to point excitation. The acquired data are exploited to modal update the parameters of the theoretical model. The deviation between the experimentally obtained eigenproperties and the results of the updated plate is minimized, for a limited frequency range, which can be altered by adjusting the updated parameters of the theoretical model, thus demonstrating that a pre-tensed orthotropic plate and a smooth tyre have similar modal behaviour, as illustrated in the following figures:

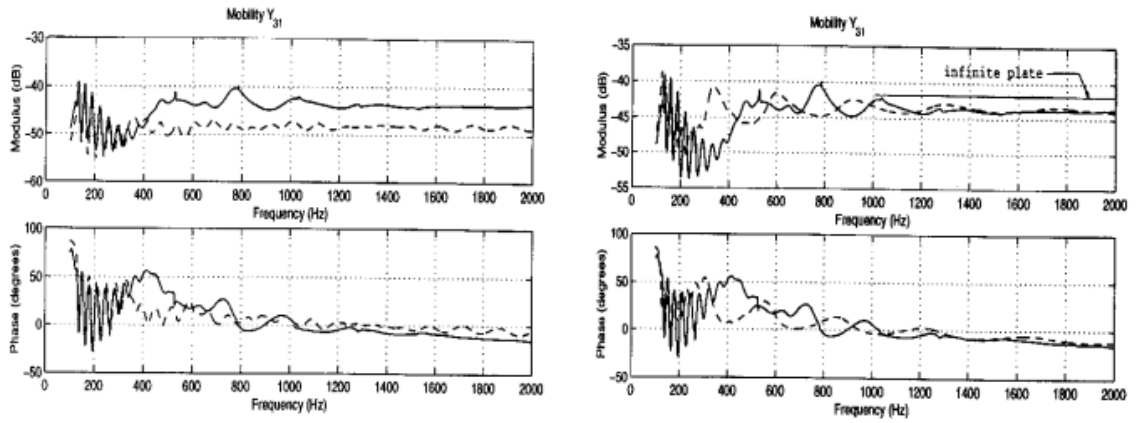


Figure 2.19 – Correlation between theoretical (pre-tensed orthotropic thin plate) and experimental results. (Left pair: model parameters updated within [20-400] Hz – Right pair: model parameters updated within [500-2000] Hz) ([84])

On the other hand, several tyre simulation attempts have used circular analytical elements to formulate a structural or even a complete tyre model. In [60], F. Kozhevnikov examines the vibrational characteristics of an unloaded in-plane tyre model by implementing two concentric bodies, namely a rigid disc and a cylinder. The modal behaviour of this model is described by two equations, the first one calculating the  $n^{\text{th}}$  natural frequency of the tyre and the second one the respective mode shape:

$$\omega_n^2 = \frac{-16\pi^4 a_0 n^4 + 4\pi^2 a_1 n^2 - a_2}{\rho r^3 (1 + 4\pi^2 n^2)} \quad 2.8-2$$

$$X_n(\varphi) = G_1^* \cos(n\varphi) + G_2^* \sin(n\varphi), \forall G_1^*, G_2^* \quad 2.8-3$$

Equations 2.8-2 and 2.8-3 produce the following mode shapes:

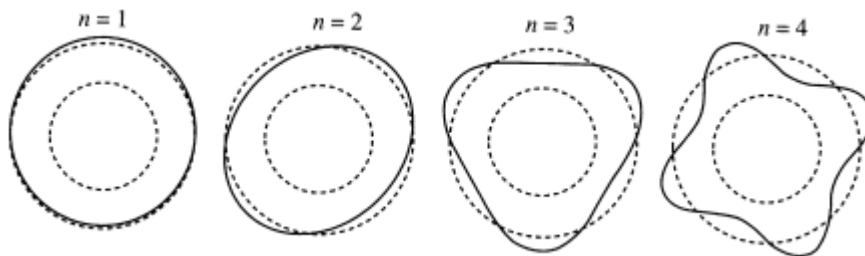


Figure 2.20 – The first four mode shapes derived by equation 2.8-3 ([60])

Several similar studies have been conducted in the past. In [62], C. Lecomte et al. examine the correlation between simulation results obtained by the tyre belt model developed in [61] and

the response of several established analytical models. This particular model consists of an orthotropic cylinder, a layout which is depicted in the following figure:

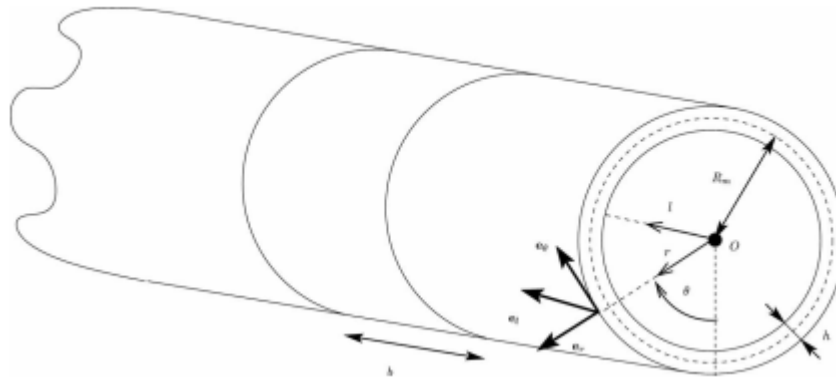


Figure 2.21 – Geometry of the infinite cylinder ([62])

The above formulation has been capable of producing valid results in the frequency range in which that particular – acoustic – study is focused (50 – 500Hz). Nevertheless, it has been noted by the authors that their proposed model should be altered in order to expand its effective frequency range, by incorporating the rotary inertia of the belt. Such a development has been included in the work of R. J. Pinnington in [85] and [86]. In that investigation, the primary aim of which is to examine the phenomena associated with the waves around and across the belt (propagating and standing respectively), the author has derived a six-order differential equation which predicts the deformation of the tyre, in the excitation frequency range between 0Hz and 4000Hz. One of the most significant features of this formulation is that the abovementioned equation is capable of including a variety of parameters, such as the inflation pressure, the rotary inertia of the wheel and its speed, in the prediction of the response of the tyre.



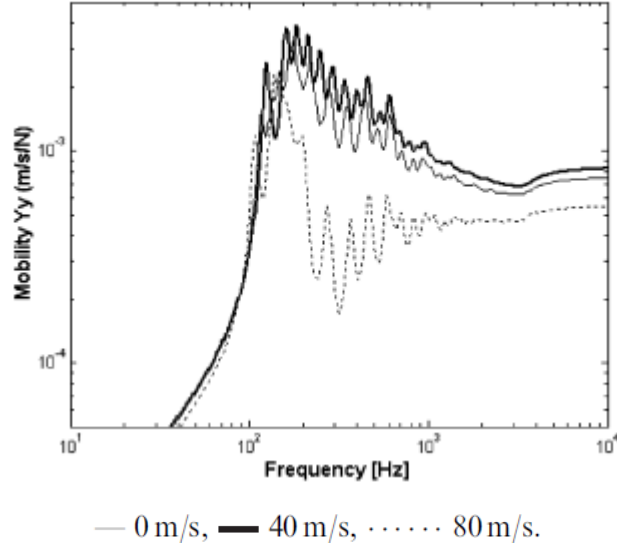


Figure 2.22 – Real part of input radial mobility as a function of speed ([85])

A. Tsotras, in [110], has conducted an in-depth research on in-plane, analytical tyre modelling. Based on previous work ([65] and [100]), he investigated its application in the field of tyre dynamics. The proposed equations of motion of a one-dimensional arch are the following:

$$-\frac{\partial^2 M_{ss}}{\partial s^2} + \frac{1}{R_s} N_{ss} + \rho d \frac{\partial^2 u_r}{\partial t^2} = 0 \quad 2.8-4$$

$$-\frac{\partial N_{ss}}{\partial s} - \frac{1}{R_s} \frac{\partial M_{ss}}{\partial s} + \rho d \frac{\partial^2 u_t}{\partial t^2} = 0 \quad 2.8-5$$

where  $M_{ss}$  is the normalised bending moment of the arch,  $N_{ss}$  is the tension pressure of the arch,  $R_s$  is the radius of the arch and  $s$  is the length along the central axis of the arch. Analysis of equations 2.8–4 and 2.8–5 provides the following mode shape pattern:

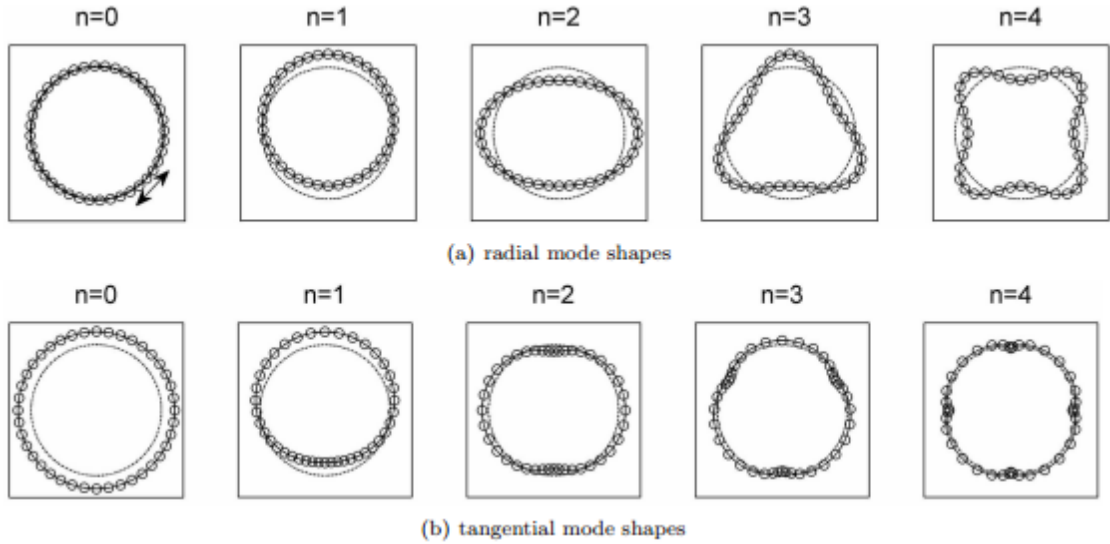


Figure 2.23 – Ring model mode shapes ([110])

A (pseudo) three dimensional analytical tyre model has been developed by P. Kindt et al. ([58]). Although the purpose of that work is to predict the tyre-generated noise, and the final version of that model was realised by applying the finite element theory, the initial approach offers the chance to examine the out-of-plane structural phenomena from an analytical point of view. The equations of motion of an elastic ring on elastic foundation are the following (the lateral motion is not included):

$$\begin{aligned} \frac{D}{R^4} \left( \frac{\partial^2 u_\theta}{\partial \theta^2} - \frac{\partial^3 u_3}{\partial \theta^3} \right) + \frac{K}{R^2} \left( \frac{\partial^2 u_\theta}{\partial \theta^2} - \frac{\partial u_3}{\partial \theta} \right) + \frac{N_{\theta\theta}^r}{R^2} \left( \frac{\partial u_3}{\partial \theta} - u_\theta \right) - \\ k_\theta u_\theta - \frac{p}{R} \left( \frac{\partial u_3}{\partial \theta} - u_\theta \right) + q_\theta = \rho h \frac{\partial^2 u_\theta}{\partial t^2} \end{aligned} \quad 2.8-6$$

$$\begin{aligned} \frac{D}{R^4} \left( \frac{\partial^3 u_\theta}{\partial \theta^3} - \frac{\partial^4 u_3}{\partial \theta^4} \right) - \frac{K}{R^2} \left( \frac{\partial u_\theta}{\partial \theta} + u_3 \right) + \frac{N_{\theta\theta}^r}{R^2} \left( \frac{\partial^2 u_3}{\partial \theta^2} - \frac{\partial u_\theta}{\partial \theta} \right) - \\ k_3 u_3 + \frac{p}{R} \left( \frac{\partial u_\theta}{\partial \theta} + u_3 \right) + q_3 = \rho h \frac{\partial^2 u_3}{\partial t^2} \end{aligned} \quad 2.8-7$$

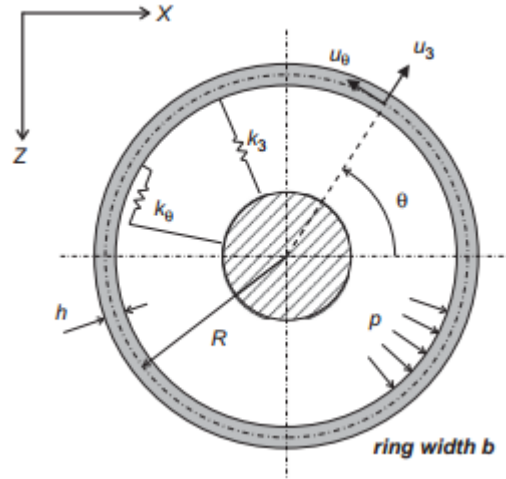


Figure 2.24 – Flexible ring on elastic foundation with internal pressure ([58])

The eigenvalues and the amplitude ratio of radial and tangential displacements can be calculated from equations 2.8–6 and 2.8–7. In addition, because of the exclusion of the lateral motion component from the equations of motion presented above, this structure is considered as a single degree of freedom system with regard to the lateral direction, hence the term “pseudo three-dimensional model”. By making this assumption, it is possible to derive the natural frequency of the lateral mode:

$$\omega_{\text{axial}}^2 = \frac{k_a}{\rho h} \quad 2.8-8$$

Another representative of this class of tyre models is the UniTire model, presented in the work of K. Guo et al. in [46]. This particular model is driven by an array of user-defined kinematic and dynamic inputs and the – purely dynamic – output consists of contact forces and the resulting moments. In essence, this model demonstrates a dual nature, partially empirical and partially physical. Similarly to the SWIFT tyre model, contact forces are calculated by an analytical expression comparable to the Magic Formula presented in section 2.2. Moreover, the physical component of this particular model consists of the calculation of tyre belt dynamics, in order to capture the first order behaviour of the tyre, and consequently the respective stiffness values have to be identified.

## 2.9 A modal approach towards the simulation of tyre deformation

As has been demonstrated in the preceding sections of this chapter, the ability of a tyre model to capture the tyre response to dynamic input depends heavily on whether the tyre belt and

the sidewall deformation is included in the formulation of the model. The FTire model, which has been demonstrated in Section 2.6, represents a broad category of tyre models in which the belt and the sidewall are taken into account via the distribution of linear and non-linear springs and dampers. On the other hand, the finite element method has been implemented into a range of tyre models, in which the tyre belt and the sidewall are divided into a number of analytical finite elements and the deformation of the whole structure is calculated by the deformation of each element.

The recent advances in modal experimental equipment, along with our understanding of structural tyre behaviour which has been enhanced by the development and use of the abovementioned models, have led to an alternative, efficient, and accurate way of simulating tyre deformation. This method, which has been a cornerstone for the present study, ranges from identification of tyre properties to development of complete tyre models derived directly from experimental modal procedures and/or modal analysis.

This particular method may be used for acquiring several tyre eigenproperties. L. H. Yam et al. in [116] have experimentally obtained the three-dimensional mode shapes of a tyre. Moreover, F. Chengjian and G. Dihua have used modal testing and analysis to examine the tyre vertical properties and their influence on force generation along the contact patch in [19]. On a relatively more complex phenomenon, tyre damping has been studied in [36] and [87]. In these studies, the non-proportional viscous damping of a physical tyre has been derived by modal experimental data, see Figure 2.25.

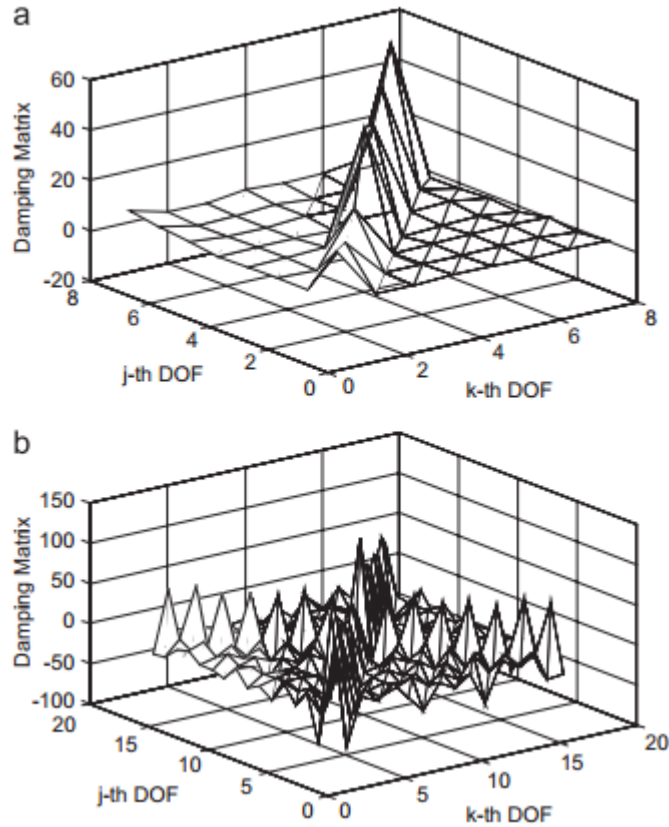


Figure 2.25 – Identification of general viscous damping in the pneumatic tyre (7.5 bar): (a) modal coordinates; (b) physical coordinates ([36])

I. Lopez et al. have extensively investigated the potential of using modal properties in tyre modelling in [64] along with the effect of tyre operation upon these properties ([63]). A similar study has been conducted by D. Guan et al. in [43], in which tyre vertical properties are described by a combination of theoretical and experimentally derived spring coefficients. In particular, the sidewall and tread stiffness coefficients are obtained from literature while the carcass stiffness is calculated from modal parameters which have been obtained by exciting a freely suspended tyre.

On the matter of tread modelling, P. Andersson et al. ([6]) have focused their research on the higher frequency range in an attempt to broaden our understanding regarding this challenging area. Although the general purpose of the present study sets the upper frequency limit significantly lower than the typical frequencies found in the work mentioned above, the outcomes of [6] have been useful in providing a valuable insight into tread modelling.

## 2.10 Assessment of the presented tyre models

The preceding presentation of the advances achieved in tyre modelling during the last three decades offers a broad overview into the current tendencies in the respective research field. It has been evident that a major issue arises in each one of these models, namely the identification of the required parameters or the acquisition of an adequate amount of experimental data.

Although the *Magic Formula* may be considered as a relatively straightforward steady-state model, an extensive range of experimental data is required for its application. This range consists of a number of curves, which represent the force or moment generation versus tyre slip, for a given set of tyre parameters, such as vertical load, camber angle etc. The procedure to obtain these curves requires a significant investment in financial and time resources, as specifically designed and manufactured equipment has to be developed along with the time-consuming routine of logging tyre forces for various slip sweeps in addition to the necessary post processing. Moreover, this particular tyre model does not take tyre deformation into account and consequently it is considered as a low-fidelity model.

Remaining in the same category of steady-state models, the shear force generation in the case of the *brush model* derives from the local longitudinal and lateral deformation of an array of elastic bristles. Every bristle located between the leading and the trailing edges of the contact patch interacts with the ground through the locally applied contact force. This force results in the deformation of the bristle and consequently the bristle generates a force which acts on the tyre belt. Similarly to the Magic Formula, force/moment versus slip curves are required so as to identify the – highly critical in the context of this particular model – structural properties of the bristles.

The *Short Wavelength Intermediate Frequency Tyre* (SWIFT) model has been an evolution of the Magic Formula (MF). As it has been demonstrated in the present study, the latter model is not capable of capturing the response of a tyre structure to an input of relatively high frequency. The SWIFT model overcomes this limitation by initially applying the relaxation length concept. In particular, in each time step, the steady-state response of the tyre is obtained by implementing the MF. This response and the differential equation associated with the relaxation length are the fundamental elements in calculating the actual response of the

structure. According to [93], this formulation is capable of generating valid results for an input frequency of up to 8Hz, which is not adequate for NVH studies. As the input frequency of the model rises, the influence of the belt rotation and deformation along with the resulting forces cannot be neglected. Consequently, in the SWIFT model formulation, a rigid ring on an elastic foundation is implemented to accommodate for these phenomena. In commercially available road tyres, the belt can be simulated as a rigid ring for an input frequency of up to approximately 60Hz, due to the deformation of the belt at higher frequencies. This constraint is one major drawback of the SWIFT model as an NVH investigation tool. Moreover, the layout of the rigid ring on elastic foundation imposes an additional constraint in terms of vertical stiffness as correlation is achieved via residual spring elements<sup>[80]</sup>. On the contrary, the tyre model introduced in Chapter 3 of the present body of work has been formulated so that vertical deflection modes are part of the proposed flexible belt model and additionally these two components share a common parameterisation process which leads to minimisation of tyre testing requirements.

One recently developed category of tyre models, which lies between the less complex empirical models and the more advanced and demanding finite element models, is the one represented by the commercially available *FTire* and *CDTire* software packages. The principle involved in these two formulations is that the tyre is modelled as a whole structure in a ‘macroscopic’ manner. This method allows for time-effective simulation studies, in comparison to models based on the finite element theory where the tyre structure is modelled in extensive detail. Additionally, these models are capable of simulating an extended range of phenomena which may affect a tyre and their simulation results are significantly more accurate in a broader frequency range than the ones derived from empirical models, such as the Magic Formula or the brush model. These impressive advantages come with a significant drawback, which is the parameter identification required by each one of these packages. In particular, the *FTire* model requires a combination of geometrical, modal and frictional tests in order to estimate an extensive list of parameters, while the *CDTire* parameters are derived by implementing an algorithm which minimises the deviation between the results of the model and experimentally obtained data.

The *finite element method* has its origin in the 1940s but it has been implemented in tyre-related studies only in the recent years. A complete tyre simulation requires the mesh generation for various materials of different properties, including the ones used in tyre

structure (rubber and steel for instance) along with the ones surrounding the tyre (wheel, road, air, etc). This is a computationally demanding task and as a result it was not a feasible option until the required computational resources became widely available. Although the finite element (FE) tyre models represent a class of high-fidelity models that generate valid results and are capable of simulating a wide range of phenomena, including tyre tread/road contact and hydroplaning, there are some significant drawbacks. Even in cases where computational power is adequately high, at least for the current standards, detailed finite element tyre models tend to be time-inefficient. Moreover, the requirement to identify material properties could introduce an additional parameterisation challenge.

The case of tyre modelling using *analytical expressions* to capture the deformation of the tyre belt is relatively similar to the one consisting of a model where the tyre structure is represented “macroscopically” by a number of stiffness and damping elements. Models found in this category are time-efficient as they introduce low demands in computational power. In addition, the respective results do not depend on numerical issues, contrary to other formulations where this dependency may introduce several problematic effects in the simulation procedure. Nevertheless, the necessity to obtain a valid set of modal parameters is still present and, as the respective identification is not always feasible and/or reliable, it may fundamentally jeopardise the quality of the simulation results.

Currently, it seems that tyre modelling using *modal techniques* may introduce a relatively new way into simulating tyre-associated phenomena. In the majority of simulation studies, the frequency range of interest, which depends on the purpose of each particular investigation, is defined during the initial stages of model formulation. Although this frequency restriction sets a limitation in the model use, it introduces a positive side-effect as it allows for the transformation from physical to modal coordinates, presented in [64]. In the generic case, the number of modes used, which is dictated by the desired frequency range, is significantly lower than the degrees of freedom of the system. Consequently, this transformation reduces the number of differential equations describing the motion of the tyre, making the model more time-effective and less demanding in computational power. In addition, instead of making an attempt to experimentally identify material properties or spring element characteristics – which are essential in order to capture tyre deformation for some models – a modal model derived directly by modal testing on the actual tyre could provide an effective method of identifying tyre belt deformation.



## **2.11 Alternative tyre modelling approach**

Each one of the models presented above imposes the necessity to perform a series of, not always efficient, measurements so as to either obtain adequate experimental data in order to describe the force generation properties of the tyre, or to identify a number of physical tyre properties, which are associated with the tyre structure and dictate its response to dynamic excitation, or both. Consequently, this Chapter has demonstrated that the currently established tyre models require the collection of a significant amount of experimental data. Having obtained these data sets, their post-processing will provide the optimum estimation of several quantities of interest and through various assumptions, which may introduce a level of inaccuracy in the simulation results, each tyre model is formulated. At this point, one may wonder whether there is an actual necessity for the abovementioned process. An alternative tyre modelling approach, that is a tyre model formulated by data derived directly from modal testing, allows for the feasible and straightforward representation of the structural part of the tyre, and consequently the broad aim of this body of work is to demonstrate that this approach could result in a fully operational three dimensional tyre model.

Accordingly, this alternative tyre modelling approach has been adopted within the present work, and the role of the structural tyre sub-model presented in Chapter 3 is to capture the tyre belt deformation, occurring when the tyre is excited either by the application of contact forces or by the tyre motion or by a combination of these two phenomena. The respective equations of motion are populated by exploiting data derived directly from modal testing performed on the physical tyre, thus it is a feasible to populate and a time-efficient model of high fidelity. In addition, the number of differential equations of motion depends on the fidelity of the model, rather than the number of degrees of freedom. This approach is particularly suitable for the case of tyre modelling because, depending on the purpose of the tyre model, the number of elastic modes taken into account is significantly lower the number of nodes representing the tyre, which typically is chosen relatively high so that distribution of contact forces is calculated with a minimum discretisation error. Moreover, as the present study is not oriented into examining tread modelling in depth, a common formulation has been implemented into the proposed tyre model so as to secure reliability and consistency in the interaction between the tyre and the ground. Vertical tread dynamics are captured by

applying an elastic layer between the tyre and the ground and shear force generation is calculated by a distributed LuGre model.

The introduction of rigid-body modes of the wheel in the proposed tyre model is one of the key elements in the present investigation. The rapidly rotating mass of the wheel affects the acceleration of every point of the tyre structure. The immediate consequence of this influence, depending on the triggered tyre flexible modes, is the structural deformation of the tyre, and this effect is of great importance in cases where the mass of the tyre is comparable to the mass of the vehicle. As it is demonstrated in Chapter 3, these two sub-models – flexible tyre belt and rigid wheel – have been formulated starting from first principles and they are solved in a parallel manner to yield the total tyre motion and deformation.

### **3. Tyre model formulation**

#### **3.1 Introduction**

As has been demonstrated in the second Chapter of the present Thesis, the ability to predict dynamic tyre phenomena depends mainly on the inclusion of tyre belt deformation modes, which occur in a frequency band exceeding 60Hz, as will be shown in Chapter 4. This imposes an additional complexity, as the current high fidelity dynamic tyre models are either demanding in terms of computational power (models adopting the finite element method), or require numerous parameters which are not always feasibly obtainable (physical and/or analytical models). This limited parameterisation and simulation efficiency of the current state-of-the-art of high-fidelity tyre models has been the motivation of the present work. In the proposed approach, the key element is the coupling between the non-linear three-dimensional macroscopic motion of the wheel with the linear tyre belt deformation, the modelling of which is performed using parameters obtained directly by eigenanalysis of modal testing data.

This particular modelling approach is described in detail in the following sections. Initially, the structure of the model is presented in Section 3.2, while in Section 3.3 the core of the model is demonstrated. Starting from a first principles approach, the motion of the wheel is divided into two distinct components, namely the macroscopic non-linear motion of the wheel as a rigid body, and the local linear deformation of the tyre belt, see Section 3.3.1. The system of equations expressing the tyre belt as a flexible body is presented in Section 3.3.2. The calculation of the rigid-body motion of the wheel is conducted in an analytical manner and demonstrated in Section 3.3.3, while the next section is dedicated to capturing the motion of every belt node with respect to the global frame of reference, a process which is essential in calculating the contact forces generated between the tyre and the road. The topic of the last sub-section of 3.3 is the formulation of the external force vector used to excite the flexible tyre belt. In this particular vector both nodal contact forces and the motion of the wheel as a rigid body are taken into account.

The implemented contact sub-model is presented in Section 3.4. Initially, the vertical force distribution in the contact patch is calculated, via an approach based on an elastic boundary concept. To this end, the global vertical position and velocity of the tyre belt nodes, which

have been obtained in the previous section, are exploited. Shear force generation in the contact patch is modelled using a distributed LuGre friction model. Having previously obtained the vertical force distribution and the global velocities of the contact nodes, the distribution of longitudinal and lateral contact forces is calculated. The last part of Section 3.4 demonstrates the rotating drum concept which is embedded within the contact sub-model. This addition has been essential as experimental data presented in Chapter 5 have been acquired by a tyre testing facility which incorporates a rotating drum.

## **3.2 Model overview**

### **3.2.1 Model formulation**

The cornerstone of the proposed model is the way in which belt response is obtained, i.e. by superposition of the responses of a non-linear rigid wheel and a linearly deformable belt. The main advantage of this approach is that a non-linear rigid body model can be developed analytically while the deformable belt model derives directly from experimental modal analysis. In total, the proposed tyre model consists of the following sub-models:

- Rigid-body motion sub-model
- Belt deformation sub-model
- Contact sub-model

The belt deformation and the rigid-body motion sub-models consist of a number of nodes, which are located in the circumference of the belt and are capable of moving in the three-dimensional space. The equations which describe these two sub-models are solved separately, in an almost parallel manner, and the superposition of the respective results defines the total response of the belt.

The contact sub-model implements a brush-like formulation to predict vertical pressure distribution and shear force generation in the contact area. In particular, the vertical pressure distribution is calculated by a number of vertical Kelvin elements, each attached to a belt node located in the contact patch. With regards to frictional forces, the distributed LuGre model – presented in the second Chapter – is used.

The excitation of the model consists of four user-defined quantities, see Figure 3.1:

- vertical load ( $F_z$ ),

- steer angle ( $\delta$ ),
- road/drum longitudinal speed ( $v_d$ ) and
- wheel angular velocity along the lateral wheel-fixed axis ( $\Omega$ ).

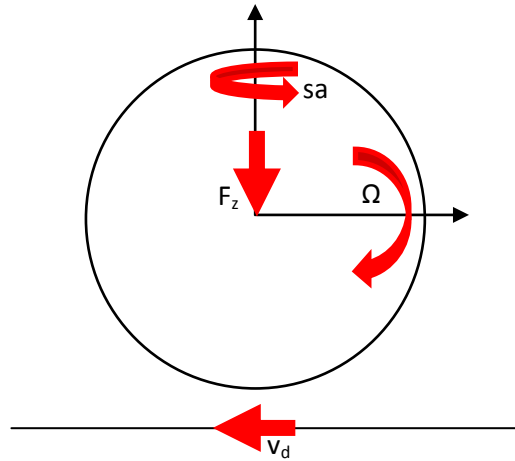


Figure 3.1 – Graphical representation of the four user-defined input quantities of the proposed tyre model

In each time-step, the belt and contact dynamics are excited by these user-imposed quantities and the resulting contact forces. Consequently, the response of the model generates a new contact force vector associated with the current time-step and used to excite the tyre in the next time-step.

### 3.2.2 Frames of reference and transformations

Since there are three distinct sub-models, it is unavoidable that various quantities have to be transformed in an appropriate form to pass from one sub-model to the next. These quantities are the nodal coordinates of the belt nodes, the respective velocity and acceleration vectors and the forces acting on these nodes. But prior to calculating the transformation matrices, the respective frames of reference have to be defined:

- Global (inertial) frame of reference ( $O_1$ )
- Rig-fixed frame of reference ( $O_2$ )
- Upright-fixed frame of reference ( $O_3$ )
- Wheel-fixed frame of reference ( $O_4$ )

These frames of reference have been selected so that the proposed tyre model replicates the following tyre testing facility:



Figure 3.2 – Indoor tyre testing facility (photograph courtesy of the Department of Aeronautical and Automotive Engineering, Loughborough University)

The global frame of reference ( $O_1$ ) is attached to the ground, that is, the blue beams of Figure 3.2. The rig-fixed frame of reference ( $O_2$ ) is attached to the red beams of the above figure and demonstrates a single degree of freedom in the vertical direction with respect to ( $O_1$ ). The upright-fixed frame of reference ( $O_3$ ) is attached to the grey beam illustrated in Figure 3.2, which is able to rotate about the vertical axis with respect to ( $O_2$ ). Finally, the wheel-fixed frame of reference ( $O_4$ ) is attached to the wheel and exhibits a single degree of freedom – rotation about the lateral axis – with respect to ( $O_3$ ).

#### **A. Wheel-fixed to upright-fixed frame of reference**

The linear and non-linear dynamics of the belt are defined with respect to the wheel-fixed coordinate system. Consequently, in each time-step, the position and motion of the belt nodes – nodal coordinates, velocity and acceleration vectors – are captured in this particular frame of reference. In addition, in order to take contact phenomena into account, it is essential that these quantities are also expressed in global terms. So, a series of transformations of these quantities is needed, starting from the most local frame of reference and moving towards the inertial one.

The wheel-fixed frame of reference is attached to the wheel, in a layout identical to the one proposed by I. Lopez et al. in [64]. Wheel rotation introduces deviation – angle  $\theta$  – between the wheel-fixed and upright-fixed frames of reference, as it can be seen in Figure 3.3.

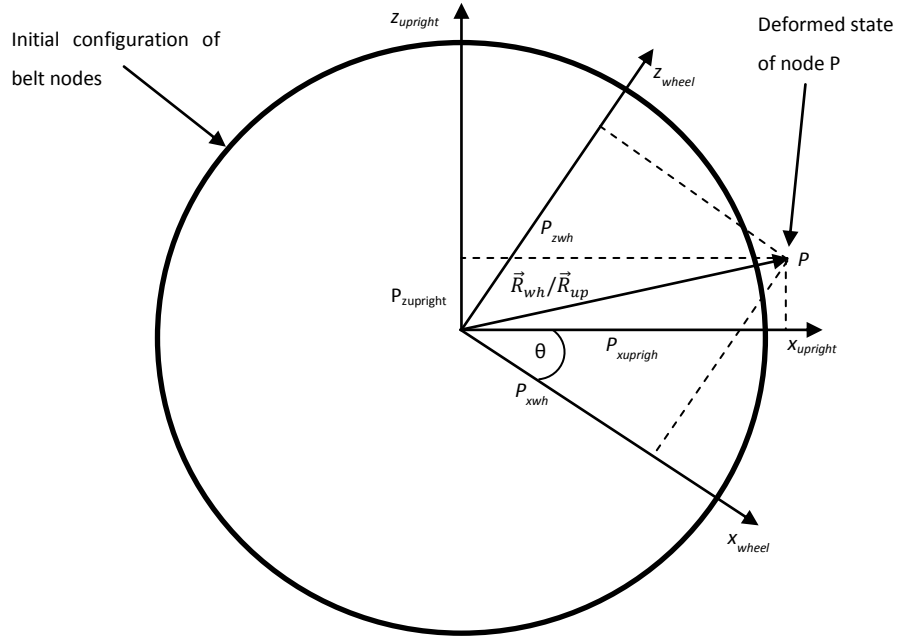


Figure 3.3 – Tyre belt node position expressed in both the wheel-fixed and the upright-fixed frames of reference

The key element in this first transformation is the following matrix<sup>[24]</sup>:

$$\mathbf{A} = \begin{bmatrix} \cos\theta & 0 & \sin\theta \\ 0 & 1 & 0 \\ -\sin\theta & 0 & \cos\theta \end{bmatrix} \quad 3.2-1$$

where  $\theta$  is the angle formed by axes  $x_{upright}$  and  $x_{wheel}$  or  $z_{upright}$  and  $z_{wheel}$ .

If the position vector of a particular node is expressed with respect to the wheel-fixed frame of reference as follows:

$$\vec{R}_{wh} = [x_{wh} \quad y_{wh} \quad z_{wh}]^T \quad 3.2-2$$

and the respective position vector with respect to the upright-fixed frame of reference is expressed as follows:

$$\vec{R}_{up} = [x_{up} \quad y_{up} \quad z_{up}]^T \quad 3.2-3$$

then these two vectors are linked by Equation 3.2-4:

$$\vec{R}_{up} = \mathbf{A} \cdot \vec{R}_{wh} \quad 3.2-4$$

and the respective velocity is obtained by time differentiation of the above equation:

$$\begin{aligned} \frac{\partial \vec{R}_{up}}{\partial t} &= \frac{\partial \mathbf{A}}{\partial t} \cdot \vec{R}_{wh} + \mathbf{A} \cdot \frac{\partial \vec{R}_{wh}}{\partial t} \Rightarrow \\ \frac{\partial \vec{R}_{up}}{\partial t} &= \frac{\partial \mathbf{A}}{\partial \theta} \cdot \frac{\partial \theta}{\partial t} \cdot \vec{R}_{wh} + \mathbf{A} \cdot \frac{\partial \vec{R}_{wh}}{\partial t} \Rightarrow \\ \frac{\partial \vec{R}_{up}}{\partial t} &= \frac{\partial \mathbf{A}}{\partial \theta} \cdot \Omega \cdot \vec{R}_{wh} + \mathbf{A} \cdot \frac{\partial \vec{R}_{wh}}{\partial t} \end{aligned} \quad 3.2-5$$

where  $\Omega$  is the user-defined angular velocity of the wheel.

The transformation of the nodal belt motion requires the additional calculation of the respective acceleration vector:

$$\begin{aligned} \frac{\partial^2 \vec{R}_{up}}{\partial t^2} &= \frac{\partial^2 \mathbf{A}}{\partial \theta^2} \cdot \Omega^2 \cdot \vec{R}_{wh} + \frac{\partial \mathbf{A}}{\partial \theta} \cdot \frac{\partial \Omega}{\partial t} \cdot \vec{R}_{wh} \\ &+ 2 \frac{\partial \mathbf{A}}{\partial \theta} \cdot \Omega \cdot \frac{\partial \vec{R}_{wh}}{\partial t} + \mathbf{A} \cdot \frac{\partial^2 \vec{R}_{wh}}{\partial t^2} \end{aligned} \quad 3.2-6$$

Transformation of quantities from the upright-fixed to the wheel-fixed frame of reference is performed by using the inverse of transformation matrix  $\mathbf{A}$  instead:

$$\mathbf{A}^{-1} = \begin{bmatrix} \cos\theta & 0 & -\sin\theta \\ 0 & 1 & 0 \\ \sin\theta & 0 & \cos\theta \end{bmatrix} \quad 3.2-7$$

$$\vec{R}_{wh} = \mathbf{A}^{-1} \cdot \vec{R}_{up} \quad 3.2-8$$

$$\frac{\partial \vec{R}_{wh}}{\partial t} = \frac{\partial \mathbf{A}^{-1}}{\partial \theta} \cdot \Omega \cdot \vec{R}_{up} + \mathbf{A}^{-1} \cdot \frac{\partial \vec{R}_{up}}{\partial t} \quad 3.2-9$$

$$\frac{\partial^2 \vec{R}_{wh}}{\partial t^2} = \frac{\partial^2 \mathbf{A}^{-1}}{\partial \theta^2} \cdot \Omega^2 \cdot \vec{R}_{up} + \frac{\partial \mathbf{A}^{-1}}{\partial \theta} \cdot \frac{\partial \Omega}{\partial t} \cdot \vec{R}_{up} \quad 3.2-10$$



$$+2 \frac{\partial \mathbf{A}^{-1}}{\partial \theta} \cdot \Omega \cdot \frac{\partial \vec{\mathbf{R}}_{\text{up}}}{\partial t} + \mathbf{A}^{-1} \cdot \frac{\partial^2 \vec{\mathbf{R}}_{\text{up}}}{\partial t^2}$$

### B. Upright-fixed to rig-fixed frame of reference

The origin and the vertical axis  $z$  of the upright-fixed coordinate system coincide with the respective one of the rig-fixed frame. Deviation between these two systems occurs due to the user-imposed steering angle, as it can be seen in the following figure:

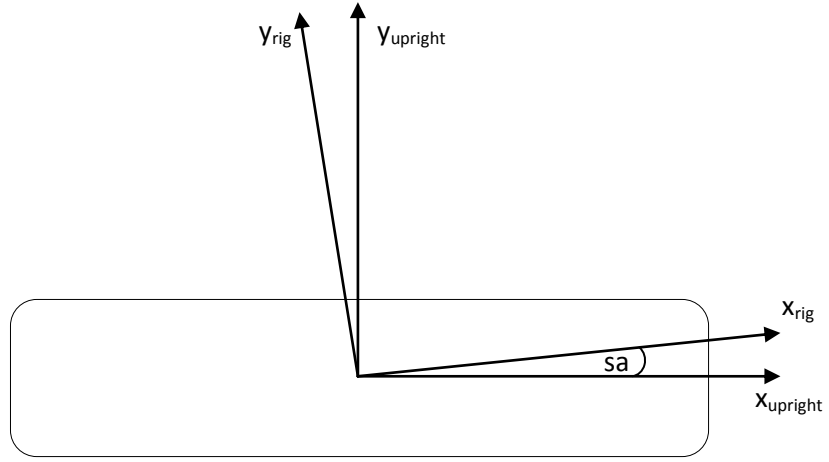


Figure 3.4 – Transformation from upright-fixed and rig-fixed frames of reference

This deviation is expressed by the following transformation matrix:

$$\mathbf{B} = \begin{bmatrix} \cos(sa) & -\sin(sa) & 0 \\ \sin(sa) & \cos(sa) & 0 \\ 0 & 0 & 1 \end{bmatrix} \quad 3.2-11$$

and the motion of each node with respect to the rig-fixed coordinate system is obtained by the following expressions:

$$\vec{\mathbf{R}}_{\text{rig}} = \mathbf{B} \cdot \vec{\mathbf{R}}_{\text{up}} \quad 3.2-12$$

$$\frac{\partial \vec{\mathbf{R}}_{\text{rig}}}{\partial t} = \frac{\partial \mathbf{B}}{\partial sa} \cdot \frac{\partial sa}{\partial t} \cdot \vec{\mathbf{R}}_{\text{up}} + \mathbf{B} \cdot \frac{\partial \vec{\mathbf{R}}_{\text{up}}}{\partial t} \quad 3.2-13$$

$$\begin{aligned} \frac{\partial^2 \vec{R}_{\text{rig}}}{\partial t^2} = & \frac{\partial^2 \mathbf{B}}{\partial sa^2} \cdot \left( \frac{\partial sa}{\partial t} \right)^2 \cdot \vec{R}_{\text{up}} + \frac{\partial \mathbf{B}}{\partial sa} \cdot \frac{\partial^2 sa}{\partial t^2} \cdot \vec{R}_{\text{up}} + 2 \frac{\partial \mathbf{B}}{\partial sa} \cdot \frac{\partial sa}{\partial t} \\ & \cdot \frac{\partial \vec{R}_{\text{up}}}{\partial t} + \mathbf{B} \cdot \frac{\partial^2 \vec{R}_{\text{up}}}{\partial t^2} \end{aligned} \quad 3.2-14$$

where  $\vec{R}_{\text{up}}$  and  $\vec{R}_{\text{rig}}$  are the position vectors of a belt node expressed in the upright-fixed and the rig-fixed frames respectively. Once again, the inverse transformation is performed by first calculating the inverse of matrix  $\mathbf{B}$ :

$$\mathbf{B}^{-1} = \begin{bmatrix} \cos(sa) & \sin(sa) & 0 \\ -\sin(sa) & \cos(sa) & 0 \\ 0 & 0 & 1 \end{bmatrix} \quad 3.2-15$$

The motion of each node, with respect to the upright-fixed frame of reference is obtained by the following equations:

$$\vec{R}_{\text{up}} = \mathbf{B}^{-1} \cdot \vec{R}_{\text{rig}} \quad 3.2-16$$

$$\frac{\partial \vec{R}_{\text{up}}}{\partial t} = \frac{\partial \mathbf{B}^{-1}}{\partial sa} \cdot \frac{\partial sa}{\partial t} \cdot \vec{R}_{\text{rig}} + \mathbf{B}^{-1} \cdot \frac{\partial \vec{R}_{\text{rig}}}{\partial t} \quad 3.2-17$$

$$\begin{aligned} \frac{\partial^2 \vec{R}_{\text{up}}}{\partial t^2} = & \frac{\partial^2 \mathbf{B}^{-1}}{\partial sa^2} \cdot \left( \frac{\partial sa}{\partial t} \right)^2 \cdot \vec{R}_{\text{rig}} + \frac{\partial \mathbf{B}^{-1}}{\partial sa} \cdot \frac{\partial^2 sa}{\partial t^2} \cdot \vec{R}_{\text{rig}} \\ & + 2 \frac{\partial \mathbf{B}^{-1}}{\partial sa} \cdot \frac{\partial sa}{\partial t} \cdot \frac{\partial \vec{R}_{\text{rig}}}{\partial t} + \mathbf{B}^{-1} \cdot \frac{\partial^2 \vec{R}_{\text{rig}}}{\partial t^2} \end{aligned} \quad 3.2-18$$

### C. Rig-fixed to global frame of reference

The last transformation required in order to express the locally defined motion of the belt in global terms, and consequently to be able to identify contact and calculate contact forces, is that between the rig-fixed and the inertial frame of reference. These two systems have their axes parallel to each other and the only deviation is the vertical coordinate of the respective origin points. During the initial time-steps of each simulation run, the centre of the tyre is located at distance  $z_0$  above the ground and these two points of origin coincide. The application of the user-imposed vertical load results in deviation between these two frames of reference:

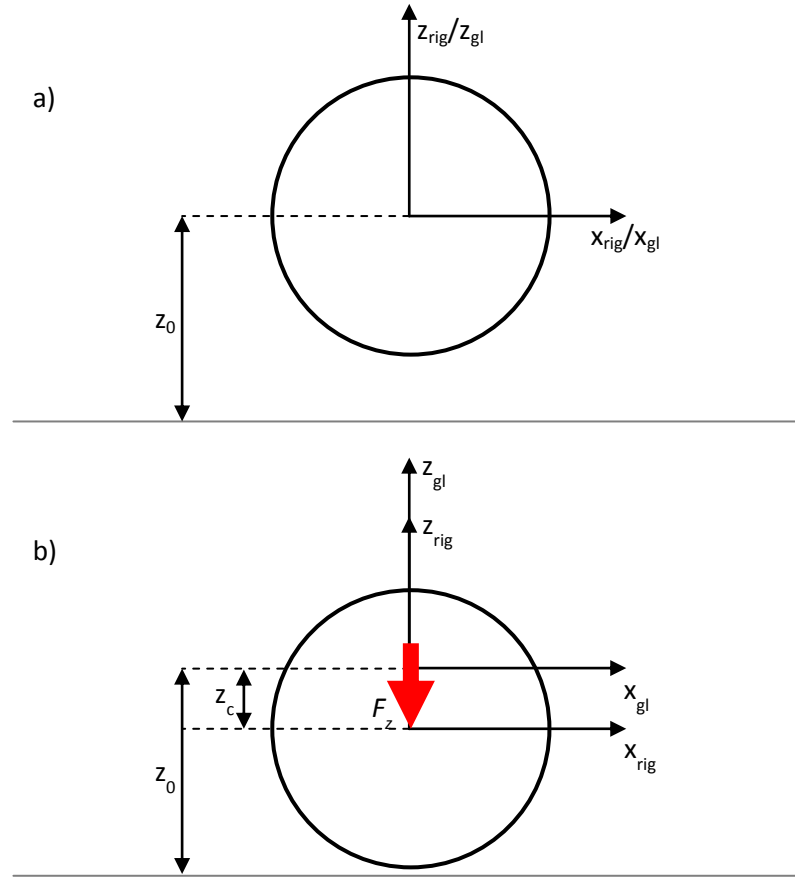


Figure 3.5 – Vertical translational degree of freedom; a) Configuration at the first time step; b) Configuration after the application of  $F_z$

The transformation between these two coordinate systems is significantly simpler than the ones described above, as no rotation is involved:

$$\vec{R}_{gl} = \vec{R}_{rig} + [0 \quad 0 \quad z_c]^T \quad 3.2-19$$

$$\frac{\partial \vec{R}_{gl}}{\partial t} = \frac{\partial \vec{R}_{rig}}{\partial t} + \left[ 0 \quad 0 \quad \frac{\partial z_c}{\partial t} \right]^T \quad 3.2-20$$

$$\frac{\partial^2 \vec{R}_{gl}}{\partial t^2} = \frac{\partial^2 \vec{R}_{rig}}{\partial t^2} + \left[ 0 \quad 0 \quad \frac{\partial^2 z_c}{\partial t^2} \right]^T \quad 3.2-21$$

Solving Equations 3.2–19 to 3.2–21 for  $\vec{R}_{rig}$  results in the inverse coordinate transformation between these two frames of reference:

$$\vec{R}_{\text{rig}} = \vec{R}_{\text{gl}} - [0 \quad 0 \quad z_c]^T \quad 3.2-22$$

$$\frac{\partial \vec{R}_{\text{rig}}}{\partial t} = \frac{\partial \vec{R}_{\text{gl}}}{\partial t} - \left[ 0 \quad 0 \quad \frac{\partial z_c}{\partial t} \right]^T \quad 3.2-23$$

$$\frac{\partial^2 \vec{R}_{\text{rig}}}{\partial t^2} = \frac{\partial^2 \vec{R}_{\text{gl}}}{\partial t^2} - \left[ 0 \quad 0 \quad \frac{\partial^2 z_c}{\partial t^2} \right]^T \quad 3.2-24$$

### 3.3 Tyre belt modelling

#### 3.3.1 Overview

The foundation of the present study and the element which differentiates this particular model from those currently established is the way in which belt deformation is simulated. As presented in the previous chapter, the vast majority of steady-state or dynamic tyre models tend to either simulate the tyre belt as a rigid and non-deformable body, or generate a complex and demanding virtual representation. For typical road tyres, high-fidelity studies require the contribution of flexible belt modes to be included in the total tyre response and consequently the first abovementioned type of tyre models is not a valid option. On the other hand, the models included in the second case require the experimental identification of numerous parameters, a process which can be extremely demanding and time consuming. Additionally, due to the complexity of these models, computational power requirements tend to be high.

The dynamic tyre model presented in this chapter consists of a number of nodes, equally distributed along the circumference of the belt. Each node is capable of moving in the three-dimensional space and the system of differential equations which governs this motion is the following:

$$\mathbf{M} \cdot \{\ddot{\mathbf{x}}\} + \mathbf{C} \cdot \{\dot{\mathbf{x}}\} + \mathbf{K} \cdot \{\mathbf{x}\} = \{\mathbf{f}_{\text{ext}}\} \quad 3.3-1$$

where  $\{\mathbf{x}\}_{3N \times 1} = [\{x_1 y_1 z_1\} \{x_2 y_2 z_2\} \dots \{x_N y_N z_N\}]^T$  is the vector containing the coordinates of each node in the wheel-fixed frame of reference,

$\mathbf{K}_{3N \times 3N}$  is the stiffness matrix of the system,

$\mathbf{C}_{3N \times 3N}$  is the non-proportional viscous damping matrix of the system,

$\mathbf{M}_{3N \times 3N}$  is the mass matrix of the system,

$\{f_{ext}\}_{3N \times 1}$  consists of the components of the external force acting on each node, and

$N$  is the number of belt nodes

It would be possible to use equation 3.3–1 in order to calculate the response of a tyre for the excitation imposed by vector  $\{f_{ext}\}$ , but this approach requires to solve a total of  $3N$  second-order differential equations which is numerically inefficient. Moreover, system matrices are typically challenging to identify. Furthermore, the assumptions made in the estimation process of these matrices, namely  $\mathbf{K}$ ,  $\mathbf{C}$  and  $\mathbf{M}$ , may introduce significant deviation between the actual motion and deformation of the tyre and simulation results.

To overcome these drawbacks, the tyre dynamics are divided into the dynamics of the non-deformable wheel and the dynamics of the flexible tyre belt. In particular, vector  $\{x\}$  is divided into two distinct components, the first one representing the rigid-body motion of the tyre, while the second one captures the local deformation of each node. This way, the dynamics of the flexible tyre may be identified by performing modal testing on a stationary tyre, as described in Chapter 4, an experimentally feasible option which also results in partial minimisation of the frequency loci veering – described in [63] – typically originating from tyre operation. It follows:

$$\{x\} = \{x_{rigid}\} + \{dx\} \quad 3.3-2$$

Substitution of Equation 3.3–2 to 3.3–1 yields:

$$\begin{aligned} \mathbf{M} \cdot (\ddot{\{x_{rigid}\}} + \ddot{\{dx\}}) + \mathbf{C} \cdot (\dot{\{x_{rigid}\}} + \dot{\{dx\}}) + \mathbf{K} \cdot (\{x_{rigid}\} + \{dx\}) = \{f_{ext}\} \Rightarrow \\ \mathbf{M} \cdot \ddot{\{x_{rigid}\}} + \mathbf{M} \cdot \ddot{\{dx\}} + \overbrace{\mathbf{C} \cdot \dot{\{x_{rigid}\}}}^A + \mathbf{C} \cdot \dot{\{dx\}} + \overbrace{\mathbf{K} \cdot \{x_{rigid}\}}^B + \mathbf{K} \cdot \{dx\} = \{f_{ext}\} \end{aligned} \quad 3.3-3$$

Terms A and B in Equation 3.3–3 are equal to zero as  $\{x_{rigid}\}$  represents the motion of the wheel as a non-deformable body. Consequently:

$$\mathbf{M} \cdot \ddot{\{x_{rigid}\}} + \mathbf{M} \cdot \ddot{\{dx\}} + \mathbf{C} \cdot \dot{\{dx\}} + \mathbf{K} \cdot \{dx\} = \{f_{ext}\} \Rightarrow$$

$$\mathbf{M} \cdot \{\ddot{\mathbf{x}}\} + \mathbf{C} \cdot \{\dot{\mathbf{x}}\} + \mathbf{K} \cdot \{\mathbf{x}\} = \{\mathbf{f}_{\text{ext}}\} - \mathbf{M} \cdot \{\ddot{\mathbf{x}}_{\text{rigid}}\} \quad 3.3-4$$

Examination of Equation 3.3–4 along with the non-proportionality of tyre belt damping<sup>[36][87]</sup>, leads to the necessity to identify the system matrices. A general overview of structural parameters identification may be found in the survey paper of G. Kerschen et al. in [54] and in the work of M. Prandina et al. in [88]. With regard to damping identification one may refer to the work conducted by S. Adhikari and J. Woodhouse in [1] and [2] and J Woodhouse in [115], while additional information is presented in [69].

The fundamental drawback of estimating system matrices from frequency response data is the requirement to identify a minimum number of structural modes, which is equal to the number of equations of motion governing the system. This means that in order to identify the matrices of a tyre belt consisting of 30 three-dimensional nodes, a total of 90 structural modes needs to be obtained. This is a significantly challenging task which is beyond the context and the scope of the present modelling approach, as the frequency band of interest is confined and modal reduction<sup>[109]</sup> is a key element of this work. Depending on the application, by including only a certain number of flexible tyre belt modes, the efficiency of the model is enhanced without extensively compromising the model fidelity in the frequency band of interest.

An alternative method of attack is to express the equations of motion in state-space<sup>[30][70]</sup> in order to transform the system from the physical to the modal domain. Thus, a new coordinate vector is defined:

$$\{\mathbf{du}\}_{6N \times 1} = \begin{Bmatrix} \{\mathbf{x}\} \\ \{\dot{\mathbf{x}}\} \end{Bmatrix} \quad 3.3-5$$

Equations 3.3–4 and 3.3–5 along with the following identity equation:

$$[\mathbf{M} \quad \mathbf{0}]\{\dot{\mathbf{u}}\} + [\mathbf{0} \quad -\mathbf{M}]\{\mathbf{u}\} = \{\mathbf{0}\} \quad 3.3-6$$

yield the state-space equations of motion:

$$\begin{bmatrix} \mathbf{C} & \mathbf{M} \\ \mathbf{M} & \mathbf{0} \end{bmatrix} \{\dot{\mathbf{u}}\} + \begin{bmatrix} \mathbf{K} & \mathbf{0} \\ \mathbf{0} & -\mathbf{M} \end{bmatrix} \{\mathbf{u}\} = \begin{Bmatrix} \{\mathbf{f}_{\text{ext}}\} - \mathbf{M}\{\ddot{\mathbf{x}}_{\text{rigid}}\} \\ \{\mathbf{0}\} \end{Bmatrix} \quad 3.3-7$$

The vector containing the rigid-body coordinates may be expressed as the linear superposition of the rigid-body modes of the wheel:

$$\{x_{\text{rigid}}\} = \Phi_{\text{RB}}\{q\} \quad 3.3-8$$

where  $\Phi_{\text{RB}}$  is the  $3N \times 6$  modal matrix containing the real rigid-body eigenvectors of the structure and  $\{q\}_{6 \times 1}$  is the vector of the modal participation factors, i.e. the contribution of each rigid-body mode to the total motion of the wheel. Since the geometry of the nodes in the wheel-fixed frame of reference is constant and given, the identification of matrix  $\Phi_{\text{RB}}$  can be conducted by exploiting the findings of the relative research area, i.e. the identification of rigid-body parameters via frequency response data – see R. A. B. Almeida et al. in [4] and [5], A. M. Fareed and F. Wahl in [32], and M. Okuma et al. in [76] and [77]. One particular case of interest, similar to the above formulation of the rigid component of the tyre belt, is presented in [77] where the centre of gravity of the test structure coincides with the origin of the reference frame used and the respective frame axes are parallel to the principal axes of inertia of the structure. Such a layout yields the following matrix of rigid-body modes:

$$\Phi_{\text{RB}} = \begin{bmatrix} \vdots & & & & & \\ 1 & 0 & 0 & 0 & z_i & -y_i \\ 0 & 1 & 0 & -z_i & 0 & x_i \\ 0 & 0 & 1 & y_i & -x_i & 0 \\ \vdots & & & & & \end{bmatrix} \quad 3.3-9$$

where  $(x_i, y_i, z_i)$  is the position vector of the  $i^{\text{th}}$  node with respect to the wheel-fixed frame of reference and each column of Equation 3.3–9 corresponds to one of the six rigid body wheel modes. These modes are depicted in the following figures:

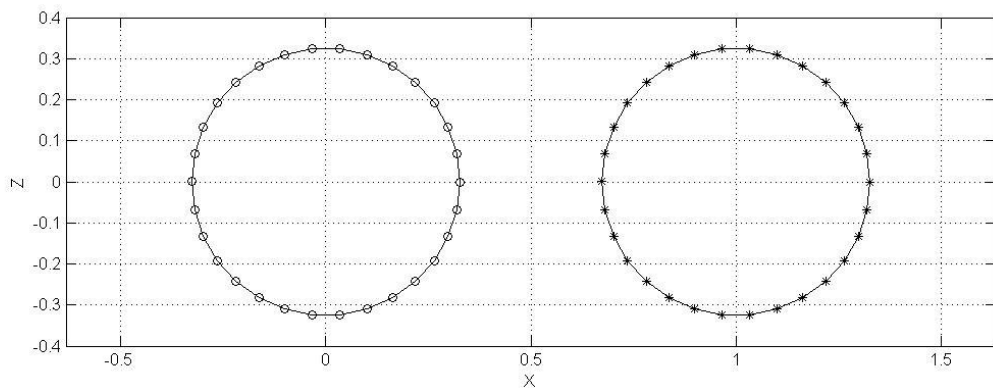


Figure 3.6 – Nodal configuration of the belt – first rigid body mode  
(-o-: Initial nodal coordinates – -x-: nodal coordinates demonstrating rigid body motion along the tyre-fixed x axis)

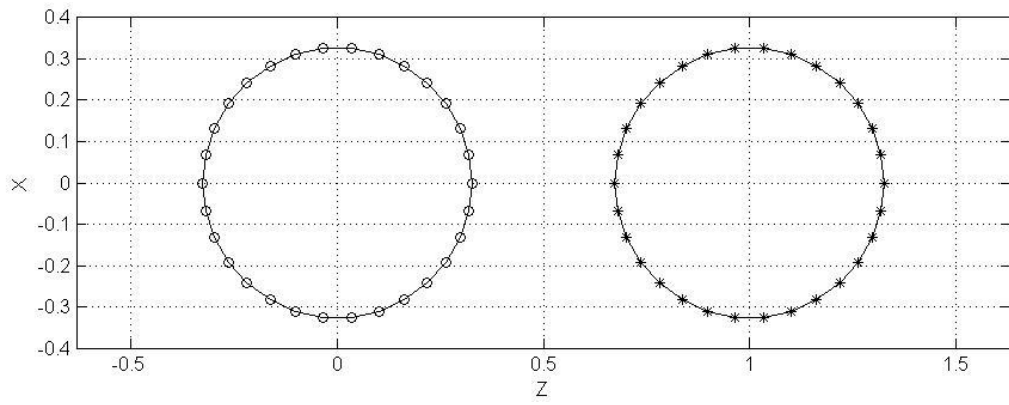


Figure 3.7 – Nodal configuration of the belt – second rigid body mode  
 (-o-: Initial nodal coordinates – -x-: nodal coordinates demonstrating rigid body motion along the tyre-fixed z axis)

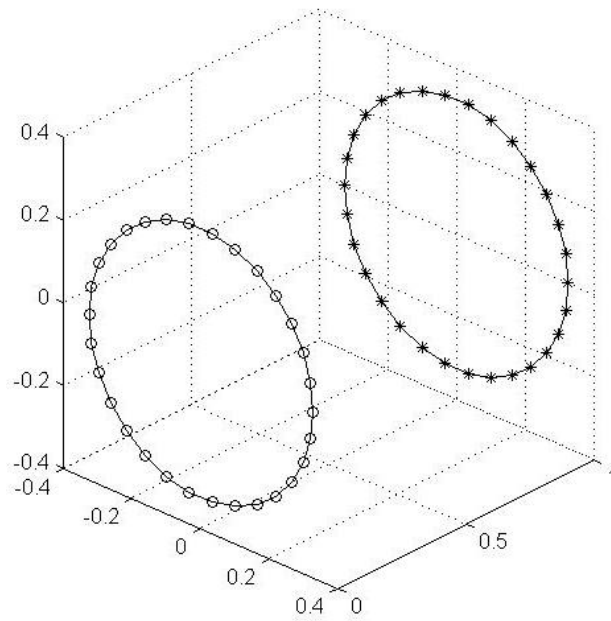


Figure 3.8 – Nodal configuration of the belt – third rigid body mode  
 (-o-: Initial nodal coordinates – -x-: nodal coordinates demonstrating rigid body motion along the tyre-fixed y axis)



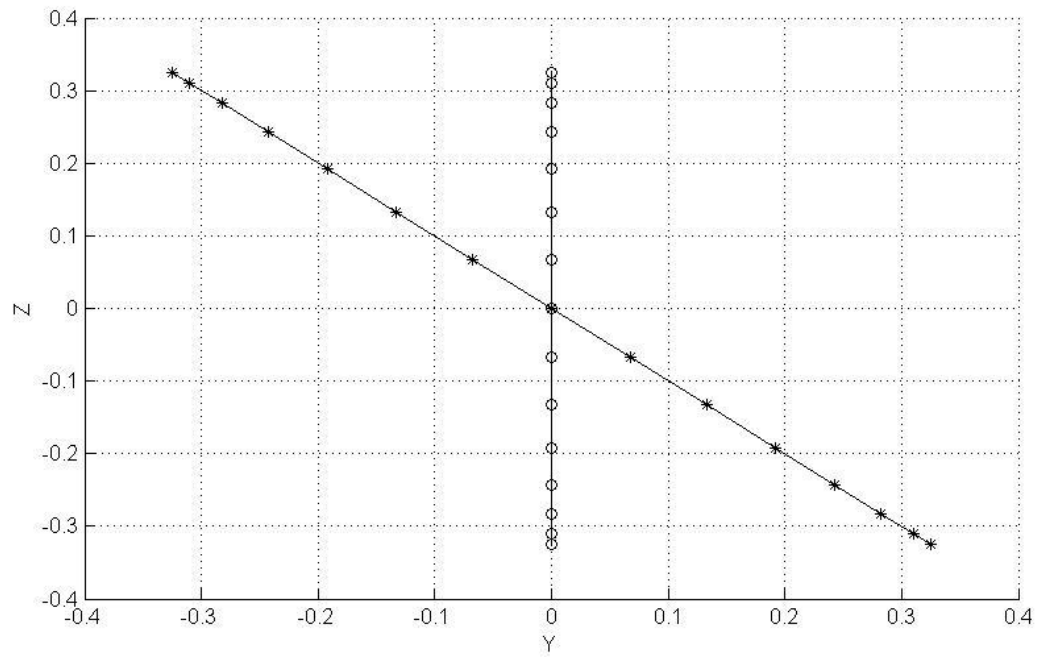


Figure 3.9 – Nodal configuration of the belt – fourth rigid body mode  
 (-o-: Initial nodal coordinates – -x-: nodal coordinates demonstrating rigid body rotation around the tyre-fixed x axis)

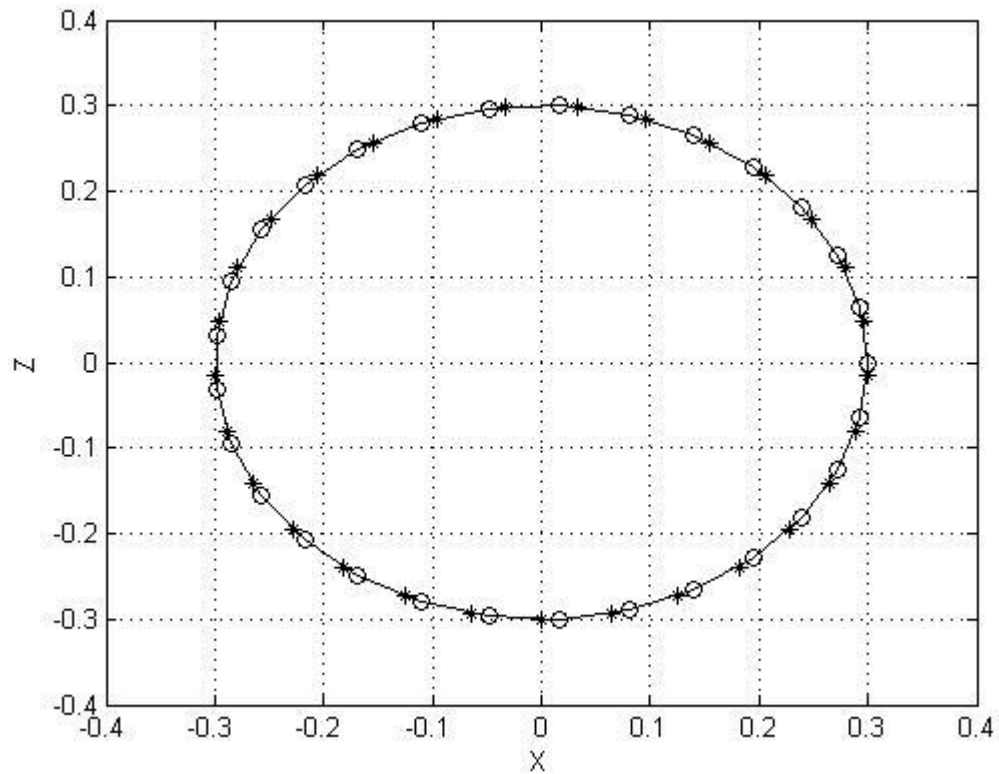


Figure 3.10 – Nodal configuration of the belt – fifth rigid body mode  
 (-o-: Initial nodal coordinates – -x-: nodal coordinates demonstrating generic rigid body rotation)

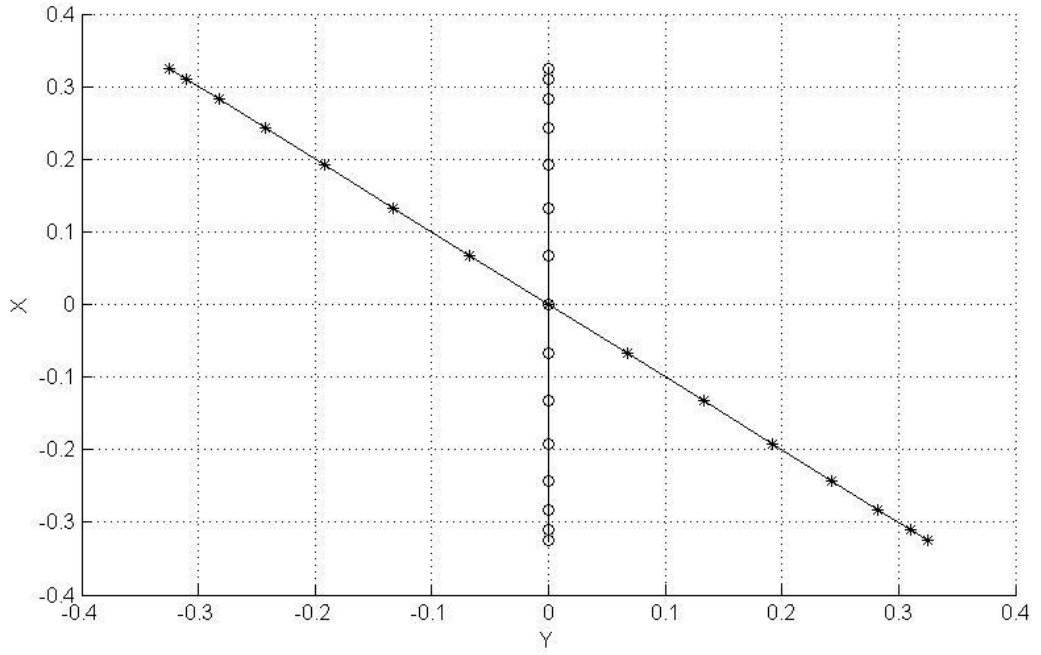


Figure 3.11 – Nodal configuration of the belt – sixth rigid body mode  
(-o-: Initial nodal coordinates – -x-: nodal coordinates demonstrating rigid body rotation around the tyre-fixed z axis)

Substitution of Equation 3.3–8 in 3.3–7 yields the following alternative form of the equations of motion:

$$\begin{bmatrix} \mathbf{C} & \mathbf{M} \\ \mathbf{M} & \mathbf{0} \end{bmatrix} \{\dot{\mathbf{d}}\mathbf{u}\} + \begin{bmatrix} \mathbf{K} & \mathbf{0} \\ \mathbf{0} & -\mathbf{M} \end{bmatrix} \{\mathbf{d}\mathbf{u}\} = \begin{Bmatrix} \{\mathbf{f}_{\text{ext}}\} - \mathbf{M}\Phi_{\text{RB}}\{\ddot{\mathbf{q}}\} \\ \{0\} \end{Bmatrix} \quad 3.3-10$$

Following the approach proposed by D. J. Ewins in [30] and by N. M. M. Maia et al. in [70], the extended coordinate vector of tyre belt deformation may be expressed as a linear combination of the state-space eigenvectors:

$$\{\mathbf{d}\mathbf{u}\}_{6N \times 1} = \begin{Bmatrix} \{\psi_1\} \\ \{\psi_1\}s_1 \end{Bmatrix} dq_1 + \begin{Bmatrix} \{\psi_2\} \\ \{\psi_2\}s_2 \end{Bmatrix} dq_2 + \dots + \begin{Bmatrix} \{\psi_{3N}\} \\ \{\psi_{3N}\}s_{3N} \end{Bmatrix}^* dq_{6N} \Rightarrow$$

$$\{\mathbf{d}\mathbf{u}\}_{6N \times 1} = \{\psi_1\}' dq_1 + \{\psi_2\}' dq_2 + \dots + \{\psi_{3N}^*\}' dq_{6N} \Rightarrow$$

$$\{\mathbf{d}\mathbf{u}\} = \Psi' \{\mathbf{d}\mathbf{q}\} \quad 3.3-11$$

where  $\Psi'_{6N \times 6N}$  is the state-space modal matrix, consisting of the complex eigenvectors  $\{\psi_i\}$  and the respective eigenvalues  $s_i$ , and  $\{\mathbf{d}\mathbf{q}\}_{6N \times 1}$  is the vector containing the modal participation

factor of each flexible mode. Note that (\*) denotes the complex conjugate of the quantity in the brackets.

As will be demonstrated in Chapter 4, in the vast majority of modal testing cases the deformation of the structure is expressed by using the first  $m$  modes, where  $m < 3N$ , either because it is not possible to obtain the full eigenvector matrix<sup>[30]</sup> or because this is part of the intentional modal reduction. As mentioned above, this modal reduction may seem to have a negative impact on the accuracy of the proposed model but, as demonstrated by A. Tsotras and G. Mavros in [109], this particular limitation enhances its efficiency in the frequency band confined by the imposed cut-off frequency, i.e. the natural frequency of the  $m^{\text{th}}$  mode. Consequently, the actual – experimentally identified – modal matrix is:

$$\Psi'_{6N \times 2m} = \begin{bmatrix} \{\psi_1\} & \dots & \{\psi_m\} & \{\psi_1^*\} & \dots & \{\psi_m^*\} \\ \{\psi_1\}s_1 & \dots & \{\psi_m\}s_m & \{\psi_1^*\}s_1^* & \dots & \{\psi_m^*\}s_m^* \end{bmatrix}$$

$$\Psi'_{6N \times 2m} = [\{\psi_1\}' \quad \dots \quad \{\psi_m\}' \quad \{\psi_1^*\}' \quad \dots \quad \{\psi_m^*\}'] \quad 3.3-12$$

Since only the first  $m$  modes are included in the modal matrix, inspection of Equation 3.3–11 reveals the necessity to alter the length of vector  $\{dq\}$  from  $6N \times 1$  to  $2m \times 1$ .

$$\{du\}_{6N \times 1} = \{\psi_1\}'dq_1 + \{\psi_2\}'dq_2 + \dots + \{\psi_m^*\}'dq_{2m} \Rightarrow$$

$$\{du\}_{6N \times 1} = \Psi'_{6N \times 2m}\{dq\}_{2m \times 1} \quad 3.3-13$$

Using Equation 3.3–13, the system of Equations 3.3–10 becomes:

$$\begin{bmatrix} \mathbf{C} & \mathbf{M} \\ \mathbf{M} & \mathbf{0} \end{bmatrix} \Psi' \{\dot{dq}\} + \begin{bmatrix} \mathbf{K} & \mathbf{0} \\ \mathbf{0} & -\mathbf{M} \end{bmatrix} \Psi' \{dq\} = \begin{Bmatrix} \{f_{\text{ext}}\} - \mathbf{M}\Phi_{\text{RB}}\{\ddot{q}\} \\ \{0\} \end{Bmatrix} \Rightarrow$$

$$\mathbf{A}\Psi' \{\dot{dq}\} + \mathbf{B}\Psi' \{dq\} = \begin{Bmatrix} \{f_{\text{ext}}\} - \mathbf{M}\Phi_{\text{RB}}\{\ddot{q}\} \\ \{0\} \end{Bmatrix} \quad 3.3-14$$

Equation 3.3–14 still contains the inertia, stiffness and damping matrices of the system which can be eliminated by defining a new modal matrix of the following form:

$$\Psi'_{\text{tot}} = \begin{bmatrix} \{\varphi_1\}_{\text{RB}} & \dots & \{\varphi_6\}_{\text{RB}} & \{\psi_1\} & \dots & \{\psi_m\} & \{\psi_1^*\} & \dots & \{\psi_m^*\} \\ \{0\} & & \{0\} & \{\psi_1\}_{s_1} & & \{\psi_m\}_{s_m} & \{\psi_1^*\}_{s_1^*} & & \{\psi_m^*\}_{s_m^*} \end{bmatrix} \quad 3.3-15$$

Pre-multiplication of the transpose of  $\Psi'_{\text{tot}}$  with the system of equations of motion, yields the following expression:

$$\Psi'_{\text{tot}}{}^T \mathbf{A} \Psi' \{\dot{d}q\} + \Psi'_{\text{tot}}{}^T \mathbf{B} \Psi' \{dq\} = \Psi'_{\text{tot}}{}^T \left\{ \begin{matrix} \{f_{\text{ext}}\} \\ \{0\} \end{matrix} - \mathbf{M} \Phi_{\text{RB}} \{\ddot{q}\} \right\} \quad 3.3-16$$

Due to the eigenvectors being orthogonal to each other, the above equation may be re-written as follows:

$$\begin{bmatrix} 0 & \dots & 0 \\ \vdots & & \vdots \\ 0 & \dots & 0 \\ a_1 & & \\ & \ddots & \\ & & a_{2m} \end{bmatrix} \{d\dot{q}\} + \begin{bmatrix} 0 & \dots & 0 \\ \vdots & & \vdots \\ 0 & \dots & 0 \\ b_1 & & \\ & \ddots & \\ & & b_{2m} \end{bmatrix} \{dq\} = \begin{bmatrix} \{\varphi_1\}_{\text{RB}}^T \\ \vdots \\ \{\varphi_6\}_{\text{RB}}^T \\ \{\psi_1\}^T \\ \vdots \\ \{\psi_m^*\}^T \end{bmatrix} \{f_{\text{ext}}\} - \begin{bmatrix} \{\varphi_1\}_{\text{RB}}^T \\ \vdots \\ \{\varphi_6\}_{\text{RB}}^T \\ \{\psi_1\}^T \\ \vdots \\ \{\psi_m^*\}^T \end{bmatrix} \mathbf{M} \Phi_{\text{RB}} \{\ddot{q}\} \quad 3.3-17$$

where  $a_i$  and  $b_i$  are the scaling factors of the state-space eigenvectors, with regard to matrices  $\mathbf{A}$  and  $\mathbf{B}$  of Equation 3.3–14 respectively, which are presented in detail in Chapter 4. Due to the formulation of the eigenvector experimental identification, scaling factors  $a_i$  are equal to unity, while factors  $b_i$  are governed by Equation 3.3–18<sup>[30]</sup>:

$$b_i = -s_i \cdot a_i \quad 3.3-18$$

Substitution of the scaling factors  $a_i$  and  $b_i$  into Equation 3.3–17 yields:

$$\begin{bmatrix} 0 & \dots & 0 \\ \vdots & & \vdots \\ 0 & \dots & 0 \\ 1 & & \\ & \ddots & \\ & & 1 \end{bmatrix} \{d\dot{q}\} + \begin{bmatrix} 0 & \dots & 0 \\ \vdots & & \vdots \\ 0 & \dots & 0 \\ -s_1 & & \\ & \ddots & \\ & & -s_m^* \end{bmatrix} \{dq\} = \begin{bmatrix} \Phi_{\text{RB}}^T \\ \{\psi_1\}^T \\ \vdots \\ \{\psi_m^*\}^T \end{bmatrix} \{f_{\text{ext}}\} - \begin{bmatrix} \Phi_{\text{RB}}^T \\ \{\psi_1\}^T \\ \vdots \\ \{\psi_m^*\}^T \end{bmatrix} \mathbf{M} \Phi_{\text{RB}} \{\ddot{q}\} \quad 3.3-19$$

In order to eliminate the – unknown – mass matrix located in the last term of the above equation, one may refer to the work of M. Okuma et al. in [76] according to which the following expression holds:

$$\Phi_{RB}^T \mathbf{M} \Phi_{RB} = \mathbf{M}_{RB} \quad 3.3-20$$

Matrix  $\mathbf{M}_{RB}$  contains the macroscopic inertia properties of the wheel and, for the particular case used in this formulation of the tyre belt nodes expressed in the wheel-fixed coordinate system, it has the following form:

$$\mathbf{M}_{RB} = \begin{bmatrix} m_{tot} & & & & & \\ & m_{tot} & & & & \\ & & m_{tot} & & & \\ & & & I_{xx} & & \\ & & & & I_{yy} & \\ & & & & & I_{zz} \end{bmatrix} \quad 3.3-21$$

where  $m_{tot}$  is the total wheel mass and  $I_{xx}$ ,  $I_{yy}$ ,  $I_{zz}$  are the moments of inertia with respect to axes  $x$ ,  $y$ ,  $z$ . Taking into account Equation 3.3–20 and the orthogonality properties of the eigenvectors, the equations of motion become:

$$\begin{bmatrix} 0 & \dots & 0 \\ \vdots & & \vdots \\ 0 & \dots & 0 \\ 1 & & \ddots \\ & & 1 \end{bmatrix} \{d\dot{q}\} + \begin{bmatrix} 0 & \dots & 0 \\ \vdots & & \vdots \\ 0 & \dots & 0 \\ -s_1 & & \\ & \ddots & \\ & & -s_m^* \end{bmatrix} \{d\dot{q}\} = \begin{bmatrix} \Phi_{RB}^T \\ \{\psi_1\}^T \\ \vdots \\ \{\psi_m^*\}^T \end{bmatrix} \{f_{ext}\} - \begin{bmatrix} \mathbf{M}_{RB} \\ [0] \end{bmatrix} \{\ddot{q}\} \quad 3.3-22$$

Inspection of equation 3.3–22 reveals the main achievements of the proposed formulation thus far:

- tyre belt dynamics are simulated using quantities which are identifiable via either feasible modal testing (eigenvalues  $s_i$  and eigenvectors  $\{\psi_i\}$ ) or analytical pre-processing (mass matrix  $\mathbf{M}_{RB}$  and rigid-body eigenvector matrix  $\Phi_{RB}$ ),
- instead of the initial 6N equations of motion, the present system includes  $(2m+6)$  equations, a number which is generally lower than the total of the state-space degrees of freedom, hence enhancing the efficiency of the proposed model and
- the rigid-body non-linear dynamics of the belt are uncoupled from the equations associated with the deformation of each node, as demonstrated by the following two systems of equations:

$$\begin{bmatrix} 0 & \dots & 0 \\ \vdots & & \vdots \\ 0 & \dots & 0 \end{bmatrix} \{\dot{dq}\} + \begin{bmatrix} 0 & \dots & 0 \\ \vdots & & \vdots \\ 0 & \dots & 0 \end{bmatrix} \{dq\} = \Phi_{RB}^T \{f_{ext}\} - M_{RB} \{\ddot{q}\} \quad 3.3-23$$

$$\begin{bmatrix} 1 & & \\ & \ddots & \\ & & 1 \end{bmatrix} \{\dot{dq}\} + \begin{bmatrix} -s_1 & & \\ & \ddots & \\ & & -s_m^* \end{bmatrix} \{dq\} = \begin{bmatrix} \{\psi_1\}^T \\ \vdots \\ \{\psi_m^*\}^T \end{bmatrix} \{f_{ext}\} - [0] \{\ddot{q}\} \quad 3.3-24$$

This uncoupling offers a convenient way to deal with these two systems of equations, which will be examined separately in the following sections.

### 3.3.2 Linear dynamics of the deformable belt

The fundamental expression describing the belt deformation is presented above in Equation 3.3-24:

$$\begin{bmatrix} 1 & & \\ & \ddots & \\ & & 1 \end{bmatrix} \{\dot{dq}\} + \begin{bmatrix} -s_1 & & \\ & \ddots & \\ & & -s_m^* \end{bmatrix} \{dq\} = \begin{bmatrix} \{\psi_1\}^T \\ \vdots \\ \{\psi_m^*\}^T \end{bmatrix} \{f_{ext}\} \quad 3.3-25$$

Calculation of modal participation factors  $\{dq\}$  yields the physical states of the belt, see Equations 3.3-5 and 3.3-13:

$$\{du\}_{6N \times 1} = \Psi'_{6N \times 2m} \{dq\}_{2m \times 1}$$

$$\{du\}_{6N \times 1} = \begin{Bmatrix} \{dx\} \\ \{\dot{dx}\} \end{Bmatrix} \quad 3.3-26$$

where:

$\{du\}$  is the state vector,

$\Psi'$  is the experimentally identified complex modal matrix containing the complex eigenvectors of the belt, the associated eigenvalues and the respective conjugate quantities and

$\{dx\}$  is the vector of the physical nodal deformation of the belt.

As will be demonstrated in the following sections, vector  $\{f_{\text{ext}}\}$  is not obtained directly as there are forces acting on the wheel centre, a point missing from the nodes included in the above system of the equations. Instead, an equivalent force vector is introduced which has the same net effect as the actual external forces and it is calculated by Equation 3.3–52.

### 3.3.3 Non-linear dynamics of the non-deformable belt

Following the introduction of the wheel motion presented in Sections 3.2.1 and 3.2.2, the wheel – as a rigid body – demonstrates three degrees of freedom in the context of the present work:

- vertical motion with respect to the inertial frame of reference,
- rotation around the global z axis and
- rotation around the wheel-fixed y axis.

The following user-defined input quantities have been defined in the same introductory sections:

- vertical force ( $F_z$ ),
- steer angle (sa) and
- wheel angular velocity ( $\Omega$ ).

It is apparent that each degree of freedom is associated with the respective model input quantity. An additional input quantity is included, namely the road/drum velocity ( $v_d$ ), but it does not affect the motion of the wheel and it is exclusively used for calculating contact forces.

The fundamental system of equations of motion describing the response of the non-deformable belt has been obtained in the preceding section by associating the participation of every rigid-body mode to the externally applied nodal forces according to equation 3.3–27:

$$\Phi_{\text{RB}}^T \{f_{\text{ext}}\} = \mathbf{M}_{\text{RB}} \{\ddot{q}\} \quad 3.3-27$$

Combining the above expression, from which vector  $\{q\}$  is obtained, with Equation 3.3–8 leads to the calculation of vector  $\{x_{\text{rigid}}\}$  which demonstrates the effect of  $\{f_{\text{ext}}\}$  on the position of each belt node. Taking into account the application point of the user-imposed quantities listed

above, the formulation of the vector containing the external forces applied to the wheel is not straightforward as the wheel centre motion is not included in the initial system of differential equations of motion, see Equation 3.3–1. The rationale supporting this choice is that modal testing of the wheel centre is not feasible without altering the structural characteristics of the wheel, as the wheel centre of typical passenger car wheels is void and a supporting structure is required. Nevertheless, three out of four user-defined quantities exciting the model (vertical force, steering angle and wheel angular velocity) are applied to the wheel centre and consequently an alternative approach is needed. However, it should be noted that contact forces are evaluated for every node, so these forces may be directly added in vector  $\{f_{\text{ext}}\}$ .

In any particular time-step, all quantities – kinematic (steering angle and wheel angular velocity) and dynamic (applied vertical force and calculated contact forces) – exciting the wheel are either known or already calculated in the previous time-step, and the motion of the rigid-wheel may be captured by applying a classic mechanics approach. This analysis commences locally, that is with respect to the wheel-fixed frame of reference  $O_4$ , where nodal coordinates of the rigid-body are fixed and the ultimate requirement is to obtain the global nodal position, velocity and acceleration after the application of contact forces and the user-defined kinematic and dynamic inputs.

As the magnitude of the wheel angular velocity ( $\Omega$ ) is defined by the user, the respective angular velocity vector is:

$${}^{O_4}\{\omega_\Omega\} = {}^{O_3}\{\omega_\Omega\} = [0 \quad \Omega \quad 0]^T \quad 3.3-28$$

The relative angular position of the wheel with respect to the upright-fixed frame of reference is calculated by integrating  $\Omega$ :

$$\theta_\Omega = \int \Omega \, dt \quad 3.3-29$$

The respective angular acceleration is obtained by differentiating  $\Omega$  with respect to time:

$${}^{O_4}\{\alpha_\Omega\} = {}^{O_3}\{\alpha_\Omega\} = \left[ 0 \quad \frac{d\Omega}{dt} \quad 0 \right]^T \quad 3.3-30$$



The above quantities –  $\theta_\Omega$ ,  $\{\omega_\Omega\}$  and  $\{\alpha_\Omega\}$  – fully describe the motion of the wheel as a result of the first degree of freedom, which is the relative rotation around the common  $^{O_4}y$  (or  $^{O_3}y$ ) axis between the wheel-fixed ( $O_4$ ) and the upright-fixed ( $O_3$ ) frame of reference. The next rigid-body degree of freedom is the relative rotation between the upright-fixed and the rig-fixed ( $O_2$ ) frame of reference around the common vertical axis  $^{O_3}z$  (or  $^{O_2}z$ ). The relative angle between these two frames is the user-imposed steering angle (sa). The resulting angular velocity and acceleration vectors are simply obtained as follows:

$$^{O_3}\{\omega_{sa}\} = ^{O_2}\{\omega_{sa}\} = \begin{bmatrix} 0 & 0 & \frac{d(sa)}{dt} \end{bmatrix}^T \quad 3.3-31$$

$$^{O_3}\{\alpha_{sa}\} = ^{O_2}\{\alpha_{sa}\} = \begin{bmatrix} 0 & 0 & \frac{d^2(sa)}{dt^2} \end{bmatrix}^T \quad 3.3-32$$

The final rigid-body degree of freedom is the vertical linear motion of the wheel with respect to the ground. This corresponds to relative vertical translational motion between the rig-fixed and the global ( $O_1$ ) frame of reference. The vertical acceleration vector of the wheel ( $^{O_1}\{a_{F_z}\}$ ) with respect to the global frame of reference – as a result of the application of the user-imposed vertical force  $F_z$  and the vertical contact forces – is obtained by the following expression:

$$^{O_1}\{a_{F_z}\} = ^{O_2}\{a_{F_z}\} = \begin{bmatrix} 0 & 0 & \frac{F_z + \sum_{i=1}^N(F_{cont}^i(3))}{m_{tot}} \end{bmatrix}^T \quad 3.3-33$$

where  $F_{cont}^i$  is the contact force vector of node  $i$  expressed in the global frame of reference:

$$F_{cont}^i = [F_x^i \quad F_y^i \quad F_z^i]^T \quad 3.3-34$$

and  $m_{tot}$  is the total mass of the tyre/wheel assembly. The respective wheel velocity vector is obtained by integrating, with respect to time, the above acceleration vector:

$$^{O_1}\{v_{F_z}\} = ^{O_2}\{v_{F_z}\} = \begin{bmatrix} 0 & 0 & \int \frac{F_z + \sum_{i=1}^N(F_{cont}^i(3))}{m_{tot}} dt \end{bmatrix}^T \quad 3.3-35$$

Finally, the relative position vector between ( $O_1$ ) and ( $O_2$ ) is calculated as follows:

$${}^{O_1}\{r_{F_z}\} = {}^{O_2}\{r_{F_z}\} = \left[ 0 \quad 0 \quad \int \int \frac{F_z + \sum_{i=1}^N (F_{cont}^i(3))}{m_{tot}} dt dt \right]^T \quad 3.3-36$$

The expressions presented above are exploited to define the non-linear motion of the wheel in space as a result of the application of the user-defined input quantities and contact forces. At this point, one may notice that only vertical contact forces are taken into account in the above analysis. In the context of the present work, and as far as the motion of the wheel as a rigid body is examined, lateral and longitudinal contact forces are reacted by the virtual rig, as the only translational degree of freedom is defined along the global vertical axis. With regard to moments generated by these forces, the rigid wheel examined in the present section demonstrates degrees of freedom along the axes of the self-aligning and the rolling resistance moments. The net effect of these moments is included in the respective user-defined input quantities, steering angle and angular wheel velocity respectively, so no control loop is required to maintain these two quantities as specified during every simulation run.

#### 3.3.4 Nodal motion expressed with respect to the global frame of reference

Having defined the macroscopic rigid-body motion of the wheel, the next step is the calculation of the global position, velocity and acceleration of each belt node. This procedure is required by the contact sub-model, so that interaction between the tyre nodes and the ground is captured and contact forces are calculated. Initially, when expressed in the wheel-fixed frame of reference ( $O_4$ ), the position vector of the  $i^{th}$  belt node – in the non-deformed configuration examined in this section – remains constant throughout the simulation process, see Figure 3.3:

$${}^{O_4}\{x\}_i = [x_i \quad y_i \quad z_i]^T \quad 3.3-37$$

The velocity and acceleration of every belt node, within the rigid-body configuration and with respect to the wheel-fixed frame of reference, is equal to zero:

$$\frac{\partial({}^{O_4}\{x\}_i)}{\partial t} = [0 \quad 0 \quad 0]^T \quad 3.3-38$$

$$\frac{\partial^2({}^{O_4}\{x\}_i)}{\partial t^2} = [0 \quad 0 \quad 0]^T \quad 3.3-39$$

Having obtained the local linear deformation of each belt node by Equation 3.3–26, the actual motion of the  $i^{\text{th}}$  node expressed in the wheel-fixed frame of reference is calculated by superimposing the non-deformed and the deformed nodal motion in accordance to the following relations:

$${}^{O_4}P_i = {}^{O_4}\{x\}_i + {}^{O_4}\{dx\}_i \quad 3.3-40$$

$$\frac{\partial({}^{O_4}P_i)}{\partial t} = \frac{\partial({}^{O_4}\{x\}_i)}{\partial t} + \frac{\partial({}^{O_4}\{dx\}_i)}{\partial t} \Rightarrow$$

$$\frac{\partial({}^{O_4}P_i)}{\partial t} = {}^{O_4}\{\dot{x}\}_i \quad 3.3-41$$

$$\frac{\partial^2({}^{O_4}P_i)}{\partial t^2} = \frac{d({}^{O_4}\{\dot{x}\}_i)}{dt} \Rightarrow$$

$$\frac{\partial^2({}^{O_4}P_i)}{\partial t^2} = {}^{O_4}\{\ddot{x}\}_i \quad 3.3-42$$

The above quantities may be expressed in the upright-fixed frame of reference ( $O_3$ ) by combining Equations 3.2–4, 3.3–29 and 3.3–30 as follows:

$${}^{O_3}P_i = \mathbf{A}(\theta_\Omega) \cdot {}^{O_4}P_i \quad 3.3-43$$

The calculation of the respective velocity and acceleration vectors follows a similar pattern based on Equation 3.2–5 for nodal velocity:

$$\frac{\partial({}^{O_3}P_i)}{\partial t} = \frac{\partial \mathbf{A}(\theta_\Omega)}{\partial \theta_\Omega} \cdot \Omega \cdot {}^{O_4}P_i + \mathbf{A}(\theta_\Omega) \cdot \frac{\partial({}^{O_4}P_i)}{\partial t} \quad 3.3-44$$

and Equations 3.2–6 and 3.3–30 for nodal acceleration:

$$\begin{aligned} \frac{\partial^2 {}^{0_3}P_i}{\partial t^2} = & \frac{\partial^2 \mathbf{A}(\theta_\Omega)}{\partial \theta_\Omega^2} \cdot \Omega^2 \cdot {}^{0_4}P_i + \frac{\partial \mathbf{A}(\theta_\Omega)}{\partial \theta_\Omega} \cdot {}^{0_4}\{\alpha_\Omega\}(2) \cdot {}^{0_4}P_i + \\ & 2 \frac{\partial \mathbf{A}(\theta_\Omega)}{\partial \theta_\Omega} \cdot \Omega \cdot \frac{\partial {}^{0_4}P_i}{\partial t} + \mathbf{A}(\theta_\Omega) \cdot \frac{\partial^2 {}^{0_4}P_i}{\partial t^2} \end{aligned} \quad 3.3-45$$

Similarly, these quantities are expressed in the rig-fixed frame of reference ( $O_2$ ) by combining the transformation equations of Section 3.2.2 with the equations presented above. In particular, the steering angle is defined by the user and the resulting velocity and acceleration vectors are provided by Equations 3.3–31 and 3.3–32 respectively. Having obtained these quantities, the position of belt nodes in  $O_2$  may be calculated by exploiting Equation 3.2–12:

$${}^{0_2}P_i = \mathbf{B}(\text{sa}) \cdot {}^{0_3}P_i \quad 3.3-46$$

The velocity of the  $i^{\text{th}}$  node expressed in  $O_2$  is obtained from Equations 3.2–13 and 3.3–31:

$$\frac{\partial {}^{0_2}P_i}{\partial t} = \frac{\partial \mathbf{B}(\text{sa})}{\partial \text{sa}} \cdot {}^{0_3}\{\omega_{\text{sa}}\}(3) \cdot {}^{0_3}P_i + \mathbf{B}(\text{sa}) \cdot \frac{\partial {}^{0_3}P_i}{\partial t} \quad 3.3-47$$

and the respective acceleration vector derives from Equations 3.2–14 and 3.3–32:

$$\begin{aligned} \frac{\partial^2 {}^{0_2}P_i}{\partial t^2} = & \frac{\partial^2 \mathbf{B}(\text{sa})}{\partial \text{sa}^2} \cdot [{}^{0_3}\{\omega_{\text{sa}}\}(3)]^2 \cdot {}^{0_3}P_i + \frac{\partial \mathbf{B}(\text{sa})}{\partial \text{sa}} \cdot \\ & {}^{0_3}\{\alpha_{\text{sa}}\}(3) \cdot {}^{0_3}P_i + 2 \frac{\partial \mathbf{B}(\text{sa})}{\partial \text{sa}} \cdot {}^{0_3}\{\omega_{\text{sa}}\}(3) \cdot \frac{\partial {}^{0_3}P_i}{\partial t} + \mathbf{B}(\text{sa}) \cdot \frac{\partial^2 {}^{0_3}P_i}{\partial t^2} \end{aligned} \quad 3.3-48$$

Finally, these quantities may be expressed in the inertial frame of reference ( $O_1$ ), as follows:

$${}^{0_1}P_i = {}^{0_2}P_i + {}^{0_1}\{r_{F_z}\} \quad 3.3-49$$

$$\frac{\partial {}^{0_1}P_i}{\partial t} = \frac{\partial {}^{0_2}P_i}{\partial t} + {}^{0_1}\{v_{F_z}\} \quad 3.3-50$$

$$\frac{\partial^2 {}^{0_1}P_i}{\partial t^2} = \frac{\partial^2 {}^{0_2}P_i}{\partial t^2} + {}^{0_1}\{a_{F_z}\} \quad 3.3-51$$

These expressions describe the motion of each belt node with respect to global coordinates. As it is demonstrated in the following sections, this process is critical in calculating contact forces between the tyre belt and the road.

### 3.3.5 External force vector

The final step in this process is the calculation of the vector containing the external forces acting on the tyre. As has been demonstrated above, this is not a straightforward task, as three user-imposed excitations are applied on the wheel centre, the motion of which is not included in the system of differential equations representing the tyre.

Taking into account the above, the concept of equivalent nodal forces is introduced. The main feature of this particular force vector is that it has the same net effect as the user-defined quantities mentioned in the preceding paragraph, but now this effect is evaluated for each node rather than the wheel centre. As a result, the vector of external nodal forces found in Equations 3.3–23 and 3.3–24 may be expressed as follows:

$$\{f_{\text{ext}}\}_{3N \times 1} = \{f_{\text{equi}}\}_{3N \times 1} + \{f_{\text{cont}}\}_{3N \times 1} \quad 3.3-52$$

where  $\{f_{\text{equi}}\}_{3N \times 1}$  consists of nodal forces which have an equivalent effect in the wheel motion as the user-defined input quantities (variation of steering angle, wheel angular velocity and vertical force),

$\{f_{\text{cont}}\}_{3N \times 1}$  consists of nodal forces generated by the interaction between the tyre/wheel assembly and the ground.

The present section is dedicated to demonstrating the implemented method of attack with regard to calculating vector  $\{f_{\text{equi}}\}_{3N \times 1}$ . For information on vector  $\{f_{\text{cont}}\}_{3N \times 1}$  the reader may refer to Section 3.4. To calculate vector  $\{f_{\text{equi}}\}_{3N \times 1}$ , contact forces are set equal to zero (that is  $\{f_{\text{cont}}\} = \{0\}_{3N \times 1}$ ) and Equation 3.3–23 is exploited and rewritten as follows:

$$\Phi_{RB}^T \{f_{ext}\} - M_{RB} \{\ddot{q}\} = \begin{Bmatrix} 0 \\ \vdots \\ 0 \end{Bmatrix} \Rightarrow$$

$$\Phi_{RB}^T [\{f_{equi}\} + \{f_{cont}\}] - M_{RB} \{\ddot{q}\} = \begin{Bmatrix} 0 \\ \vdots \\ 0 \end{Bmatrix} \Rightarrow$$

$$\Phi_{RB}^T \{f_{equi}\} - M_{RB} \{\ddot{q}\} = \begin{Bmatrix} 0 \\ \vdots \\ 0 \end{Bmatrix} \Rightarrow$$

$$\Phi_{RB}^T \{f_{equi}\} = M_{RB} \{\ddot{q}\} \Rightarrow$$

$$\overbrace{\Phi_{RB}^T M_{RB}^{-1} \Phi_{RB}^T}^Q \{f_{equi}\} = \Phi_{RB} \{\ddot{q}\} \quad 3.3-53$$

At this point, the fact that contact forces have been set equal to zero does not introduce an artificial simplification to the model. On the contrary, as  $\{f_{equi}\}$  corresponds only to external forces derived from the user-imposed input quantities, the inclusion of contact forces in the above equations would lead to erroneous results. Additionally, contact forces are eventually added to vector  $\{f_{equi}\}$  according to Equation 3.3–52.

Combination of Equations 3.3–8 and 3.3–53 yields:

$$Q \{f_{equi}\} = \{x_{rigid}^{\ddot{}}\} \quad 3.3-54$$

where, in the current context,  $\{x_{rigid}^{\ddot{}}\}_{3N \times 1}$  represents the non-linear three dimensional acceleration of each belt node due to the external user-imposed excitation applied to the wheel structure, as it is implied by term  $\{f_{equi}\}$  in the left-hand side of Equation 3.3–54.

Vector  $\{x_{rigid}^{\ddot{}}\}$  is calculated analytically by taking into account the translational velocity and acceleration of the wheel centre and the respective angular acceleration and velocity as a result of the user-imposed excitation. In addition, the position vector of each belt node is required which, for the case of the non-deformable belt and with respect to the wheel-attached frame of reference, remains constant throughout the simulation process. In

particular, as it has been demonstrated in the work of G. Mavros in [73], the acceleration of the  $i^{\text{th}}$  belt node is calculated as follows:

$$\begin{Bmatrix} \ddot{x}_{\text{rigid}} \\ \ddot{y}_{\text{rigid}} \\ \ddot{z}_{\text{rigid}} \end{Bmatrix}_i = \begin{Bmatrix} \ddot{x}_c \\ \ddot{y}_c \\ \ddot{z}_c \end{Bmatrix} + \mathbf{J}_1 + \mathbf{J}_2 \quad 3.3-55$$

$$\mathbf{J}_1 = \begin{Bmatrix} -\dot{y}_c \dot{z}_c + \dot{z}_c \dot{y}_c \\ -\dot{z}_c \dot{x}_c + \dot{x}_c \dot{z}_c \\ -\dot{x}_c \dot{y}_c + \dot{y}_c \dot{x}_c \end{Bmatrix} \quad 3.3-56$$

$$\mathbf{J}_2 = \begin{Bmatrix} -P_x^i \cdot (\dot{y}_c^2 + \dot{z}_c^2) + P_y^i \cdot (\dot{x}_c \dot{z}_c - \dot{z}_c \dot{x}_c) + P_z^i \cdot (\dot{x}_c \dot{y}_c + \dot{y}_c \dot{x}_c) \\ -P_y^i \cdot (\dot{z}_c^2 + \dot{x}_c^2) + P_z^i \cdot (\dot{y}_c \dot{z}_c - \dot{z}_c \dot{y}_c) + P_x^i \cdot (\dot{x}_c \dot{z}_c + \dot{z}_c \dot{x}_c) \\ -P_z^i \cdot (\dot{x}_c^2 + \dot{y}_c^2) + P_x^i \cdot (\dot{z}_c \dot{x}_c - \dot{x}_c \dot{z}_c) + P_y^i \cdot (\dot{y}_c \dot{z}_c + \dot{z}_c \dot{y}_c) \end{Bmatrix} \quad 3.3-57$$

where:

${}^{O_4}\{\mathbf{a}_c\} = [\dot{x}_c \dot{y}_c \dot{z}_c]^T$  is the linear acceleration vector of the wheel centre,

${}^{O_4}\{\boldsymbol{\alpha}_c\} = [\ddot{x}_c \ddot{y}_c \ddot{z}_c]^T$  is the angular acceleration vector of the wheel,

${}^{O_4}\{\mathbf{v}_c\} = [\dot{x}_c \dot{y}_c \dot{z}_c]^T$  is the linear velocity vector of the wheel centre,

${}^{O_4}\{\boldsymbol{\omega}_c\} = [\dot{x}_c \dot{y}_c \dot{z}_c]^T$  is the angular velocity vector of the wheel and

${}^{O_4}\{\mathbf{P}^i\} = [P_x^i P_y^i P_z^i]^T$  is the position vector of the  $i^{\text{th}}$  node.

It should be noted that all the above quantities are expressed with respect to the wheel-fixed ( $O_4$ ) frame of reference. The above velocity and acceleration vectors originate from the following 3 user-imposed excitation quantities:

- vertical force ( $F_z$ ),
- steer angle ( $\delta$ ) and
- wheel angular velocity ( $\Omega$ ).

As has been demonstrated above, the applied vertical force results in a linear vertical acceleration of the wheel with respect to the global frame of reference ( $O_1$ ). By taking into account the total mass of the wheel-tyre assembly, the equivalent acceleration resulting only from the application of the user-defined vertical force is simply calculated as follows:

$${}^{O_1}\{\mathbf{a}_{F_z}\}_{\text{equi}} = \begin{bmatrix} 0 & 0 & F_z/m_{\text{tot}} \end{bmatrix}^T \quad 3.3-58$$

The calculation of the respective linear velocity is achieved by integrating Equation 3.3–58 with respect to time:

$${}^{O_1}\{v_{F_z}\}_{\text{equi}} = \begin{bmatrix} 0 & 0 & \int (F_z/m_{\text{tot}}) dt \end{bmatrix}^T \quad 3.3-59$$

To populate Equations 3.3–55 to 3.3–57, the above two vectors have to be expressed in the local ( $O_4$ ) frame of reference. To this end, they are initially expressed in the rig-fixed frame of reference ( $O_2$ ). Since the respective axes of the global and the rig-fixed frames are parallel to each other, see Figure 3.12, the following expressions hold:

$$\begin{aligned} {}^{O_2}\{a_{F_z}\}_{\text{equi}} &= {}^{O_1}\{a_{F_z}\}_{\text{equi}} \Rightarrow \\ {}^{O_2}\{a_{F_z}\}_{\text{equi}} &= \begin{bmatrix} 0 & 0 & F_z/m_{\text{tot}} \end{bmatrix}^T \end{aligned} \quad 3.3-60$$

$$\begin{aligned} {}^{O_2}\{v_{F_z}\}_{\text{equi}} &= {}^{O_1}\{v_{F_z}\}_{\text{equi}} \Rightarrow \\ {}^{O_2}\{v_{F_z}\}_{\text{equi}} &= \begin{bmatrix} 0 & 0 & \int (F_z/m_{\text{tot}}) dt \end{bmatrix}^T \end{aligned} \quad 3.3-61$$

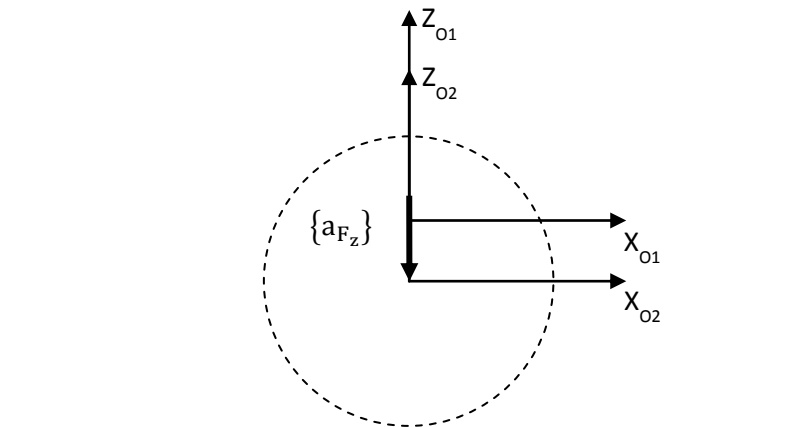


Figure 3.12 – Expression of vertical acceleration vector in the inertial and the rig-fixed frame of reference



The next step is to express vector  $\{a_{F_z}\}_{\text{equi}}$  with respect to  $O_3$ . As it is illustrated in Figure 3.13, vector  $^{O_2}\{a_{F_z}\}_{\text{equi}}$  expressed in  $O_2$  is equal to vector  $^{O_3}\{a_{F_z}\}_{\text{equi}}$  expressed in  $O_3$ , as these two coordinate systems share a common z axis. Consequently:

$$^{O_3}\{a_{F_z}\}_{\text{equi}} = ^{O_2}\{a_{F_z}\}_{\text{equi}} \Rightarrow$$

$$^{O_3}\{a_{F_z}\}_{\text{equi}} = \begin{bmatrix} 0 & 0 & F_z/m_{\text{tot}} \end{bmatrix}^T \quad 3.3-62$$

The same principle applies to velocity vector  $^{O_2}\{v_{F_z}\}_{\text{equi}}$  :

$$^{O_3}\{v_{F_z}\}_{\text{equi}} = ^{O_2}\{v_{F_z}\}_{\text{equi}} \Rightarrow$$

$$^{O_3}\{v_{F_z}\}_{\text{equi}} = \begin{bmatrix} 0 & 0 & \int (F_z/m_{\text{tot}}) dt \end{bmatrix}^T \quad 3.3-63$$

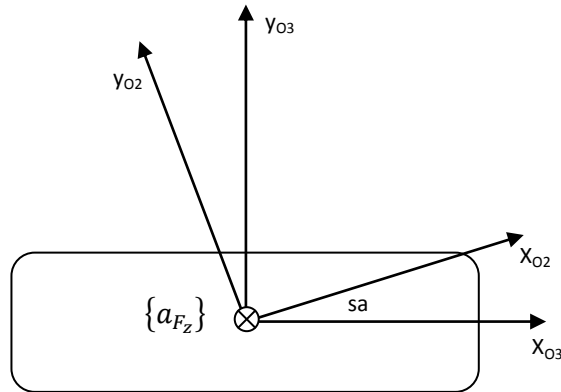


Figure 3.13 – Expression of vertical acceleration vector in the rig-fixed and the upright-fixed frame of reference

With reference to the user-induced steering angle, the respective angular velocity and acceleration are required by Equations 3.3–55 to 3.3–57. It follows from the above that these vectors have a single component along the common z axis of  $O_2$  and  $O_3$ , and consequently they may be directly expressed in  $O_3$ . In particular, the respective angular velocity vector is provided by equation 3.3–31:

$${}^{O_3}\{\omega_{sa}\} = \begin{bmatrix} 0 & 0 & \frac{d(sa)}{dt} \end{bmatrix}^T \quad 3.3-64$$

Angular acceleration vector derived by steering angle variation is provided by equation 3.3–32:

$${}^{O_3}\{\alpha_{sa}\} = \begin{bmatrix} 0 & 0 & \frac{d^2(sa)}{dt^2} \end{bmatrix}^T \quad 3.3-65$$

The final transformation of the user-defined quantities is conducted between  $O_3$  and  $O_4$ . As has been established in section 3.2.1, the transformation matrix between these two coordinates systems is the following:

$$\mathbf{A}(\theta_\Omega) = \begin{bmatrix} \cos\theta_\Omega & 0 & \sin\theta_\Omega \\ 0 & 1 & 0 \\ -\sin\theta_\Omega & 0 & \cos\theta_\Omega \end{bmatrix} \quad 3.3-66$$

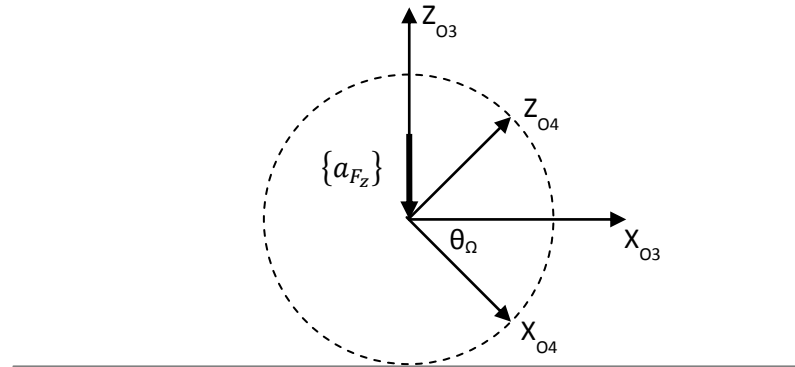


Figure 3.14 – Expression of vertical acceleration vector in the upright-fixed and the wheel-fixed frame of reference

Angular deviation  $\theta_\Omega$  between  $O_3$  and  $O_4$  has been previously calculated in Equation 3.3–29. Vertical acceleration vector  $\{a_{F_z}\}$ , originating from the user-defined vertical load  $F_z$ , is expressed in  $O_3$  in equation 3.3–62 and the respective linear vertical velocity may be found in Equation 3.3–63. These quantities are expressed in  $O_4$  as follows:

$${}^{O_4}\{a_{F_z}\}_{\text{equi}} = \mathbf{A}(\theta_\Omega) \cdot {}^{O_3}\{a_{F_z}\}_{\text{equi}} \Rightarrow$$

$${}^{O_4}\{a_{F_z}\}_{\text{equi}} = \begin{bmatrix} \cos\theta_\Omega & 0 & \sin\theta_\Omega \\ 0 & 1 & 0 \\ -\sin\theta_\Omega & 0 & \cos\theta_\Omega \end{bmatrix} \cdot \begin{bmatrix} 0 \\ 0 \\ F_z/m_{\text{tot}} \end{bmatrix} \Rightarrow$$

$${}^{O_4}\{a_{F_z}\}_{\text{equi}} = \begin{bmatrix} \sin\theta_\Omega \cdot \frac{F_z}{m_{\text{tot}}} \\ 0 \\ \cos\theta_\Omega \cdot \frac{F_z}{m_{\text{tot}}} \end{bmatrix} \quad 3.3-67$$

Velocity vector  $\{v_c\}$ , which is collinear to acceleration vector  $\{a_c\}$ , is expressed in  $O_4$  following an identical approach:

$${}^{O_4}\{v_{F_z}\}_{\text{equi}} = \begin{bmatrix} \sin\theta_\Omega \cdot \int \frac{F_z}{m_{\text{tot}}} dt \\ 0 \\ \cos\theta_\Omega \cdot \int \frac{F_z}{m_{\text{tot}}} dt \end{bmatrix} \quad 3.3-68$$

Angular velocity and acceleration vectors, found in Equations 3.3-64 and 3.3-65, are also rotated by  $\theta_\Omega$  so as to be expressed in  $O_4$ . First, angular velocity  ${}^{O_3}\{\omega_{sa}\}$  is transformed into  ${}^{O_4}\{\omega_{sa}\}$ :

$${}^{O_4}\{\omega_{sa}\} = \mathbf{A}(\theta_\Omega) \cdot {}^{O_3}\{\omega_{sa}\} \Rightarrow$$

$${}^{O_4}\{\omega_{sa}\} = \begin{bmatrix} \cos\theta_\Omega & 0 & \sin\theta_\Omega \\ 0 & 1 & 0 \\ -\sin\theta_\Omega & 0 & \cos\theta_\Omega \end{bmatrix} \cdot \begin{bmatrix} 0 \\ 0 \\ \frac{d(sa)}{dt} \end{bmatrix} \Rightarrow$$

$${}^{O_4}\{\omega_{sa}\} = \begin{bmatrix} \sin\theta_\Omega \cdot \frac{d(sa)}{dt} \\ 0 \\ \cos\theta_\Omega \cdot \frac{d(sa)}{dt} \end{bmatrix} \quad 3.3-69$$

In addition, slip-angle induced angular acceleration is expressed with respect to  $O_4$ :

$${}^{O_4}\{\alpha_{sa}\} = \begin{bmatrix} \sin\theta_\Omega \cdot \frac{d^2(sa)}{dt^2} \\ 0 \\ \cos\theta_\Omega \cdot \frac{d^2(sa)}{dt^2} \end{bmatrix} \quad 3.3-70$$

The final user-imposed input quantity of the model, defining the motion of the wheel as a rigid body, is angular velocity  $\Omega$  which consists of a single component along the y axis of  $O_4$ , see Equation 3.3–28:

$${}^{O_4}\{\omega_\Omega\} = \begin{bmatrix} 0 \\ \Omega \\ 0 \end{bmatrix} \quad 3.3-71$$

The respective angular acceleration is obtained by Equation 3.3–30:

$${}^{O_4}\{\alpha_\Omega\} = \begin{bmatrix} 0 \\ \frac{d(\Omega)}{dt} \\ 0 \end{bmatrix} \quad 3.3-72$$

The velocity and acceleration vectors calculated above are exploited to populate the corresponding vectors found in Equations 3.3–55 to 3.3–57. With exclusive reference to user-defined quantities, the motion of the wheel is described by four vectors; two vectors for translational and two for rotational motion. Since vertical load is the only translational user input, the user-induced translational motion of the wheel is only affected by the acceleration and velocity vectors derived by vertical load  $F_z$ . In particular:

$${}^{O_4}\{a_c\} = {}^{O_4}\{a_{F_z}\}_{\text{equi}} \Rightarrow$$

$$\begin{bmatrix} {}_x a_c \\ {}_y a_c \\ {}_z a_c \end{bmatrix} = \begin{bmatrix} \sin\theta_\Omega \cdot \frac{F_z}{m_{\text{tot}}} \\ 0 \\ \cos\theta_\Omega \cdot \frac{F_z}{m_{\text{tot}}} \end{bmatrix} \quad 3.3-73$$

$${}^{O_4}\{V_c\} = {}^{O_4}\{V_{F_z}\}_{\text{equi}} \Rightarrow$$

$$\begin{bmatrix} xV_c \\ yV_c \\ zV_c \end{bmatrix} = \begin{bmatrix} \sin\theta_\Omega \cdot \int \frac{F_z}{m_{tot}} dt \\ 0 \\ \cos\theta_\Omega \cdot \int \frac{F_z}{m_{tot}} dt \end{bmatrix} \quad 3.3-74$$

With regard to the rotational motion of the wheel, the acceleration and velocity vectors are calculated by combining the motion due to slip angle variation with the motion derived by the primary angular velocity of the wheel ( $\Omega$ ):

$${}^{O_4}\{\alpha_c\} = {}^{O_4}\{\alpha_{sa}\} + {}^{O_4}\{\alpha_\Omega\} \Rightarrow$$

$$\begin{bmatrix} x\alpha_c \\ y\alpha_c \\ z\alpha_c \end{bmatrix} = \begin{bmatrix} \sin\theta_\Omega \cdot \frac{d^2(sa)}{dt^2} \\ \frac{d(\Omega)}{dt} \\ \cos\theta_\Omega \cdot \frac{d^2(sa)}{dt^2} \end{bmatrix} \quad 3.3-75$$

$${}^{O_4}\{\omega_c\} = {}^{O_4}\{\omega_{sa}\} + {}^{O_4}\{\omega_\Omega\} \Rightarrow$$

$$\begin{bmatrix} x\omega_c \\ y\omega_c \\ z\omega_c \end{bmatrix} = \begin{bmatrix} \sin\theta_\Omega \cdot \frac{d(sa)}{dt} \\ \Omega \\ \cos\theta_\Omega \cdot \frac{d(sa)}{dt} \end{bmatrix} \quad 3.3-76$$

The non-linear acceleration of each node is obtained from Equation 3.3–55 and vector  $\{\ddot{x}_{rigid}\}$  is populated. Visual inspection of Equation 3.3–54 would suggest that the equivalent force vector could be calculated by multiplying the inverse of matrix  $\mathbf{Q}$  by the nodal acceleration vector calculated above. However, this is not possible due to the origin of matrix  $\mathbf{Q}$ , see Equation 3.3–53. Since the rank of matrix  $\mathbf{Q}$  is equal to 6 and the equations included in the system of 3.3–55 are 3N, with 3N significantly higher than 6, direct inversion is impossible and the system of Equations 3.3–55 is classified as rank deficient. A typical method to approach similar rank deficient systems is by obtaining the reduced singular value decomposition<sup>[23][101]</sup> (SVD) of matrix  $\mathbf{Q}$ , which demonstrates the following form:

$$\mathbf{Q} = \mathbf{U}\mathbf{\Sigma}(\mathbf{V})^T \quad 3.3-77$$

Compared to the typical SVD of a system which is not rank deficient, the three matrices introduced above are sub-matrices of the original ones. In particular, matrix  $\mathbf{\Sigma}$  consists of the 6x6 principal sub-matrix of the complete matrix  $\mathbf{\Sigma}_{\text{tot}}$ , and matrices  $\mathbf{U}$  and  $\mathbf{V}$  consist of the first 6 columns of the original matrices,  $\mathbf{U}_{\text{tot}}$  and  $\mathbf{V}_{\text{tot}}$  respectively. Substitution of matrix  $\mathbf{Q}$  in equation 3.3–54 yields:

$$\mathbf{U}\mathbf{\Sigma}(\mathbf{V})^T\{f_{\text{equi}}\} = \{x_{\text{rigid}}\} \quad 3.3-78$$

which may be solved for  $\{f_{\text{equi}}\}$  as follows:

$$\{f_{\text{equi}}\} = \overbrace{\mathbf{V}\mathbf{\Sigma}^{-1}(\mathbf{U})^T}^A \{x_{\text{rigid}}\} \quad 3.3-79$$

As a demonstration of the method presented above, the wheel is represented by 1680 circumferential nodes and it is excited by applying a user-defined vertical force of 1000N at the wheel centre. Having set the wheel mass equal to 10kg, every belt node is vertically accelerated at  $100\text{m/s}^2$ . Consequently the following expression holds:

$$\{x_{\text{rigid}}\} = \{\dots \quad 0 \quad 0 \quad 100 \quad \dots\}^T \quad 3.3-80$$

By applying the above nodal acceleration vector in Equation 3.3–79, the equivalent force vector is calculated as follows:

$$\{f_{\text{equi}}\} = \{\dots \quad 0 \quad 0 \quad 0.5952 \quad \dots\}^T \quad 3.3-81$$

The z-component of the above expression is the equivalent of distributing the centrally applied vertical force to all the 1680 nodes. Hence, by analytically calculating the nodal non-linear acceleration (vector  $\{x_{\text{rigid}}\}$ ), it is possible to obtain the equivalent force vector which applies directly to the nodes and it also takes into account dynamic and kinematic user-defined inputs applied to the wheel centre. Moreover, term A of Equation 3.3–79 is not time-dependent, therefore its admittedly elaborate calculation is performed only once as part of the initialisation procedure of the proposed tyre model.

Based on the singular value decomposition presented in Equation 3.3–77, vector  $\{f_{\text{equi}}\}$  is obtained by Equation 3.3–79. Following the methodology presented in Section 3.4, vector  $\{f_{\text{cont}}\}$  – consisting of the contact forces between the tyre and the ground – is calculated and used in Equation 3.3–52 along with the equivalent forces vector  $\{f_{\text{equi}}\}$ . Finally, vector  $\{f_{\text{ext}}\}$  obtained by Equation 3.3–52 is consequently used in Equation 3.3–25 to excite the flexible dynamics of the tyre belt.

### 3.4 Estimation of contact forces

#### 3.4.1 Vertical tread modelling

With regard to modelling vertical tread dynamics, several alternative approaches may be found in the literature. These approaches range from tyre models having the tyre elastically founded to the ground by a single Kelvin element, to brush-like models integrating a more advanced tread representation, where the contact patch is formed by several bristles with three-dimensional stiffness and damping properties along the radial, the tangential and the lateral axis of each tread node.

The elastic foundation of the tyre on a single spring/damper unit offers an economical and efficient way of predicting the total vertical force applied to the contact patch and it is suitable for studies where the calculation of the vertical load distribution is not critical, for example in real-time vehicle handling simulations. In cases where the vertical load distribution is required, three main analytical approaches may be found in literature:

- spatially constant vertical load distribution,
- parabolic vertical load distribution, and
- trapezoidal vertical load distribution.

The first case is a rather coarse representation of the vertical force distribution applied to the contact patch. Moreover, such an approach does not satisfy the boundary conditions at the leading and trailing edges of the contact patch, where the vertical load is equal to zero. The second and third cases allow for modelling a more realistic vertical force variation along the contact patch. Both approaches may generate valid results depending on the combination of the magnitude of the applied vertical force and the structural characteristics of the tyre. Experimental results (W. Hall et al. in [49], S. Kim et al. in [56], M. Pau et al. in [82] and E. Sakai in [91]) suggest that, for a given tyre, the vertical force distribution in the contact patch demonstrates a parabolic shape – maximum force at the centre of the contact patch and zero

force at both the leading and trailing edges – for cases where the applied vertical load is relatively low. On the contrary, as the applied vertical load increases, the shape of the vertical force distribution switches to trapezoidal – a flat central area of constant vertical force surrounded by two slopes adjacent to both contact patch edges. In addition, the geometry of the contact patch and the vertical force distribution depend on tyre operation, as demonstrated in the work of H. Shiobara et al. in [98] and [99].

Studies investigating both low and high vertical loads need to incorporate both the abovementioned parabolic and trapezoidal cases. A common approach<sup>[110]</sup> is the utilisation of the following two modelling features:

- flexible belt dynamics and
- tread sub-model consisting of radial, tangential, and lateral bristle-like Kelvin elements.

Such an implementation allows for switching between the two distributions of vertical force. Once contact occurs, the tread elements located between the leading and trailing edges are deformed radially and tangentially. These local deformations result in the application of contact forces to the belt. During the initial contact stages – and before a high enough load is applied to the tyre – the arc of the flexible belt corresponding to the contact patch retains its circular shape and consequently the nodal contact forces demonstrate a parabolic shape. An increase in the applied vertical load would cause that particular belt arc to straighten, due to belt compliance and the increased contact forces. Contrary to the lower vertical load case, the vertical forces applied to the central points of the contact patch exhibit a constant value, while the respective forces applied close to the two contact edges decrease abruptly, hence the term “trapezoidal” vertical force distribution.

In the context of the present work, a tread model of intermediate complexity is implemented. While the flexible belt dynamics represent the core of the proposed modelling approach, the two elements forming the implemented tread model, namely vertical tread dynamics and shear force generation, have been chosen on the grounds of being efficient in order to keep in line with the generic purpose of this study. Implementing a tread model similar to the one demonstrated in [57] or the one in [110], that is one three-dimensional Kelvin element per belt node, would impose a further  $3N$  second-order differential equations to solve in each time step, where  $N$  is the number of tread nodes.



A less demanding version of this approach derives by neglecting tread mass, similar in that respect to the work of A. Zanten et al. in [117] and the work of J. Zhou et al. in [119], so that the tread model is associated with 3N first-order differential equations of motion, an approach which is fundamentally equivalent to the tread formulation adopted in the present study. In particular, in this work each belt node is associated with an elastic bristle, leading to a brush-like tread representation. Each bristle demonstrates three-dimensional stiffness which breaks down into a number of purely vertical Kelvin elements, used for modelling tread dynamics along the vertical direction – analysed in the following paragraphs – and a distributed LuGre friction model for estimation of shear forces along the contact area, see Section 2.5 in Chapter 2 for the respective theoretical background, and Section 3.4.2 for the present implementation.

As is depicted in the following diagram, an elastic boundary has been placed between the tyre belt and the ground level, in a layout similar to the one proposed by the Hankook Tire model<sup>[66]</sup>. In each time step, the global vertical position of the belt nodes is examined and, if found within this elastic boundary, the respective Kelvin element has an effect on the vertical motion of the tyre. The width of the elastic boundary ( $l_0$ ) may be interpreted as the free length of these Kelvin elements.

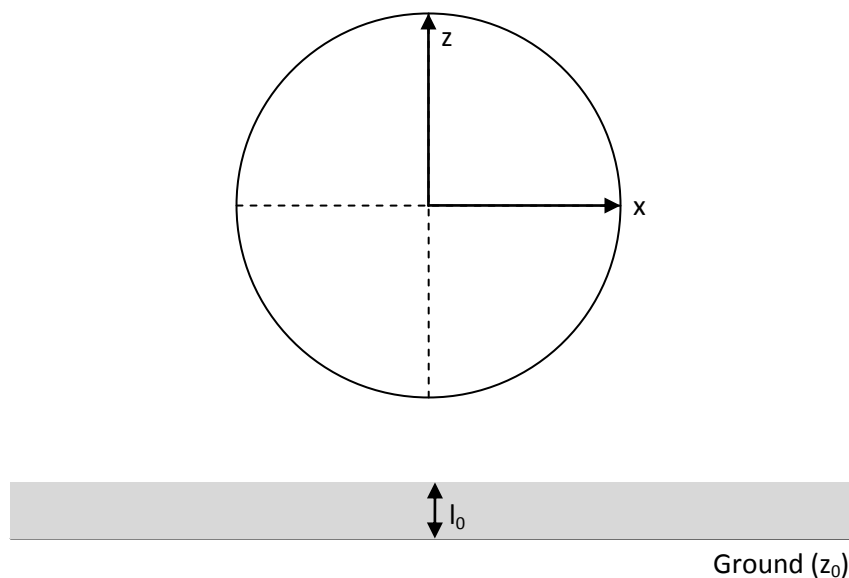


Figure 3.15 – Illustration of the elastic boundary introduced between the tyre belt and the ground

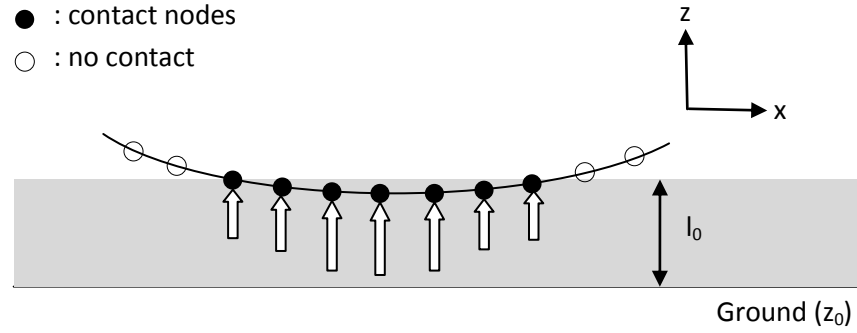


Figure 3.16 – Distinction between nodes locate within the elastic boundary (contact nodes) and nodes located above the elastic boundary (no contact nodes)

As this elastic boundary consists of simple Kelvin elements, the force law governing this contact phenomenon is described by the following equation:

$$F_z = \begin{cases} 0 & , \delta_z \leq 0 \\ k_z \delta_z d_{xy} - c_z v_z d_{xy} & , \delta_z > 0 \end{cases} \quad 3.4-1$$

where:  $v_z$  is the nodal velocity along the  $z$  axis of the global coordinate system [m/s]

$k_z$  is the elastic boundary vertical stiffness per unit length ( $= 1.1 \cdot 10^6 \text{ N/m}^2$ )

$c_z$  is the elastic boundary vertical damping per unit length ( $= 4.5 \cdot 10^3 \text{ Ns/m}^2$ )

$d_{xy}$  is the projection of the distance between two adjacent nodes on the global  $xy$  plane [m]

$\delta_z$  is obtained by the following expression:

$$\delta_z = z_0 + l_0 - z_{\text{node}} \quad 3.4-2$$

Term  $d_{xy}$  is included in Equation 3.4–1 to allow for vertical stiffness and damping constants to be expressed in a “per unit length” form. This approach enables the contact model to be valid for any number of belt nodes included in the belt sub-model. Moreover,  $k_z$  has been obtained by the tread simulation model presented in [80], while  $c_z$  has been set to a value which provides a reasonable stiffness to damping ratio when compared to previous studies, see for example the work of A. Tsotras in [110].

The use of purely vertical Kelvin elements may represent a less detailed tread modelling approach as opposed to similar attempts which incorporate Kelvin elements along the radial, the tangential, and the lateral direction of every tyre belt node<sup>[110]</sup>. The main drawback inherited by the present approach is that longitudinal shear forces along the contact patch –

for the case where only vertical load is applied and the tyre is otherwise stationary – are exclusively based on nodal velocity, because of the implemented LuGre contact model, rather than tread deformation. On the other hand, implementation of radial / tangential / lateral tread elements in the present study would lead to a more complicated tread model, compared to the one presented above. Additionally it would not be in line with the adopted LuGre model presented in the following section and used to calculate shear forces generated in the contact area.

### 3.4.2 Force generation in the contact area

The contact sub-model implemented within the proposed tyre modelling approach consists of a distributed LuGre model and it is based on the work conducted by E. Velenis et al. in [112] and [113]. This class of models has already been presented in Chapter 2. The approach adopted in this work has been inspired by the work of J. Deur et al. in [26] where the tyre belt flexibility and its effect on contact-related phenomena is investigated. In the context of the present model, the main inputs of the contact sub-model are the following three quantities:

- vertical force distribution,
- longitudinal nodal velocity relative to the ground, and
- lateral nodal velocity relative to the ground.

The first input of the contact model is the vertical force distribution ( $F_z$ ), expressed in the global frame of reference, which is obtained by evaluating Equation 3.4–1 for every node in contact to the ground. The second and third inputs consist of the relative velocity of the contact belt nodes with respect to the ground. This relative velocity may be analysed in two components, one longitudinal and one lateral and, similarly to the vertical force distribution, they are both expressed with respect to the global frame of reference ( $O_1$ ).

Two quantities influence this relative velocity, namely the user defined kinematic inputs and the deformation velocity of every contact node. For the  $i^{\text{th}}$  belt node, the longitudinal component of the relative to the ground velocity is provided by the following expression:

$${}_i v_{rx} = \frac{\partial {}^{0_1}P_i}{\partial t}(1) + v_d \quad 3.4-3$$

where  $\frac{\partial^{0_1}P_i}{\partial t}(1)$  is obtained from Equation 3.3–50 and represents the velocity component of the  $i^{\text{th}}$  node expressed along the x axis of  $O_1$  and  $v_d$  is the user defined drum velocity. The respective expression for the lateral relative velocity component is:

$${}_i v_{ry} = \frac{\partial^{0_1}P_i}{\partial t}(2) \quad 3.4-4$$

The parameters for the contact sub-model presented in the section are obtained by the work conducted by E. Velenis et al. in [113] and they are summarised in the following table:

<b>Table 3.1: Contact parameters for the LuGre sub-model</b>							
$\sigma_{0x}$	$\sigma_{0y}$	$\mu_{kx}$	$\mu_{ky}$	$\mu_{sx}$	$\mu_{sy}$	$\gamma$	$v_s$
[1/m]	[1/m]	[-]	[-]	[-]	[-]	[-]	[m/s]
247	211	0.75	0.79	1.24	1.18	1	4.02

For all the contact nodes, normalised dimension  $\zeta$  is defined between the leading and the trailing edges, as is illustrated in the following figure:

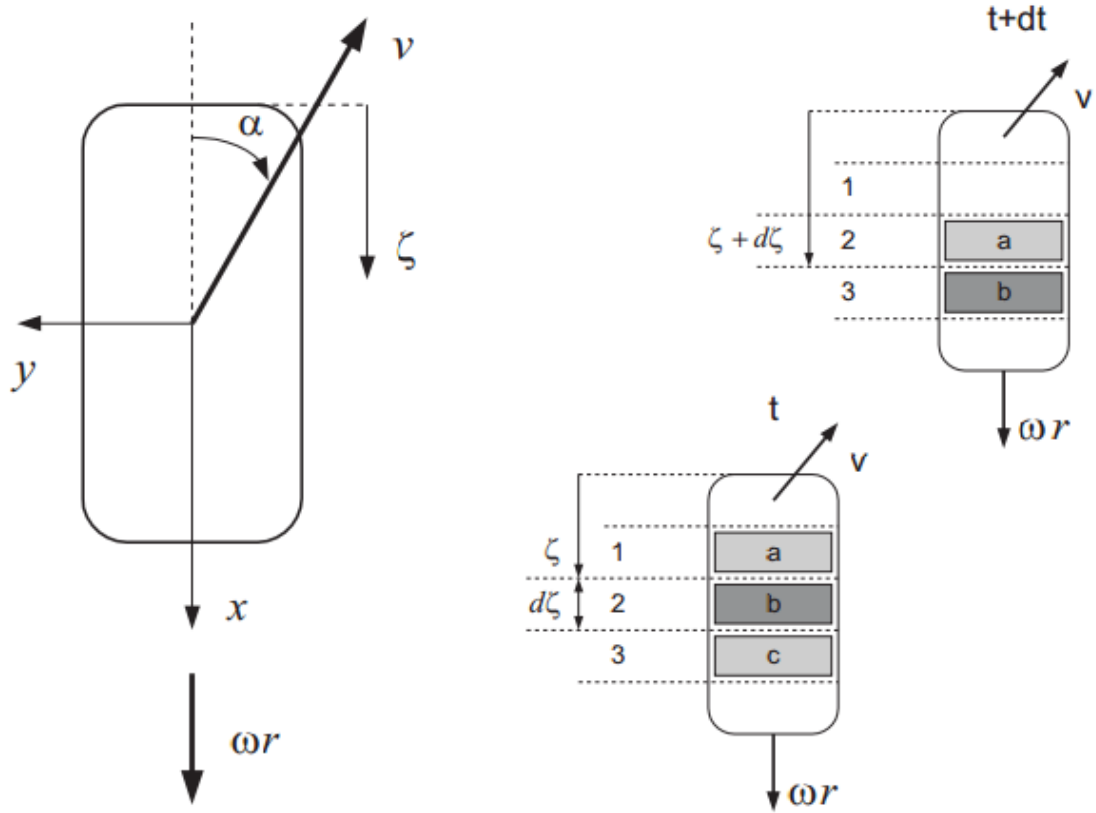


Figure 3.17 – Frames of reference and velocities at the contact patch ([113])

In every time step, and for every  $\zeta$  position along the contact patch, the longitudinal and lateral deflection of the contact elements are denoted as  $z_x(t, \zeta)$  and  $z_y(t, \zeta)$ , respectively. The differential equations governing these deflections for the  $i^{\text{th}}$  contact node have the following form<sup>[113]</sup>:

$$\frac{d}{dt} {}_i z_j = {}_i v_{rj} - C_{0j}({}_i v_{rj}) \cdot {}_i z_j \quad 3.4-5$$

where  $j$  stands for either  $x$  or  $y$ ,  ${}_i v_{rj}$  is provided by Equations 3.4-3 and 3.4-4 and  $C_{0j}({}_i v_{rj})$  is equal to:

$$C_{0j}({}_i v_{rj}) = \frac{\lambda(\{{}_i v_r\}) * \sigma_{0j}}{\mu_{kj}^2} \quad 3.4-6$$

Function  $\lambda({}_i v_r)$  is calculated by the following expression:

$$\lambda(\{ {}_i v_r \}) = \frac{\| \mathbf{M}_k^2 \cdot \{ {}_i v_r \} \|}{g(\{ {}_i v_r \})} \quad 3.4-7$$

with  $\mathbf{M}_k = \text{diag}(\mu_{kx}, \mu_{ky})$ ,  $\{ {}_i v_r \} = [{}_i v_{rx} \ {}_i v_{ry}]^T$  and

$$g(\{ {}_i v_r \}) = \frac{\| \mathbf{M}_k^2 \cdot \{ {}_i v_r \} \|}{\| \mathbf{M}_k \cdot \{ {}_i v_r \} \|} + \left( \frac{\| \mathbf{M}_s^2 \cdot \{ {}_i v_r \} \|}{\| \mathbf{M}_s \cdot \{ {}_i v_r \} \|} - \frac{\| \mathbf{M}_k^2 \cdot \{ {}_i v_r \} \|}{\| \mathbf{M}_k \cdot \{ {}_i v_r \} \|} \right) e^{\left( \frac{\| \{ {}_i v_r \} \|}{v_s} \right)^y} \quad 3.4-8$$

Having obtained the longitudinal and lateral deformation of every contact element, the effective coefficient of friction is calculated:

$${}_i \mu_j = -\sigma_{0j} \cdot {}_i z_j \quad 3.4-9$$

As a result, for the  $i^{\text{th}}$  contact node under investigation, the contact forces in the global x-y plane are obtained as follows:

$${}_i F_x = {}_i \mu_x \cdot {}_i F_z \quad 3.4-10$$

$${}_i F_y = {}_i \mu_y \cdot {}_i F_z \quad 3.4-11$$

By obtaining the respective force values along the global longitudinal, lateral and vertical directions, contact vector  $\{f_{\text{cont}}\}$  found in Equation 3.3–52 may be populated. This vector is essential in exciting both the flexible and the rigid-body components of the proposed tyre model. Moreover, the following expressions hold for the total longitudinal and lateral contact forces:

$$SF_x = \sum_{i=1}^N {}_i F_x = \sum_{i=1}^N ({}_i \mu_x \cdot {}_i F_z) \quad 3.4-12$$

$$SF_y = \sum_{i=1}^N {}_i F_y = \sum_{i=1}^N ({}_i \mu_y \cdot {}_i F_z) \quad 3.4-13$$

### 3.4.3 Implementation of drum surface instead of even road

Several tyre testing facilities perform tests in the controlled environment of a laboratory rather than on a road surface. In these cases, due to spatial restrictions, the test road is usually represented by a rotating drum. Experimental results presented in Chapter 5 have been acquired using a similar layout and consequently the proposed tyre model is offering the option to switch between an even horizontal road and a rotating drum.

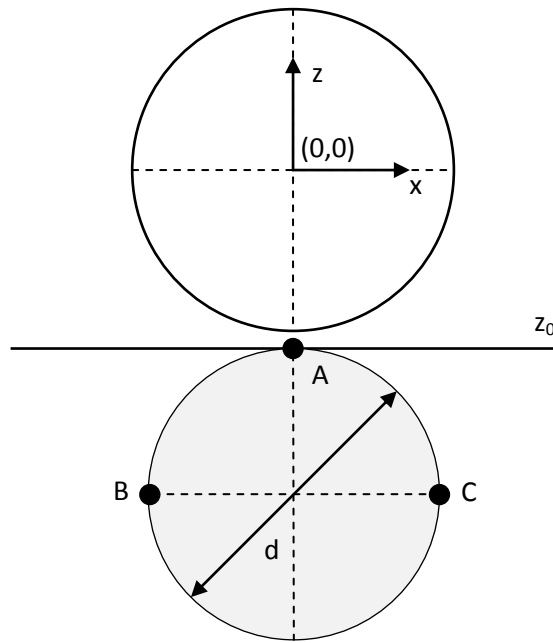


Figure 3.18 – Illustration of the 'tyre on a drum' option offered by the proposed tyre model

In the above diagram, the origin of the global reference system is located at the initial wheel centre. The vertical position of the horizontal ground is equal to  $z_0 = -0.3063\text{m}$  and it is a model parameter specified by the user. In addition, the diameter of the rotating drum used for the experimental measurements presented in Chapter 5 is equal to  $d = 0.60\text{m}$ . The upper half of the drum may be expressed as a function of the longitudinal position  $x$  by implementing a quadratic expression to fit a parabola to the top of the drum circumference (the area surrounding point A):

$$z_{\text{drum}}(x) = ax^2 + bx + c \quad 3.4-14$$

For points A, B and C presented in Figure 3.18 the following coordinates apply:

Table 3.2: X and Z coordinates of drum key ponts		
Point	X	Z
A	0	$z_0 = -0.3063$
B	$-d/2 = -0.30$	$z_0 - d/2 = -0.6063$
C	$d/2 = 0.30$	$z_0 - d/2 = -0.6063$

By combining the above coordinates with Equation 3.4–14, the following coefficients are obtained:

Table 3.3: Coefficients of drum quadratic expression		
A	B	c
-3.3333	0.0000	-0.3063

Consequently, Equation 3.4–14 becomes:

$$z_{\text{drum}}(x) = -3.33x^2 - 0.3063 \quad 3.4-15$$

A better representation of the drum surface would be the following circle equation:

$$(x - x_c)^2 + (z_{\text{drum}} - z_c)^2 = r^2 \quad 3.4-16$$

where  $x_c$  and  $z_c$  are the coordinates of the drum centre and  $r$  is the drum radius. Depending on the global longitudinal position of each belt node in contact to the ground ( $x_{\text{node}}$ ),  $z_{0\text{node}} = z_{\text{drum}}(x_{\text{node}})$  is evaluated and used in Equation 3.4–2, instead of  $z_0$ .

### 3.5 Remarks on Chapter 3

In this chapter, an alternative method for tyre modelling has been presented. As has been demonstrated in Chapter 2, the currently established tyre models require the identification of a significant number of parameters, a drawback which compromises the accuracy and the adaptability of any model. Since the experimental identification of several parameters seems inevitable, one may wonder why not examine the tyre directly, and consequently the objective of this study is to develop a method which will enable engineers to rapidly generate accurate



and effective tyre models by having to conduct only the minimum amount of experimental work or any other identification procedure.

The core of the proposed method is the system of second-order differential equations describing the motion of the nodes representing the tyre belt. This particular system, widely used in the respective literature towards this purpose, has been subjected to several alterations in order to be transformed into a form able to minimise the parameterisation requirements observed in some of the current tyre models. In particular, the motion of each belt node has been divided into two separate components, one representing the global motion of the rigid wheel and a second one taking into account local belt deformation.

An important asset of this formulation is that it allows for modal superposition and modal reduction to be implemented. This procedure reduces the number of differential equations to be solved, from the initial  $3N$  equations (where  $N$  denotes the number of belt nodes implemented in the model) to a figure directly proportional to the number of the modes selected to be used rather than the degrees of freedom of the system. However, the main improvement in this proposed tyre model is that the equations of motion are populated by quantities which are feasible to obtain experimentally, instead of the typically challenging to identify system matrices.

This feature significantly increases the model fidelity without compromising the quality of the generated results, assuming that an adequate number of flexible modes is included and the model is operating in a frequency range confined by the maximum eigenvalue associated with the included modes. The outcome of the above demanding procedure is a structural tyre model of varying fidelity which may be excited by forces developed within the contact patch and by the motion of the wheel itself, a feature which is of importance for cases where the tyre mass and inertia are comparable to those corresponding to the vehicle.

With reference to the contact sub-model exciting the tyre, a number of vertical Kelvin elements attached to the tyre belt nodes capture the vertical contact force distribution developed by the vertical interaction between the tyre and the road. Having obtained the vertical force applied to every contact node and having calculated the global nodal velocity – deriving by the motion and the deformation of the tyre belt – a distributed LuGre friction model is implemented to capture the shear contact forces. Although this formulation may not

be the most efficient, it offers a unique opportunity to study in detail the effect of tyre belt modal behaviour on several contact phenomena, as every contact node is examined separately and not in a lumped manner.

The parameters required by the proposed tyre model are summarised below:

- tyre belt eigenvectors, see vectors  $\{\psi_i\}$  in equation 3.3–25
- tyre belt eigenvalues, see terms  $s_i$  in equation 3.3–25
- mass and inertia matrix of tyre/rim assembly, see matrix  $\mathbf{M}_{RB}$  in equation 3.3–23
- initial coordinates of tyre belt nodes, see equation 3.3–9
- parameters of vertical contact sub-model, see equation 3.4–1
- parameters of shear contact sub-model, see Table 3.1

## 4. Identification of tyre modal parameters

### 4.1 Previously conducted research on modal parameter identification of pneumatic tyres

Tyre modal parameter identification has been a topic of extensive research during the past few decades. This field ranges from frequency response function (FRF) acquisition, to calculation of tyre eigenproperties, depending on the scope of each work. Consequently, this section is dedicated to presenting valuable research findings in this field which are of interest within the context of the present work. In particular, Z. Geng et al. in [36] and A. A. Popov et al. in [87] have developed a tyre damping model by conducting a series of modal testing experiments. The tyre in-plane modes were excited using a chirp-sweeping input generated by a shaker along the radial direction of the tyre. The respective response was measured by placing an accelerometer in 16 distinct, equi-spaced locations along the circumference of the tyre. One of the first conclusions drawn in this investigation is that a pneumatic tyre can be considered as a linear (see Figure 4.1) and reciprocal (see Figure 4.2) structure.

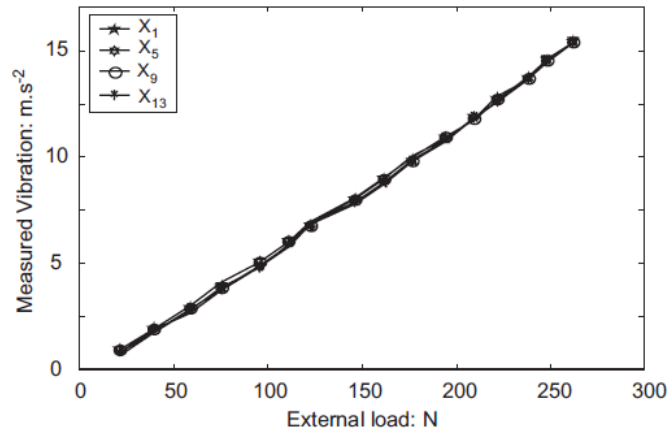


Figure 4.1 – Linearity of the tyre structure under steady sinusoidal excitation with different amplitudes ([36])

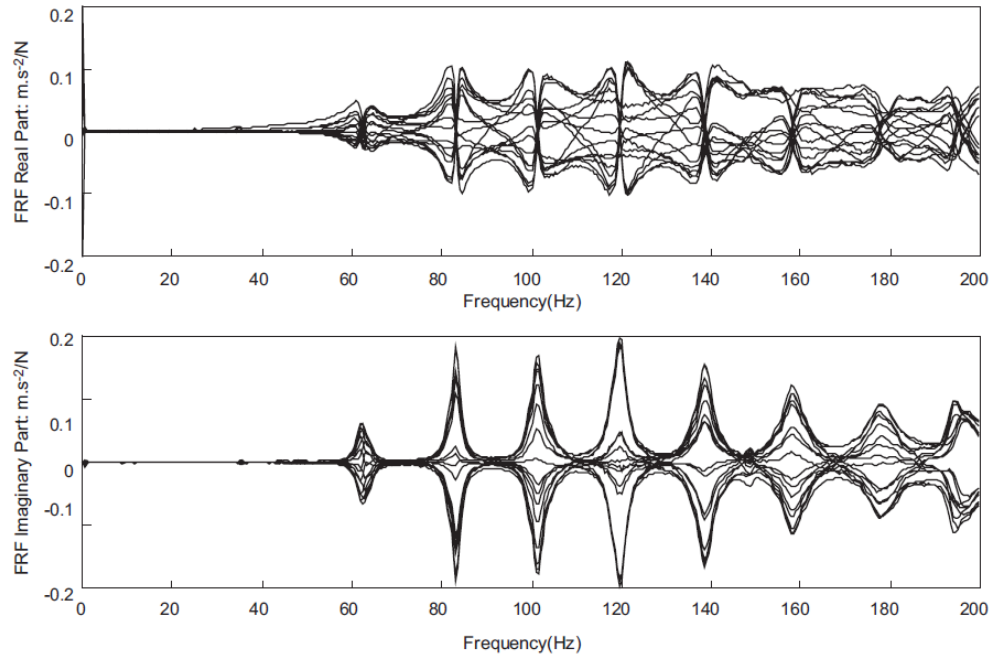


Figure 4.2 – Real and imaginary parts of the frequency response functions ([36])

Having obtained the FRFs of the tyre, the next step in that particular research is the identification of the damping matrix; consequently, a theoretical foundation is needed. Initially, the proportional damping model is adopted but the respective curve-fitting procedure is unable to match the experimental data, at frequencies exceeding 120 Hz, as can be observed in Figure 4.3.

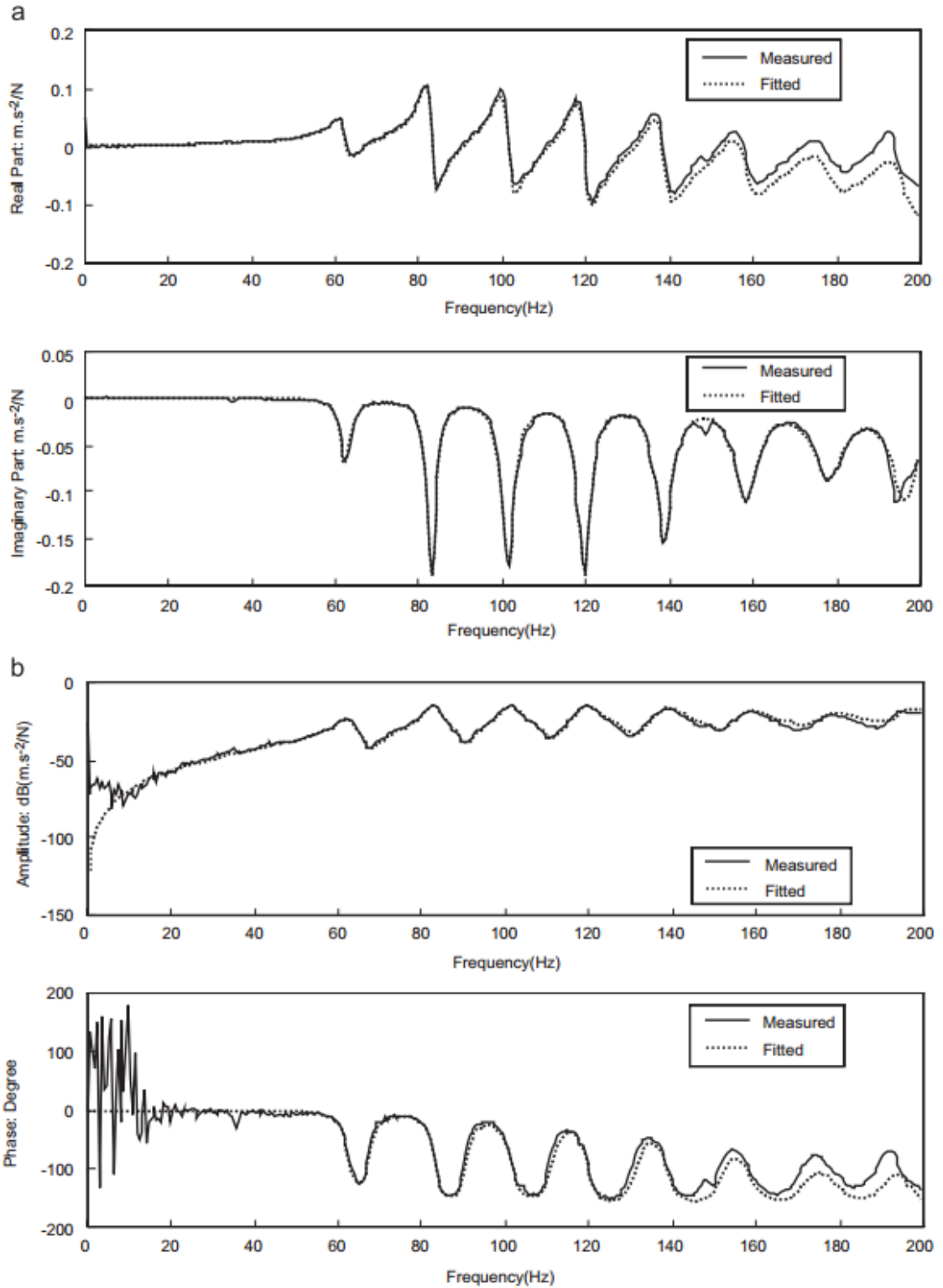


Figure 4.3 – Measured and fitted frequency response functions; a) real and imaginary parts, b) amplitudes and phase angles ([36])

The complex modal interpretation is investigated further in [1], [2] and [115], where *Rayleigh's small-damping approximation* is presented. According to this approach, the modal analysis of a lowly-damped system may undergo a few alterations:

- frequency response functions described within the second-order space,

- use of natural frequencies and real normal modes instead of complex eigenvalues and eigenvectors, and
- damping distribution derived from the eigenvectors.

In the more general case of non-proportional viscous damping, which is proposed as more appropriate for the case of the pneumatic tyre in [36] and [87], the respective characteristic equation is the following:

$$\det[-\lambda_n^2 \mathbf{M} + i\lambda_n \mathbf{C} + \mathbf{K}] = 0 \quad 4.1-1$$

Assuming that  $\{\varphi_n\}$  and  $\{\omega_n\}$  are the unit-mass normalised eigenvectors and the undamped natural frequencies of the system, Equations 4.1-2 and 4.1-3 hold:

$$\{\varphi_n\}^T \mathbf{M} \{\varphi_n\} = 1 \quad 4.1-2$$

$$\mathbf{K} \{\varphi_n\} = \omega_n^2 \mathbf{M} \{\varphi_n\} \quad 4.1-3$$

Rayleigh's small-damping assumption states that the complex eigenvalues ( $\lambda_n$ ) and the complex eigenvectors ( $\{\psi_n\}$ ) of a lowly-damped dynamic system are similar to the undamped natural frequencies ( $\omega_n$ ) and the unit-mass normalised eigenvectors ( $\{\varphi_n\}$ ), respectively, yielding the following expression:

$$\{\psi_n\} = \sum_{k=1}^N a_k^{(n)} \{\varphi_k\} \quad 4.1-4$$

where  $a_n^{(n)} = 1$  and  $|a_k^{(n)}| \ll 1, \forall k \neq n$ .

Equations 4.1-2, 4.1-3 and 4.1-4, combined with Equation 4.1-1, generate an alternative form of the eigenvalue problem associated with the examined dynamic system:

$$-\lambda_n^2 a_k^{(n)} + i\lambda_n \sum_{j=1}^N a_j^{(n)} C'_{kj} + \omega_k^2 a_k^{(n)} = 0 \Rightarrow$$

$$-\lambda_n^2 a_k^{(n)} + i\lambda_n \left( a_n^{(n)} C'_{kn} + a_k^{(n)} C'_{kk} + \sum_{j \neq k \neq n}^N a_j^{(n)} C'_{kj} \right) + \omega_k^2 a_k^{(n)} = 0 \quad 4.1-5$$

Equation 4.1–5 yields the following expression for the term  $a_k^{(n)}$ :

$$a_k^{(n)} \approx \frac{i\lambda_n C'_{kn}}{(\lambda_n - \lambda_k)(\lambda_n + \lambda_k^*)} \quad 4.1-6$$

Substitution of Equation 4.1–6 in 4.1–4 and rearrangement of terms result in the following expression for the complex eigenvectors:

$$\{\psi\}_n \approx \{\varphi\}_n + i \sum_{k \neq n}^N \frac{i\lambda_n C'_{kn}}{(\lambda_n - \lambda_k)(\lambda_n + \lambda_k^*)} \{\varphi\}_k \quad 4.1-7$$

In the equations above, matrix  $\mathbf{C}'$  denotes the modal damping matrix and  $\lambda_k^*$  is the complex conjugate of complex eigenvalue  $\lambda_k$ . The above three equations are a key element to the present study, as they represent a valid and established way to identify damping distribution of a tyre structure. It should be noted that the modal damping matrix ( $\mathbf{C}'$ ) satisfies the following transformation:

$$\mathbf{C}' = \bar{\boldsymbol{\varphi}}^T \mathbf{C} \bar{\boldsymbol{\varphi}} \quad 4.1-8$$

where  $\mathbf{C}$  is the damping matrix of the system expressed in spatial coordinates and  $\bar{\boldsymbol{\varphi}}$  is the normalised eigenvector matrix. Typically, matrix  $\mathbf{C}$  is unknown and only part of matrix  $\bar{\boldsymbol{\varphi}}$  is identifiable. Consequently, matrix  $\mathbf{C}'$  is derived as follows<sup>[36]</sup>:

$$C'_{kn} = -\text{Re} \left( \frac{i(\lambda_n - \lambda_k)(\lambda_n + \lambda_k^*)}{\lambda_n} B_{kn} \right), k \neq n \quad 4.1-9$$

$$C'_{nn} = 2\text{Im}(\lambda_n) \quad 4.1-10$$

with  $B_{kn}$  satisfying the following expression:

$$\{\theta\}_n = \sum_{k=1}^M B_{kn} \{\bar{\varphi}\}_k \quad 4.1-11$$

and  $\{\theta\}_n$  obtained by:

$$\text{Re}(\{\theta\}_n) = \text{Re}(\{\bar{\psi}\}_n) - \{\varphi\}_n \quad 4.1-12$$

$$\text{Im}(\{\theta\}_n) = \text{Im}(\{\bar{\psi}\}_n) \quad 4.1-13$$

Still discussing the same bodies of work mentioned above, Z. Geng et al. in [36] and A. A. Popov et al. in [87] used this assumption and a set of experimentally obtained eigenvalues and eigenvectors to calculate the modal damping components. The outcome is presented in Figure 4.4:

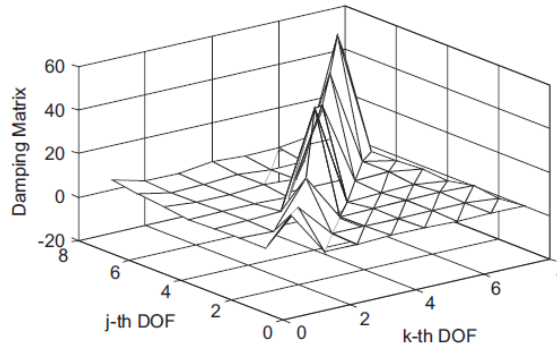


Figure 4.4 – Identification of general viscous damping in the pneumatic tyre expressed in modal coordinates ([36])

Moreover, on tyre modelling using experimentally obtained modal parameters, a field which is of great interest for this particular study, extensive work has been conducting in Tsinghua University by the research groups of G. Dihua and D. H. Guan. Published material representing the work of these groups may be found in [19], [44] and [116]. One fundamental difference between these works and the research of Z. Geng et al. in [36] and A. A. Popov et al. in [87] presented above, is the supporting structure of the tested tyre. In particular, the latter studies are conducted by having the tyre rigidly attached to a seismic table, while the former studies compare a rigidly attached to a freely suspended tyre. The respective results revealed the superiority of the free-free boundary condition, due to the introduction of two additional non-tyre-related modes in the case of the rigid attachment.



In [44], the linearity of the tyre is examined and confirmed by comparing the excitation force applied on the tyre (single point excitation) with the resulting natural frequencies and damping ratios. A second valuable investigation of that study is that performed with reference to the appropriate device to excite the tyre, namely an electromagnetic exciter. The option to use a hammer has been rejected due to its limited frequency spectrum. In the same body of work, a sinusoidal sweep signal driving the exciter is preferred compared to a white noise signal due to the leakage occurring in the second case, an issue which has been addressed in the present study by applying a Hamming window to the experimentally acquired data. Nevertheless, the frequency response functions from [44] comparing white noise to sinusoidal sweep excitation are presented in the following two figures:

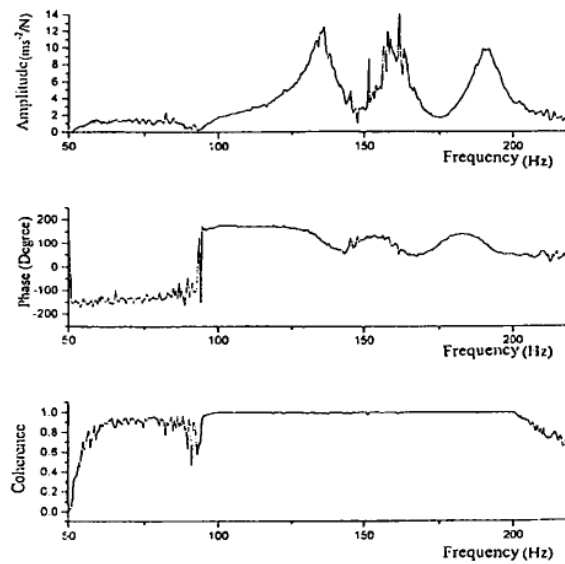


Figure 4.5 – Frequency response function for white noise excitation ([44])

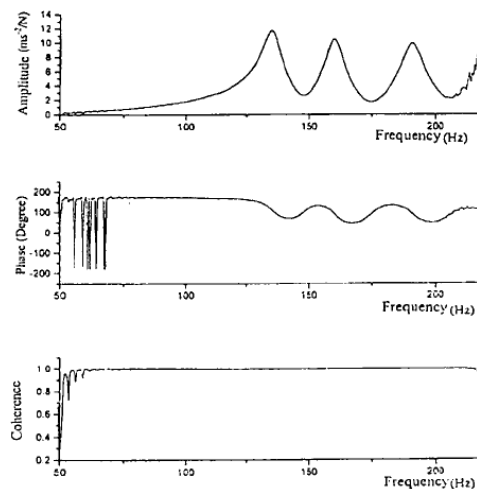


Figure 4.6 – Frequency response function for sinusoidal sweep excitation ([44])

A further step is conducted in [116] where the tyre is excited by a sinusoidal sweep signal in the radial and tangential directions, and its response is acquired in the radial, tangential and lateral directions. The respective FRFs are obtained and consequently the mode shapes are calculated. This procedure led to the following conclusions:

- *“modes in different directions have nearly the same modal frequencies,*
- *modes of the same order but in different directions have the same number of nodal lines, and*
- *the position of nodal lines and the points for maximum amplitudes are the same for radial and lateral mode shapes, whereas the positions of nodal lines and the maximum amplitudes are exchanges in tangential mode shapes and the corresponding radial mode shapes.”<sup>[116]</sup>*

Another point of interest is the comparison between radial and tangential excitation. It has been observed that tangential excitation triggers lower response levels. As a result the quality of the experimental data cannot match the one of the radial excitation case, as the signal to noise ratio (SNR) is lower. Consequently, experimental errors are expected to be higher in the case of tangential excitation – a hypothesis which has been tested and demonstrated in that study. It is noteworthy that this observation has been replicated in the present study, see Section 4.4.

Similar to the work presented in this Thesis, the abovementioned procedures of tyre modal parameter identification are exploited by F. Chengjian and G. Dihua in [19], where the modal parameters, i.e. mode shape, natural frequency and damping ratio, of the in-plane bending modes located between 0Hz and 350Hz have been identified. The tyre deformation is calculated by the following expression:

$$\{D\} = \mathbf{H} \cdot \{f\} \quad 4.1-14$$

where  $\{D\}$  is the deformation vector, containing radial and tangential elements,  $\{f\}$  is the force vector acting on the tyre and  $\mathbf{H}$  is the transfer matrix, which consists of four distinct sub-matrices (see equation 4.1–15). The symbols in the subscript of each sub-matrix state the direction of the displacement and the direction of the imposed excitation, respectively.

$$\mathbf{H} = \begin{bmatrix} \mathbf{H}_{rr} & \mathbf{H}_{tr} \\ \mathbf{H}_{rt} & \mathbf{H}_{tt} \end{bmatrix} \quad 4.1-15$$

Equation 4.1–14 can be rewritten, for a single carcass element, as follows:

$$\begin{Bmatrix} r \\ t \end{Bmatrix} = \begin{bmatrix} H_{rr} & H_{tr} \\ H_{rt} & H_{tt} \end{bmatrix} \begin{Bmatrix} f_r \\ f_t \end{Bmatrix} \quad 4.1-16$$

In Equation 4.1–16, vector  $\begin{Bmatrix} r \\ t \end{Bmatrix}$  represents the total radial and tangential deformation as a result of the application of the external force vector  $\begin{Bmatrix} f_r \\ f_t \end{Bmatrix}$ .

The tyre model presented above has been virtually tested against a flat surface for several vertical loads. The resulting vertical and shear forces are presented in Figure 4.7. These results are in accordance with the outcome of various different simulation formulations<sup>[42][108]</sup>.

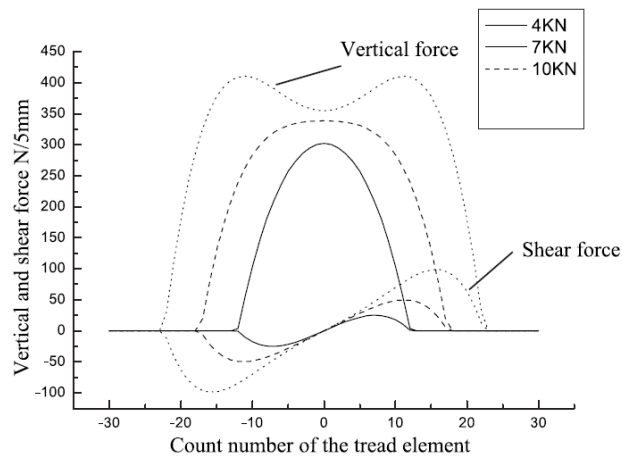


Figure 4.7 – Calculation results of contact forces distributions under three static loads ([19])

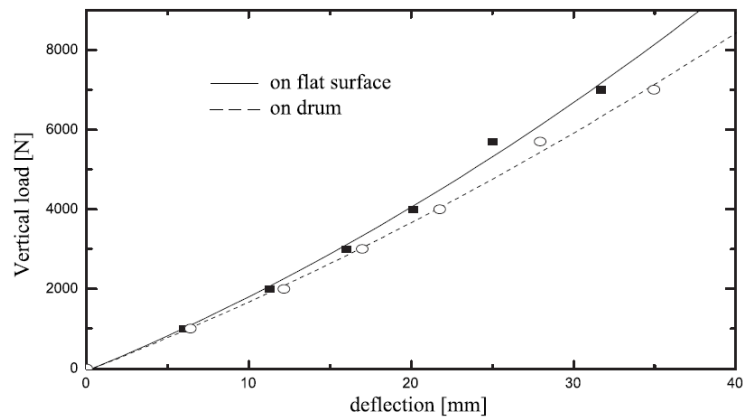


Figure 4.8 – The calculated static vertical force as function of the static deflection ([19])

The model described by Equations 4.1–14 to 4.1–16 has been assessed in [20]. Initially, this particular tyre model – which has been formulated by modal parameters identified in a limited frequency band up to 300Hz – demonstrates deviation when compared to experimental data, in terms of vertical stiffness (Figure 4.9) and footprint area (Figure 4.10). The modal reduction implemented by the upper limit of 300Hz is considered as a significant factor for the deviation occurred between the simulation outcome and the measurements, so the upper frequency limit of the associated modal analysis is increased to 700Hz, which allows for the introduction of ten additional modes. These alterations slightly improved the vertical stiffness calculated correlation (Figure 4.11) and minimised the error between the footprint length calculation and the respective measured data (Figure 4.12). The observation about the relation between modal reduction and vertical stiffness has been replicated by the proposed tyre model in Chapter 5 and, for the case of the proposed tyre model, correlation has been achieved for a limited vertical load range; in general, different levels of modal reduction would allow for tyre models of varying fidelity, depending on the simulation requirements. In essence, a single tyre modelling approach is feasible and could be used for any task, ranging from real-time tyre models to NVH studies.

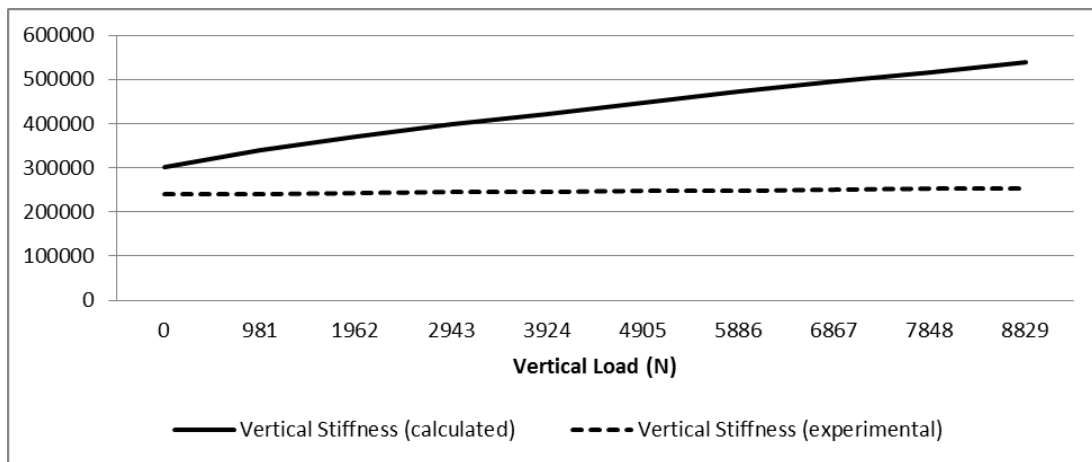


Figure 4.9 – Vertical stiffness versus vertical load (300Hz) ([20])

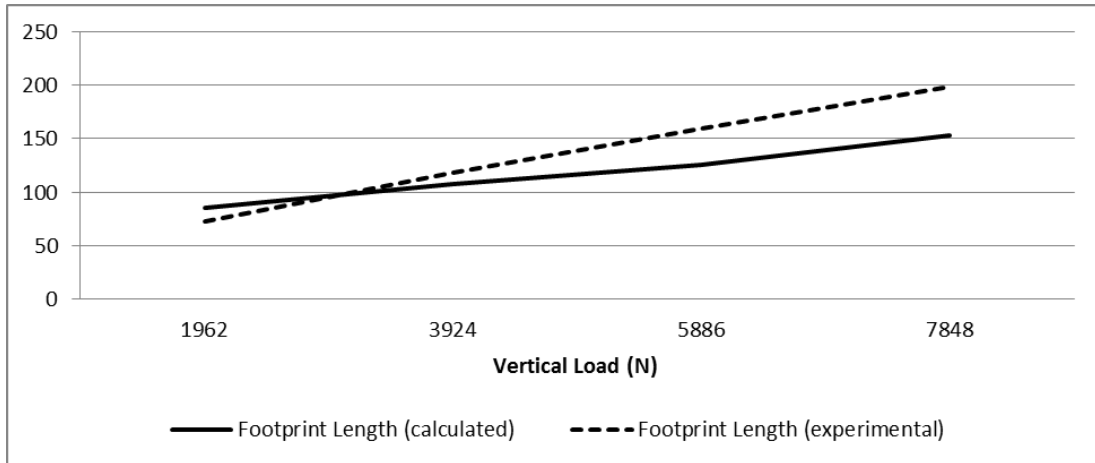


Figure 4.10 – Footprint length versus vertical load (300Hz) ([20])

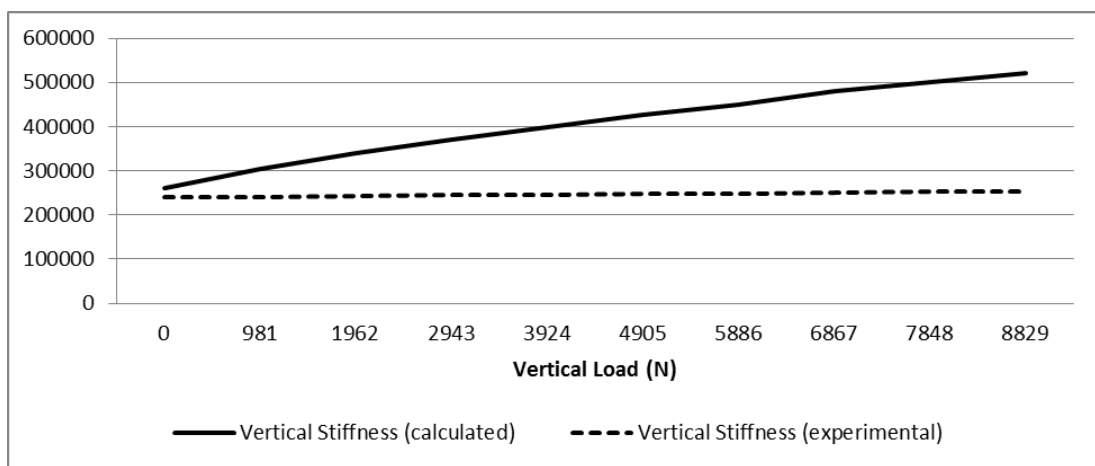


Figure 4.11 – Vertical stiffness versus vertical load (700Hz) ([20])

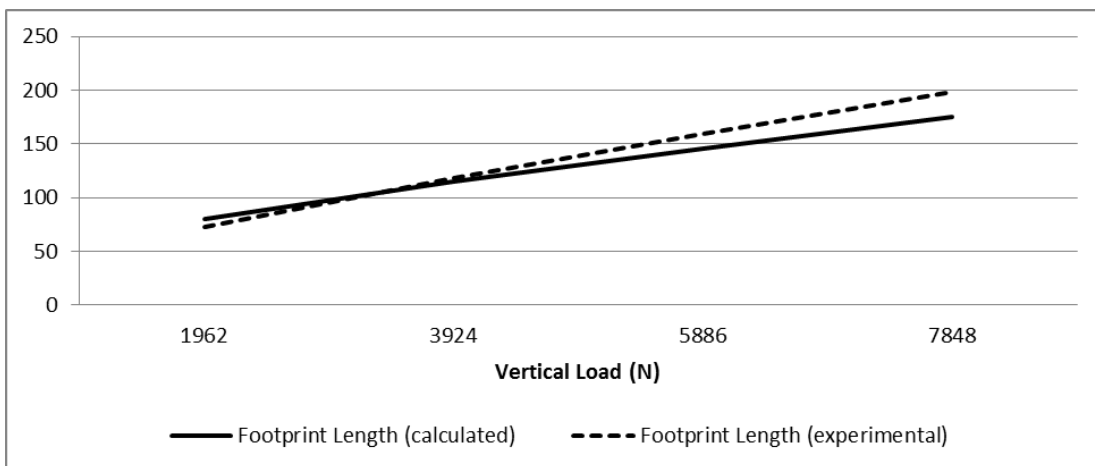


Figure 4.12 – Footprint length versus vertical load (700Hz) ([20])

To improve further the accuracy of this tyre model, the non-linear sidewall concept is implemented. The overall vertical deflection, as a result of the application of the vertical load, is governed by three distinct stiffness elements, which are connected in a serial layout:

- sidewall stiffness element,
- carcass stiffness element (described by the tyre model presented above) and
- tread stiffness element.

Consequently, the resulting overall vertical deformation derives from the calculation of the deformation of the above elements, in addition to the deformation associated with the stiffness of the carcass. This formulation leads to simulation results which are significantly closer to the experimental data (Figure 4.13 and Figure 4.14).

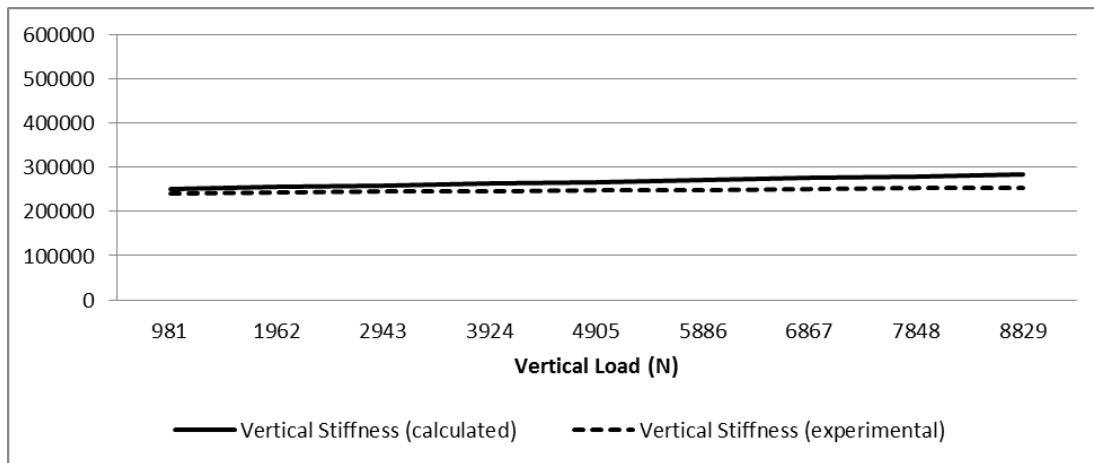


Figure 4.13 – Vertical stiffness versus vertical load (non-linear sidewall) ([20])

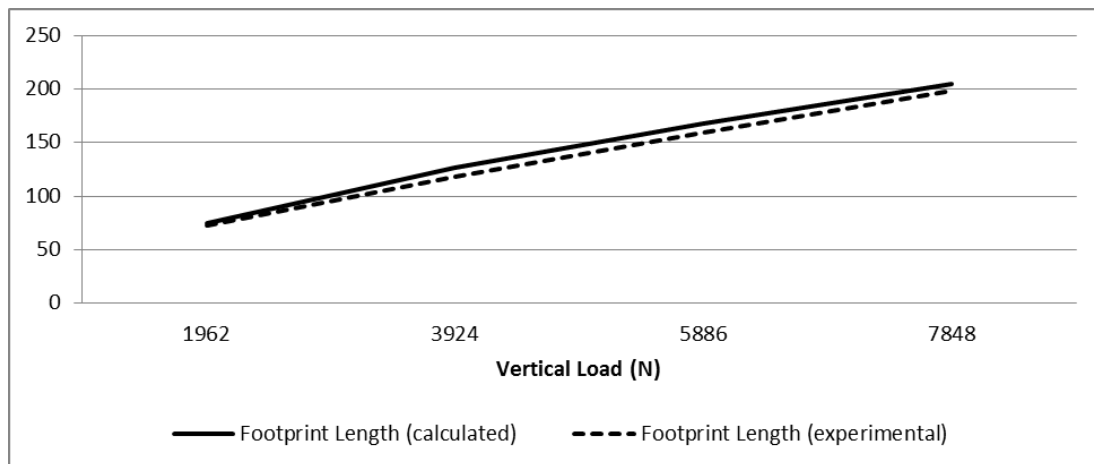


Figure 4.14 – Footprint length versus vertical load (non-linear sidewall) ([20])

The work presented in the preceding paragraphs, namely the formulation of tyre models via experimental identification of modal parameters and the investigation of the three dimensional modal behaviour of tyre structures, led to the development of an out-of-plane dynamic tyre model directly by exploitation of experimental modal parameters<sup>[97]</sup>. Initially, a geometrical description of the contact area is performed. According to that description, lateral contact forces arise when the centreline of the footprint does not coincide with the centreline

of the tyre, in the top-down view. The deviation of these two lines, denoted as  $\{\Delta y_t\}$ , generates lateral forces, which are described by the vector  $\{f\}$  and they are calculated by the following expression:

$$\{f\} = K_c \cdot \{\Delta y_t\} \quad 4.1-17$$

where  $K_c$  is the lateral stiffness of the contact elements.

Moving on, the transfer function of the tyre to lateral excitation ( $H^t$ ) is obtained by identifying modal parameters up to 200Hz. Assuming that the excitation is applied at point  $l$ , the response at location  $p$  is described by an element of the total transfer function matrix (see equation 4.1-18). At this point, the authors perform a critical transformation, from time domain to space frequency domain, by introducing the space frequency which is equal to time related frequency divided by the magnitude of the wheel speed vector. As a result, an alternative form of the transfer function in the space frequency domain can be obtained by Equation 4.1-19.

$$H_{lp}^t = \sum_{r=1}^N \frac{\varphi_{lr} \cdot \varphi_{pr}}{k_r + S^2 + S \cdot c_r} \quad 4.1-18$$

$$H_{lp}^x = \sum_{r=1}^N \frac{\varphi_{lr} \cdot \varphi_{pr}}{k_r + V^2 \cdot S^2 + V \cdot S \cdot c_r} \quad 4.1-19$$

A further evolution of Equation 4.1-19 includes the effect of tyre rotation in its dynamic response (“induced transfer function”). The driving point induced transfer function has a similar form with the one presented above for the stationary tyre:

$$\bar{H}_{ll}^x(S) = \sum_{r=1}^N \frac{\varphi_{ll}^2}{2} \left[ \frac{1}{k_r + V^2 \left( S + \frac{r-1}{R} j \right)^2 + V \left( S + \frac{r-1}{R} j \right) c_r} + \frac{1}{k_r + V^2 \left( S - \frac{r-1}{R} j \right)^2 + V \left( S - \frac{r-1}{R} j \right) c_r} \right] \quad 4.1-20$$

This induced transfer function may be used for calculating the lateral deformation of the contact area in the  $i^{\text{th}}$  longitudinal position, as a result of the action of contact force  $f_j(S)$  at point  $j$  and the rotation of the tyre, which is included in the induced transfer function ( $\bar{H}_{ij}^X$ ):

$$y_c(S, x_i) = \bar{H}_{ij}^X \cdot f_j(S) \quad 4.1-21$$

Equation 4.1–21 is a vital element of the study presented above, as it enables the authors to obtain analytical expressions for the transfer functions of the lateral force and the self-aligning moment with respect to several quantities of interest, such as the slip angle of the tyre, the yaw angle and the lateral displacement of the contact area. The calculated results are in relatively good agreement with experimental data (Figure 4.15 and Figure 4.16). Moreover, the way in which the transfer function of the self-aligning moment with respect to the yaw angle of the tyre is affected by wheel speed is depicted in Figure 4.17.

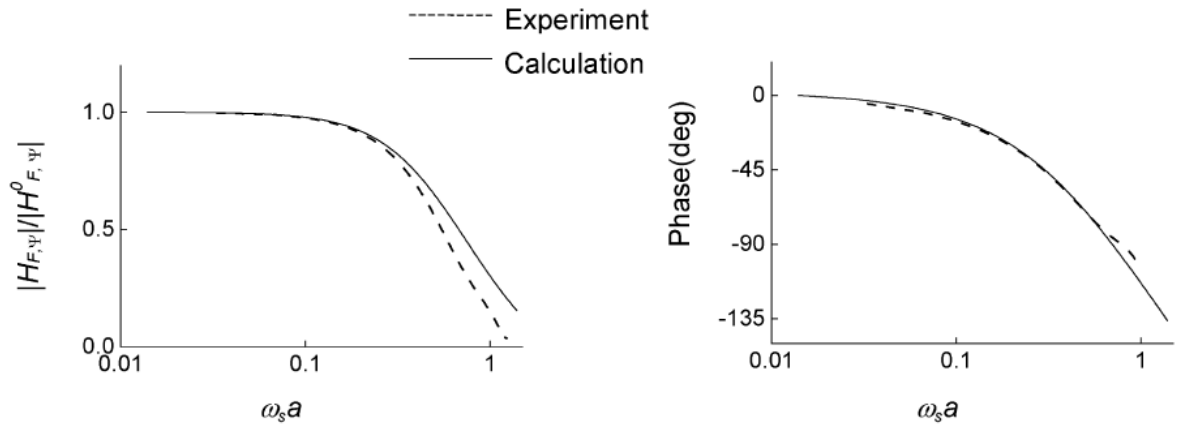


Figure 4.15 – Comparison between calculated and test results of transfer function of lateral force to yaw angle ([97])

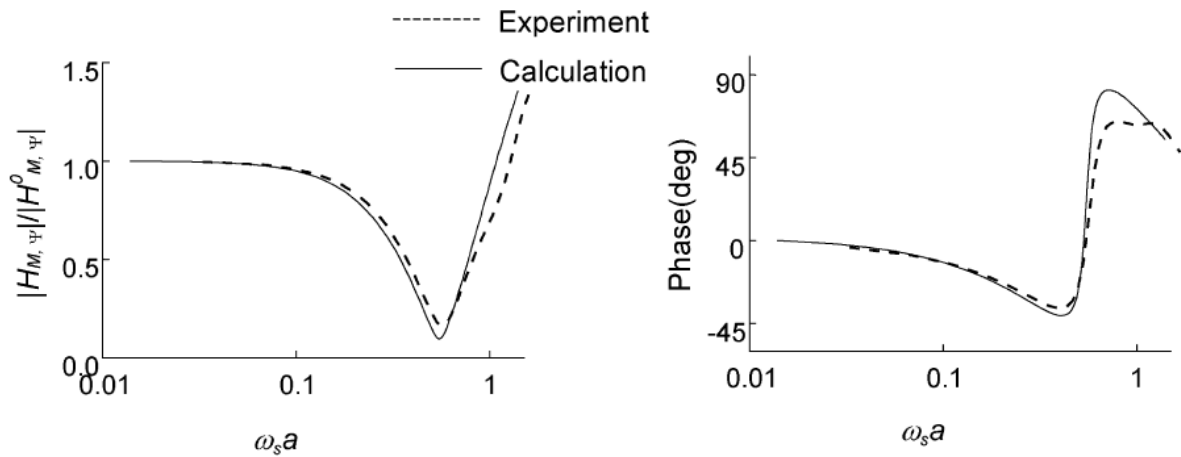


Figure 4.16 – Comparison between calculated and test results of transfer function of self-aligning moment to yaw angle ([97])



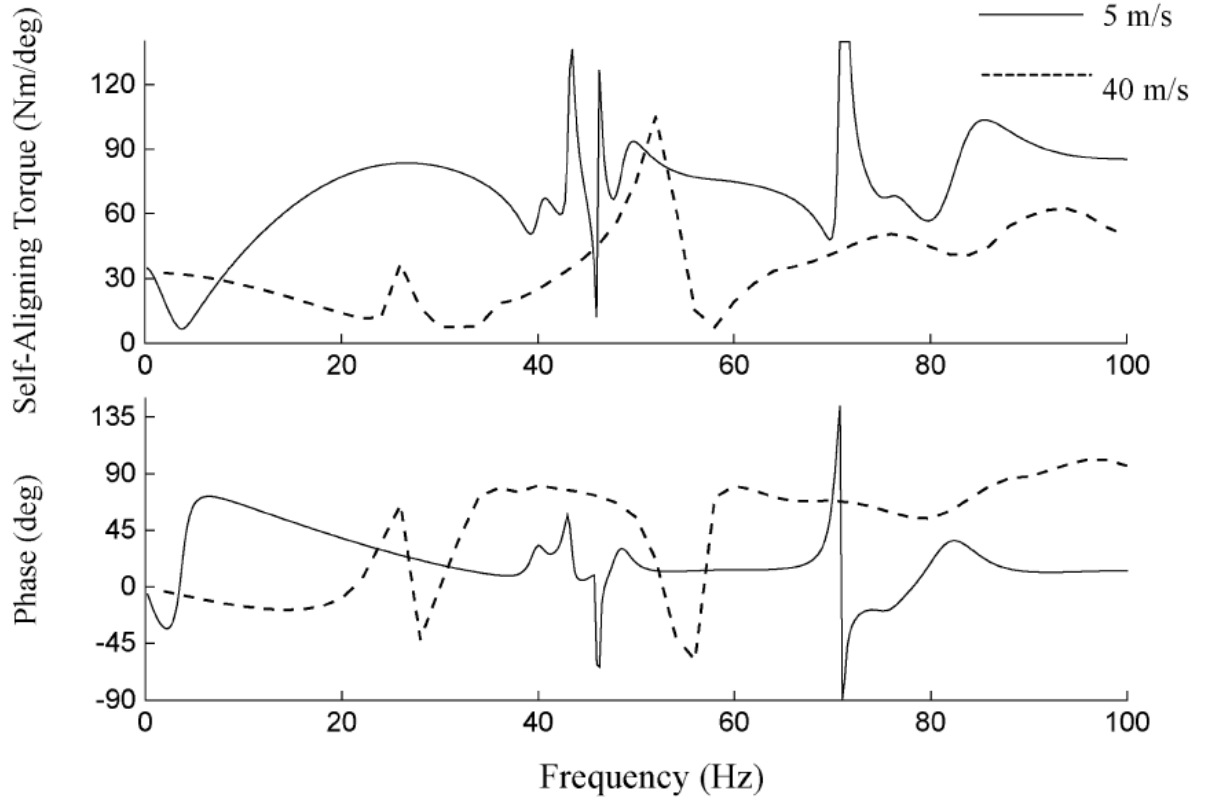


Figure 4.17 – Transfer function of self-aligning moment to yaw angle for high frequency range at two velocities ([97])

A study incorporating free-free boundary conditions may be found in the work of J. Perisse et al. in [84], where the modal parameters of a tyre are identified and exploited to modal update the analytical tyre model (“*orthotropic thin plate under tension*”) presented in Section 2.8. The experimental layout is similar to the one developed by the researchers of Tsinghua University mentioned above. The main difference between these two works is the type of the excitation signal sent to the shaker. While the research groups of D. H. Guan and G. Dihua use sinusoidal signals to excite tyre structures, J. Perisse et al. adopt random excitation and averaging procedures, similar to the technique adopted in the present work. Having obtained the respective point mobility FRF (Figure 4.18), the low-frequency modes, which are of interest for the proposed tyre model, are identified by the application of a global curve fitting method which expresses the FRF using the partial fraction series form<sup>[30]</sup>.

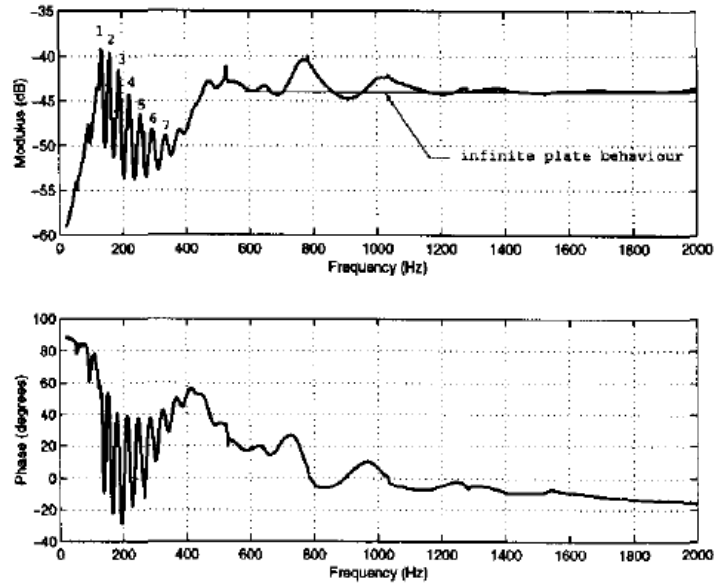


Figure 4.18 – Point mobility of the tyre measured at the centre of the belt ([84])

Moreover, the authors in [84] investigate the influence of the size of the excitation area on the obtained data. Experimental results support the conclusion that a larger excitation area will lead to a point mobility of lower magnitude. As can be seen in Figure 4.19, while the lower frequency band (“*modal domain*”) remains relatively unaffected, the higher band (“*non-modal domain*”) seems more sensitive to this particular effect (“*local stiffness*”). To compensate for this phenomenon, a corrective term is needed. A typical form of this term is depicted in Figure 4.20. Although it seems that the excitation area must be as small as possible, there is a lower limit which, according to [25], is equal to the thickness of the examined structure.

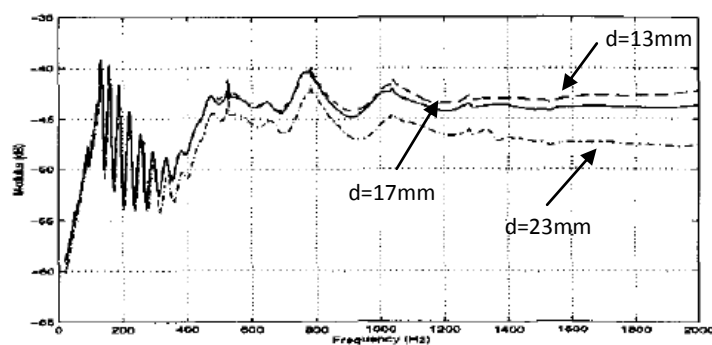


Figure 4.19 – Influence of driving force area on point mobility ([84])

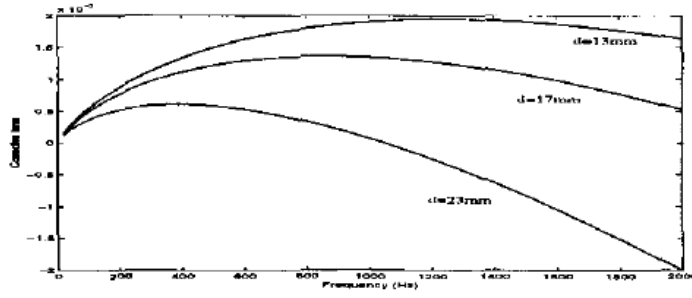


Figure 4.20 – Corrective term due to local stiffness effect for several excitation circular areas ([84])

## 4.2 Theoretical approach

For a system with  $3N$  degrees of freedom, where  $N$  is the number of nodes representing the structure, the correlation between the applied forces and the response of each degree of freedom is captured via the frequency response function matrix which is expressed – in the frequency domain – by the following equation:

$$\{x(\omega)\} = [\alpha(\omega)] \cdot \{F(\omega)\} \Rightarrow$$

$$\begin{bmatrix} x_1(\omega) \\ x_2(\omega) \\ \vdots \\ x_{3N}(\omega) \end{bmatrix} = \begin{bmatrix} \alpha_{11}(\omega) & & \alpha_{13N}(\omega) \\ \alpha_{21}(\omega) & & \alpha_{23N}(\omega) \\ \vdots & \dots & \vdots \\ \alpha_{3N1}(\omega) & & \alpha_{3N3N}(\omega) \end{bmatrix} \cdot \begin{bmatrix} F_1(\omega) \\ F_2(\omega) \\ \vdots \\ F_{3N}(\omega) \end{bmatrix} \quad 4.2-1$$

where  $\alpha_{ij}(\omega)$  is the receptance frequency response function (FRF) associated with the displacement  $x_i(\omega)$  of the  $i^{\text{th}}$  degree of freedom and the force  $F_j(\omega)$  applied on the  $j^{\text{th}}$  degree of freedom. Inspection of equation 4.2–1 leads to the conclusion that, in order to fully describe a structure, one has to obtain a sum of  $(3N)^2$  frequency response functions.

In the particular case of the three-dimensional pneumatic tyre, the elements of vector  $\{x\}$  are presented in groups of three, as they correspond to the three components associated with the three spatial coordinates defining the motion of each node. Due to the geometry of the tyre belt, these coordinates are expressed in a node-specific radial/tangential coordinate system (see Figure 4.21) instead of a Cartesian one having its origin attached to the wheel centre. The same formulation applies to vector  $\{F\}$ .

$$\begin{bmatrix} \begin{Bmatrix} r^{X_1} \\ l^{X_1} \\ t^{X_1} \end{Bmatrix} \\ \begin{Bmatrix} r^{X_2} \\ l^{X_2} \\ t^{X_2} \end{Bmatrix} \\ \vdots \\ \begin{Bmatrix} r^{X_N} \\ l^{X_N} \\ t^{X_N} \end{Bmatrix} \end{bmatrix} = \begin{bmatrix} \alpha_{11}(\omega) & & \alpha_{13N}(\omega) \\ \alpha_{21}(\omega) & & \alpha_{23N}(\omega) \\ \vdots & \dots & \vdots \\ \alpha_{3N1}(\omega) & & \alpha_{3N3N}(\omega) \end{bmatrix} \cdot \begin{bmatrix} \begin{Bmatrix} r^{F_1} \\ l^{F_1} \\ t^{F_1} \end{Bmatrix} \\ \begin{Bmatrix} r^{F_2} \\ l^{F_2} \\ t^{F_2} \end{Bmatrix} \\ \vdots \\ \begin{Bmatrix} r^{F_N} \\ l^{F_N} \\ t^{F_N} \end{Bmatrix} \end{bmatrix} \quad 4.2-2$$

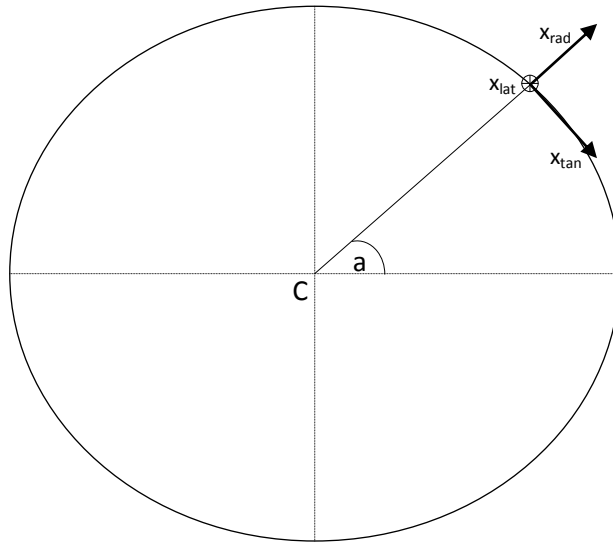


Figure 4.21 – Radial/lateral/tangential node-specific frame of reference

Based on the findings of Z. Geng, A. A. Popov and D. J. Cole in [36] and A. A. Popov and Z. Geng in [87], the number of the required frequency response functions can be reduced to a figure in the order of  $5N$ . Initially, as demonstrated in section 4.1, the real and the imaginary parts of each FRF are distributed symmetrically along the frequency axis, an observation which leads to the conclusion that the principle of reciprocity holds:

$$\alpha_{ij}(\omega) = \alpha_{ji}(\omega) \quad 4.2-3$$

As a result of the above equation, only the upper or lower triangular FRF matrix of equation 4.2–2 needs to be experimentally populated. Moreover, the abovementioned researchers have examined the application of the proportional viscous damping model in order to replicate the experimentally obtained frequency response of the tyre structure, an approach which could not replicate the experimentally obtained frequency response of the tyre

structure. Therefore, an alternative – non proportional – viscous damping model has been adopted, which seems to describe the modal behaviour of the pneumatic tyre more accurately. The receptance FRF of this particular damping model demonstrates the following form (note that the superscript \* refers to the complex conjugate of each quantity):

$$\alpha_{ij}(\omega) = \sum_{r=1}^m \left[ \frac{\varphi_{ir}\varphi_{jr}}{a_r(i\omega - s_r)} + \frac{(\varphi_{ir}\varphi_{jr})^*}{a_r^*(i\omega - s_r^*)} \right] \quad 4.2-4$$

According to the above equation, the response of the  $i^{\text{th}}$  degree of freedom due to the excitation applied on the  $j^{\text{th}}$  degree of freedom can be described as the sum of the contribution of each one of the  $m$  modes of the structure. Scaling factor  $a_r$  depends on mode identification and, for the purposes of the present work, is equal to unity – see Equations 3.3–17 to 3.3–19. In addition, each structural mode is associated with its unique eigenvalue  $s_r$ :

$$s_r = -\omega_r\xi_r + i\omega_r\sqrt{1 - \xi_r^2} \quad 4.2-5$$

where  $\omega_r$  is the damped natural frequency of mode  $r$  and  $\xi_r$  is the respective damping ratio. Combination of the above two equations yields the following expression for the receptance FRF:

$$\alpha_{ij}(\omega) = \sum_{r=1}^m \left[ \frac{\varphi_{ir}\varphi_{jr}}{a_r(\omega_r\xi_r + i(\omega - \omega_r\sqrt{1 - \xi_r^2}))} + \frac{\varphi_{ir}^*\varphi_{jr}^*}{a_r^*(\omega_r\xi_r + i(\omega + \omega_r\sqrt{1 - \xi_r^2}))} \right] \quad 4.2-6$$

The numerators of the two fractions in Equation 4.2–6 are the residues of mode  $r$ , which form the eigenvector matrix:

$$[\Psi] = \begin{bmatrix} \varphi_{11} & \varphi_{12} & \dots & \varphi_{1(m-1)} & \varphi_{1m} \\ \vdots & \vdots & & \vdots & \vdots \\ \varphi_{3N1} & \varphi_{3N2} & & \varphi_{3N(m-1)} & \varphi_{3Nm} \end{bmatrix}_{3N \times m} = [\{\psi_1\} \quad \dots \quad \{\psi_m\}] \quad 4.2-7$$

From Equations 4.2–2 and 4.2–6 one may deduce that matrix  $[\Psi]$  can be populated by obtaining only one set of three consecutive columns or three consecutive rows –

corresponding to a unique node (“node  $j$ ”) – of the receptance FRF matrix, according to the modal constants consistency<sup>[70]</sup>:

$$\begin{bmatrix} \begin{pmatrix} r^{X_1} \\ l^{X_1} \\ t^{X_1} \end{pmatrix} \\ \begin{pmatrix} r^{X_2} \\ l^{X_2} \\ t^{X_2} \end{pmatrix} \\ \vdots \\ \begin{pmatrix} r^{X_N} \\ l^{X_N} \\ t^{X_N} \end{pmatrix} \end{bmatrix} = \begin{bmatrix} \alpha_{1,3(j-1)+1} & \alpha_{1,3(j-1)+2} & \alpha_{1,3(j-1)+3} \\ \alpha_{2,3(j-1)+1} & \alpha_{2,3(j-1)+2} & \alpha_{2,3(j-1)+3} \\ \alpha_{3,3(j-1)+1} & \alpha_{3,3(j-1)+2} & \alpha_{3,3(j-1)+3} \\ \alpha_{4,3(j-1)+1} & \alpha_{4,3(j-1)+2} & \alpha_{4,3(j-1)+3} \\ \alpha_{5,3(j-1)+1} & \alpha_{5,3(j-1)+2} & \alpha_{5,3(j-1)+3} \\ \alpha_{6,3(j-1)+1} & \alpha_{6,3(j-1)+2} & \alpha_{6,3(j-1)+3} \\ \vdots & \vdots & \vdots \\ \alpha_{3N-2,3(j-1)+1} & \alpha_{3N-2,3(j-1)+2} & \alpha_{3N-2,3(j-1)+3} \\ \alpha_{3N-1,3(j-1)+1} & \alpha_{3N-1,3(j-1)+2} & \alpha_{3N-1,3(j-1)+3} \\ \alpha_{3N,3(j-1)+1} & \alpha_{3N,3(j-1)+2} & \alpha_{3N,3(j-1)+3} \end{bmatrix}_{3N \times 3} \cdot \begin{pmatrix} r^{F_j} \\ l^{F_j} \\ t^{F_j} \end{pmatrix} \quad 4.2-8$$

Equation 4.2–8 implies the necessity to obtain  $9N$  frequency response functions which, compared to the initial  $(3N)^2$ , represents a significant improvement in the efficiency of the experimental procedure. A final step, which will reduce this number to  $5N$ , is the ad hoc assumption made in this work that there is no energy exchange between in and out-of-plane modes, which means that an in-plane excitation will trigger only in-plane response, a response which will not be triggered by an out-of-plane force acting on the tyre belt. The rationale supporting this assumption is that, in the context of the present work, the key validation element is the response of the proposed tyre model in terms of vertical stiffness and hysteresis due to lateral slip. Even with the abovementioned assumption in place, by experimentally obtaining the purely in-plane and out-of-plane modes and populating the proposed tyre model, there is sufficient information to study these two validation scenarios, as demonstrated in Chapter 5. Nevertheless, a complete three-dimensional tyre model requires the omitted frequency response functions, as this assumption is not valid for physical tyres where there is cross-talking between the excitation of any degree of freedom and the resulting three-dimensional response of every node (see Figure 4.22). The benefit of adopting this assumption may be quantified, in terms of experimental efficiency by comparing expression 4.2–8 to the following updated equation:

$$\begin{bmatrix} \begin{pmatrix} r^{X_1} \\ l^{X_1} \\ t^{X_1} \end{pmatrix} \\ \begin{pmatrix} r^{X_2} \\ l^{X_2} \\ t^{X_2} \end{pmatrix} \\ \vdots \\ \begin{pmatrix} r^{X_N} \\ l^{X_N} \\ t^{X_N} \end{pmatrix} \end{bmatrix} = \begin{bmatrix} \alpha_{1,3(j-1)+1} & 0 & \alpha_{1,3(j-1)+3} \\ 0 & \alpha_{2,3(j-1)+2} & 0 \\ \alpha_{3,3(j-1)+1} & 0 & \alpha_{3,3(j-1)+3} \\ \alpha_{4,3(j-1)+1} & 0 & \alpha_{4,3(j-1)+3} \\ 0 & \alpha_{5,3(j-1)+2} & 0 \\ \alpha_{6,3(j-1)+1} & 0 & \alpha_{6,3(j-1)+3} \\ \vdots & \vdots & \vdots \\ \alpha_{3N-2,3(j-1)+1} & 0 & \alpha_{3N-2,3(j-1)+3} \\ 0 & \alpha_{3N-1,3(j-1)+2} & 0 \\ \alpha_{3N,3(j-1)+1} & 0 & \alpha_{3N,3(j-1)+3} \end{bmatrix}_{3N \times 3} \cdot \begin{pmatrix} r^{F_j} \\ l^{F_j} \\ t^{F_j} \end{pmatrix} \quad 4.2-9$$

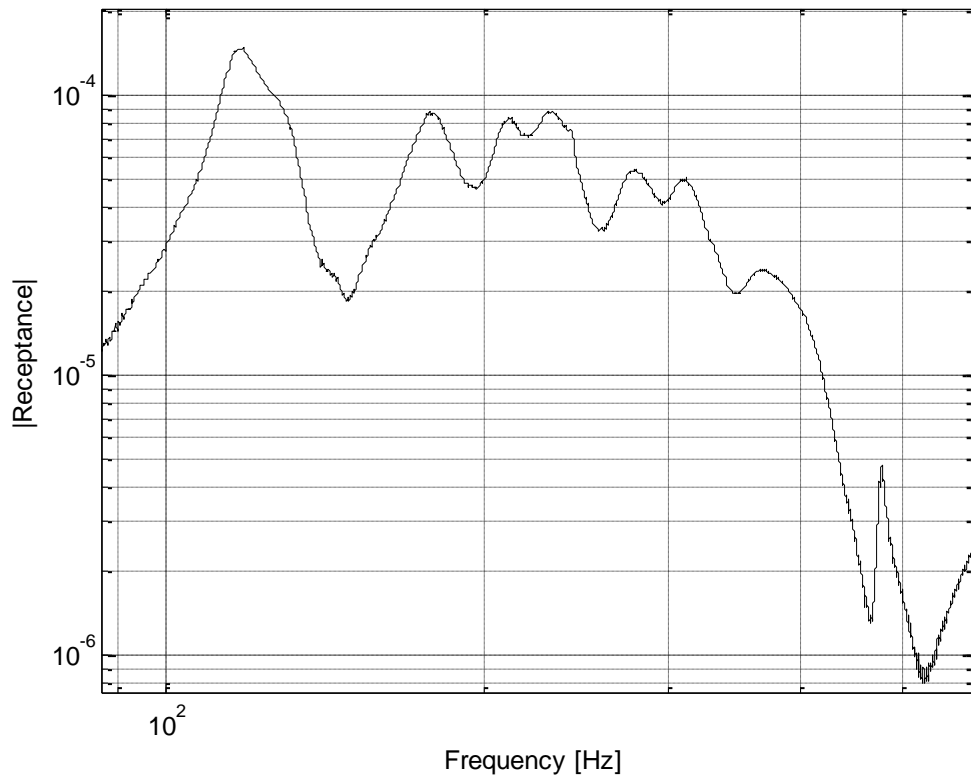


Figure 4.22 – Frequency response function (lateral response)/(radial excitation)

The main outcome of the analysis presented above is that the transformation from the spatial to the modal model requires the acquisition of a number of receptance FRF equal to  $5N$ , where  $N$  is the number of nodes representing the structure, as opposed to the initial  $(3N)^2$ . For the particular case of the investigated pneumatic tyre, which in the present work is represented by 30 equi-spaced three-dimensional nodes, this approach reduced the number of frequency response functions from 8100  $((3N)^2)$  to 270  $(9N)$  and finally to 150  $(5N)$ .

## 4.3 Experimental set-up

### 4.3.1 Overview

In Chapter 3, the proposed tyre model has been presented. Examination of Equation 3.3–25 reveals the necessity to experimentally identify the eigenvalues of the tyre belt and to populate the respective complex eigenvector matrix. In addition, because of the way nodal motion is defined and captured in the context of the proposed tyre model, the eigenvalues and the eigenvectors of the tyre belt have to be identified from frequency response functions containing rigid-body modes as well, an observation which dictated the adopted – free-free – boundary condition of the tyre. Moreover, the theoretical approach developed in the previous section, and specifically Equation 4.2–9, provides a thorough insight into the experimental challenges imposed in the present project. In particular, two distinct experimental procedures have been developed, the first one associated with the in-plane modes of the tyre and the second one with the out-of-plane modes. The fundamental distinction between these two procedures is the orientation of the tyre:

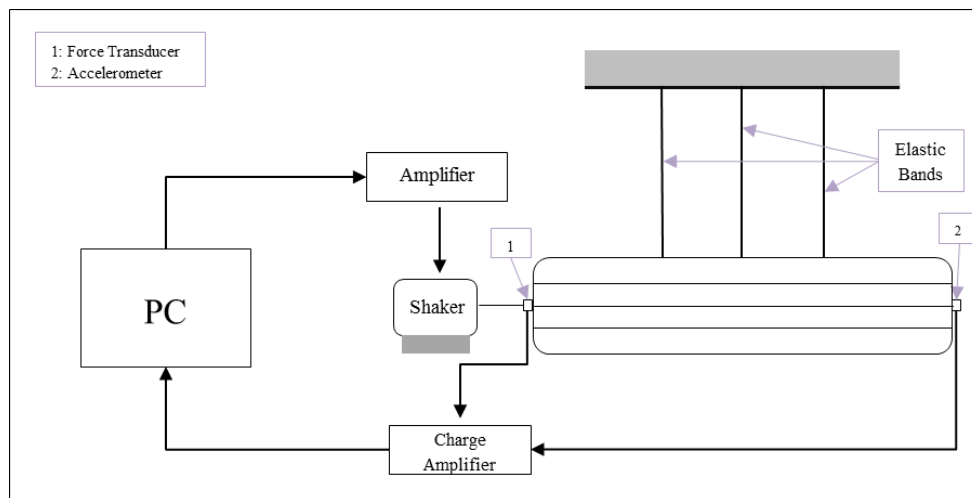


Figure 4.23 – Experimental layout for measurement of in-plane tyre belt modes



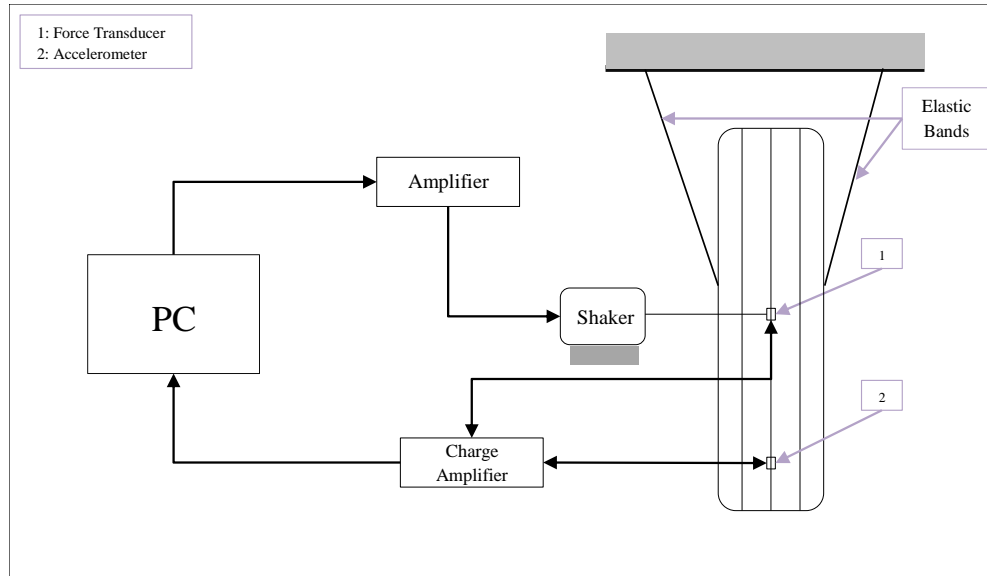


Figure 4.24 – experimental layout for measurement of out-of-plane tyre belt modes

As the elastic bands constraining the tyre are relatively stiff along their axial direction, the suspension of the tyre is altered between in-plane and out-of-plane tests. This is necessary in order to ensure that the excitation force is applied in a direction perpendicular to the axial direction of the bands, so as to eliminate reaction forces applied from the bands to the wheel.

Due to the digital nature of data acquisition, an analogue band pass filter is implemented in order to minimise aliasing effects jeopardising the quality of the acquired digital signals corresponding to the excitation – force – and the response – acceleration – of each component in the frequency response function matrix of Equation 4.2–9. These filtered signals have been analysed and the corresponding acceleration frequency response functions have been obtained by applying the method introduced by P. D. Welch in [114], the selection of which has been based on the nature of the applied excitation, i.e. white Gaussian noise. In addition, to minimise the leakage phenomenon mentioned in [44], a Hanning window has been applied to the experimentally acquired data. Each excitation sequence has been repeated five times and the respective acceleration frequency response functions ( $A_{ij}(\omega)$ ) have been obtained. To populate Equation 4.2–9, the respective receptance frequency response functions are calculated from the corresponding acceleration frequency response functions as follows<sup>[30]</sup>:

$$\alpha_{ij}(\omega) = -\frac{A_{ij}(\omega)}{\omega^2} \quad 4.3-1$$

These experimentally obtained receptance frequency response functions have been averaged to yield the final receptance frequency response function. The experimental equipment and parameters used and adopted for the modal tests described in this Chapter are presented in the following table.

<b>Table 4.1: Experimental equipment and parameters</b>	
Tyre	Continental 195/50 R15
Sampling rate	20000 [Hz]
Analogue band-pass filter	[1 3000] [Hz]
Force transducer	Brüel & Kjær – Type 8230
Accelerometer	Brüel & Kjær – Type 4332
Charge Amplifier	Brüel & Kjær – Nexus Type 2691-A-0S2
Modal Shaker	Brüel & Kjær – LDS V201
Acquisition Card	NI PCIe-6259

#### 4.3.2 Boundary conditions

In general, any tyre modal testing procedure commences with the appropriate structural support of the physical tyre. One common challenge in this type of modal testing is the isolation of the tyre from resonances originating from the support structure. Since the desired outcome of these tests is the identification of certain tyre properties, it is vital to ensure that the support structure does not significantly affect the experimentally obtained data. To this end two options have been used in previous studies. The first one includes the attachment of the tyre to an adequately rigid foundation (“grounded support”), such as the seismic table used in the work of A. A. Popov and Z. Geng in [87]. According to D. J. Ewins in [30], this supporting type could lead to questionable measurements as real-world support structures are generally not able to properly ground any test piece, especially close to their natural frequencies where resonances occur.

Nevertheless, as the tyre has to eventually be supported, an alternative formation found in literature is the suspension of the wheel by a number of elastic cords<sup>[19][43][116]</sup>, a supporting layout which is usually described by the term “free-free boundary condition”, a term adopted within the present body of work. Although this particular supporting layout does not represent a theoretically perfect option, it can lead to valid measurements, as long as attention is paid to some key-points found in the work of D. J. Ewins in [30] and the tyre-related research conducted by D. H. Guan et al. in [43] and [116]. Moreover, as has been mentioned above and having in mind the general scope of the proposed modal testing – which is associated with the identification of tyre model properties to be used in the tyre modelling environment presented in Chapter 3 – it is required that the identified properties are obtained from a modal set containing the contribution of rigid-body modes, which is another factor in favour of the free-free boundary condition.

The first preliminary check of an elastic support structure refers to the natural frequencies of the rigid body modes of the test piece. Since the test tyre does not float into space, its six lower natural frequencies, which in a pure free-free modal test would be associated with the rigid body modes, are not equal to zero. The critical point, with regard to these frequencies, is the comparison between their magnitudes and the magnitude of the frequency corresponding to the first elastic mode. In the work conducted by T. G. Carne et al. in [18], it is mentioned that the natural frequencies related to the rigid-body motion of a test piece should be kept lower than 10% of the frequency of the first bending mode, see Figure 4.25 and Figure 4.26. In the particular case of modal testing conducted for this project, this requirement has been satisfied as natural frequencies corresponding to pseudo rigid-body modes have been confined in the [0.5Hz – 5Hz] frequency band, while the natural frequency corresponding to the first flexible mode has been identified equal to 59.39Hz. Nevertheless, it should be noted that the correlation between the experimentally identified and the actual damping seems to be more sensitive in terms of the elastic mode frequency over the rigid-body mode frequency ratio – see Figure 4.26 – compared to the respective correlation between the experimentally identified and the actual natural frequency – see Figure 4.25. This could substantially influence the identified damping of the first few elastic modes but, as elastic modes are identified in higher natural frequencies, the effect of this phenomenon is kept to a minimum.

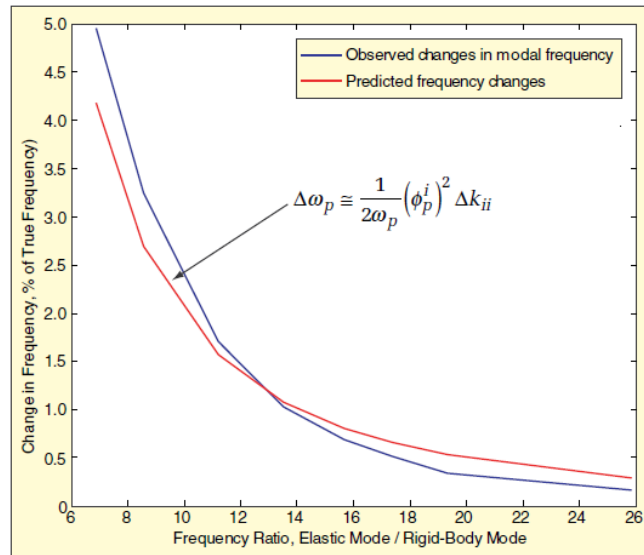


Figure 4.25 – Changes in modal frequency as a function of the frequency ratio ([18])

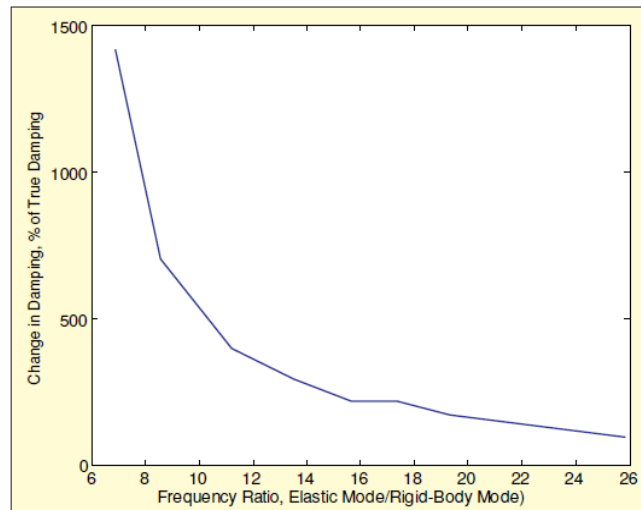


Figure 4.26 – Changes in modal damping as a function of the frequency ratio ([18])

Moreover, the location of the points where the elastic bands attach to the tyre could jeopardise the accuracy of the acquired data, especially in the cases where the stiffness of the bands is non-negligible. The bands should be located close to the nodal points of each mode of the tyre in order to avoid exciting the band modes. The direction of the bands is critical as well, due to their construction and the high value of longitudinal to radial stiffness ratio. Depending on the tyre mode of interest, the bands should be as perpendicular as possible to the primary direction of vibration in order to avoid any deformation in the band longitudinal direction and the associated forces, which could affect the motion and the vibration of the tyre. This requirement has also been satisfied by modifying the modal testing layout depending on the excitation direction, see Figure 4.23 and Figure 4.24.

The tyre belt has been excited via an electromagnetic shaker (Brüel & Kjær – LDS V201) along the radial, tangential and lateral directions of the first belt node. The shaker has been connected to the node using a drive rod, which has been aligned with the excitation direction of each test. In order to enhance the quality of the acquired data, the selected rod is stiff along its axial direction and relatively flexible along every other axis. This configuration ensures that the excitation of secondary degrees of freedom is minimised. The force transducer (Brüel & Kjær – Type 8230) is located between the drive rod and the tyre so as to eliminate the effect of the excitation equipment on the acquired frequency response.

## 4.4 Modal parameter identification procedures and results

### 4.4.1 Identification of eigenvalues and eigenvectors

Having obtained the necessary receptance frequency response functions, defined in equation 4.2–9, the next challenging step has been to use these experimental data to identify the eigenproperties of the tested tyre. At this point, one may refer to the receptance FRF expression (equation 4.2–6):

$$\alpha_{ij}(\omega) = \sum_{r=1}^m \left[ \frac{\varphi_{ir}\varphi_{jr}}{(\omega_r\xi_r + i(\omega - \omega_r\sqrt{1 - \xi_r^2}))} + \frac{\varphi_{ir}^*\varphi_{jr}^*}{(\omega_r\xi_r + i(\omega + \omega_r\sqrt{1 - \xi_r^2}))} \right] \quad 4.4-1$$

In theory,  $m$  tends to infinity, as new modes are triggered with increasing excitation frequency. But, in practice, the number  $m$  of identifiable modes has an upper limit which is defined by the experimental equipment used and the conducted modal testing. As a result, only a certain number of modes may be studied. This restricted frequency band may be expressed by the following equation, which is an alternative version of equation 4.4–1 including the residual terms  $C_1$  and  $C_3$ :

$$\alpha_{ij}(\omega) = -\frac{C_1}{\omega^2 M_{ij}^R} + \sum_{r=1}^m \left[ \frac{\varphi_{ir}\varphi_{jr}}{(\omega_r\xi_r + i(\omega - \omega_r\sqrt{1 - \xi_r^2}))} + \frac{\varphi_{ir}^*\varphi_{jr}^*}{(\omega_r\xi_r + i(\omega + \omega_r\sqrt{1 - \xi_r^2}))} \right] + \frac{C_3}{K_{ij}^R} \quad 4.4-2$$

Nevertheless, these identifiable modes can provide a valuable insight into the dynamics of the tyre belt, so the quantities of equation 4.4–1 – or equivalently the quantities corresponding to term  $C_2$  in equation 4.4–2 – need to be identified. With regard to this particular challenge, there are several methods of attack<sup>[30][70]</sup> and the selection between them has been done by taking into account the quality of the experimental data and the availability of computational power. In general, these methods are divided into two categories, based on the way they deal with the modes of the structure. The Single Degree of Freedom (SDOF) methods identify one mode at a time, and consequently such a method should be applied more than once on the same set of experimental data in order to identify several modes. On the other hand, the Multi Degrees of Freedom (MDOF) methods identify all the modes located within a frequency band at once, but they tend to be more demanding in terms of computational power compared to the SDOF methods.

In the present work, a dual approach has been adopted. The eigenvalues of the modes of interest are identified by fitting a predefined fractional expression directly to the experimentally acquired data while the respective residues are identified by introducing an additional post-processing level, presented below, in order to minimise the influence of out-of-band modes. The rationale behind this approach has been that typically the residue of a mode is heavily affected by adjacent modes compared to the effect of the respective natural frequency and damping ratio.

Consequently, the eigenvalue of a particular mode is identified by selecting a frequency band surrounding the mode, see  $\omega_1$  and  $\omega_2$  in Figure 4.27. In addition, a frequency close to the resonance frequency of the mode under investigation is specified. As has been stated above, a fractional expression, similar to the one presented in term  $C_2$  of equation 4.4–2, is fitted to experimental data found in the  $[\omega_1 \ \omega_2]$  frequency band. Depending on the proximity of the mode of interest to neighbouring modes, additional terms may be included at the user's will. In that case, the fitting process will yield the natural frequency and the damping ratio associated with each included term. As a result, although a single mode is investigated, there is information of adjacent modes, depending on the number of included terms. The selection of the identified properties for the pair of natural frequency and damping ratio corresponding to the examined mode, is conducted in terms of natural frequency. The identified natural frequencies are compared to the user-defined coarse resonance frequency, and the one found closest to that frequency reveals the pair corresponding to the investigated mode. Finally, this

process is repeated for every resonance in every experimentally acquired receptance frequency response function.

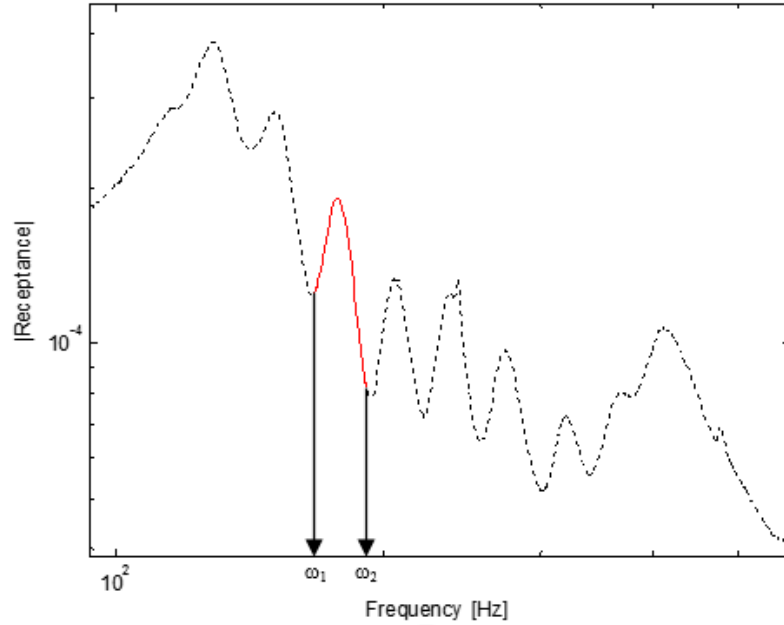


Figure 4.27 – User-defined band surrounding the investigated flexible mode of the tyre belt

With reference to residue identification, and the aforementioned problematic influence of out-of-band modes, one particular SDOF method (“Dobson’s method”<sup>[70]</sup> or “General inverse analysis method”<sup>[30]</sup>), originally developed by B. J. Dobson in [26], takes into account that influence and, as a result, the identified modal properties correspond only to the investigated modes. This is achieved by making the assumption that the residuals – terms  $C_1$  and  $C_3$  in Equation 4.4–2 – are constant in the vicinity of each resonance. The relevant published material is based on the hysteretic damping model and consequently an alternative version of the Dobson’s method has been developed for the purposes of the present work, since the non-proportional viscous damping model is more appropriate in describing the damping phenomena associated with the pneumatic tyre, as demonstrated in Section 4.1. The receptance FRF of a single in-band mode derives from the following expression:

$${}_r\alpha_{ij}(\omega) = \frac{\varphi_{ir}\varphi_{jr}}{(i\omega - s_r)} + \frac{\varphi_{ir}^*\varphi_{jr}^*}{(i\omega - s_r^*)} + K \Rightarrow$$

$${}_r\alpha_{ij}(\omega) = \frac{{}_rA_{ij} + {}_rB_{ij}i}{(i\omega - s_r)} + \frac{({}_rA_{ij} - {}_rB_{ij}i)}{(i\omega - s_r^*)} + K \Rightarrow$$

$${}_r\alpha_{ij}(\omega) = \frac{({}_rA_{ij} + {}_rB_{ij}i)(i\omega - s_r^*) + ({}_rA_{ij} - {}_rB_{ij}i)(i\omega - s_r)}{(i\omega - s_r)(i\omega - s_r^*)} + K \quad 4.4-3$$

where K represents the effect of the remaining modes on  ${}_r\alpha_{ij}(\omega)$ . For a user-specified frequency  $\omega_f$  (“fixing frequency”) close to the natural frequency of mode r, Equation 4.4–3 yields:

$${}_r\alpha_{ij}(\omega_f) = \frac{({}_rA_{ij} + {}_rB_{ij}i)(i\omega_f - s_r^*) + ({}_rA_{ij} - {}_rB_{ij}i)(i\omega_f - s_r)}{(i\omega_f - s_r)(i\omega_f - s_r^*)} + K \quad 4.4-4$$

Following B. J. Dobson’s approach<sup>[26]</sup>, the residual term K is assumed to remain constant for frequencies close to the resonant frequency of mode r. Thus, it can be eliminated by defining a new function as follows:

$$D(\omega) = \frac{({}_r\alpha_{ij}(\omega) - {}_r\alpha_{ij}(\omega_f))(i\omega - s_r)}{(i\omega - s_r^*)(i\omega_f - s_r)(i\omega_f - s_r^*)} \quad 4.4-5$$

It is apparent that the subtraction located in the first parenthesis of the right hand side of Equation 4.4–5 eliminates the residual terms K. This particular equation demonstrates the main difference between the Dobson’s original method and the proposed extended version, i.e. the necessity to identify the eigenvalue associated with mode r in advance, a task which can be conducted using any SDOF or MDOF method as these values are less sensitive to adjacent or even out-of-band modes than the residues. As a function of frequency, Equation 4.4–5 results in a quadratic expression:

$$D(\omega) = (2{}_rA_{ij}\omega_f i - 2{}_rA_{ij}a - 2{}_rB_{ij}b)\omega^2 + (-2{}_rA_{ij}\omega_f^2 - 2(a^2 + b^2) + 2(-2{}_rA_{ij}a - 2{}_rB_{ij}b)a)\omega i + C \quad 4.4-6$$

where a and b are the real and imaginary part of eigenvalue  $s_r$  respectively. Since all the quantities included in Equation 4.4–5 have been acquired via modal testing or identified via the post-processing procedure presented above, it is possible to make an estimation of  $D(\omega)$  based only on experimental  $({}_r\alpha_{ij}(\omega), {}_r\alpha_{ij}(\omega_f))$  and identified  $(s_r^*, s_r)$  data. This estimation has the following form:



$$D(\omega) = K_1\omega^2 + K_2\omega + K_3 \quad 4.4-7$$

Comparison of the experimentally obtained terms of the polynomial in 4.4–7 with the analytical terms of 4.4–6 leads to the calculation of the residue constants A and B. By denoting as  $\Lambda_1$  and  $\Lambda_2$  the real and the imaginary part, respectively, of the known term  $K_1$  the following system holds:

$$\left. \begin{aligned} \Lambda_1 = \text{Re}(K_1) &= -2 \, {}_rA_{ij}a - 2 \, {}_rB_{ij}b \\ \Lambda_2 = \text{Im}(K_1) &= 2 \, {}_rA_{ij}\omega_f \end{aligned} \right\} \Rightarrow$$

$$\begin{aligned} {}_rA_{ij} &= \frac{\Lambda_2}{2\omega_f} \\ {}_rB_{ij} &= \frac{-2 \, {}_rA_{ij}a - \Lambda_1}{2b} \end{aligned} \quad 4.4-8$$

It should be noted that only term  $K_1$  has been exploited in the above expressions, see definition of  $\Lambda_1$  and  $\Lambda_2$ . The rationale supporting this choice is that residue constants derived by  $K_1$  where more consistent, compared to the respective residue constants obtained by  $K_2$  or  $K_3$ , for the case of a simple analytical test model used for the validation of the proposed identification method.

Provided that the fixing frequency is close enough to the natural frequency of mode  $r$ , its value should not affect the estimation of A and B derived by Equation 4.4–8. Nevertheless, due to experimentally induced errors and inaccuracy in the fitting procedure of Equation 4.4–7, it seems that the selection of  $\omega_f$  does influence the outcome of Equation 4.4–8 and as a result the identified frequency response function is sensitive to the fixing frequency selection, as is illustrated in the following figure:

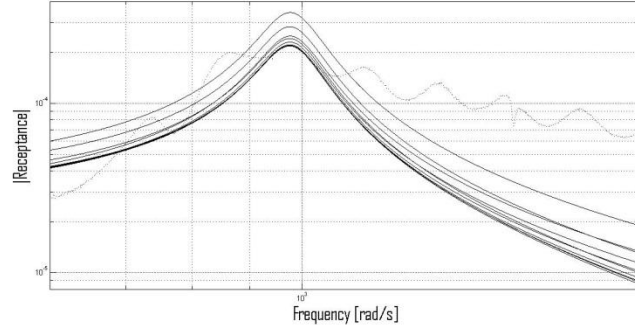


Figure 4.28 – Variation of identified receptance frequency response function as a function of fixing frequency  $\omega_f$

Taking into account that the FRF of mode  $r$  is dominant in the vicinity of the resonant frequency  $\omega_r$ , a criterion is defined in order to select the most appropriate set of  $A$  and  $B$ . According to this criterion the deviation between the value of the estimated FRF in the natural frequency of mode  $r$  and the respective value obtained by experimental data should be minimal:

$$\left| |\alpha(\omega_r)_{\text{exp}}| - |\alpha(\omega_r)_{\text{est}}| \right| \rightarrow 0 \quad 4.4-9$$

The pair of  $A$  and  $B$  that minimises the above criterion is the best estimation of the residue constants for mode  $r$ :

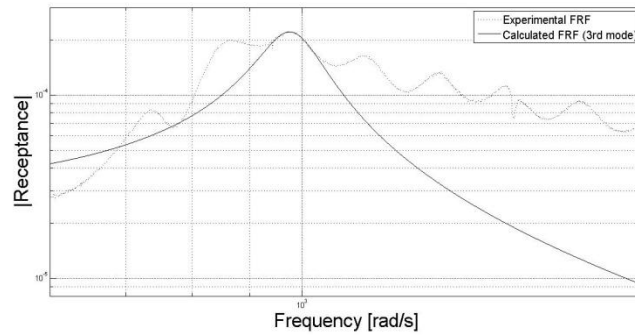


Figure 4.29 – Selected receptance frequency response function based on the criterion introduced in equation 4.4-9

Following the procedure described above, it has been possible to identify the natural frequency, the damping ratio and the respective residue for each category of modes – radial, lateral and tangential. The residue vector of each radial mode has the following form:

$$\{\text{rad}A + \text{rad}Bi\} = [\varphi_1\varphi_1 \quad 0 \quad \varphi_3\varphi_1 \quad \dots \quad \varphi_k\varphi_1 \quad 0 \quad \varphi_{(k+2)}\varphi_1 \quad \dots \quad \varphi_{(3N-2)}\varphi_1 \quad 0 \quad \varphi_{3N}\varphi_1]^T \quad 4.4-10$$

while for the case of tangential modes, the respective vector is:

$$\{\tan A + \tan Bi\} = [\varphi_1 \varphi_3 \quad 0 \quad \varphi_3 \varphi_3 \quad \dots \quad \varphi_k \varphi_3 \quad 0 \quad \varphi_{(k+2)} \varphi_3 \quad \dots \quad \varphi_{(3N-2)} \varphi_3 \quad 0 \quad \varphi_{3N} \varphi_3]^T \quad 4.4-11$$

The eigenvector components of each radial mode are easily obtained by Equation 4.4–10, as the residue of the driving point is included in the residue vector, which yields  $\phi_1$ . Dividing the residue vector of radial mode  $r$  by  $\phi_1$ , which is unique for each mode of the structure, the associated complex eigenvector is calculated:

$$\{\psi_r\} = \frac{\{\text{rad}A + \text{rad}Bi\}}{\phi_1} \Rightarrow$$

$$\{\psi_r\} = [\varphi_1 \quad 0 \quad \varphi_3 \quad \dots \quad \varphi_{3N-3} \quad 0 \quad \varphi_{3N}]^T \quad 4.4-12$$

Similarly, for the case of tangential modes, the key component is  $\phi_3$ , found in the residue vector of equation 4.4–11 and the respective eigenvector is the following:

$$\{\psi_t\} = \frac{\{\tan A + \tan Bi\}}{\phi_3} \Rightarrow$$

$$\{\psi_t\} = [\varphi_1 \quad 0 \quad \varphi_3 \quad \dots \quad \varphi_{3N-3} \quad 0 \quad \varphi_{3N}]^T \quad 4.4-13$$

With regard to the lateral modes of the tyre belt, a similar approach is adopted. In this case, the residue vector has the form presented in the following equation:

$$\{\text{lat}A + \text{lat}Bi\} = [0 \quad \varphi_2 \varphi_2 \quad 0 \quad \dots \quad 0 \quad \varphi_k \varphi_2 \quad 0 \quad \dots \quad 0 \quad \varphi_{(3N-1)} \varphi_2 \quad 0]^T \quad 4.4-14$$

and the resulting eigenvector of each lateral mode is obtained using the component  $\phi_2$ :

$$\{\psi_l\} = \frac{\{\text{lat}A + \text{lat}Bi\}}{\phi_2} \Rightarrow$$

$$\{\psi_l\} = [0 \quad \varphi_2 \quad 0 \quad \dots \quad 0 \quad \varphi_{3N-1} \quad 0]^T \quad 4.4-15$$

#### 4.4.2 Identified properties

At this point, following the procedures described above, frequency response data have been used to identify the radial, tangential and lateral modes of the tyre belt. The eigenvalue corresponding to each identified mode yields the respective natural frequency and damping ratio, and these quantities are presented in the following tables:

Table 4.2: In-plane Radial Modes					
Mode	Nat. Freq. [Hz] (radial resp.)	Nat Freq. [Hz] (tangential resp.)	Delta [%]	Damp. Ratio [%] (radial resp.)	Damp. Ratio [%] (tangential resp.)
1	115	118	2.58	3.63	3.81
2	131	133	1.51	6.19	5.91
3	155	153	1.30	6.61	6.28
4	180	180	0.00	5.93	6.26
5	208	207	0.48	5.48	6.05
6	242	241	0.41	3.28	2.35
7	275	276	0.36	5.81	5.91
8	320	321	0.31	5.61	6.71
9	371	370	0.27	6.87	6.87
10	413	420	1.68	7.05	5.77

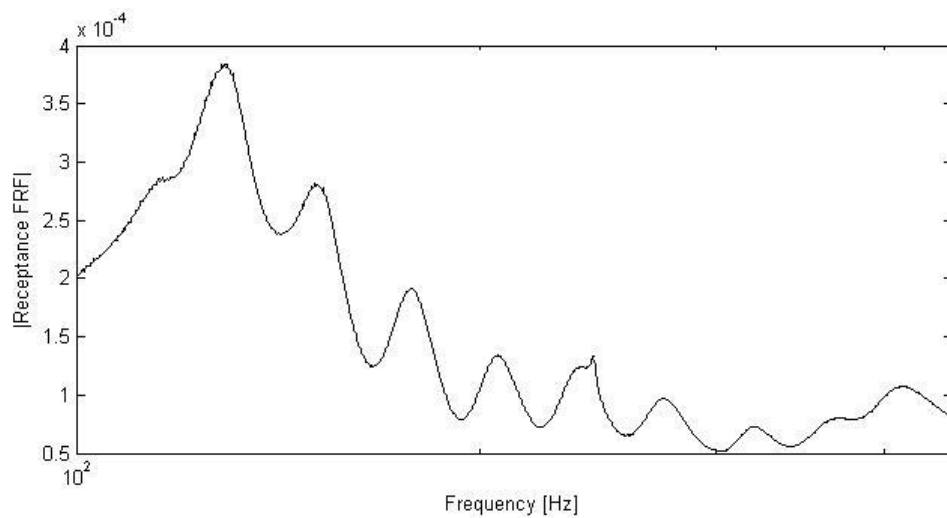


Figure 4.30 – Frequency response function corresponding to a radially excited tyre belt mode

Table 4.3: In-plane Tangential Modes					
Mode	Nat. Freq. [Hz] (radial resp.)	Nat Freq. [Hz] (tangential resp.)	Delta [%]	Damp. Ratio [%] (radial resp.)	Damp. Ratio [%] (tangential resp.)
1	108	106	1.87	4.14	3.54
2	116	117	0.86	4.22	4.09
3	134	135	0.74	6.50	6.63
4	153	150	1.98	6.06	6.25
5	177	177	0.00	5.28	6.48
6	196	198	1.02	4.23	8.18
7	207	208	0.48	4.64	5.26
8	236	238	0.84	4.47	4.24
9	273	272	0.37	4.51	4.56
10	318	318	0.00	4.74	4.58
11	375	375	0.00	5.95	5.18
12	404	403	0.25	4.06	4.59
13	473	459	3.00	1.64	2.20

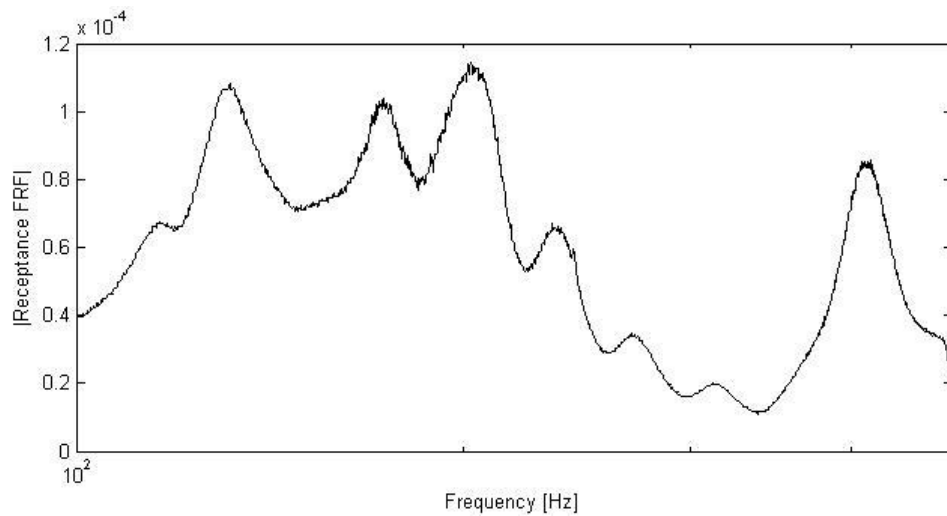


Figure 4.31 – Frequency response function corresponding to a tangentially excited tyre belt mode

Table 4.4: Out-of-plane Modes		
Mode	Natural Frequency [Hz]	Damping Ratio [%]
1	59.39	2.75
2	72.95	4.83
3	103.19	4.38
4	114.91	3.70

5	131.26	4.49
6	152.63	5.50
7	174.56	4.78
8	195.14	4.38
9	216.03	3.44
10	246.21	3.67
11	274.12	4.68

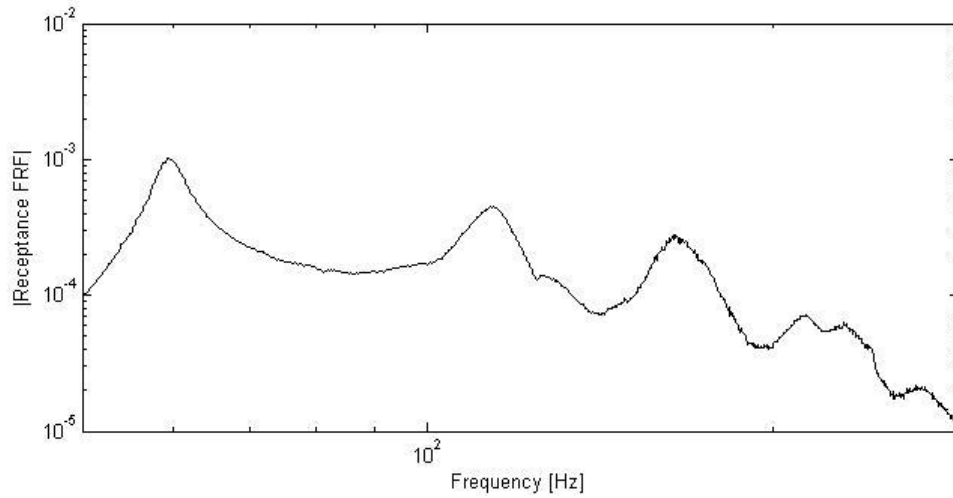


Figure 4.32 – Frequency response function corresponding to a laterally excited tyre belt mode

The agreement between the radial and the tangential response of each, radially or tangentially excited, mode is expressed by function Delta:

$$\Delta = \frac{|\omega_r - \omega_t|}{(\omega_r + \omega_t)/2} \quad 4.4-16$$

Previous research on tyre modal analysis, L. H. Yam et al. in [116], suggests that any tyre structural mode measured along different directions – for example radial and tangential in the case examined in this work – should demonstrate resonances occurring in close frequencies, a requirement which is quantified by function Delta in equation 4.4–16. It is noteworthy that the maximum value of Delta is kept to a certain minimum, as it is equal to 2.58% and 3.00% for the case of radial and tangential modes respectively, hence demonstrating the quality of the acquired data and the accuracy of the associated post-processing procedures described above. The natural frequencies of the in-plane and the out-of-plane modes are compared in the following figure, which demonstrates the agreement – in terms of natural frequency –

between the radial and the tangential responses of each mode and also between radial, tangential and lateral modes:

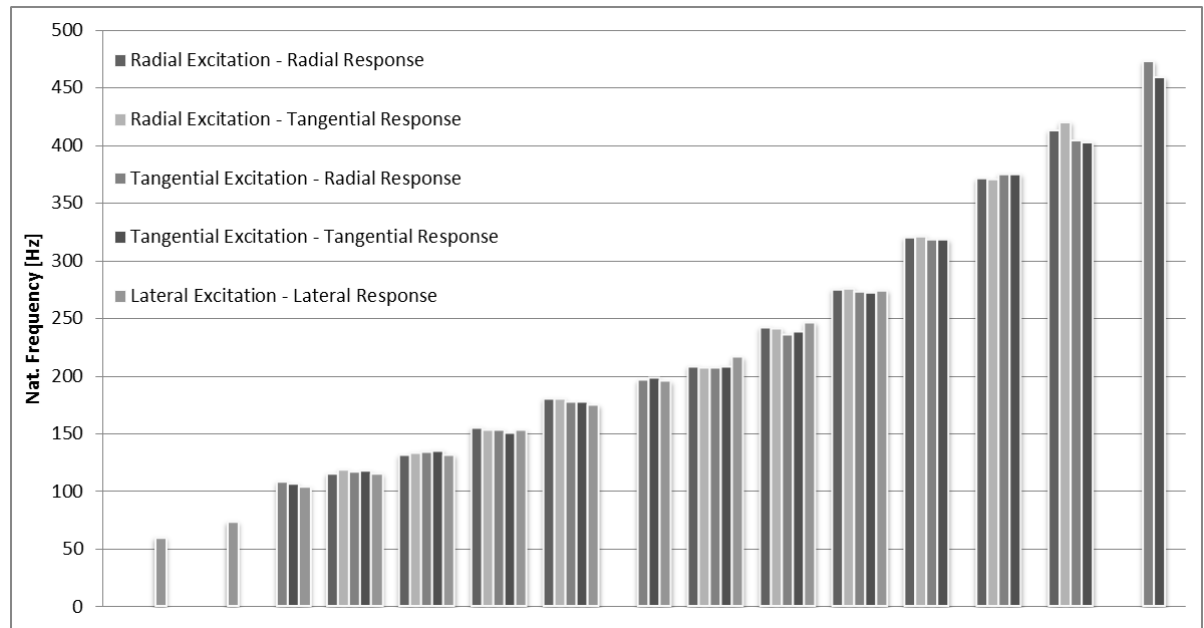


Figure 4.33 – Comparison of the identified natural frequencies for all the tested combinations of excitation and response

Close examination of the above diagram and also of Tables 4.1 and 4.2 reveals partial inconsistency between radial, tangential and lateral modes. Although there is agreement between these three mode categories for the majority of cases presented above, there are two missing radial modes. In particular, the first and sixth identified tangential modes – or similarly the third and eighth lateral modes – have no counterpart in the radially excited modes. This has been predicted in the analytical work of A. Tsotras in [110], where the tyre belt is modelled as a flexible ring, and this inconsistency originates from the free-free boundary condition. Specifically, the radial modes associated with the first and sixth tangential modes and the third and eighth lateral modes were originally flexible but became rigid-body modes, because of the adopted boundary condition. Moreover, one may notice the existence of two lateral modes which do not correspond to any in-plane mode, see modes 1 and 2 in Table 4.3 and also the first two modes in Figure 4.33. This phenomenon has been investigated further and the respective conclusion is presented below, in Section 4.4.3.

Moving the discussion to the identified residues which yield the eigenvector components of each mode, tyre belt modes are complex, due to the non-proportional nature of tyre damping, and as a result the respective eigenvectors do not demonstrate fixed nodal points. This complexity is depicted in the following Argand diagrams, where the relative phase between

the components of each eigenvector is distributed in the range  $[-180^\circ, 180^\circ]$ , a typical behaviour of non-standing waves. On the contrary, real eigenvectors associated with simpler damping phenomena demonstrate relative phase angles close to  $0^\circ$  or  $180^\circ$ .

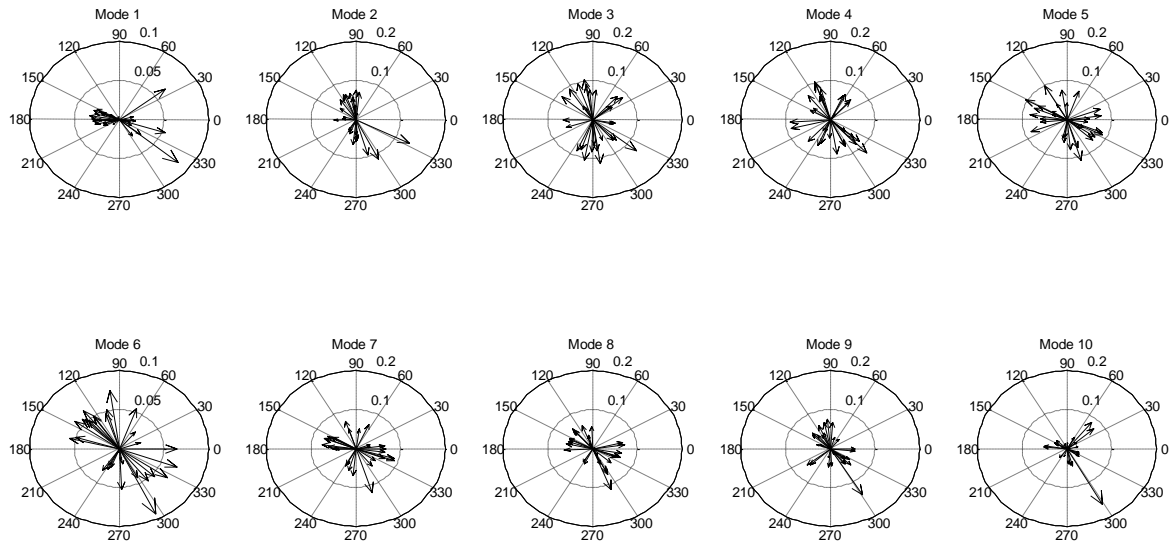


Figure 4.34 – Identified residues: complex radial modes, radial response (top row: modes 1 to 5; bottom row: modes 6 to 10)

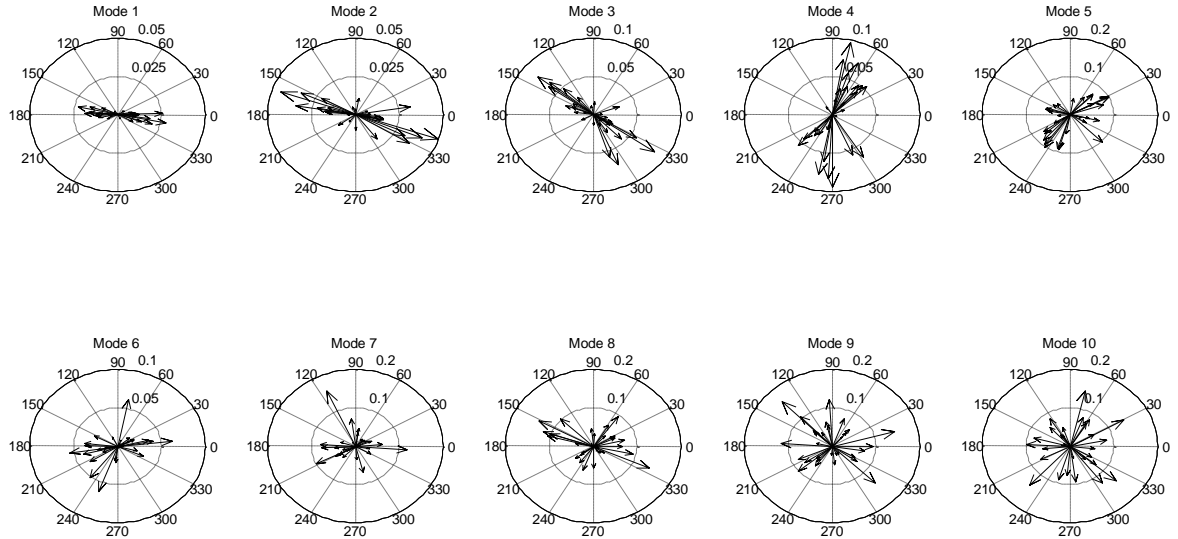


Figure 4.35 – Identified residues: complex radial modes, tangential response (top row: modes 1 to 5; bottom row: modes 6 to 10)



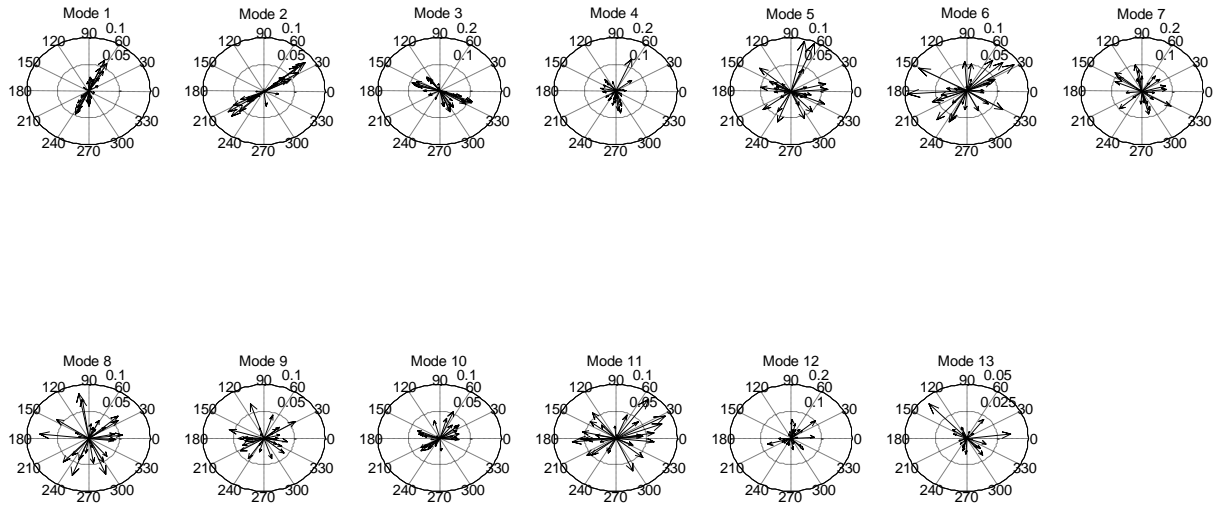


Figure 4.36 – Identified residues: complex tangential modes, radial response (top row: modes 1 to 7; bottom row: modes 8 to 13)

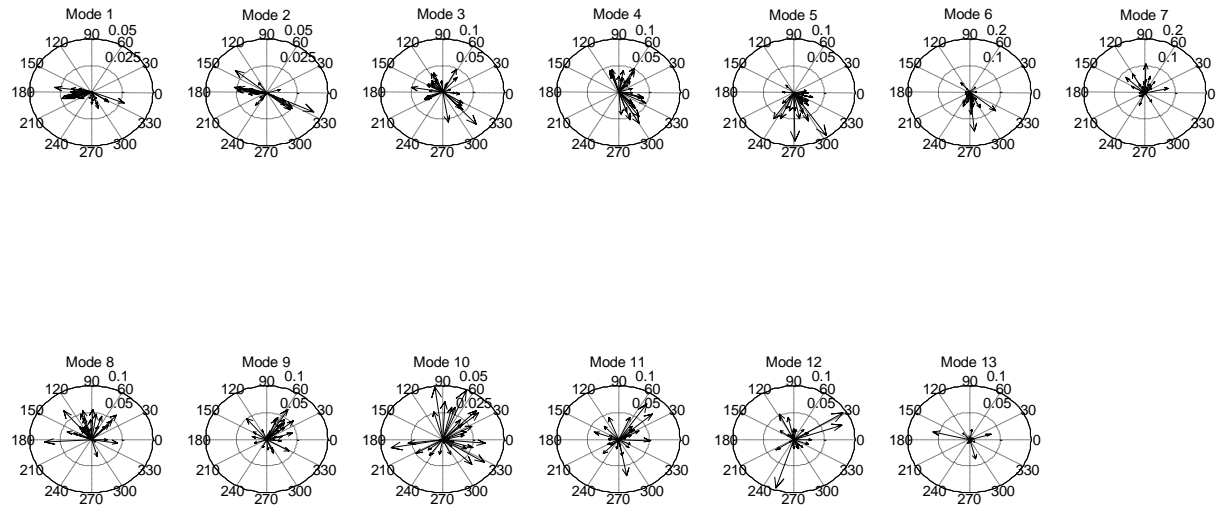


Figure 4.37 – Identified residues: complex tangential modes, tangential response (top row: modes 1 to 7; bottom row: modes 8 to 13)

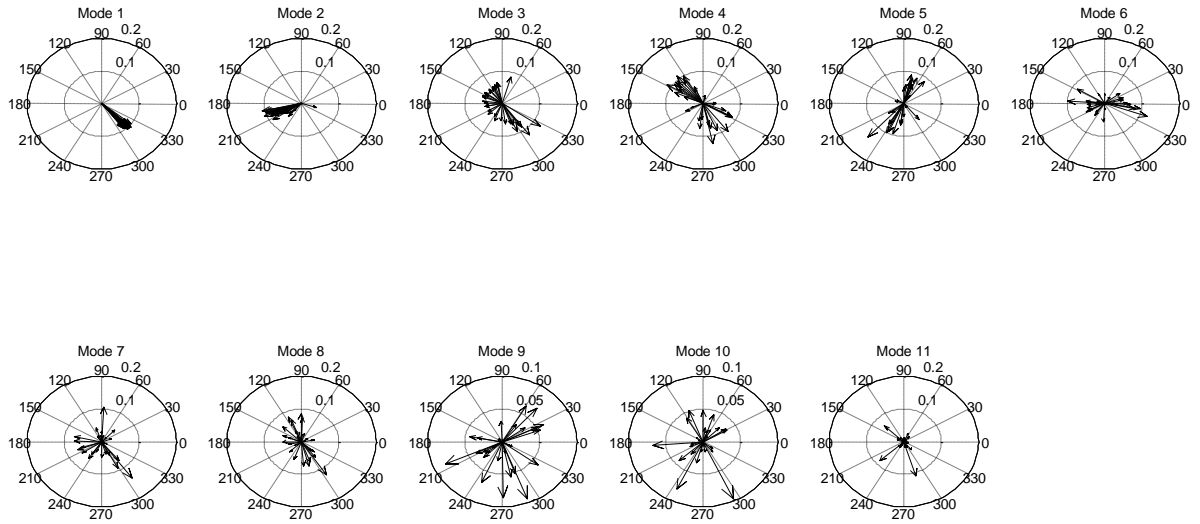


Figure 4.38 – Identified residues: complex lateral modes, lateral response (top row: modes 1 to 6; bottom row: modes 7 to 13)

#### 4.4.3 Complex to real normal modes

Since the residues identified in the section above are complex and represent travelling waves, a conversion method is required in order to obtain the equivalent standing mode shapes. This step is of importance as it allows for visual validation of the identified mode shapes and also, in a more generic scope, it could be exploited as a correlation tool between the identified modes and those derived by an analytical or an FEM tyre belt model. In the context of the present work, the outcome of such a transformation, from complex to real, is validated by having previous tyre-related analytical<sup>[110]</sup> and experimental<sup>[116]</sup> research as reference points.

Obviously, the easiest method is to discard the complex phase element and simply assign a phase of 0 or 180 degrees to the modulus of each eigenvector component<sup>[30]</sup>. While this approach is suitable for modes demonstrating quasi-real behaviour, i.e. the mode components lie in groups of a limited phase range (see Figure 4.39), it cannot be used to estimate a real mode shape corresponding to a heavily complex mode (see Figure 4.40) as it is not clear which components correspond to 0° and which to 180°.

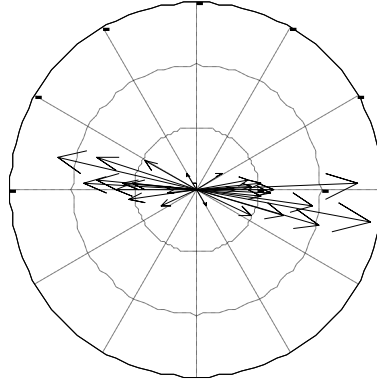


Figure 4.39 – Complex eigenvector components demonstrating an “almost” real behaviour

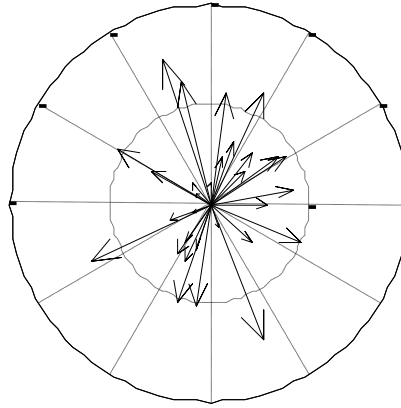


Figure 4.40 – Complex eigenvector components demonstrating a heavily complex behaviour

An alternative method has been developed by G. W. Asher in [7] and it extracts the undamped modes of a generally damped structure by applying a mono-phase and multi-point excitation. Having identified a complex set of eigenvectors  $\Psi$  and eigenvalues  $\lambda$ , it is possible to calculate the associated frequency response function:

$$\alpha(\omega) = \Psi(\lambda - \omega^2)\Psi^T \quad 4.4-17$$

The undamped natural frequencies can be obtained as follows:

$$\det(\text{Re}(\alpha(\omega))) = 0 \quad 4.4-18$$

and the respective undamped eigenvectors by the following expression:

$$\Phi = \text{Im}(\alpha(\omega))\{\bar{F}\} \quad 4.4-19$$

The force vector located in equation 4.4–19 is calculated in a similar way using the complex frequency response function:

$$\text{Re}(\alpha(\omega))\{\bar{F}\} = \{0\} \quad 4.4-20$$

As is implied by the above analysis, this method requires multi-point excitation and consequently it is not suitable for the present work since the experimental procedure follows a single input – single output pattern, but it could be implemented in a future attempt to obtain the structural properties of a tyre via modal testing.

E. Balmes in [11] developed a conversion method which is in agreement with the experimental work presented in the above sections. In that work, the real modes of the structure derive from the identified system matrices. Following E. Balmes' approach the system matrices are identified based on Equations 4.4–21 to 4.4–23:

$$\mathbf{M} = (\boldsymbol{\Psi}\boldsymbol{\Lambda}\boldsymbol{\Psi}^T)^{-1} \quad 4.4-21$$

$$\mathbf{C} = -\mathbf{M}\boldsymbol{\Psi}\boldsymbol{\Lambda}^2\boldsymbol{\Psi}^T\mathbf{M} \quad 4.4-22$$

$$\mathbf{K} = -(\boldsymbol{\Psi}\boldsymbol{\Lambda}^{-1}\boldsymbol{\Psi}^T)^{-1} \quad 4.4-23$$

where  $\boldsymbol{\Lambda}_{6N \times 6N}$  is the eigenvalue matrix and  $\boldsymbol{\Psi}_{3N \times 6N}$  is the eigenvector matrix, with N being the number of nodes along the tyre circumference. As has been demonstrated above, the main drawback of this approach is that one has to experimentally identify a number of modes at least equal to the degrees of freedom of each particular system in order to obtain a valid set of system matrices. As most systems consist of numerous degrees of freedom, the above requirement is experimentally challenging and, in most cases, the set of modes is defined as incomplete, i.e. the size of matrix  $\boldsymbol{\Psi}$  is  $3N \times 2m$  where m is the number of identified modes.

The problem of incomplete sets of modes is addressed by U. Fuellekrug in [33]. In that work, the real normal modes and the undamped natural frequencies of a complete modal model are obtained by the following equation:

$$\overbrace{\mathbf{M}^{-1}\mathbf{K}}^A \{\varphi_r\} = \omega_r^2 \{\varphi_r\} \quad 4.4-24$$

with the mass modified stiffness matrix (term A) given by:

$$\begin{aligned} [\mathbf{M}^{-1}\mathbf{K} \quad \mathbf{M}^{-1}\mathbf{C}] \begin{bmatrix} \{\psi_1\} & \dots & \{\psi_{6N}\} \\ \lambda_1\{\psi_1\} & \dots & \lambda_{6N}\{\psi_{6N}\} \end{bmatrix} \\ = -[\lambda_1^2\{\psi_1\} \quad \dots \quad \lambda_{6N}^2\{\psi_{6N}\}] \end{aligned} \quad 4.4-25$$

In cases of incomplete models, a transformation is proposed. Initially, matrix  $\mathbf{X}$  is defined as follows:

$$\mathbf{X} = [\text{Re}(\{\psi_1\}) \quad \dots \quad \text{Re}(\{\psi_m\})] \quad 4.4-26$$

where  $m$  is the number of identified modes. The key point of this approach is to apply the singular value decomposition technique on matrix  $\mathbf{X}$ .

$$\mathbf{X} = \mathbf{T}\mathbf{\Sigma}(\mathbf{V}^*)^T \quad 4.4-27$$

The transformation from physical to reduced coordinates (denoted by  $\sim$ ) is conducted using the transformation matrix  $\mathbf{T}_{2N \times m}$ , found in the expression above. Therefore, the complex eigenvectors expressed in reduced coordinates are obtained by:

$$\{\widetilde{\psi}_r\} = \mathbf{T}^T \{\psi_r\} \quad 4.4-28$$

Exploiting this new reduced set of eigenvectors and expressions 4.4-24 and 4.4-25, the undamped natural frequencies and the real modes may be calculated:

$$[\widetilde{\mathbf{M}}^{-1}\widetilde{\mathbf{K}} \quad \widetilde{\mathbf{M}}^{-1}\widetilde{\mathbf{C}}] \begin{bmatrix} \{\widetilde{\psi}_1\} & \dots & \{\widetilde{\psi}_{6N}\} \\ \lambda_1\{\widetilde{\psi}_1\} & \dots & \lambda_{6N}\{\widetilde{\psi}_{6N}\} \end{bmatrix} = -[\lambda_1^2\{\widetilde{\psi}_1\} \quad \dots \quad \lambda_{6N}^2\{\widetilde{\psi}_{6N}\}] \quad 4.4-29$$

$$\overbrace{\widetilde{\mathbf{M}}^{-1}\widetilde{\mathbf{K}}}^A \{\widetilde{\varphi}_r\} = \omega_r \{\widetilde{\varphi}_r\} \quad 4.4-30$$

Having obtained the real normal modes in reduced coordinates, the inverse transformation is needed in order to express these modes in physical coordinates:

$$\{\varphi_r\} = \mathbf{T}\{\widetilde{\varphi}_r\} \quad 4.4-31$$

It should be noted that a similar approach is adopted by W. Tong et al. in [106].

In the present work, the concept of the transformation matrix between damped and undamped eigenvectors is retained, although in a simpler implementation originally proposed by N. Niedbal in [74]. The relation between complex and real modes is described by the following transformation:

$$\Phi = \Psi \mathbf{T}_1 \mathbf{T}_2 \quad 4.4-32$$

where  $\mathbf{T}_1$  and  $\mathbf{T}_2$  are the transformation matrices,  $\Phi$  is the real eigenvector matrix and  $\Psi$  is the complex eigenvector matrix. The real part of matrix  $\mathbf{T}_1$  is chosen arbitrarily equal to the identity matrix  $\mathbf{I}$ . The respective imaginary part is calculated by the equation below:

$$\text{Im}(\mathbf{T}_1) = -\left(\text{Re}(\Psi^T)\text{Re}(\Psi)\right)^{-1} \text{Re}(\Psi^T)\text{Im}(\Psi)\text{Re}(\mathbf{T}_1) \quad 4.4-33$$

Using the transformation matrix  $\mathbf{T}_1$  along with the experimentally identified eigenvalues of the system, two auxiliary matrices are obtained:

$$\mathbf{M} = \mathbf{T}_1^T \mathbf{T}_1 \quad 4.4-34$$

$$\mathbf{K} = \mathbf{T}_1^T [\mathbf{s}^2] \mathbf{T}_1 \quad 4.4-35$$

Matrices  $\mathbf{M}$  and  $\mathbf{K}$  formulate the eigenproblem which yields the undamped natural frequencies of the system ( $\omega_r$ ) and the transformation matrix  $\mathbf{T}_2$ :

$$[\mathbf{K} - [\omega_r^2]\mathbf{M}] \mathbf{T}_2 = \{0\} \quad 4.4-36$$

Substitution of matrices  $\mathbf{T}_1$  and  $\mathbf{T}_2$  in equation 4.4-32 yields the real eigenvectors of the system. The fundamental asset of the method presented above is that, given the experimentally identified eigenvalues and complex modes of any system, it demonstrates an efficient and

easy-to-implement formulation for the calculation of the respective undamped natural frequencies and real eigenvectors, taking into account the unavoidable modal truncation.

By adopting this technique to post-process the complex results presented in the preceding section, the following real mode shapes are obtained:

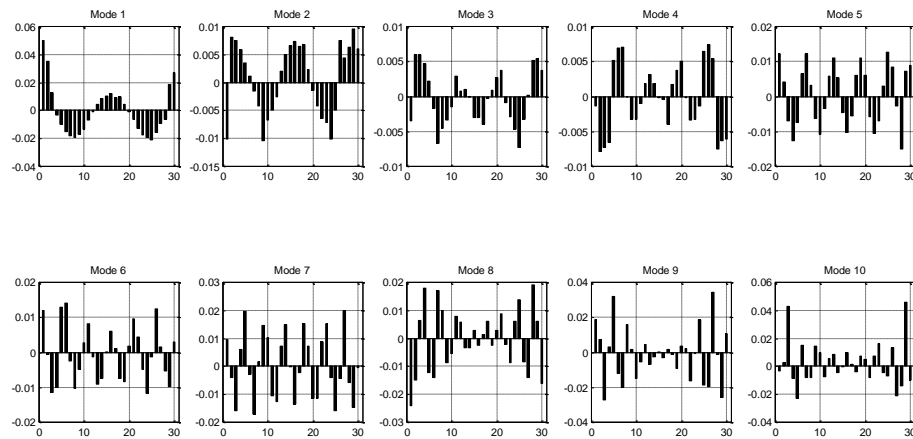


Figure 4.41 – Real mode shapes; radial excitation radial response (top row: modes 1 to 5; bottom row: modes 6 to 10)

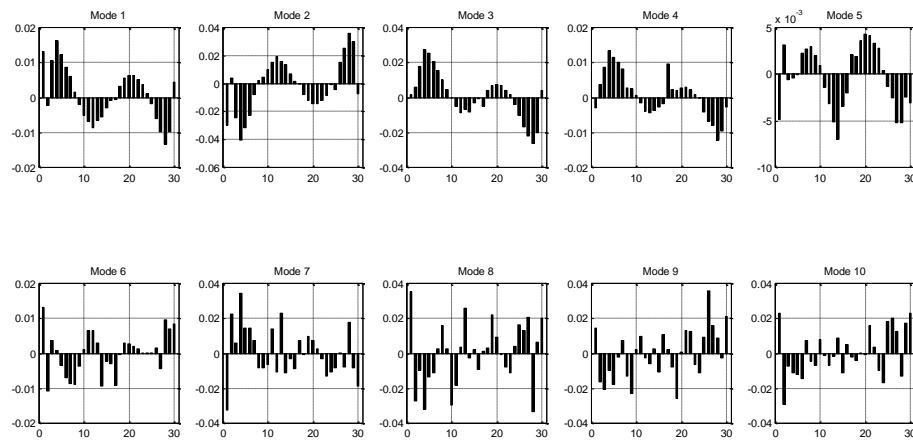


Figure 4.42 – Real mode shapes; radial excitation, tangential response (top row: modes 1 to 5; bottom row: modes 6 to 10)

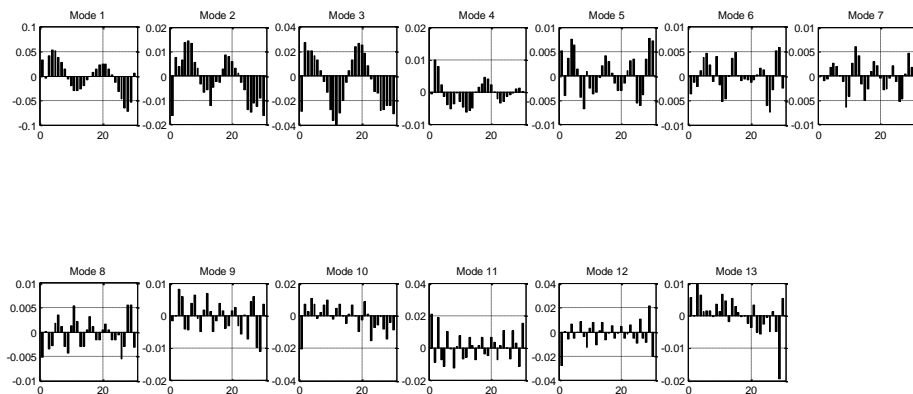


Figure 4.43 – Real mode shapes; tangential excitation, radial response (top row: modes 1 to 7; bottom row: modes 8 to 13)

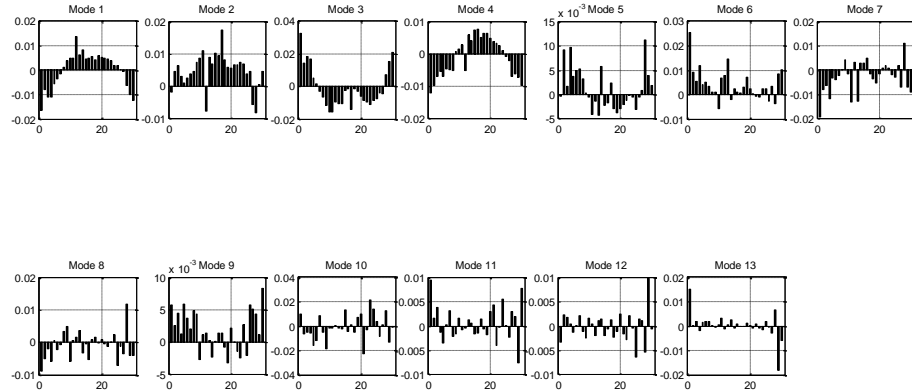


Figure 4.44 – Real mode shapes; tangential excitation, tangential response (top row: modes 1 to 7; bottom row: modes 8 to 13)

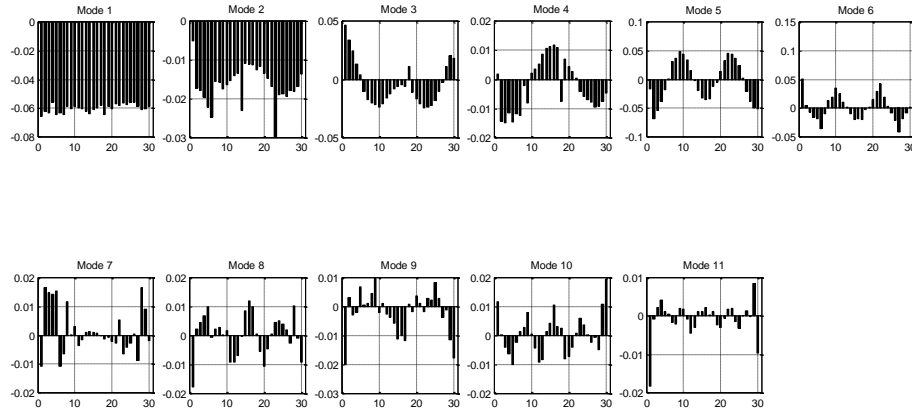


Figure 4.45 – Real mode shapes; lateral excitation, lateral response (top row: modes 1 to 6; bottom row: modes 7 to 11)

The horizontal axes of the above diagrams represent the index of each belt node and the vertical axes represent the respective amplitude of each mode shape.

#### 4.4.4 Digital filtering

Previously conducted analytical research<sup>[110]</sup> proposes that each mode shape demonstrates a sinusoidal form of a unique spatial frequency ( $\omega_s$ ) along the circumference of the tyre belt (variable  $l$ ):

$$Y(l) = Z\sin(\omega_s l) \quad 4.4-37$$



Visual inspection of the figures above reveals that, due to experimentally induced inaccuracy and numerical errors, the identified mode shapes actually consist of several sinusoidal waves. Therefore, instead of Equation 4.4–37, the following expression holds:

$$Y(l) = \sum_{i=1}^{\infty} (Z_i \sin(\omega_{si} l)) \quad 4.4-38$$

This leakage hypothesis is supported by expressing these spatial waves in the spatial frequency domain via the Fast Fourier Transform. A typical example of such a spatial frequency spectra is presented in the following figure. This particular diagram is associated with the radial response of the 2<sup>nd</sup> radially excited mode.

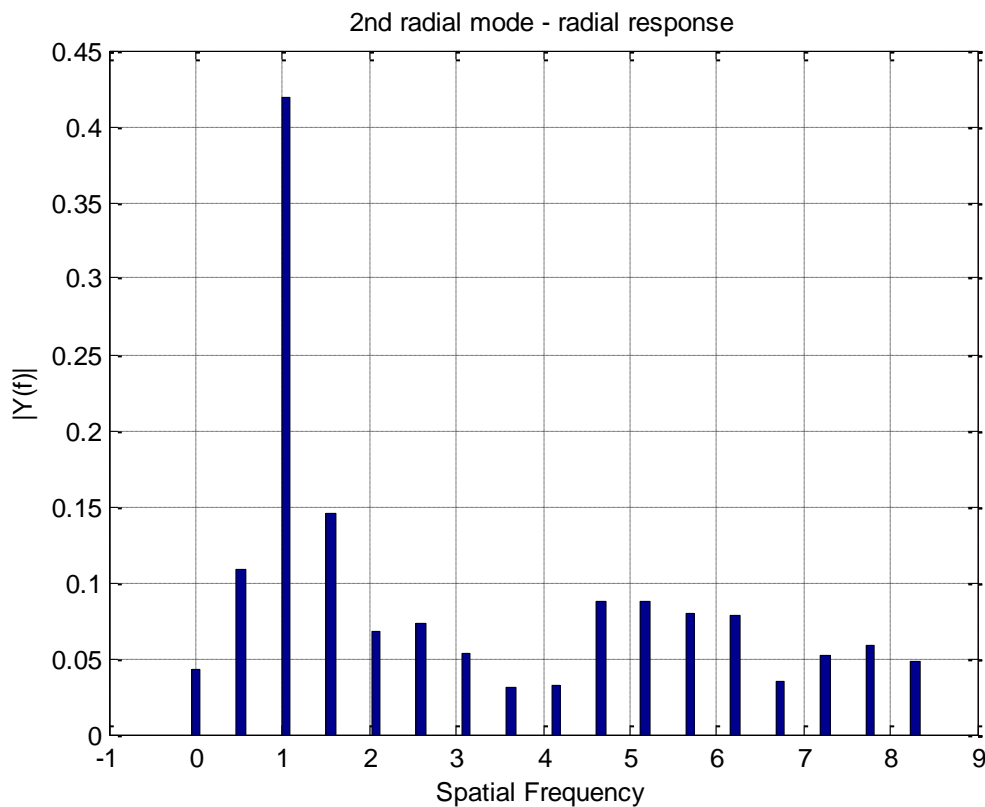


Figure 4.46 – Waveform corresponding to a real mode shape analysed in the space domain.

Taking into account the further scope of the present experimental work, i.e. the identification of eigenvectors and eigenvalues corresponding to a physical tyre so that they are used in a simulation environment, the effect of this noise on the waveform of each mode shape should be minimised. The purpose of this digital filtering process is the calculation of a set of spatially smooth mode shapes, without any loss of fundamental information compared to the

experimentally identified ones. It is conducted by eliminating every spatial wave component except that which demonstrates the maximum amplitude. By denoting as  $r_{\max}$  the index of the dominant component of the spatial frequency spectrum (for example, in the above diagram  $r_{\max}=3$ ), an alternative form of Equation 4.4–38 holds:

$$Z_i \sin(\omega_{si} l) = 0, \forall i \neq r_{\max} \quad 4.4-39$$

$$Y(l) = Z_{r_{\max}} \sin(\omega_{r_{\max}} l) \quad 4.4-40$$

As is evident from the above equations, these new frequency spectra consist of a single component. The following figure demonstrates the digitally filtered equivalent of Figure 4.46:

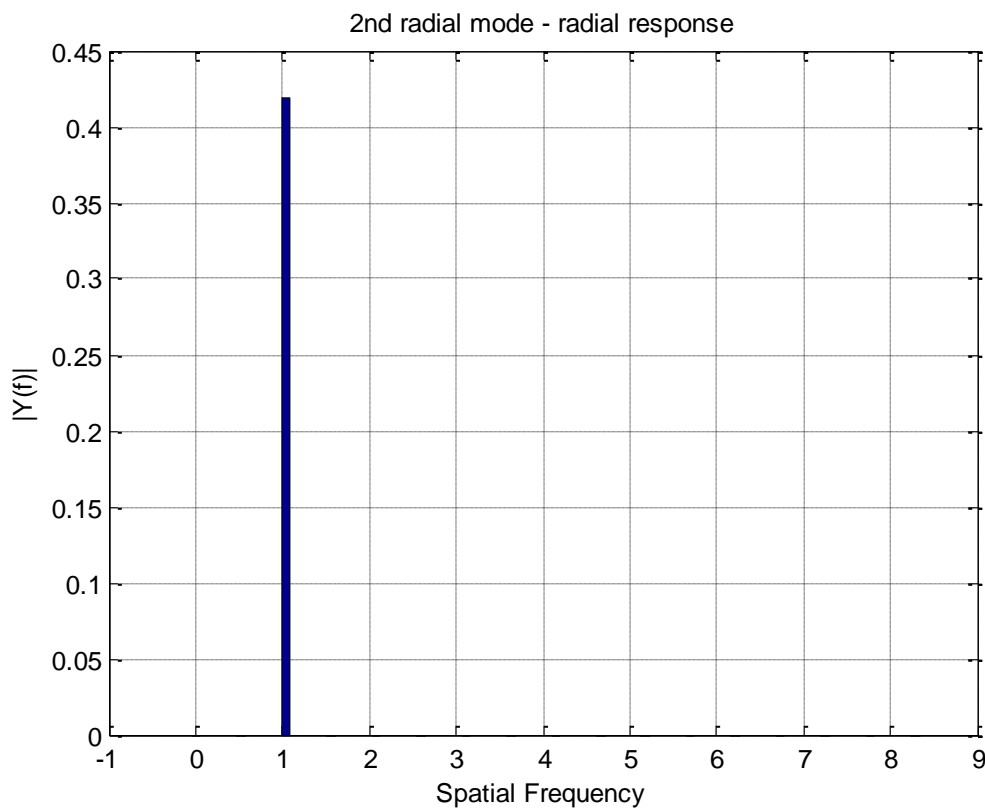


Figure 4.47 – Application of equations 4.4–39 and 4.4–40 in the spatial frequency spectrum of Figure 4.46

The main drawback of this digital filtering approach is that manufacturing asymmetries – which would manifest as secondary spatial waveforms – are excluded from the final reconstructed waveform, as the filtering algorithm does not distinguish between spatial noise induced by experimental error and actual tyre response. Nevertheless, the new spectrum of

each waveform, along with implementation of the Inverse Fast Fourier Transformation, yield smooth and digitally filtered mode shapes, presented in the following figures:

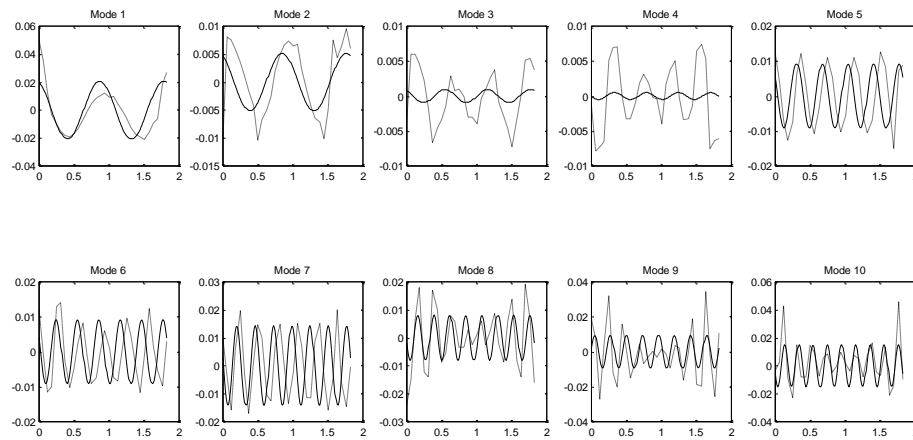


Figure 4.48 – Radial response of radially excited modes, comparison of original (dotted lines) and filtered (solid lines) waveforms (starting from the left, top row: modes 1 to 5, bottom row: modes 6 to 10)

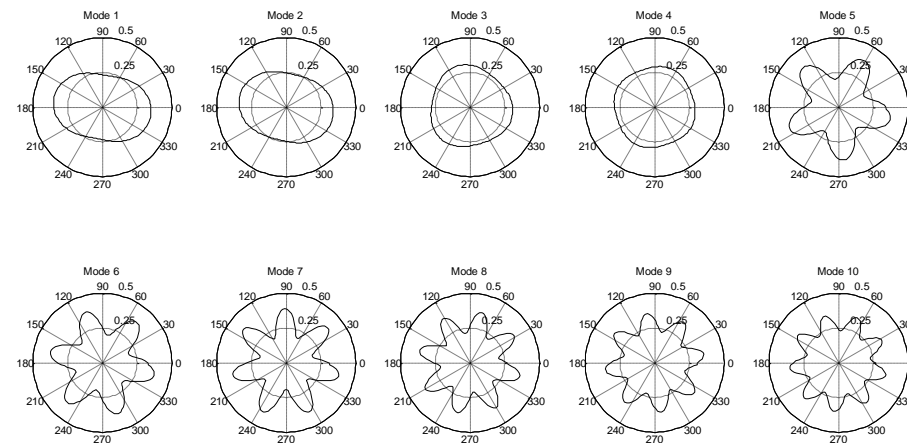


Figure 4.49 – Radial response of radially excited modes (starting from the left, top row: modes 1 to 5, bottom row: modes 6 to 10)

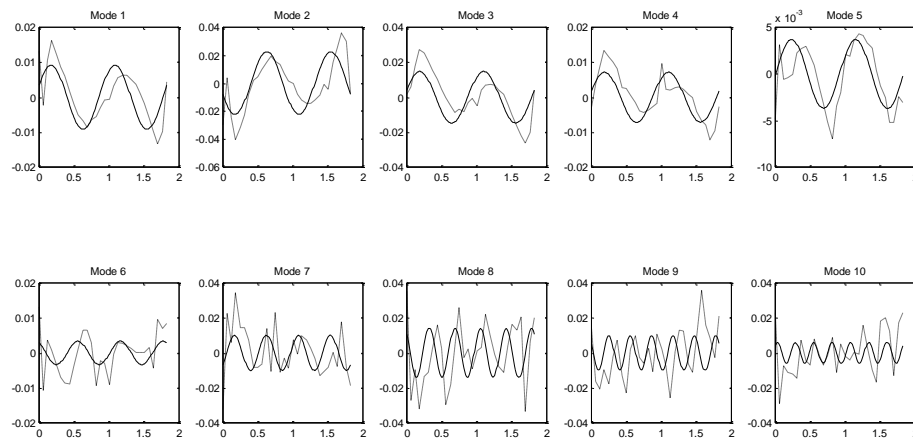


Figure 4.50 – Tangential response of radially excited modes, comparison of original (dotted lines) and filtered (solid lines) waveforms (starting from the left, top row: modes 1 to 5, bottom row: modes 6 to 10)

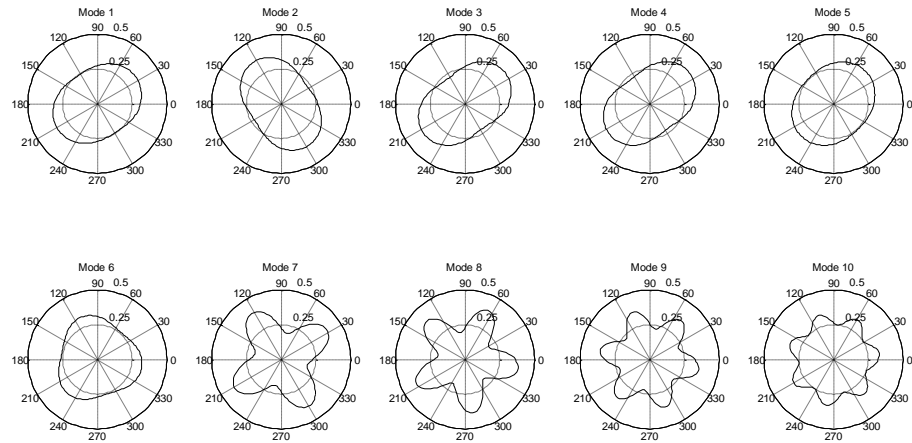


Figure 4.51 – Tangential response of radially excited modes (starting from the left, top row: modes 1 to 5, bottom row: modes 6 to 10)

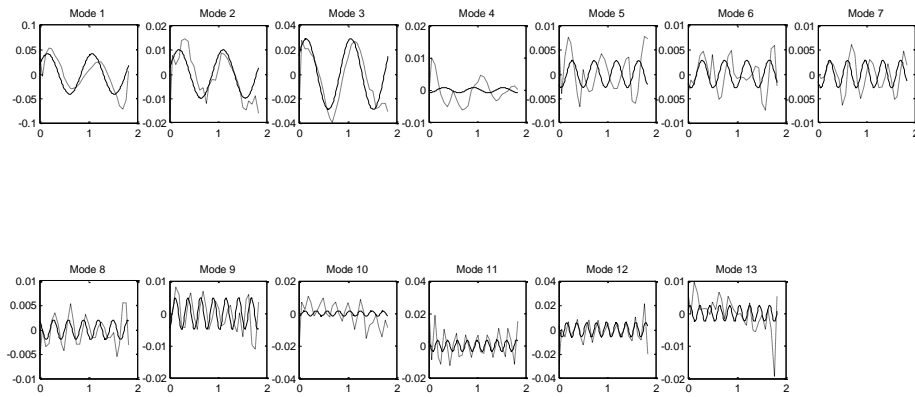


Figure 4.52 – Radial response of tangentially excited modes, comparison of original (dotted lines) and filtered (solid lines) waveforms (starting from the left, top row: modes 1 to 7, bottom row: modes 8 to 13)

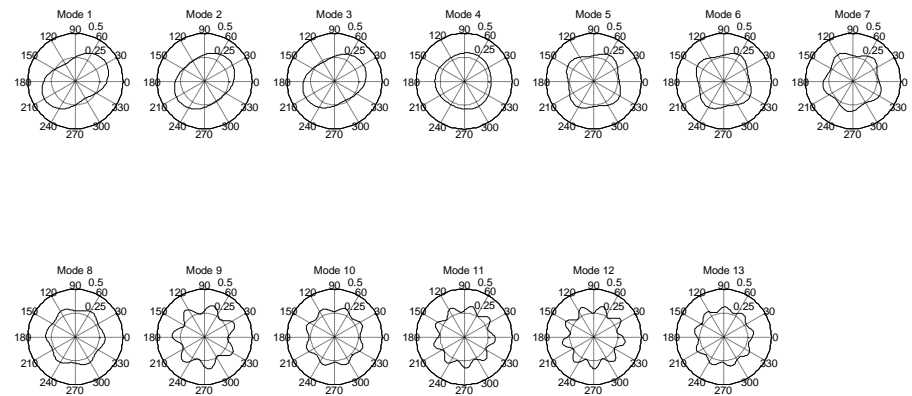


Figure 4.53 – Radial response of tangentially excited modes (starting from the left, top row: modes 1 to 7, bottom row: modes 8 to 13)

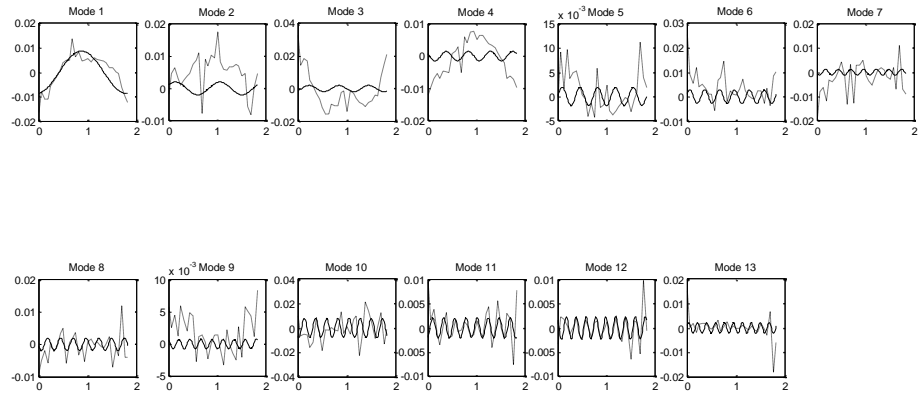


Figure 4.54 – Tangential response of tangentially excited modes, comparison of original (dotted lines) and filtered (solid lines) waveforms (starting from the left, top row: modes 1 to 7, bottom row: modes 8 to 13)

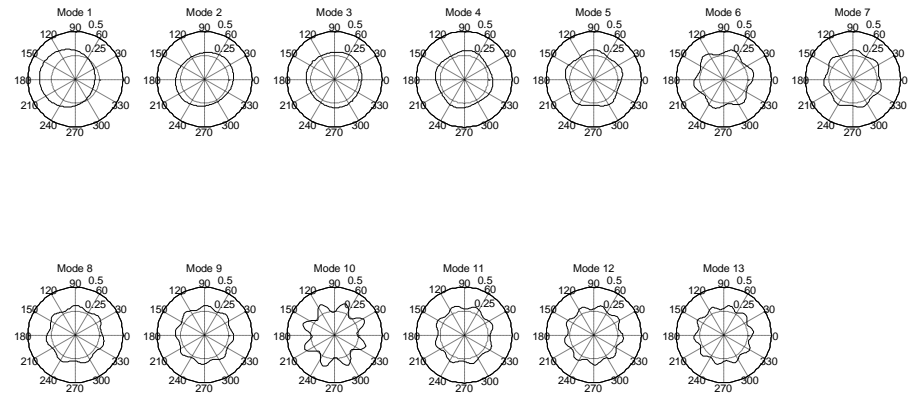


Figure 4.55 – Tangential response of tangentially excited modes (starting from the left, top row: modes 1 to 7, bottom row: modes 8 to 13)

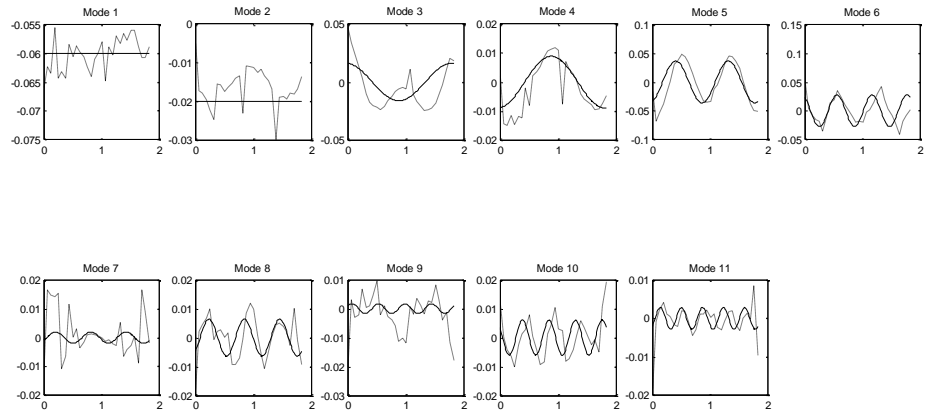


Figure 4.56 – Real lateral mode shapes, comparison of original (dotted lines) and filtered (solid lines) waveforms (starting from the left, top row: modes 1 to 6, bottom row: modes 7 to 11)

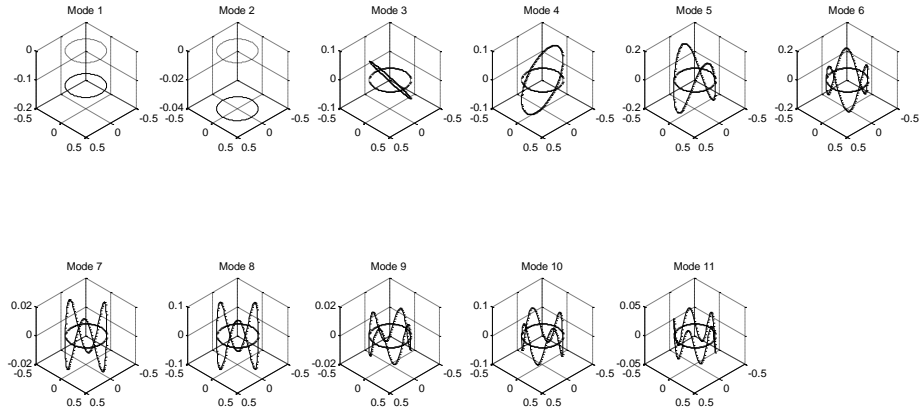


Figure 4.57 – Real lateral mode shapes (starting from the left, top row: modes 1 to 6, bottom row: modes 7 to 11)

It should be noted that tangential response has been illustrated as radial deformation in Figure 4.51 and Figure 4.55, for clarity purposes.

The above smooth mode shapes coupled with the complex phase component of the initial experimentally identified modes result in a new set of complex modes, capable of being used in the tyre model presented in the previous chapter. In addition, the reconstructed mode shapes may be evaluated in tyre belt centreline locations other than the initial 30 nodes, a process which results in reconstructed mode shapes demonstrating an artificial increase in the spatial degrees of freedom. This enhanced representation of the tyre belt is a key element for the contact sub-model as the discretisation of – vertical or shear – contact forces is significantly finer and close to reality, compared to the case where the tyre is only represented by 30 circumferential nodes. Nevertheless, the main limitation of this approach is the phase discretisation, as phasing information is only obtained for the initial 30 nodes. Consequently, the complex phase component of the reconstructed nodes is equal to the complex phase component of the closest original node.

The methods and the procedures presented in the sections above are summarised in the following flowchart (for the case of in-plane modes only; however, an equivalent approach is applied to out-of-plane modes as well), which is divided into three distinct parts: part (A) demonstrates the purely experimental part presented in Section 4.3, part (B) describes the identification of modal properties of Sections 4.4.1 to 4.4.3, and part (C) refers to the digital filtering of the current section:

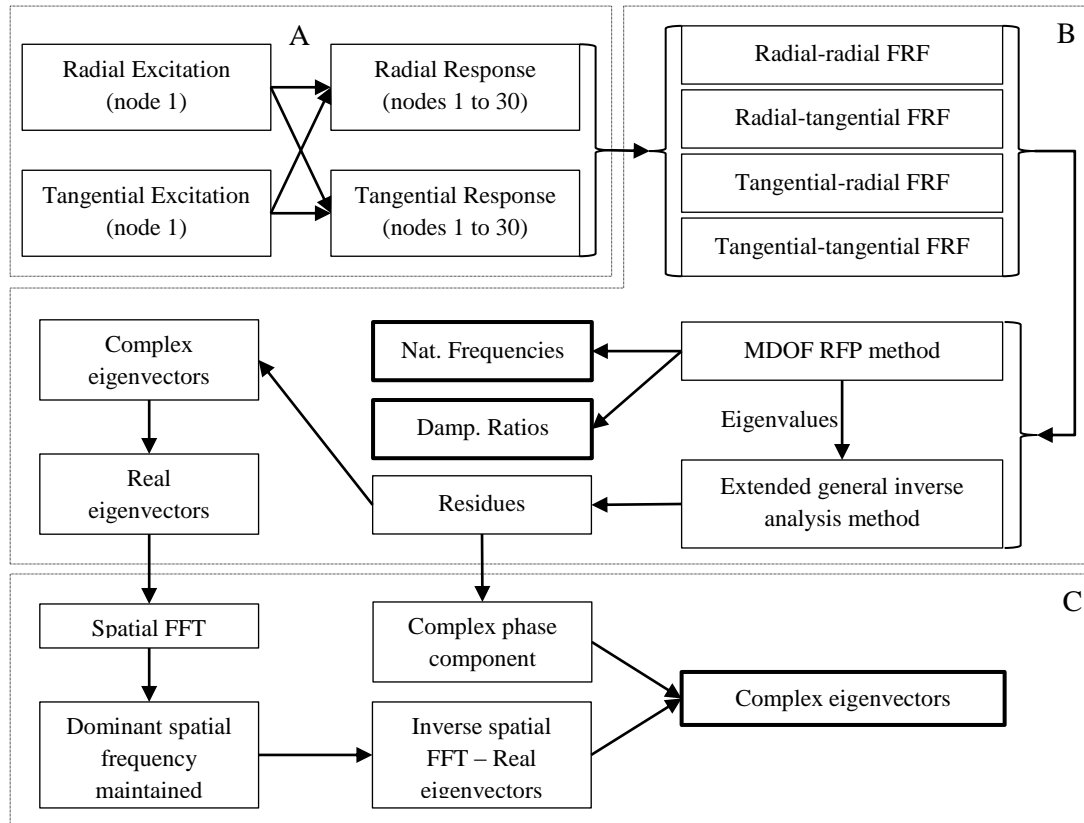


Figure 4.58 – Flowchart describing the identification process of in-plane structural tyre belt modes

#### 4.4.5 From radial/tangential to wheel-fixed coordinates

Due to the geometry of the tyre belt, the eigenvectors identified in the previous sections are expressed with respect to the radial/tangential/lateral (rtl) node-specific frame of reference of Figure 4.21. Inspection of Equation 3.3–25 reveals the necessity to transform these eigenvectors to another node-specific frame of reference (xyz), oriented in parallel to the wheel-fixed Cartesian frame of reference defined in Chapter 3. This section is dedicated to presenting the adopted approach. As has been demonstrated above, the deformation of the structure, as a result of a three-dimensional force vector acting on the first node, is obtained via the receptance FRF matrix of Equation 4.2–9:

$$\begin{bmatrix} \begin{pmatrix} r^{X_1} \\ l^{X_1} \\ t^{X_1} \end{pmatrix} \\ \begin{pmatrix} r^{X_2} \\ l^{X_2} \\ t^{X_2} \end{pmatrix} \\ \vdots \\ \begin{pmatrix} r^{X_N} \\ l^{X_N} \\ t^{X_N} \end{pmatrix} \end{bmatrix} = \begin{bmatrix} \alpha_{1,1} & 0 & \alpha_{1,3} \\ 0 & \alpha_{2,2} & 0 \\ \alpha_{3,1} & 0 & \alpha_{3,3} \\ \alpha_{4,1} & 0 & \alpha_{4,3} \\ 0 & \alpha_{5,2} & 0 \\ \alpha_{6,1} & 0 & \alpha_{6,3} \\ \vdots & \vdots & \vdots \\ \alpha_{3N-2,1} & 0 & \alpha_{3N-2,3} \\ 0 & \alpha_{3N-1,2} & 0 \\ \alpha_{3N,1} & 0 & \alpha_{3N,3} \end{bmatrix}_{3N \times 3} \cdot \begin{pmatrix} r^{F_1} \\ l^{F_1} \\ t^{F_1} \end{pmatrix} \Rightarrow$$

$$\begin{bmatrix} \begin{pmatrix} r^{X_1} \\ l^{X_1} \\ t^{X_1} \end{pmatrix} \\ \begin{pmatrix} r^{X_2} \\ l^{X_2} \\ t^{X_2} \end{pmatrix} \\ \vdots \\ \begin{pmatrix} r^{X_N} \\ l^{X_N} \\ t^{X_N} \end{pmatrix} \end{bmatrix} = \mathbf{H}_{rlt} \cdot \begin{pmatrix} r^{F_1} \\ l^{F_1} \\ t^{F_1} \end{pmatrix} \quad 4.4-41$$

Similarly, the tyre belt deformation with respect to the wheel-fixed coordinate system is obtained by an equivalent equation:

$$\begin{bmatrix} \begin{pmatrix} x^{X_1} \\ y^{X_1} \\ z^{X_1} \end{pmatrix} \\ \begin{pmatrix} x^{X_2} \\ y^{X_2} \\ z^{X_2} \end{pmatrix} \\ \vdots \\ \begin{pmatrix} x^{X_N} \\ y^{X_N} \\ z^{X_N} \end{pmatrix} \end{bmatrix} = \mathbf{H}_{xyz} \cdot \begin{pmatrix} x^{F_1} \\ y^{F_1} \\ z^{F_1} \end{pmatrix} \quad 4.4-42$$

The transformation matrix between these two frames of reference depends on the position of each node. By denoting as  $a_i$  the angle formed by the position vector of node  $i$  and the  $x$  axis of the wheel-fixed frame of reference, the respective transformation matrix is calculated:



$$\mathbf{T}_{\mathbf{MT}_i} = \begin{bmatrix} \cos a_i & 0 & -\sin a_i \\ 0 & 1 & 0 \\ \sin a_i & 0 & \cos a_i \end{bmatrix} \quad 4.4-43$$

The transformation of the deformation vector from the rtl to the xyz coordinate system is governed by the following equation:

$$\begin{bmatrix} \begin{pmatrix} x^{X_1} \\ y^{X_1} \\ z^{X_1} \end{pmatrix} \\ \begin{pmatrix} x^{X_2} \\ y^{X_2} \\ z^{X_2} \end{pmatrix} \\ \vdots \\ \begin{pmatrix} x^{X_N} \\ y^{X_N} \\ z^{X_N} \end{pmatrix} \end{bmatrix} = \begin{bmatrix} \mathbf{T}_{\mathbf{MT}_1} & & \\ & \mathbf{T}_{\mathbf{MT}_2} & \\ & & \ddots \\ & & & \mathbf{T}_{\mathbf{MT}_N} \end{bmatrix} \begin{bmatrix} \begin{pmatrix} r^{X_1} \\ l^{X_1} \\ t^{X_1} \end{pmatrix} \\ \begin{pmatrix} r^{X_2} \\ l^{X_2} \\ t^{X_2} \end{pmatrix} \\ \vdots \\ \begin{pmatrix} r^{X_N} \\ l^{X_N} \\ t^{X_N} \end{pmatrix} \end{bmatrix} \Rightarrow$$

$$\begin{bmatrix} \begin{pmatrix} r^{X_1} \\ l^{X_1} \\ t^{X_1} \end{pmatrix} \\ \begin{pmatrix} r^{X_2} \\ l^{X_2} \\ t^{X_2} \end{pmatrix} \\ \vdots \\ \begin{pmatrix} r^{X_N} \\ l^{X_N} \\ t^{X_N} \end{pmatrix} \end{bmatrix} = \begin{bmatrix} \mathbf{T}_{\mathbf{MT}_1} & & \\ & \mathbf{T}_{\mathbf{MT}_2} & \\ & & \ddots \\ & & & \mathbf{T}_{\mathbf{MT}_N} \end{bmatrix}^{-1} \begin{bmatrix} \begin{pmatrix} x^{X_1} \\ y^{X_1} \\ z^{X_1} \end{pmatrix} \\ \begin{pmatrix} x^{X_2} \\ y^{X_2} \\ z^{X_2} \end{pmatrix} \\ \vdots \\ \begin{pmatrix} x^{X_N} \\ y^{X_N} \\ z^{X_N} \end{pmatrix} \end{bmatrix} \quad 4.4-44$$

Moreover, with regard to the force vectors of Equations 4.4–41 and 4.4–42, the following expression holds:

$$\begin{pmatrix} x^{F_1} \\ y^{F_1} \\ z^{F_1} \end{pmatrix} = \mathbf{T}_{\mathbf{MT}_1} \begin{pmatrix} r^{F_1} \\ l^{F_1} \\ t^{F_1} \end{pmatrix} \Rightarrow$$

$$\begin{Bmatrix} rF_1 \\ lF_1 \\ tF_1 \end{Bmatrix} = (\mathbf{T}_{MT1})^{-1} \begin{Bmatrix} xF_1 \\ yF_1 \\ zF_1 \end{Bmatrix} \quad 4.4-45$$

Since the position vector of the first node, which is the application node of the force vector, lies along the x axis of the xyz coordinate system, angle  $a_1$  is equal to zero and the respective transformation matrix of the first node becomes:

$$\mathbf{T}_{MT1} = \begin{bmatrix} 1 & 0 & 0 \\ 0 & 1 & 0 \\ 0 & 0 & 1 \end{bmatrix} \quad 4.4-46$$

Substitution of Equation 4.4-46 in Equation 4.4-45 yields the following expression for the first node:

$$\begin{Bmatrix} rF_1 \\ lF_1 \\ tF_1 \end{Bmatrix} = \begin{Bmatrix} xF_1 \\ yF_1 \\ zF_1 \end{Bmatrix} \quad 4.4-47$$

Combination of Equations 4.4-41, 4.4-44 and 4.4-47 yields:

$$\begin{bmatrix} \mathbf{T}_{MT1} & & & \\ & \mathbf{T}_{MT2} & & \\ & & \ddots & \\ & & & \mathbf{T}_{MTN} \end{bmatrix}^{-1} \begin{bmatrix} \begin{Bmatrix} xX_1 \\ yX_1 \\ zX_1 \end{Bmatrix} \\ \begin{Bmatrix} xX_2 \\ yX_2 \\ zX_2 \end{Bmatrix} \\ \vdots \\ \begin{Bmatrix} xX_N \\ yX_N \\ zX_N \end{Bmatrix} \end{bmatrix} = \mathbf{H}_{rlt} \begin{Bmatrix} xF_1 \\ yF_1 \\ zF_1 \end{Bmatrix} \Rightarrow$$

$$\begin{bmatrix} \begin{pmatrix} x^{X_1} \\ y^{X_1} \\ z^{X_1} \end{pmatrix} \\ \begin{pmatrix} x^{X_2} \\ y^{X_2} \\ z^{X_2} \end{pmatrix} \\ \vdots \\ \begin{pmatrix} x^{X_N} \\ y^{X_N} \\ z^{X_N} \end{pmatrix} \end{bmatrix} = \begin{bmatrix} \mathbf{T}_{MT1} & & \\ & \mathbf{T}_{MT2} & \\ & & \ddots \\ & & & \mathbf{T}_{MTN} \end{bmatrix} \mathbf{H}_{rlt} \begin{pmatrix} x^{F_1} \\ y^{F_1} \\ z^{F_1} \end{pmatrix} \quad 4.4-48$$

Comparison between 4.4-42 and 4.4-48 reveals the following relation for the receptance FRF matrix expressed in the xyz coordinate system:

$$\mathbf{H}_{xyz} = \begin{bmatrix} \mathbf{T}_{MT1} & & \\ & \mathbf{T}_{MT2} & \\ & & \ddots \\ & & & \mathbf{T}_{MTN} \end{bmatrix} \mathbf{H}_{rlt} \quad 4.4-49$$

Inspection of the above expression, for an arbitrary node i, yields:

$$\begin{bmatrix} H_{x_i x_1} & 0 & H_{x_i z_1} \\ 0 & H_{y_i y_1} & 0 \\ H_{z_i x_1} & 0 & H_{z_i z_1} \end{bmatrix} = \begin{bmatrix} \cos a_i & 0 & -\sin a_i \\ 0 & 1 & 0 \\ \sin a_i & 0 & \cos a_i \end{bmatrix} \begin{bmatrix} H_{r_i r_1} & 0 & H_{r_i t_1} \\ 0 & H_{y_i y_1} & 0 \\ H_{t_i r_1} & 0 & H_{t_i t_1} \end{bmatrix} \quad 4.4-50$$

The first element of the matrix located in the left hand side of the above equation is equal to:

$$H_{x_i x_1} = \sum_{j=1}^m \left[ \frac{\Psi_{x_1 j} \Psi_{x_i j}}{s - s_j} + \frac{\Psi_{x_1 j}^* \Psi_{x_i j}^*}{s - s_j^*} \right] \quad 4.4-51$$

A second expression for that particular element may be obtained from equation 4.4-50:

$$H_{x_i x_1} = \cos a_i H_{r_i r_1} - \sin a_i H_{t_i r_1} \Rightarrow$$

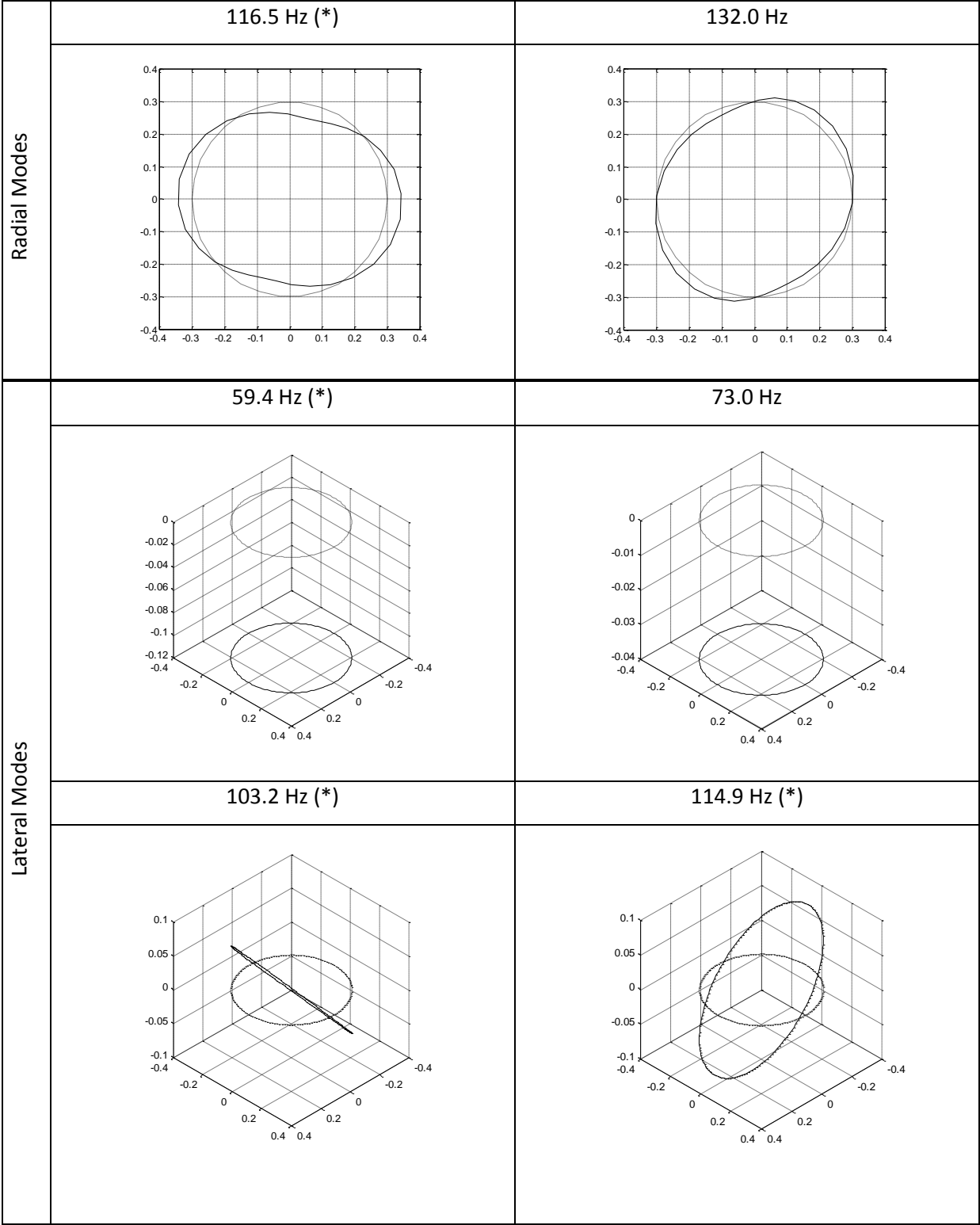
$$\begin{aligned}
& \sum_{j=1}^m \left[ \frac{\Psi_{x1j} \Psi_{x1j}}{s - s_j} + \frac{\Psi_{x1j}^* \Psi_{x1j}^*}{s - s_j^*} \right] = \\
& \cos a_i \sum_{j=1}^m \left[ \frac{\Psi_{r1j} \Psi_{r1j}}{s - s_j} + \frac{\Psi_{r1j}^* \Psi_{r1j}^*}{s - s_j^*} \right] - \sin a_i \sum_{j=1}^m \left[ \frac{\Psi_{r1j} \Psi_{t1j}}{s - s_j} + \frac{\Psi_{r1j}^* \Psi_{t1j}^*}{s - s_j^*} \right] \Rightarrow \\
& \sum_{j=1}^m \left[ \frac{\Psi_{x1j} \Psi_{x1j}}{s - s_j} + \frac{\Psi_{x1j}^* \Psi_{x1j}^*}{s - s_j^*} \right] = \\
& \sum_{j=1}^m \left[ \frac{\cos a_i \Psi_{r1j} \Psi_{r1j}}{s - s_j} + \frac{\cos a_i \Psi_{r1j}^* \Psi_{r1j}^*}{s - s_j^*} \right] - \sum_{j=1}^m \left[ \frac{\sin a_i \Psi_{r1j} \Psi_{t1j}}{s - s_j} + \frac{\sin a_i \Psi_{r1j}^* \Psi_{t1j}^*}{s - s_j^*} \right] \Rightarrow \\
& \sum_{j=1}^m \left[ \frac{\Psi_{x1j} \Psi_{x1j}}{s - s_j} + \frac{\Psi_{x1j}^* \Psi_{x1j}^*}{s - s_j^*} \right] = \\
& \sum_{j=1}^m \left[ \frac{\cos a_i \Psi_{r1j} \Psi_{r1j} - \sin a_i \Psi_{r1j} \Psi_{t1j}}{s - s_j} + \frac{\cos a_i \Psi_{r1j}^* \Psi_{r1j}^* - \sin a_i \Psi_{r1j}^* \Psi_{t1j}^*}{s - s_j^*} \right]
\end{aligned} \tag{4.4-52}$$

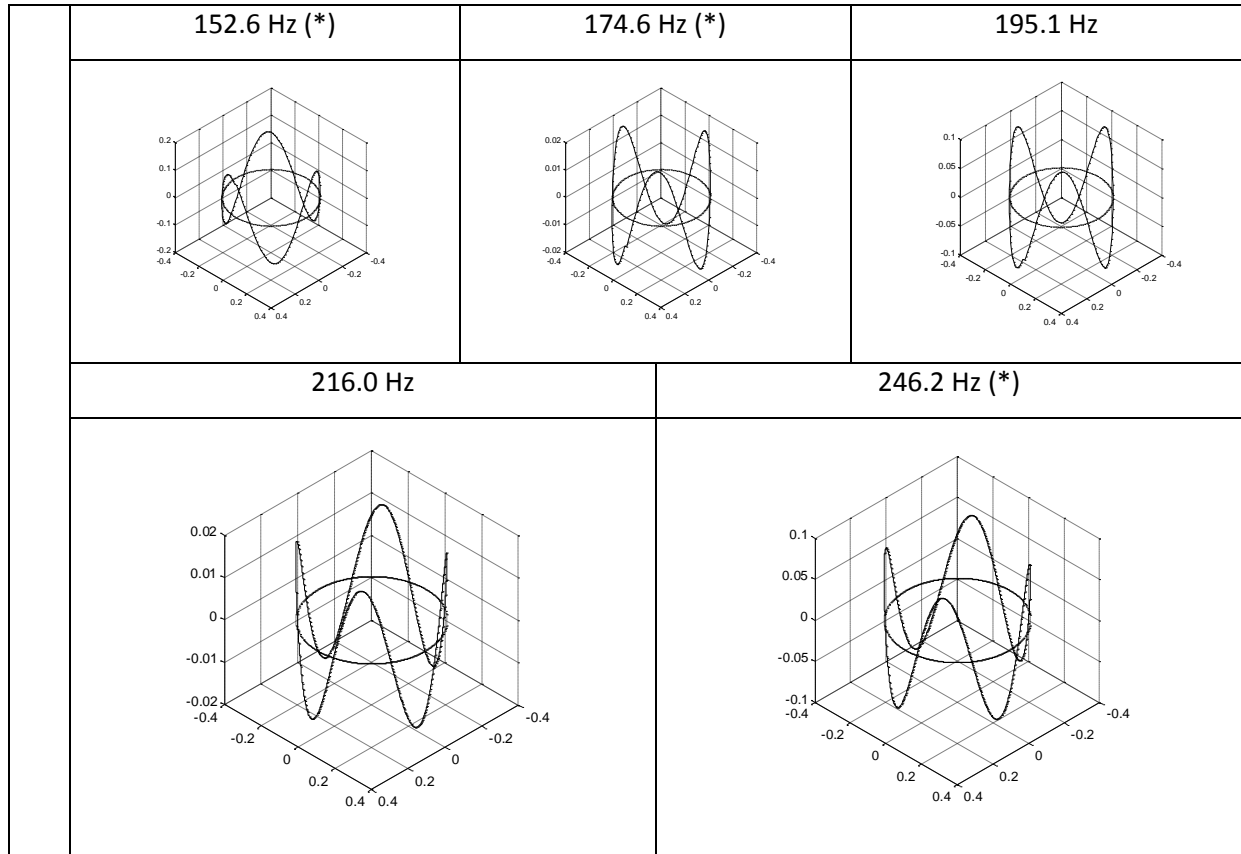
Examination of Equation 4.4–52 and application of the above approach to every element in the left hand side of equation 4.4–50 yield the respective expressions for the calculation of the transformed eigenvector components. The key point of the above procedure is that the experimentally identified residues – expressed in the radial/tangential frame of reference – can easily be transformed into the xyz frame of reference given the position, i.e. angle  $a_i$ , of each belt node, starting from the driving point to initially identify  $\Psi_{x1j}$  and  $\Psi_{z1j}$ . Due to the lateral axis of the radial/tangential frame of reference being parallel to the y axis of the xyz frame of reference, no transformation is needed for the respective eigenvector components.

#### 4.4.6 Apparent repeated mode shapes

Visual inspection of the modal testing results presented in Section 4.4.4 reveals a series of repeated mode shapes which are not in accordance with previously conducted analytical<sup>[110]</sup> and experimental<sup>[116]</sup> research. Since it is not consistent for two or more modes associated with two or more natural frequencies to demonstrate mode shapes of equal spatial frequency, one concludes that the state of the tyre/rim assembly should include distinct characteristics for those cases. To further investigate those characteristics, the motion of the rim has been acquired and analysed, in order to experimentally verify the existence of rim modes coinciding with belt modes. The following table summarises the correlation between each case of repeated modes and the respective rim resonances, denoted by (\*). For each case of repeated

mode shapes, there is one – at most – instance of exclusive belt deformation. The remaining instances include rim motion and/or deformation along with belt deformation and as a result they demonstrate a different tyre/rim state compared to the case of exclusive belt deformation, a finding which is in accordance with previous results<sup>[110] [116]</sup>.





#### 4.4.7 Multiple modes

There are certain configurations of the belt nodes – within the frequency band dictated by the maximum identified natural frequency – which cannot be expressed as a linear combination of the identified modes. As is described in [30], axisymmetric structures demonstrate multiple modes, i.e. two modes occurring at the same natural frequency. For the experimental layout employed in the present work only one mode can be identified, for a given natural frequency.

These non-identifiable modes are estimated by adopting an analytical approach, which will be demonstrated in detail for the simple case of the first real radial mode. The exact same method has been applied to the remaining modes. As has been analysed in Chapter 3, the relation between each mode and the physical coordinates of a structure is expressed by the following equation:

$$\{dx\} = dq_r \{\psi_r\} \quad 4.4-53$$

where  $\{\psi\}_r$  is the eigenvector of mode  $r$ ,  $dq_r$  is the associated modal participation factor and  $\{dx\}$  is the vector containing the respective physical deformation of each degree of freedom.

The value of the modal participation factor controls how each eigenvector – only the first real radial one in this particular case of demonstration – contributes to the total deformation state of the tyre belt, a relation which is depicted in the following figure:

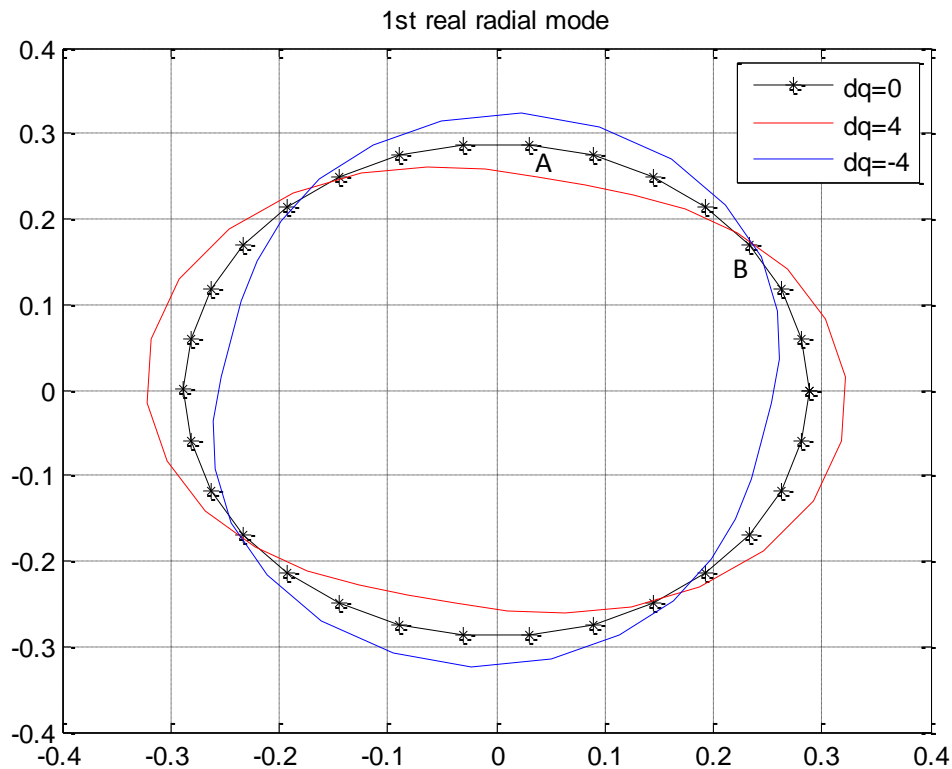


Figure 4.59 – Illustration of the real mode shapes, corresponding to the first radial mode, calculated for a positive and a negative modal participation factor

It is evident that, for  $dq \in (-\infty, \infty)$ , point A will always be the point where the maximum deformation occurs while point B will always remain stationary. This observation derives from the exclusive use of this particular eigenvector, which is not able to account for any alternative deformation pattern. To overcome this problematic situation, a second eigenvector (corresponding to the same eigenvalue) has been introduced. This new eigenvector is orthogonal to the experimentally identified one and it is calculated by rotating the original eigenvector by a certain angle. The exact value of this angle depends on the number of peaks demonstrated by the mode shape, i.e. the number of points similar to point A in the above figure, and it is the one which will reverse the deformation pattern between points A and B; with reference to the analytically calculated orthogonal eigenvector, the new point A will always remain stationary while point B will demonstrate the maximum deformation for any given  $dq$ . If  $p_1$  is the number of peaks observed in the first real radial mode shape, then the associated rotation angle is obtained by the following expression:

$$\delta\phi_1 = 2\pi/4p_1 \Rightarrow$$

$$\delta\phi_1 = \pi/2p_1 \quad 4.4-54$$

which yields  $\delta\phi_1 = 0.785 \text{ rad} = 45^\circ$  for  $p_1=2$ . Having calculated the rotation angle, the following equation holds for the new orthogonal eigenvector:

$$\{\psi_1\}_{\text{orth}} = \mathbf{T}_{\text{tot}}\{\psi_1\} \quad 4.4-55$$

where  $\mathbf{T}_{\text{tot}}$  is the total transformation matrix:

$$\mathbf{T}_{\text{tot}} = \begin{bmatrix} \mathbf{T}_{\text{orth}} & 0 & 0 \\ 0 & \mathbf{T}_{\text{orth}} & 0 \\ 0 & 0 & \mathbf{T}_{\text{orth}} \end{bmatrix} \quad 4.4-56$$

and  $\mathbf{T}_{\text{orth}}$  is the transformation matrix of each node containing the rotation angle  $\delta\phi_1$ :

$$\mathbf{T}_{\text{orth}} = \begin{bmatrix} \cos(\delta\phi_1) & 0 & -\sin(\delta\phi_1) \\ 0 & 1 & 0 \\ \sin(\delta\phi_1) & 0 & \cos(\delta\phi_1) \end{bmatrix} \quad 4.4-57$$

Consequently, Equation 4.4-53 is extended to include the new additional eigenvector as follows:

$$\{dx\} = \overbrace{dq_1\{\psi_1\}}^A + \overbrace{dq_1^{\text{orth}}\{\psi_1\}_{\text{orth}}}^B \quad 4.4-58$$

The effect of each term in Equation 4.4-58 is demonstrated in the following diagram where modal participation factors ( $dq_1$  and  $dq_1^{\text{orth}}$ ) are both set equal to 4:



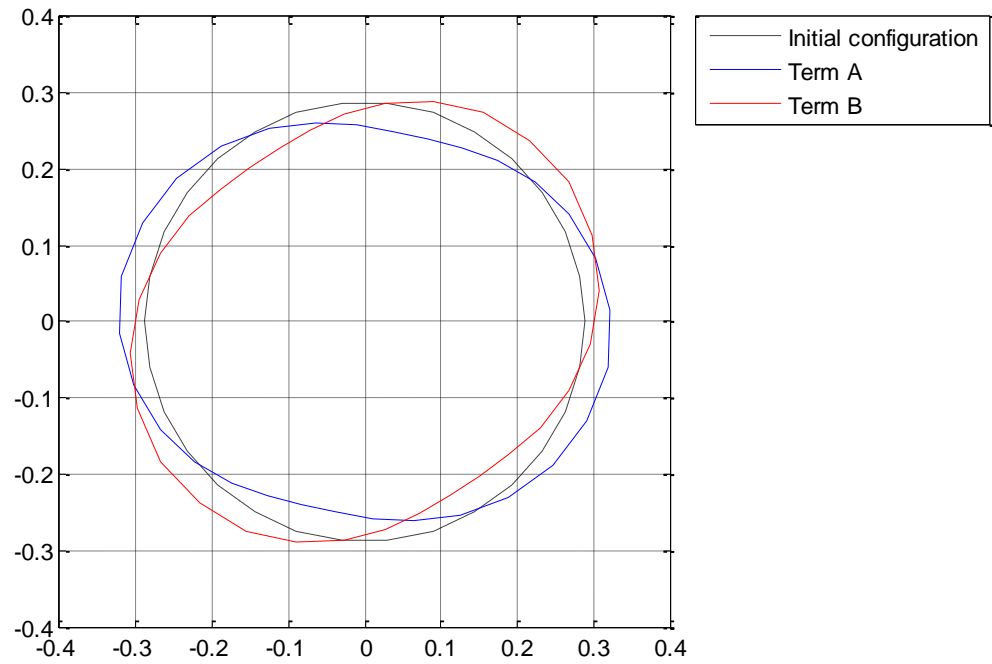


Figure 4.60 – First radial mode: comparison between the experimentally identified real mode shape (term A) and the calculated orthogonal one (term B)

By comparing the two deformed states of the tyre belt in Figure 4.60 – terms A and B respectively – it is evident that the nodes demonstrating the minimum deformation in term A are the ones which exhibit the maximum deformation in term B. Therefore, Equation 4.4–58 is able to describe every possible nodal configuration corresponding to the first real radial mode.

## 5. Tyre model validation

### 5.1 Introduction

The validation of the proposed tyre modelling approach is presented in the following sections and is conducted by comparing simulation results to either literature or experimental data, for the following three scenarios:

- Vertical stiffness
- Transient lateral slip for varying longitudinal speed
- Transient lateral slip for varying vertical load

These scenarios have been selected on the basis that they capture various phenomena related to tyre deformation and they allow for demonstrating the proposed model capability in including belt flexibility in the tyre response.

With regard to the first scenario, namely tyre vertical stiffness, it is noteworthy that it highlights the model capability in terms of modelling flexible belt dynamics. In addition, this particular test scenario exposes the current fundamental limitations of the proposed tyre modelling approach, which are inherited from the nature of the conducted modal testing and also from the performed modal reduction, as is described by the modal matrix in Equation 3.3–13. Initially, in Section 5.3.2, tyre vertical stiffness is investigated for a series of tyre belt fidelity cases, under the application of the same vertical load range. This process is performed exclusively within the virtual environment developed in this work. Sections 5.3.3 and 5.3.4 are dedicated to data acquisition and to comparing these experimental data to simulation results, respectively. The experimental facility used to obtain the experimental data, which consist of the vertical position of the wheel centre and the applied vertical force, is presented in Section 5.2.

For the remaining two test cases, namely transient lateral slip tyre behaviour as a function of longitudinal speed and vertical load, the tyre response and the influence of the flexible belt dynamics are compared against trends obtained from the literature, due to limitations imposed by the available experimental facility during the conduction of the present work.

## 5.2 Experimental layout

The required experimental data acquisition for the vertical stiffness test scenario has been conducted using the indoor tyre rig developed by the Department of Aeronautical and Automotive Engineering, Loughborough University, which is depicted in Figure 5.1. The selection of this particular indoor facility – over an outdoor one – is based on the necessity to perform each test in as controlled conditions as possible. In outdoor rigs, factors beyond control (i.e. road contamination or different types of road surface) may jeopardise the quality of the acquired data. As these tests have been replicated by the tyre model in a virtual environment, non-controlled experimental conditions could lead to false conclusions with respect to the validity of the modelling approach.

In this particular rig, during typical operation, the tyre is pressed against a rotating steel drum. Similarly to the tyre model demonstrated in the present work, the user-defined tyre testing input parameters are as follows:

- vertical load, via the application of hydraulic force
- manual adjustment of the tyre slip angle
- drum angular velocity
- brake hydraulic pressure

In terms of data acquisition, the rig incorporates an array of sensors and strain gauges, so as the following quantities are measured during each run:

- slip angle
- vertical load
- longitudinal force
- lateral force
- tread temperature
- angular velocity
- vertical deformation



Figure 5.1 – Indoor tyre testing facility (photograph courtesy of the Department of Aeronautical and Automotive Engineering, Loughborough University)

## 5.3 Vertical stiffness

### 5.3.1 Theoretical and experimental background

Typically, tyre vertical stiffness is calculated by applying a vertical force on the wheel centre and measuring the resulting vertical deflection. The available literature has been summarised and presented by V. Alkan et al. in [3]. In general, pneumatic tyre vertical stiffness is mainly dependent on tyre structure and testing parameters, i.e. rotational velocity, inflation pressure, shear force generation and camber angle<sup>[41]</sup>.

Tyre vertical stiffness ( $C_{F_z}$ ) is equal to the ratio of an infinitesimal change in vertical force ( $\partial F_z$ ) over the resulting infinitesimal change in vertical position ( $\partial z$ )<sup>[15]</sup>:

$$C_{F_z} = \frac{\partial F_z}{\partial z} \quad 5.3-1$$

This ratio demonstrates a non-linear behaviour for higher load and deflection combinations, as is presented in the experimental work of R. K. Taylor et al. in [105] on agricultural tyres and in the work of K. Ramji et al. in [90] on small-sized pneumatic tyres, with the latter being more relevant to the present study. Investigation on this field has also been conducted by I. J. M. Besselink et al. ([15]), where the cases of the stationary and the rotating tyre have been compared in terms of vertical stiffness, for both conventional and run-flat tyres. In that particular work, the non-linear nature of the vertical force / vertical displacement relationship is experimentally confirmed, as expected. It should be noted that this non-linearity is

significantly more apparent and evident for the case of run-flat tyres compared to conventional ones.

Several proposed approaches, which allow for modelling vertical stiffness related phenomena, may be found in the literature. As this is one of the fundamental requirements for structural dynamics and NVH studies, tyre models focused on these fields incorporate vertical flexible tyre dynamics<sup>[8][28]</sup>. In [41], P. Gruber et al. present a finite element tyre model which is compared against experimental data for the case of vertical stiffness. In that particular work, emphasis was placed on the influence of camber angle and friction on the tyre vertical stiffness. Correlation has been achieved for both upright and cambered tyres. G. Gim et al. have adopted a different approach<sup>[38]</sup>, namely the development of an analytical method for the calculation of the tyre vertical stiffness. Similarly to the work of P. Gruber et al, dependencies between vertical load, vertical deflection, camber angle and lateral force are examined and the resulting analytical expressions describing these phenomena consist of empirical factors. In terms of validation, good correlation is demonstrated between simulation results generated by this model and measured data.

The case of the stationary tyre is examined below, both experimentally and virtually. It should be noted that the proposed modelling approach does not fundamentally exclude the remaining factors affecting vertical stiffness; namely, friction, inflation pressure and camber angle. An extended model is required incorporating the following modifications, albeit beyond the scope of the present work:

- Contrary to the ad hoc assumption made in the present study, that there is no energy exchange between in and out-of-plane modes – see Section 4.2 – a more close to reality approach is required. A complete three dimensional modal representation of the tyre – including cross-talking between in and out-of-plane modes – would allow for communication between radial, tangential and lateral modes, and consequently the full effect of shear forces on vertical stiffness would be feasible to predict.
- Repetition of the modal testing procedure presented in Sections 4.2 to 4.4 for a range of inflation pressures and incorporation of the inflation pressure as a parameter in both the identified eigenvalues and the identified eigenvectors (although Y. Guan et al. in [45] suggest that the effect of inflation pressure on tyre belt eigenvectors is minimal) used to populate Equation 3.3–22, which – for this study – is the fundamental system of equations of motion of the tyre belt.

- Currently, the model consists of nodes which are initially located in a unique plane, that defined by global axes  $x$  and  $z$ . In order to take into account the effect of camber angle on vertical stiffness, additional nodes – located in planes offset laterally to the central one – are needed. These additional nodes would allow for capturing the lateral tread modes and consequently the vertical stiffness dependency on camber angle.
- Fundamentally, the proposed tyre model takes into account only certain tyre belt deformation modes. This limitation, which enhances the model efficiency, has a direct effect on the tyre response, as higher frequency belt modes are excluded. Moreover, the fact that the included tyre belt modes have been identified close to the nodal equilibrium position introduces a certain unreliability factor for cases of large belt deformation, the influence of which is demonstrated in the following sections.

### **5.3.2 Vertical stiffness dependency on tyre belt fidelity**

One essential asset of the proposed tyre modelling approach is the capability of adapting to varying fidelity demands by including or excluding particular flexible modes of the tyre belt, a feature which is demonstrated by Equation 3.3–12, and number  $m$  in particular which represents the number of included flexible belt modes. Similar investigations on the relation between tyre belt fidelity and vertical stiffness may be found in the literature, for example the work of A. Tsotras in [110], where the calculated vertical load is examined, for an imposed array of vertical tyre deformations and for cases of different modal reduction resulting in the following diagram:

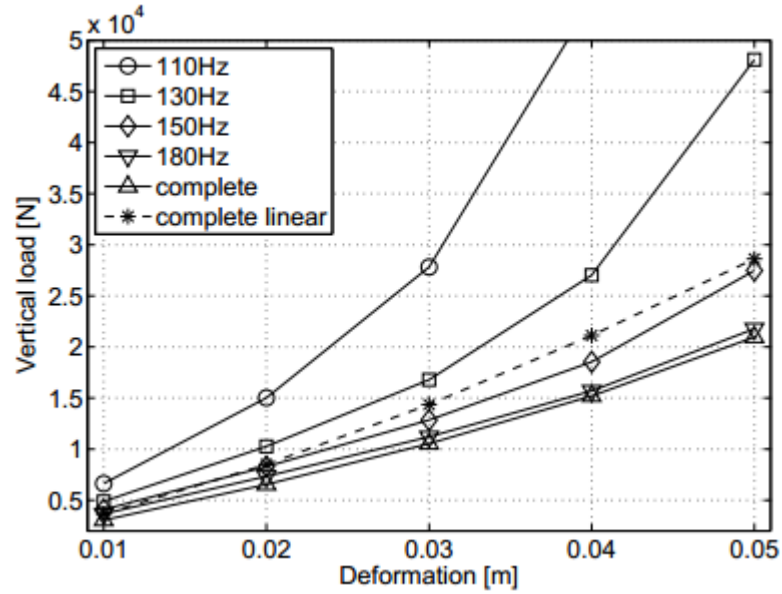


Figure 5.2 – The total vertical load as a function of the imposed deformation for various degrees of reduction ([110])

From the above figure, it is apparent that higher model fidelity results in lower vertical stiffness. The explanation for this observation is that a limited modal reduction will lead to the inclusion of additional flexible modes, and the associated effect they have on total tyre deformation, compared to cases of extensive modal reduction where the total tyre deformation is the result of the participation of a limited number of modes. In the present work, a similar investigation has been conducted. The tyre is excited by a vertical load, applied on the wheel centre, and the vertical deflection of the tyre belt is monitored for different levels of modal reduction or equivalently for varying model fidelity. The excitation signal is presented in the following figure:

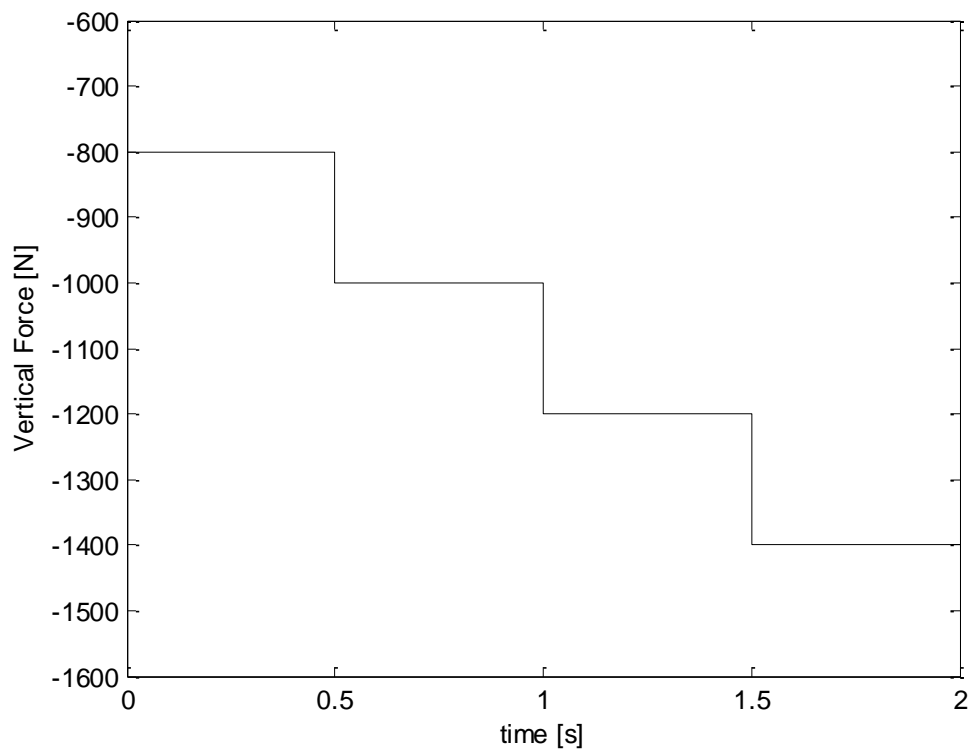


Figure 5.3 – Vertical force applied at the wheel centre

The following modal reduction cases have been examined:

Table 5.1: Modal reduction scenarios		
	Radial modes	Tangential modes
First radial mode only (115Hz)	1	0
In-plane modes up to 133Hz	2	3
In-plane modes up to 150Hz	3	4
In-plane modes up to 207Hz	5	7

For comparison purposes, vertical deformation observed for the first modal reduction case at -800N is set as the point of reference. The resulting vertical deformations for the remaining vertical loads and modal reduction cases are presented in the following table:

Table 5.2: Vertical deflection measured at the wheel centre				
Vertical deflection [mm]				
	-800N	-1000N	-1200N	-1400N
First radial mode only (115Hz)	0.00	1.34	2.63	3.68



In-plane modes up to 133Hz	0.14	1.51	2.76	3.99
In-plane modes up to 150Hz	0.16	1.52	2.77	4.03
In-plane modes up to 207Hz	0.19	1.55	2.80	4.05

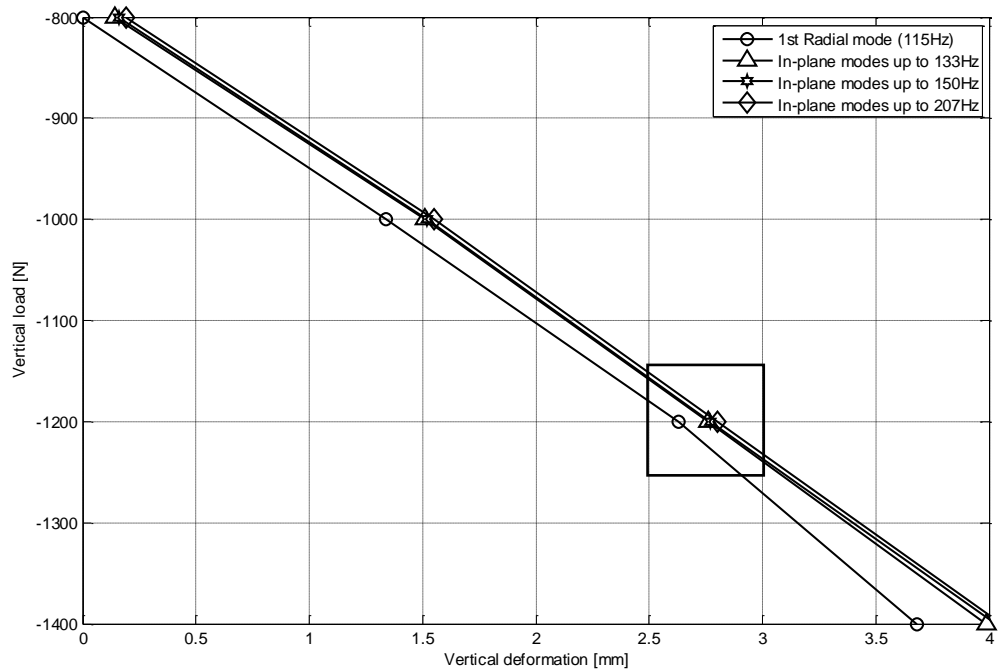


Figure 5.4 – Vertical load versus vertical deformation of the tyre belt for four cases of modal reduction

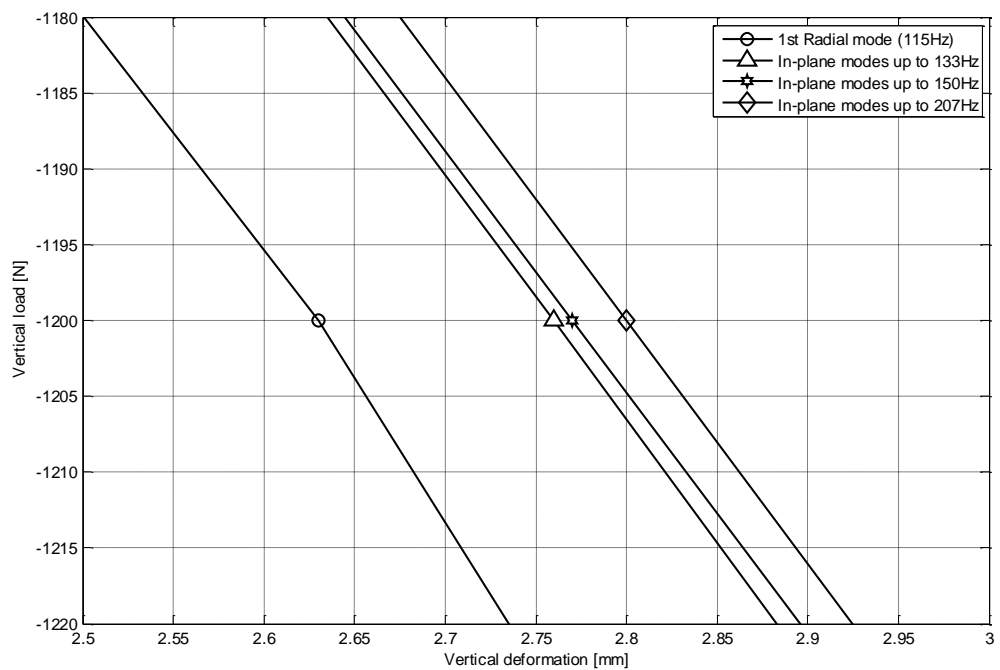


Figure 5.5 – Detail of Figure 5.4, area in the rectangle

The four test cases presented above demonstrate the effect of modal reduction to the vertical deformation of the tyre belt and, as expected, inclusion of additional modes results in increased tyre belt compliance. In addition, the impact of this phenomenon exhibits an increasing behaviour with increased vertical load, as the four curves become more separated in the higher load area (bottom right corner of Figure 5.4). In terms of vertical stiffness – as it is defined by Equation 5.3–1 – and the respective dependency on model fidelity, the four test cases analysed above yield the following values:

<b>Table 5.3: Tyre vertical stiffness dependency as a function of tyre belt fidelity</b>		
	Vertical stiffness $C_{F_z}$	$\Delta C_{F_z}$
First radial mode only (115Hz)	163N/mm	-
In-plane modes up to 133Hz	156 N/mm	4.29%
In-plane modes up to 150Hz	155 N/mm	4.91%
In-plane modes up to 207Hz	155 N/mm	4.91%

Although the imposed vertical load has been kept at minimum levels, the inclusion of additional belt modes has a direct impact on tyre vertical deformation and consequently on tyre vertical stiffness. For the cases examined in the present section, comparison of the first two cases of the above table reveals the dependency of  $C_{F_z}$  on model fidelity, as the addition of one radial and three tangential belt modes resulted in a vertical stiffness reduction of 4.29%. Inclusion of all the in-plane modes up to 150Hz has led to an additional reduction of 0.62%, while no further reduction has been noticed for the last test case, an effect which is partially due to the limited vertical load applied on the tyre belt.

### 5.3.3 Data acquisition

In this section, vertical tyre compliance and stiffness are experimentally examined for the case of the non - rotating tyre, using the tyre test rig presented in Section 5.2. The hydraulic vertical load applied on the tyre is determined by the user at will, while the acting force value is acquired and stored at a sample rate of 100Hz. The full vertical force time history is depicted in the following figure:

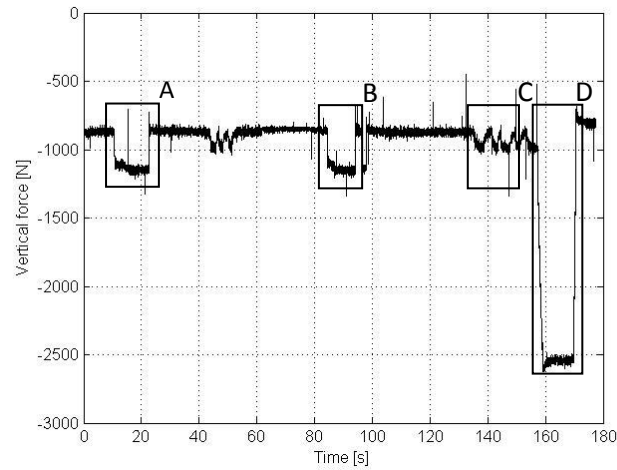


Figure 5.6 – Vertical stiffness test, total vertical force applied at the wheel centre versus time

The time history of the wheel centre vertical displacement resulting from the imposed vertical force of Figure 5.6 is presented below:

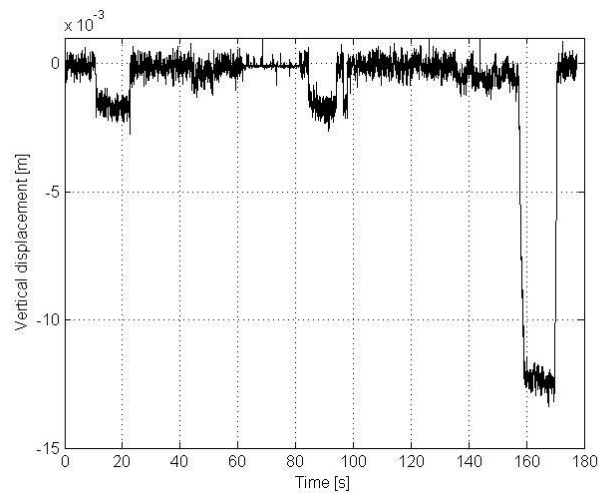


Figure 5.7 – Vertical stiffness test, total wheel centre vertical displacement versus time

To enhance the post-processing efficiency, only the four characteristic areas marked in Figure 5.6 are examined. This allowed for the exclusion of low-interest areas, for example areas where only the net vertical load of the tyre rig is applied. The four selected areas were chosen on the basis that they capture several aspects of the tyre vertical dynamics. Areas A and B represent a step change in the applied vertical load. Area C represents a vertical load profile of higher frequency whereas area D consists of a gradual transition from a lower (1000N) to a higher (2600N) applied vertical load. These areas are magnified for clarity in the following vertical load and vertical displacement diagrams:

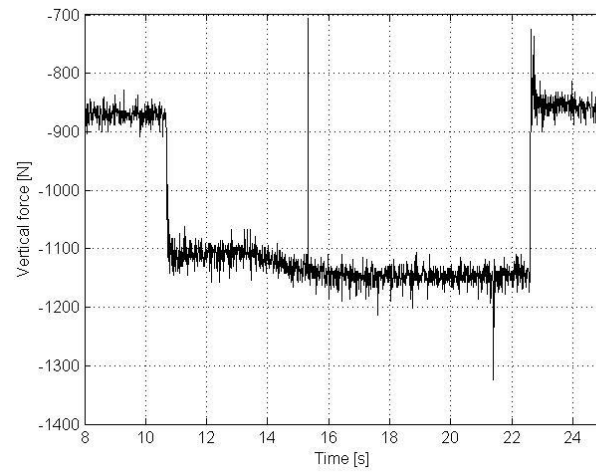


Figure 5.8 – Vertical stiffness test, vertical force versus time (Area A)

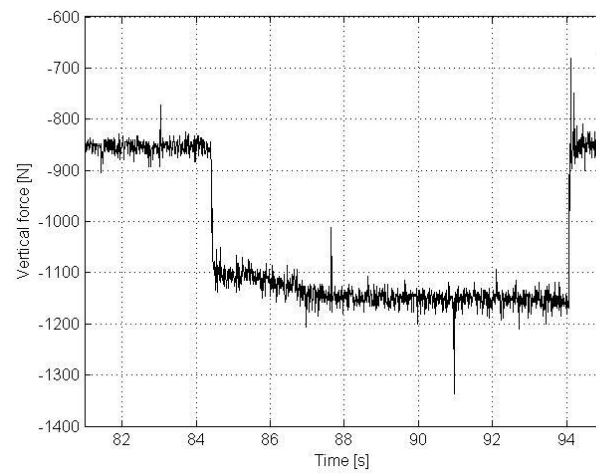


Figure 5.9 – Vertical stiffness test, vertical force versus time (Area B)

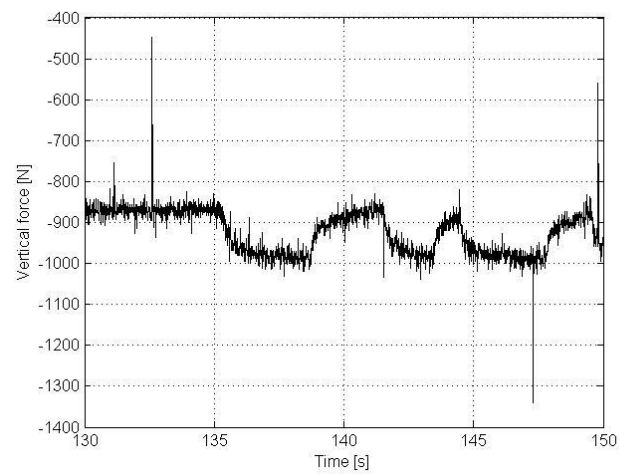


Figure 5.10 – Vertical stiffness test, vertical force versus time (Area C)

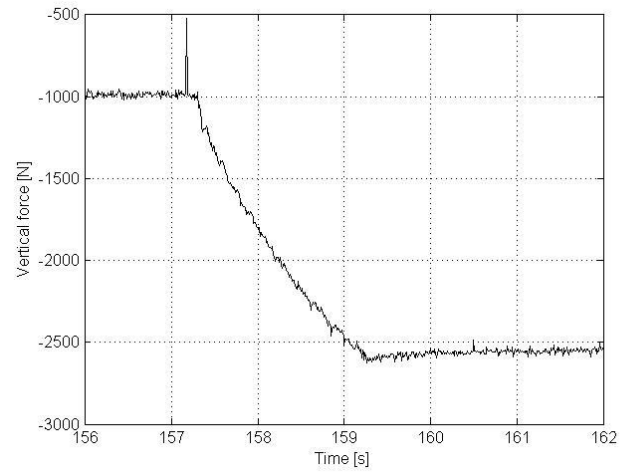


Figure 5.11 – Vertical stiffness test, vertical force versus time (Area D)

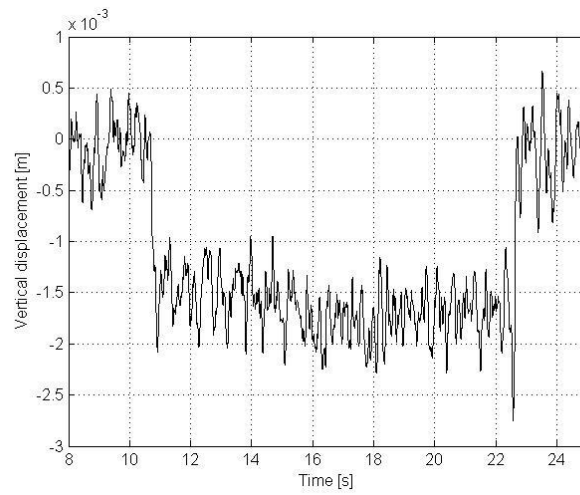


Figure 5.12 – Vertical stiffness test, wheel centre vertical displacement versus time (Area A)

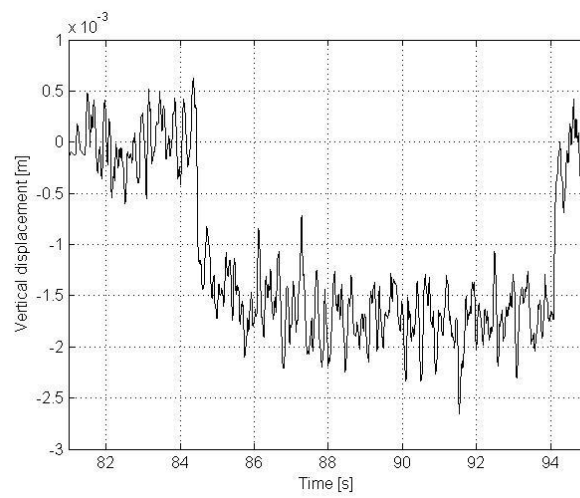


Figure 5.13 – Vertical stiffness test, wheel centre vertical displacement versus time (Area B)

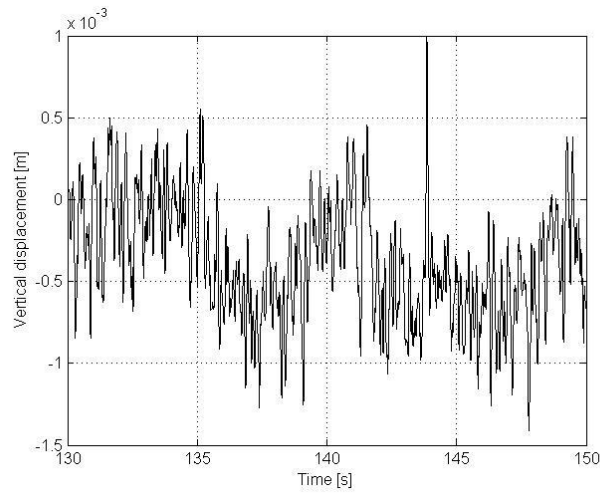


Figure 5.14 – Vertical stiffness test, wheel centre vertical displacement versus time (Area C)

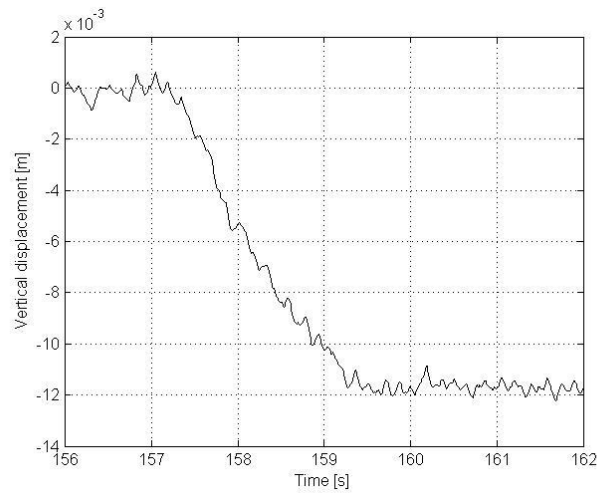


Figure 5.15 – Vertical stiffness test, wheel centre vertical displacement versus time (Area D)

A particular case of interest is that presented by area D. Because of the gradual nature of the transition between the initial and the final state of the tyre, all the intermediate vertical load / vertical displacement pairs are acquired, a property which is not the case for areas A and B. Theoretically, for each one of areas A and B, the vertical load versus vertical displacement diagram consists of only two points, namely the one representing the initial state and the one representing the final state of the force and displacement curves. Although these two areas are critical for the validation of the present study, they provide significantly less information when compared to area D, with regard to the relation between the vertical load and the vertical displacement. The locus generated by the data points forming area D leads to the conclusion that – for the given vertical load range – the relation between the vertical load and the vertical displacement is almost linear, i.e. vertical stiffness is constant:

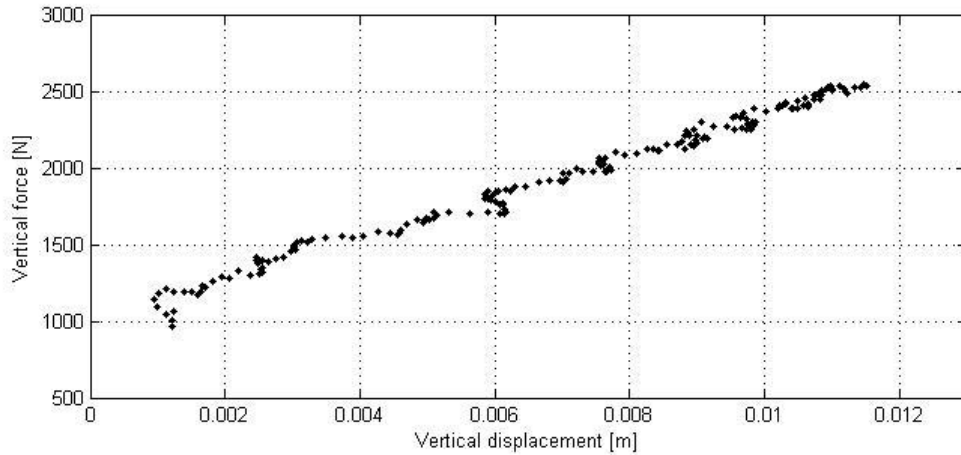


Figure 5.16 – Vertical stiffness test, wheel vertical force versus wheel centre vertical displacement (Area D)

It should be noted that experimentally induced limitations did not allow for the application of a higher vertical load so as to reach the non-linear vertical stiffness region. In the context of the present work, this is not considered as a significant drawback as the nature of the performed modal testing and the identified belt modes are limited to the linear vertical stiffness region around the equilibrium position of the tyre belt nodes.

The next required step is to fit a linear expression in the experimentally derived data points of the above figure. As it has been demonstrated by Equation 5.3–1 in Section 5.3.1, the gradient of this expression is the vertical stiffness of the tyre for the vertical load range between 1000N and 2600N:

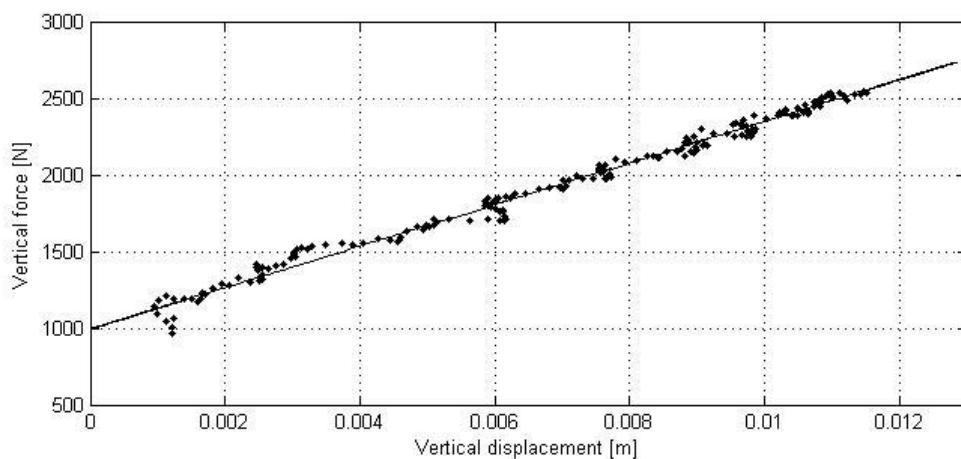


Figure 5.17 – Vertical stiffness test, wheel vertical force versus wheel centre vertical displacement including fitted linear expression (Area D)

The linear expression describing the above fitted line (blue line in Figure 5.17) is presented below:

$$F_z = [C_{F_z}]_{\text{Dexp}} \cdot \delta + C_1 \quad 5.3-2$$

where:  $F_z$  [N] is the vertical force applied on the tyre,

$\delta$  [m] is the wheel centre vertical displacement,

$[C_{F_z}]_{\text{Dexp}} = 136054$  N/m is the experimentally obtained vertical stiffness as defined by

Equation 5.3-1

$C_1 = 995.17$  N is the constant term.

To demonstrate the nature of the constant term  $C_1$  of the above expression, Figure 5.16 and Figure 5.17 should be analysed further. In both these figures – and consequently in expression 5.3-2 – the wheel centre vertical displacement is expressed as the deviation from the absolute vertical position of the tyre when the initial – for area D – vertical force of 1000N is applied. If – instead of the vertical deviation – the absolute vertical position of the wheel centre were to be used, then the above constant term would be eliminated as the above fitted linear expression would cross point (0, 0), i.e. for an applied vertical force of 0N the wheel centre will remain in its initial vertical position, which is equal to 0m. Clearly this is not the case in the above two diagrams, as the fitted expression passes through point (0, 995.17). However, the attempt to express the vertical position of the tyre as the deviation from a vertical position other than the initial one makes comparing experimental data and simulation results feasible, as typically they do not have a common inertial frame of reference. Nevertheless, the quantity of interest in the above expression, which is the tyre vertical stiffness, is not affected by this approach, as it is calculated by taking into account changes of both vertical load and vertical position rather than absolute values.

An interesting comparison may be made between the experimental findings of this section and the simulation results presented in Section 5.3.2. The tyre vertical stiffness obtained by the experimental results above is equal to  $[C_{F_z}]_{\text{Dexp}} = 136054$  N/m. In theory, this value captures the contribution of an infinite number of structural modes, since it derives from experimental data. Simulation results, corresponding to modal parameters derived by the tyre which generated the above experimental results, have been presented in the previous section. For the case of maximum simulation fidelity, i.e. inclusion of all the in-plane tyre belt modes up to 207Hz, the calculated vertical stiffness is  $[C_{F_z}]_{\text{sim}} = 155000$  N/m. Direct comparison of the above two vertical stiffness figures provides an indication of the vertical stiffness



dependency on vertical load range but, importantly, it also quantifies the actual contribution of an infinite number of excluded in-plane modes in the total model response. In particular, based on the values presented above, the performed modal reduction – exclusion of all the in-plane modes beyond 207Hz – resulted in the following vertical stiffness overestimation:

$$\varepsilon = \frac{|[C_{F_z}]_{\text{sim}} - [C_{F_z}]_{\text{Dexp}}|}{[C_{F_z}]_{\text{Dexp}}}$$

$$\varepsilon = 13.93\%$$

5.3–3

#### 5.3.4 Simulation results and comparison to experimental data

Similar to Section 5.3.2, the above scenario, i.e. vertical loading of the tyre by the force time history depicted in Figure 5.6, is replicated exploiting the virtual environment of the tyre model developed in the present work. The simulation runs presented in this section are based on the virtual non-rotating tyre being vertically loaded by the corresponding vertical force acquired during the respective experimental procedure. The required user-defined input quantities are summarised in the following table:

<b>Table 5.4: Vertical stiffness test – User defined input quantities</b>				
Vertical load (Fz) [N]	Area A	Area B	Area C	Area D
	Figure 5.8	Figure 5.9	Figure 5.10	Figure 5.11
Slip angle (sa)	0°	0°	0°	0°
Drum speed (vr)	0 m/s	0 m/s	0 m/s	0 m/s
Wheel angular velocity (ω)	0 rad/s	0 rad/s	0 rad/s	0 rad/s

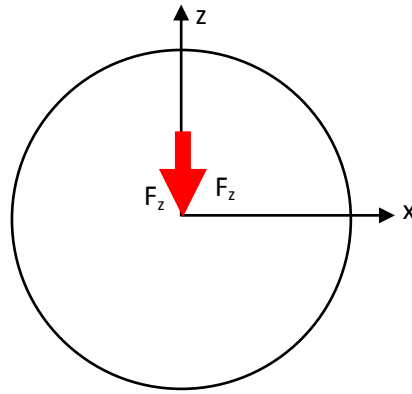


Figure 5.18 – Vertical stiffness test, graphical representation of user-defined quantities

while the main simulation parameters are presented below:

<b>Table 5.5: Vertical stiffness test – Main simulation parameters</b>	
Time step	0.0005 s
Number of belt / tread nodes	1160
Number of radial belt modes	7
Number of tangential belt modes	9
Number of lateral belt modes	11

Keeping in mind the rationale behind the proposed modelling approach, i.e. effective identification of modelling parameters and efficient tyre simulation, the chosen time step and node number combination represents a reasonable compromise between simulation accuracy and simulation elapsed time. The comparison between the time histories of the experimentally obtained wheel centre vertical deflection for areas A, B, C and D, depicted in Figure 5.12 to Figure 5.15, and those calculated based on the above simulation parameters is presented below:

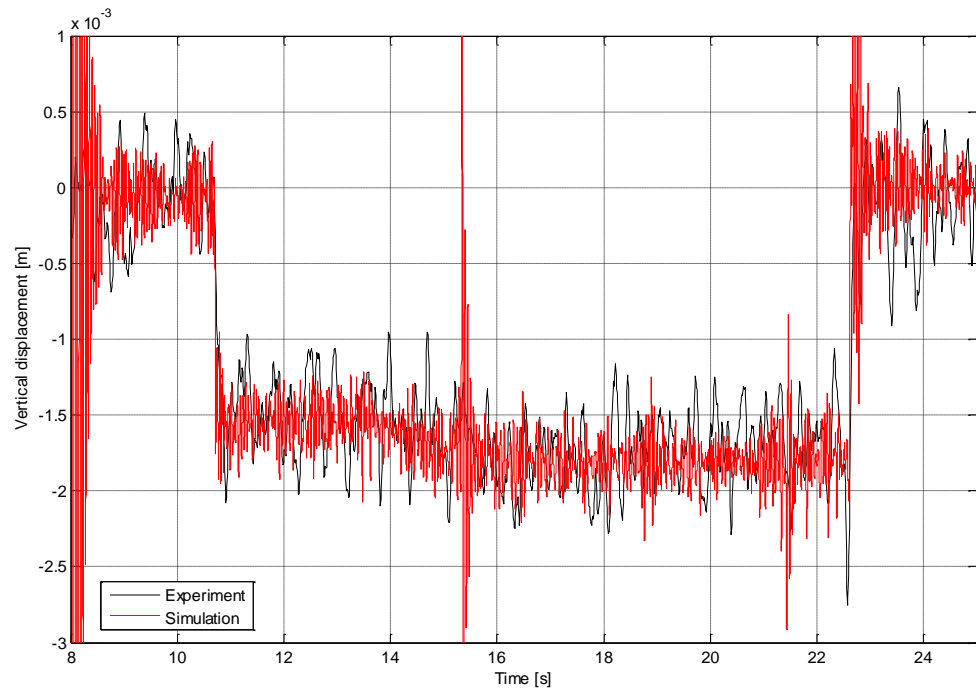


Figure 5.19 – Vertical stiffness test, comparison between experimental and simulation data in terms of wheel centre vertical displacement (Area A)

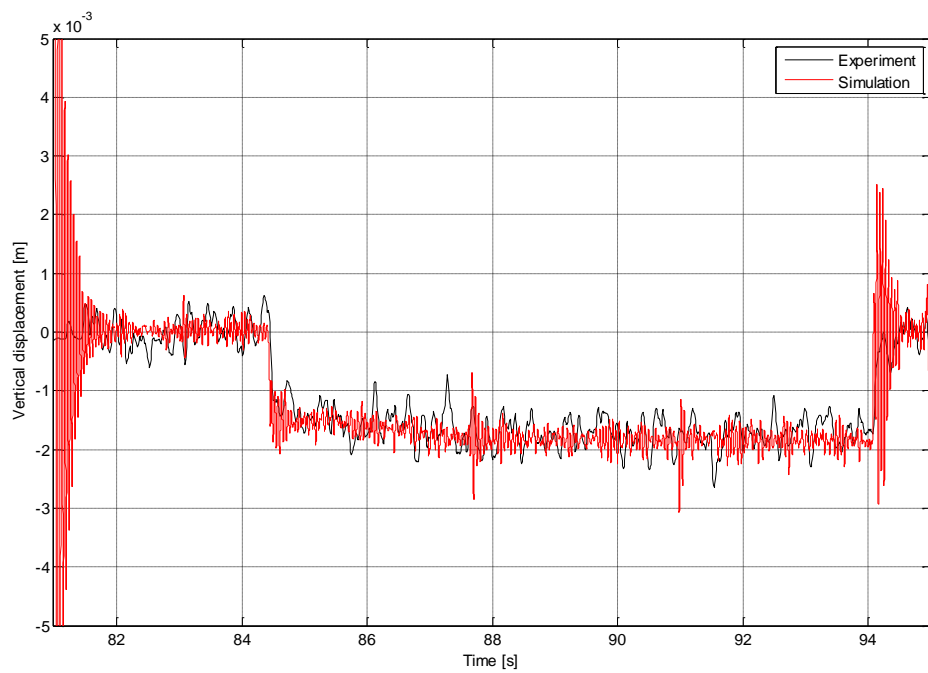


Figure 5.20 – Vertical stiffness test, comparison between experimental and simulation data in terms of wheel centre vertical displacement (Area B)

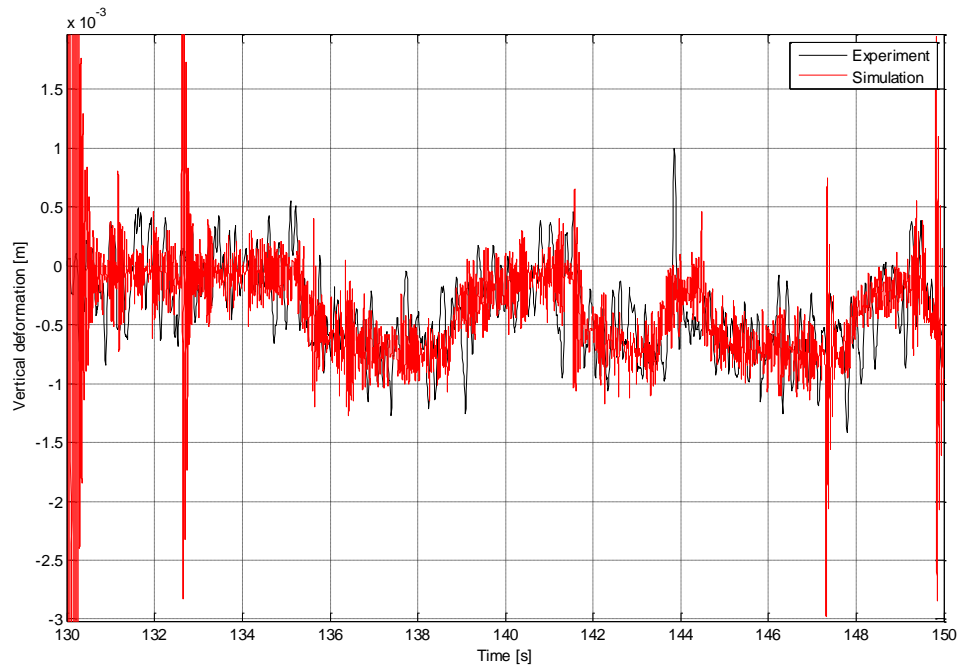


Figure 5.21 – Vertical stiffness test, comparison between experimental and simulation data in terms of wheel centre vertical displacement (Area C)

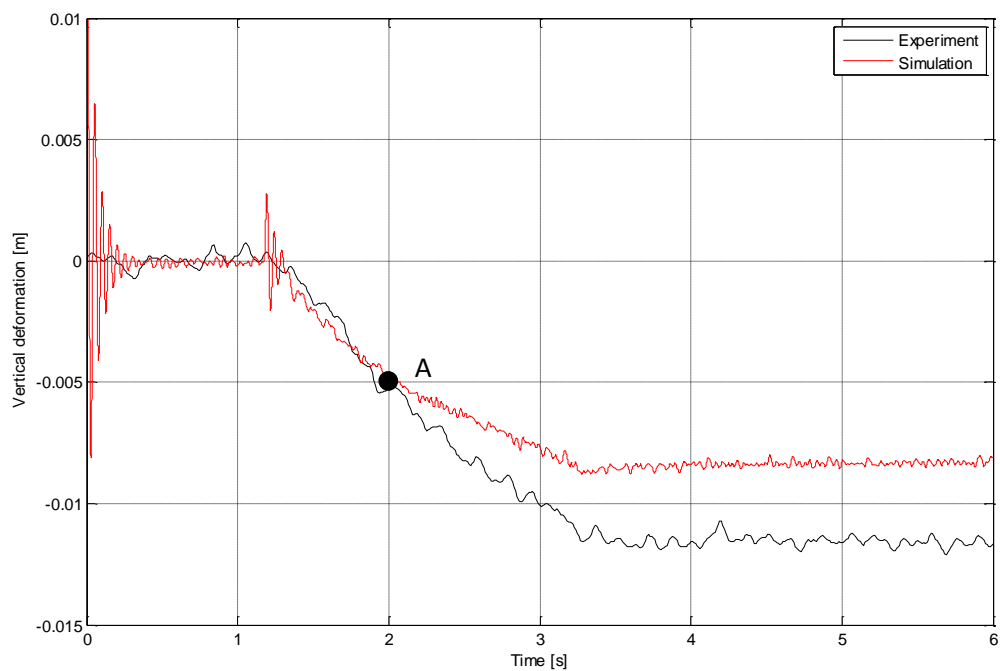


Figure 5.22 – Vertical stiffness test, comparison between experimental and simulation data in terms of wheel centre vertical displacement (Area D)

The high initial oscillations of the simulated tyre, observed in all four of the above test cases, originate from the difference in the initial condition between experiment and simulation. Contrary to the virtual tyre, which is initially suspended freely and not in contact to the ground,

the real-world test tyre is already loaded in the initial time instance of each of the above scenarios. Nevertheless, after a few tenths of a second these oscillations are dampened and most importantly the two tyres are in a similar state at the start of each transition phase.

The above figures, and specifically Figure 5.19 to Figure 5.21, demonstrate that correlation between experiment and simulation has been achieved for both step-like and pseudo-random vertical force variations. In these three particular test cases, vertical tyre force has not exceeded 1200N, demonstrating that the number of included flexible belt modes offers reasonable accuracy in the vertical force range up to 1200N. Loading the tyre beyond that point leads to deviation between experiment and simulation because of the limitations presented in Section 5.3.1, which are associated to either the proposed tyre model or the experimentally identified quantities used to populate the flexible tyre belt model.

This phenomenon is demonstrated in Figure 5.22, where the tyre is loaded up to almost 2600N. Initially, correlation is achieved up to the point in which vertical force is equal to 1750N, see point A in Figure 5.22. Beyond this vertical force and up to the maximum measured vertical force of 2600N, significant deviation is observed between experiment and simulation. Following the investigation on vertical stiffness as a function of model fidelity presented in Section 5.3.2, it is deduced that the main source of deviation presented Figure 5.22 is the limited number of flexible belt modes included in the tyre model.

This observed deviation may be quantified by calculating the tyre vertical stiffness corresponding to simulation results for Area D. Following a process similar to the one presented above for the experimental data of Area D, the locus of points obtained by the applied vertical force and the simulated wheel centre displacement reveals the relationship between these two quantities. A linear expression is fitted to these points and the respective gradient is equal to the vertical stiffness of the virtual tyre.

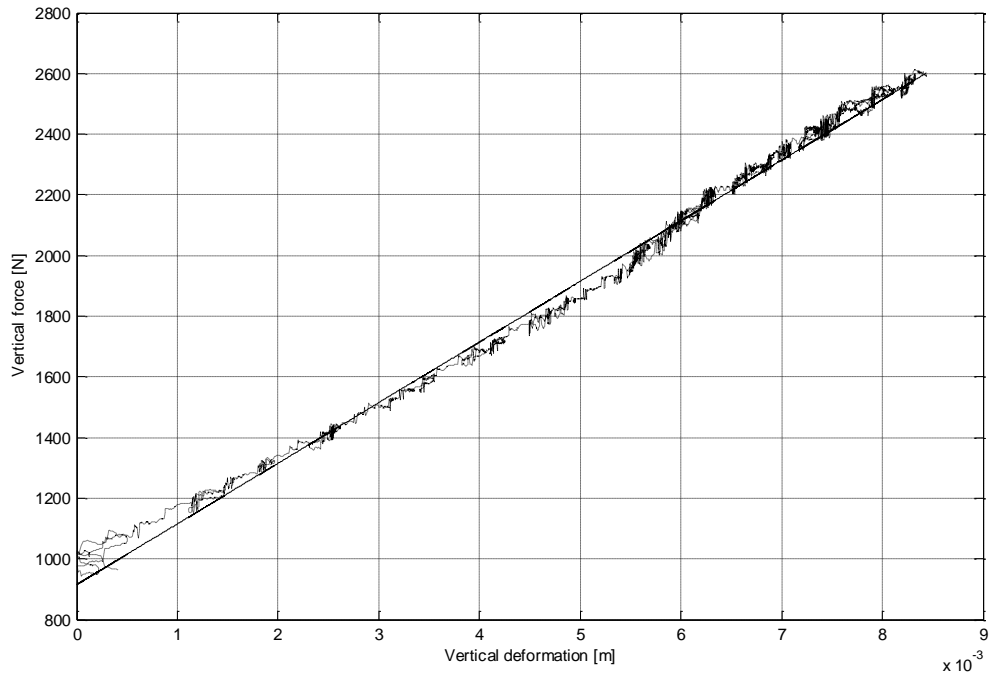


Figure 5.23 – Vertical stiffness test, virtual wheel vertical force versus wheel centre vertical displacement including fitted linear expression (Area D)

The fitted linear expression of the above diagram is described by the following equation:

$$F_z = [C_{F_z}]_{Dsim} \cdot \delta + C_2 \quad 5.3-4$$

where:  $F_z$  is the vertical force applied on the tyre,

$\delta$  is the wheel centre vertical displacement,

$[C_{F_z}]_{Dsim} = 199833 \text{ N/m}$  is the vertical stiffness as defined by Equation 5.3–1, obtained by the tyre model presented in this work,

$C_2 = 915.19 \text{ N}$  is the constant term and

$R^2 = 99.39\%$ .

Value  $[C_{F_z}]_{Dsim}$  represents a critical element in this section as it is providing a quantified comparison element between simulation results and experimental data. As both the physical and the virtual tyre have been excited by the exact same vertical force time history, the deviation between  $[C_{F_z}]_{Dsim}$ , which includes a finite number of modes, and  $[C_{F_z}]_{Dexp}$ , which – in theory – includes the contribution of all the flexible tyre belt modes, derives directly from the modal reduction adopted in the proposed tyre model. The consequent vertical stiffness overestimation is calculated as follows:

$$\varepsilon = \frac{|[C_{F_z}]_{\text{Dexp}} - [C_{F_z}]_{\text{Dsim}}|}{[C_{F_z}]_{\text{Dexp}}} \Rightarrow$$

$$\varepsilon = 46.88\%$$

5.3–5

Clearly, the above overestimation value demonstrates that additional tyre belt modes are required, and the number of required belt modes increases with the increased vertical force. This is illustrated by the four test cases presented above. Correlation between the virtual and the physical tyre has been achieved for cases A to C, where the applied vertical force is confined within a limited range. On the other hand, case D exposes a weakness of the proposed modelling approach as the imposed modal reduction, along with the non-linear deformation of the tyre which is not captured by the flexible tyre belt sub-model, leads to significant deviation between experimental data and simulation results. In these cases, i.e. cases of relatively high vertical load, a less aggressive modal reduction approach is highly advisable to the tyre model user.

## 5.4 Transient lateral slip

### 5.4.1 Introduction

Following the investigation on the influence of flexible belt dynamics on tyre vertical stiffness presented in the preceding sections, an additional study is conducted below. It has been well established within literature that contact forces between a tyre and the road are highly influenced by tyre deformation<sup>[80]</sup>. This influence is clearly observed in cases where the tyre is subjected to variation of slip angle or driving torque as it is illustrated in the experimentally obtained Figure 5.24<sup>[68]</sup>.

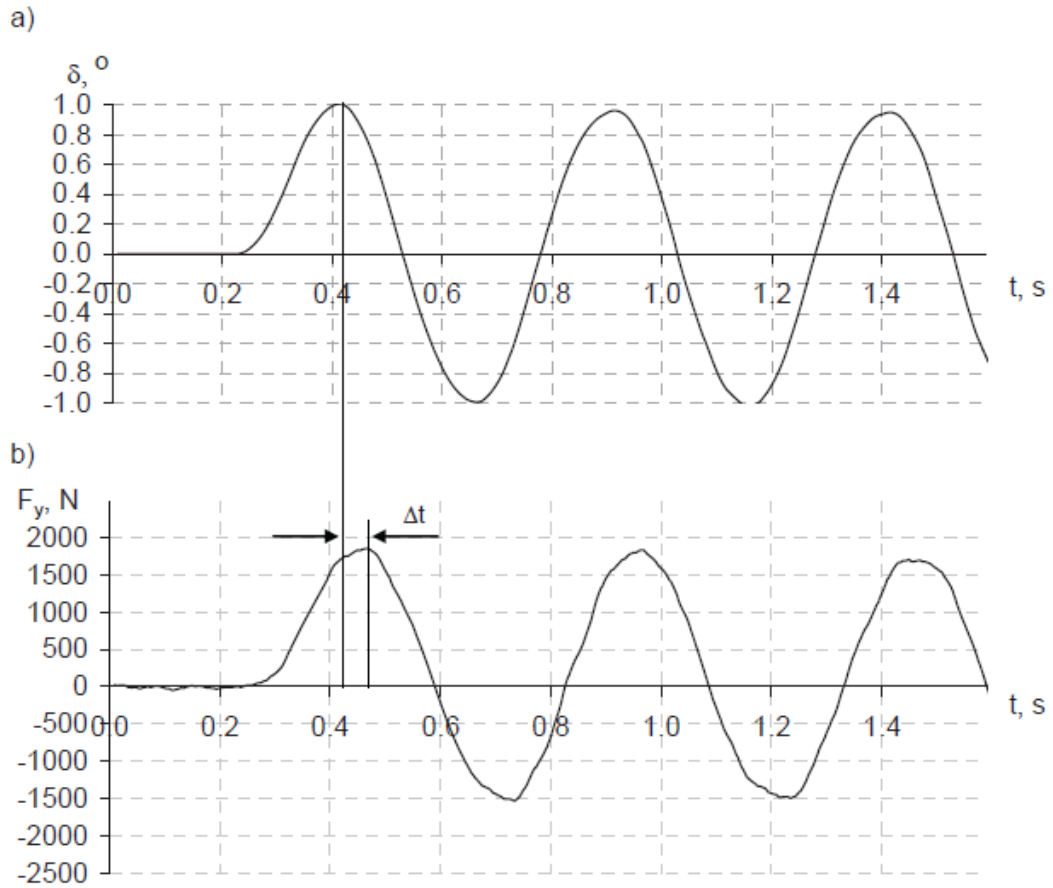


Figure 5.24 – Changes of lateral reaction force  $F_y$ , transmitted by wheel, as a response for the wheel cornering angle  $\delta$  oscillatory changes ( $v=30\text{km/h}$ ,  $f=2\text{Hz}$ ); a) changes of the wheel cornering angle  $\delta$  - input signal; b) changes of lateral force reaction  $F_y$ , transmitted by wheel - output signal([68])

This delay is typically identified by introducing the *relaxation length* concept, which is defined as the length required so that a certain level (63%) of the steady-state longitudinal or lateral force is achieved<sup>[80]</sup>, after the introduction of slip angle or driving torque step-like variation. The proposed tyre model is capable of capturing this first-order behaviour, as is illustrated in the following figure:



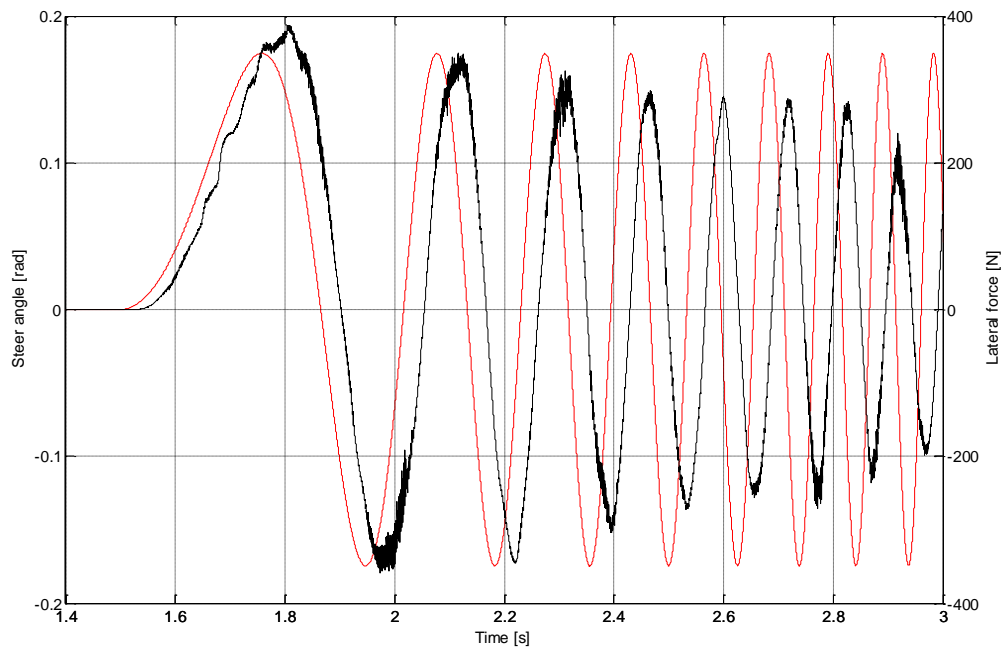


Figure 5.25 - Time delay and frequency dependency of lateral force generation

In the context of the present work, two cases of lateral force hysteresis are examined. In these cases, the tyre model is excited by varying the steering angle using a sinusoidal signal of increasing frequency, see Figure 5.26. Tyre relaxation behaviour is captured for three different drum velocities and three different vertical loads, for the first and second test cases respectively. These tests and the selected user-defined input parameters are summarised in the following table:

Table 5.6: Tyre hysteresis to slip angle variation – Virtual testing parameters					
Test	Drum velocity	Vertical load	Rad. modes	Tan. modes	Lat. modes
1a	2.0 m/s	1000 N	7	9	11
1b	2.5 m/s	1000 N	7	9	11
1c / 2a	3.0 m/s	1000 N	7	9	11
2b	3.0 m/s	1200 N	7	9	11
2c	3.0 m/s	1400 N	7	9	11
2d	3.0 m/s	1600 N	7	9	11

For each test, the tyre model is excited by varying the user-defined steering angle. The resulting digital signal – expressed in the time domain – is stored as the model input:

$$sa(k) = \begin{cases} 0 & , k \leq k_{set} \\ A \cdot \sin(\omega_{excit} k F_s), & k > k_{set} \end{cases} \quad 5.4-1$$

where  $A$  is the amplitude of the steering angle,  $\omega_{excit}$  is the time-dependent excitation frequency,  $F_s$  is the sampling frequency and  $k$  is the sampling index. Let  $T_{tot}$  denote the total simulation duration,  $k$  fulfils the following expression:

$$0 \leq k \leq T_{tot} \cdot F_s \Rightarrow$$

$$0 \leq k \leq N \quad 5.4-2$$

with  $N$  being the total number of samples obtained. Initially, before sample  $k_{set}$  is reached, steering angle is kept equal to zero and the only model input is the applied vertical load, so that the virtual tyre settles. The steering angle time history is demonstrated below:

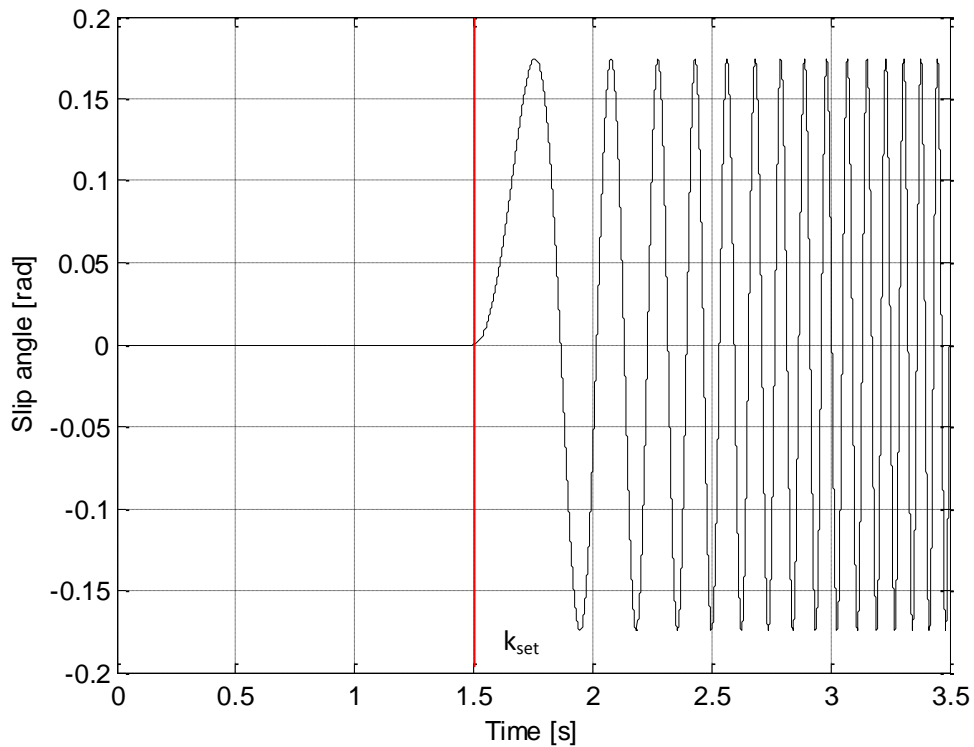


Figure 5.26 – Steering angle variation, expressed in the time domain

The steering angle data series presented above may be expressed in the frequency domain by applying the following Fast Fourier Transformation expression:

$$sa(f_n) = \frac{1}{N} \sum_{k=0}^{N-1} \left[ sa(k) \cdot e^{-j \frac{2\pi kn}{N}} \right] \quad 5.4-3$$

A similar approach is adopted in the post-processing procedure of the output digital signal, namely the resulting lateral force:

$$SF_y(f_n) = \frac{1}{N} \sum_{k=0}^{N-1} \left[ F_y(k) \cdot e^{-j \frac{2\pi kn}{N}} \right] \quad 5.4-4$$

The above frequency spectra are exploited to calculate the transfer function of the virtual tyre, as follows:

$$TF(f_n) = \frac{SF_y(f_n)}{sa(f_n)} \quad 5.4-5$$

The transfer function introduced in Equation 5.4–5 is modelled by a first-order expression:

$$TF(s) = \frac{K_p}{\tau s + 1} \quad 5.4-6$$

In the above expression, time constant  $\tau$  is the time required so that the system output, i.e. the lateral force generated by the virtual tyre, reaches 63% of the steady-state value after a step change is imposed on the model input. It follows that calculation of time constant  $\tau$  is vital in calculating the relaxation length of the virtual tyre. By fitting Equation 5.4–6 to the transfer function curve derived by the input and output frequency spectra of each test, constant  $\tau$  is obtained and the respective relaxation length  $\sigma$  may be calculated by taking into account the forward tyre speed  $v_d$ :

$$\sigma = \tau \cdot v_d \quad 5.4-7$$

This process is performed in the following two sections. As it has been demonstrated above, these sections are dedicated to examining relaxation length behaviour for varying longitudinal speed and vertical load. The assessment of the results is performed based on trends for these phenomena found in literature.

#### 5.4.2 Slip angle frequency sweep – Longitudinal velocity variation

Initially, model transient behaviour is examined in terms of longitudinal speed variation. The respective simulation parameters are a subset of the one presented in the above section and they are re-introduced below:

Table 5.7: Tyre first-order behaviour – Virtual testing parameters					
Longitudinal velocity variation tests					
Test	Drum velocity	Vertical load	Rad. modes	Tan. modes	Lat. modes
1a	2.0 m/s	1000 N	7	9	11
1b	2.5 m/s	1000 N	7	9	11
1c	3.0 m/s	1000 N	7	9	11

The primary model excitation is the slip angle time history presented in Figure 5.26. With regard to the remaining three user-defined model inputs, vertical load is common for all three tests and equal to 1000N, longitudinal drum velocity is specified in the above table, and wheel rotational velocity is adjusted accordingly to result into zero longitudinal slip. The resulting lateral force is obtained for each one of the tests found in the above table and the respective time histories are presented in Figure 5.27 to Figure 5.29:

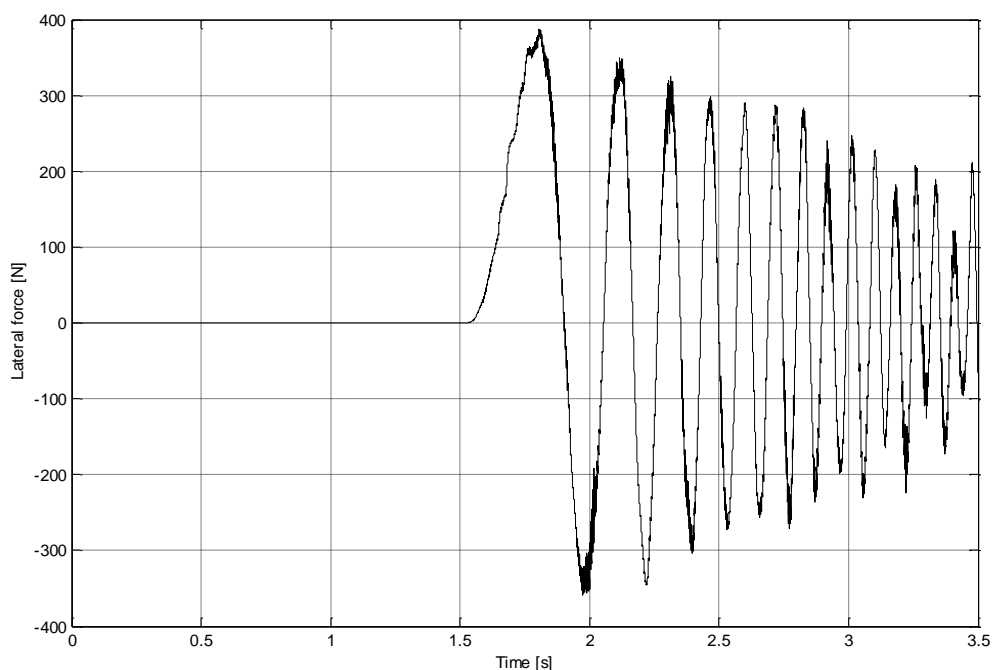


Figure 5.27 – Lateral force, time domain ( $v_d=2\text{m/s}$ ,  $F_z=1000\text{N}$ )

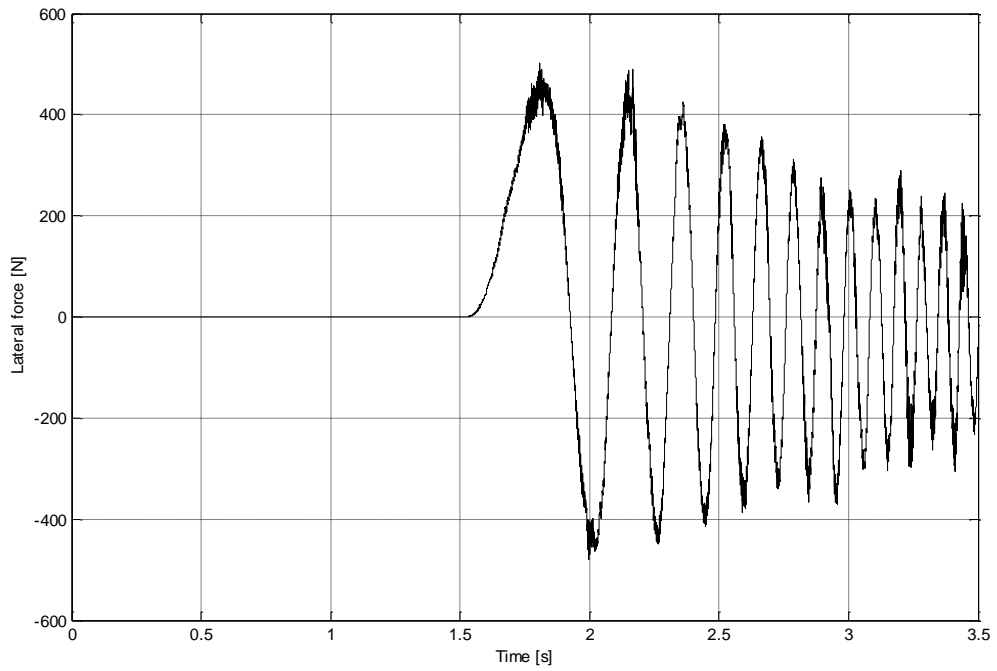


Figure 5.28 – Lateral force, time domain ( $v_d=2.5\text{m/s}$ ,  $F_z=-1000\text{N}$ )

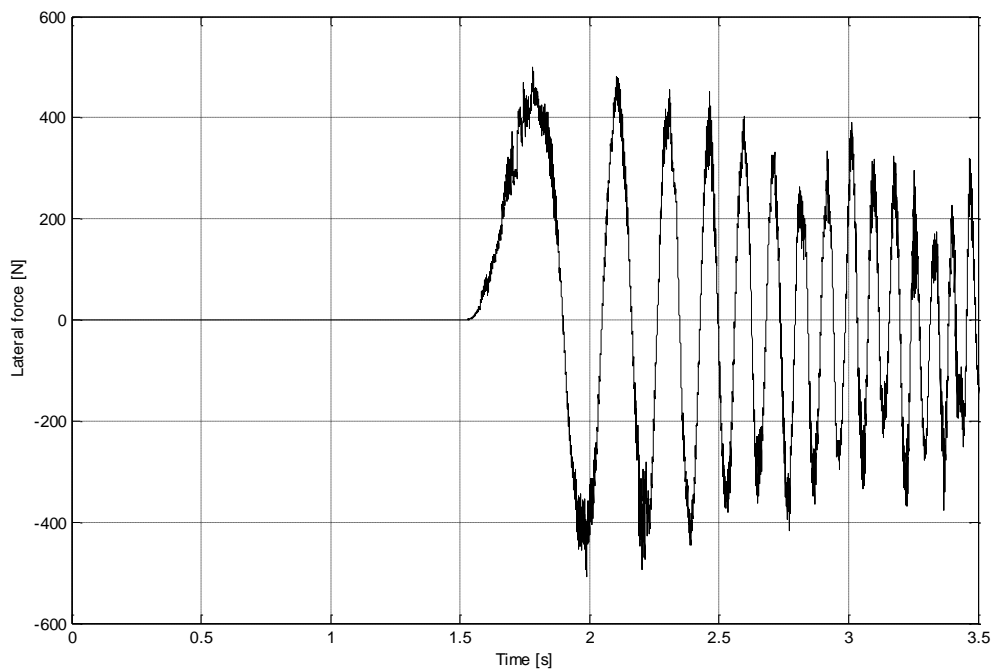


Figure 5.29 – Lateral force, time domain ( $v_d=3\text{m/s}$ ,  $F_z=-1000\text{N}$ )

By modelling the virtual tyre as a first-order system, the transfer function relating the steering angle input with the lateral force output demonstrates the following form:

$$TF(s) = \frac{SF_y(s)}{sa(s)} \Rightarrow$$

$$TF(s) = \frac{K}{s - p} \quad 5.4-8$$

Fitting of expression 5.4–8 to the experimentally derived expression 5.4–5 results in obtaining the poles  $p$  of the system for each one of the above test cases:

<b>Table 5.8: Tyre first-order behaviour – Simulation results</b>		
<b>Longitudinal velocity variation tests</b>		
<b>Test</b>	<b>Drum Velocity</b>	<b>Pole</b>
1a	2.0 m/s	-3.0532
1b	2.5 m/s	-3.1349
1c	3.0 m/s	-3.7014

Expression 5.4–8 may be rearranged to yield Expression 5.4–6 as follows:

$$TF(s) = \frac{(-1/p)K}{(-1/p)(s - p)} \Rightarrow$$

$$TF(s) = \frac{K_P}{(-1/p)s + 1} \Rightarrow$$

$$TF(s) = \frac{K_P}{\tau s + 1} \Rightarrow \quad 5.4-9$$

where time constant  $\tau$  is equal to:

$$\tau = -\frac{1}{p} \quad 5.4-10$$

Application of Expression 5.4–10 to the system poles obtained above yields the time constant for each test case. Moreover, these time constants lead to the calculation of the relaxation length via Equation 5.4–7. These results are presented in the following table:

<b>Table 5.9: Tyre first-order behaviour – Simulation results</b>				
<b>Longitudinal velocity variation tests</b>				
<b>Test</b>	<b>Drum Velocity</b>	<b>Pole</b>	<b>Time Constant</b>	<b>Relaxation Length</b>
1a	2.0 m/s	-3.0532	0.3275 s	0.6550 m
1b	2.5 m/s	-3.1349	0.3190 s	0.7975 m
1c	3.0 m/s	-3.7014	0.2702 s	0.8106 m

In addition, the cut-off frequency of the system may be calculated:

$$f_c = \frac{1}{2\pi\tau} \quad 5.4-11$$

Which yields the final result table for the simulation runs conducted within this section:

<b>Table 5.10: Tyre first-order behaviour – Simulation results</b>					
<b>Longitudinal velocity variation tests</b>					
<b>Test</b>	<b>Drum Velocity</b>	<b>Pole</b>	<b>Time Constant</b>	<b>Cut-off frequency</b>	<b>Relaxation Length</b>
1a	2.0 m/s	-3.0532	0.3275 s	0.4860 Hz	0.6550 m
1b	2.5 m/s	-3.1349	0.3190 s	0.4989 Hz	0.7975 m
1c	3.0 m/s	-3.7014	0.2702 s	0.5890 Hz	0.8106 m

The trend observed in the results presented above is in agreement with measured trends found in literature, for example the work of H. Pacejka in [80], the experimental work of P. Bandel et al. in [12], or the work of W. Luty in [68]. In particular, the cut-off frequency of a physical tyre, excited by a sinusoidal variation of the steering angle, increases with increased wheel longitudinal speed, see Figure 5.30. As it may be seen in the results presented above, a similar trend is observed for the tyre model presented in this work.

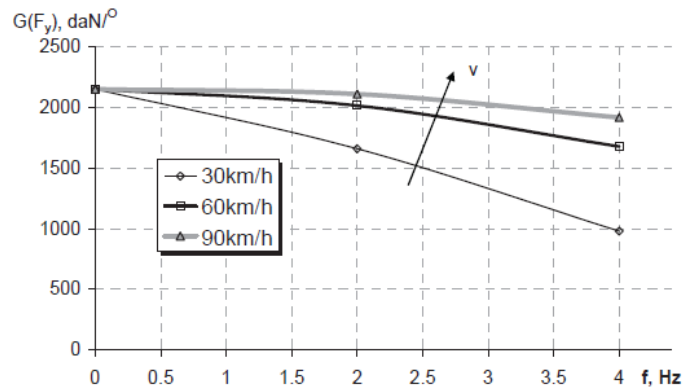


Figure 5.30 – Amplitude characteristics, determined in frequency domain, for different wheel rolling speed, in conditions of the wheel cornering angle oscillatory changes([68])

#### 5.4.3 Slip angle frequency sweep – Vertical load variation

Similarly to the test cases presented above, this section is dedicated to investigate the dependency between vertical force variation and transient tyre response. The simulation parameters are presented in the following table:

Table 5.11: Tyre first-order behaviour – Virtual testing parameters					
Vertical force variation tests					
Test	Drum speed	Vertical load	Rad. modes	Tan. modes	Lat. modes
2a	3.0 m/s	1000 N	7	9	11
2b	3.0 m/s	1200 N	7	9	11
2c	3.0 m/s	1400 N	7	9	11
2d	3.0 m/s	1600 N	7	9	11

In this case, the primary model input is the vertical load which varies between 1000N and 1600N in increments of 200N. As has already been demonstrated in Section 5.3.4, correlation has been achieved between the virtual and the physical tyre for this particular vertical loading range and level of modal reduction displayed in the above table. The virtual tyre is again excited by the slip angle signal presented in Figure 5.1. Drum longitudinal speed is kept constant at 3m/s and wheel rotational speed is adjusted so that zero longitudinal slip is achieved, resulting in pure lateral slip. Following the excitation of the tyre model via the



steering angle signal presented in Figure 5.26, the lateral force time histories corresponding to the tests presented in the above table are depicted below:

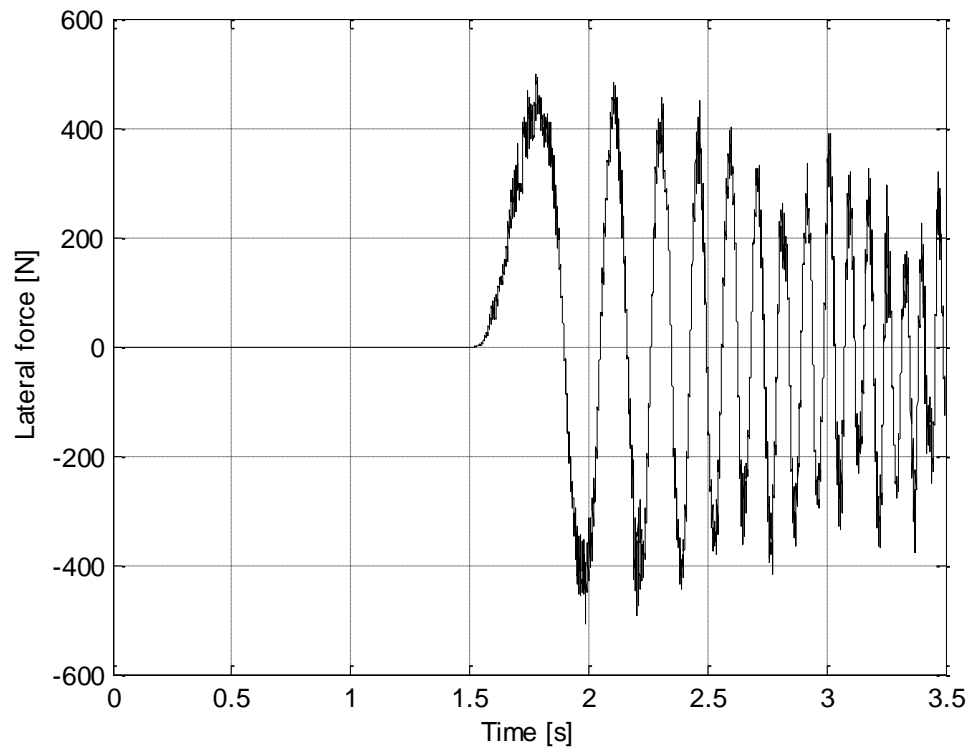


Figure 5.31 – Lateral force expressed in the time domain ( $v_d = 3\text{m/s}$ ,  $F_z = 1000\text{N}$ )

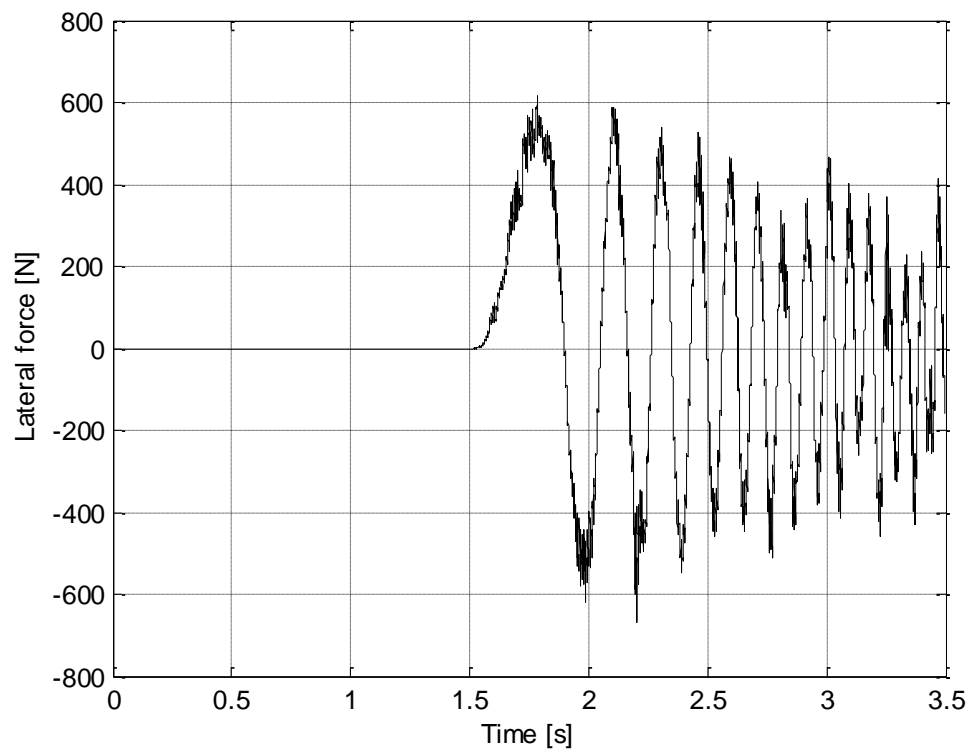


Figure 5.32 – Lateral force expressed in the time domain ( $v_d = 3\text{m/s}$ ,  $F_z = 1200\text{N}$ )

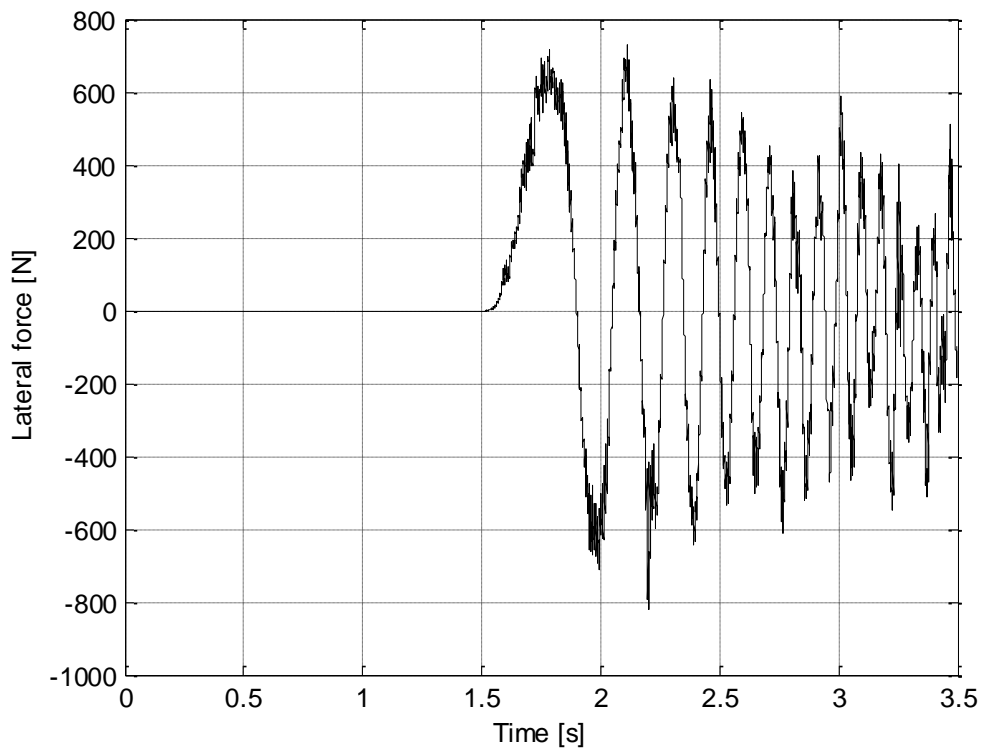


Figure 5.33 – Lateral force expressed in the time domain ( $v_d = 3\text{m/s}$ ,  $F_z = 1400\text{N}$ )

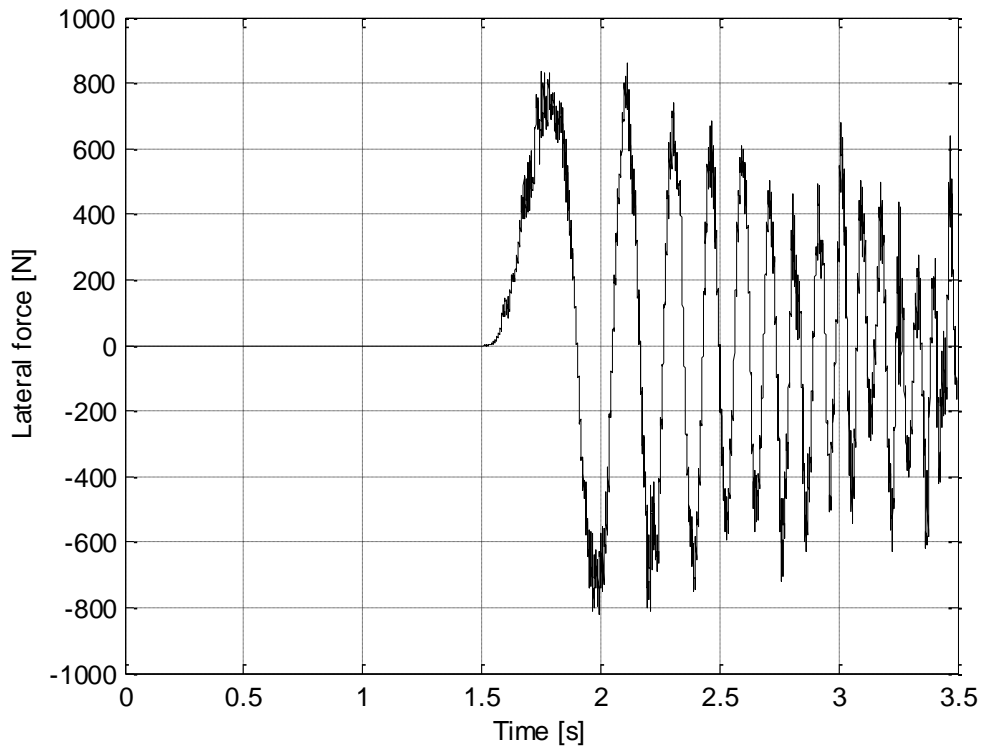


Figure 5.34 – Lateral force expressed in the time domain ( $v_d = 3\text{m/s}$ ,  $F_z = 1600\text{N}$ )

A direct visual comparison of the above diagrams is possible by normalising the lateral force for each one of the above cases, in order to compensate for the different levels of maximum lateral force generated by the different applied vertical forces. This normalisation is based on the following expression:

$$\overline{SF}_y = \frac{SF_y}{\max(|SF_y|)} \quad 5.4-12$$

The normalised lateral force time histories are displayed in the following diagram and a close up of area A is presented in Figure 5.36:

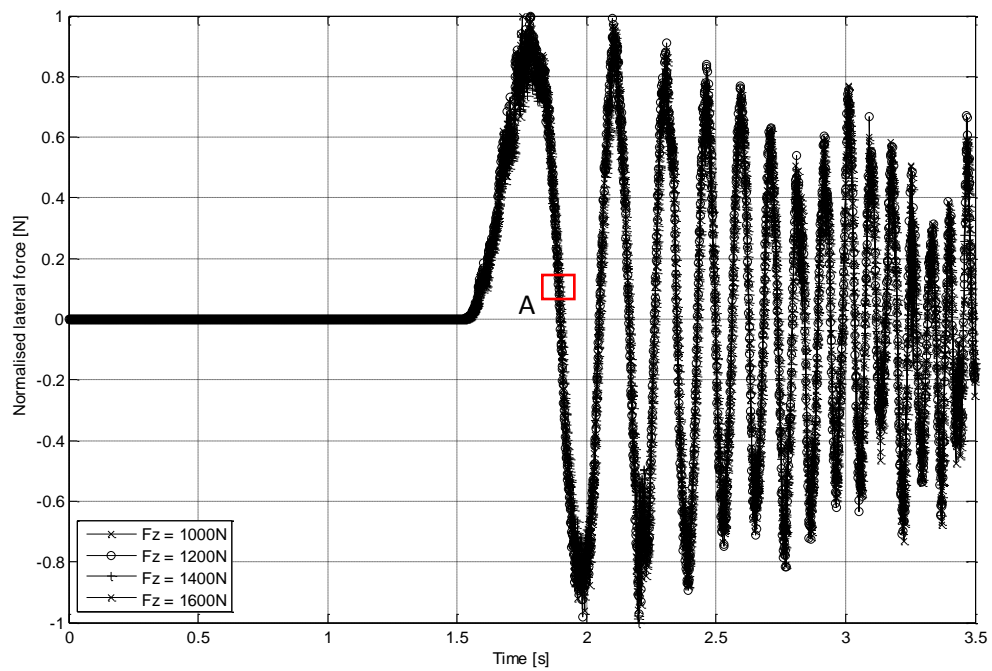


Figure 5.35 – Normalised lateral force time histories ( $v_d = 3\text{m/s}$ ,  $F_z: 1000\text{N} - 1600\text{N}$ )

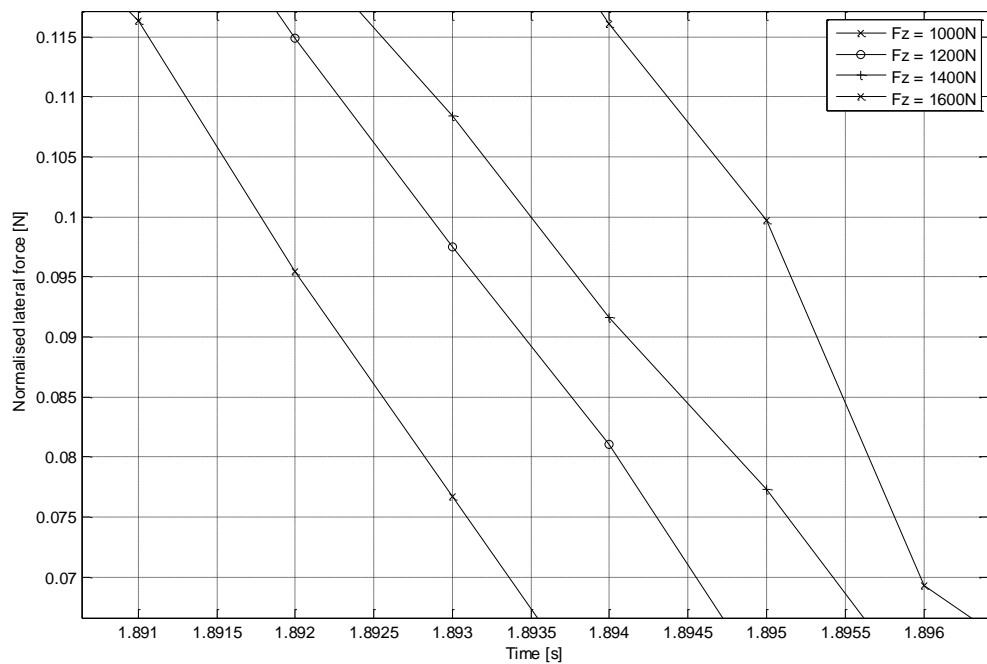


Figure 5.36 – Normalised lateral force time histories, close up of area A.

The above observation is a rather interesting one, as the response of the proposed tyre model to a lateral slip excitation demonstrates a vertical load sensitivity, which originates from the deformation of the tyre model. Similarly to the previous section, the delay presented in Figure 5.36 is quantified by adopting the relaxation length approach. The vertical force applied on the

tyre is related to the respective relaxation length via the cornering stiffness, and this mechanism is governed by the following equation<sup>[16]</sup>:

$$\sigma = \frac{C_{Fsa}}{C_y} \quad 5.4-13$$

where  $C_{Fsa}$  and  $C_y$  are the cornering and the lateral stiffness respectively. According to H. Pacejka in [80], for typical passenger car tyres, the dependency of relaxation length on vertical load is similar to the one of cornering stiffness on vertical load, hence lateral stiffness  $C_y$  in equation 5.4–13 is a neutral factor compared to the contribution of cornering stiffness  $C_{Fsa}$  for varying vertical load. The parabolic relation between cornering stiffness and vertical load has been extensively documented in literature, see for example [38] and [80]:

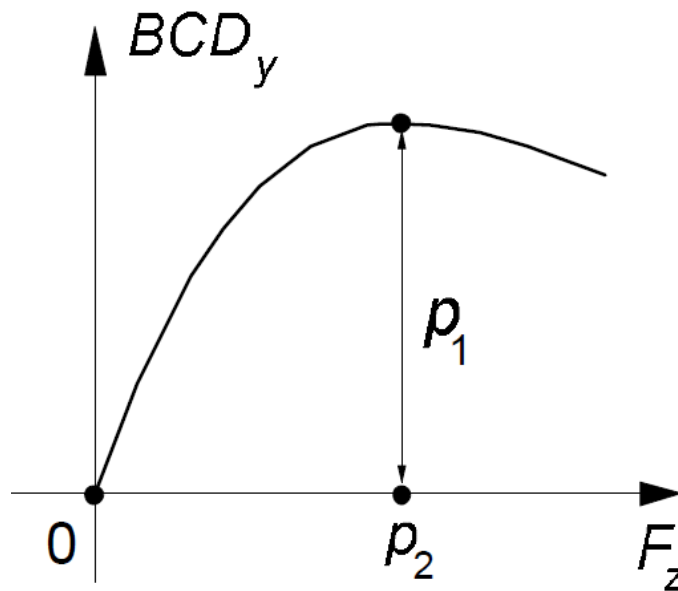


Figure 5.37 – Cornering stiffness vs vertical load ([80])

For the case of limited applied vertical load and zero camber angle examined in this work, cornering stiffness is considered as monotonically increasing with vertical load and therefore, based on the above, the same trend should apply between relaxation length and vertical load. Dependency between relaxation length and vertical load is further supported by experimental data presented in the work of W. Luty in [67]. In particular, for three distinct load cases, measured relaxation length demonstrates the following behaviour:

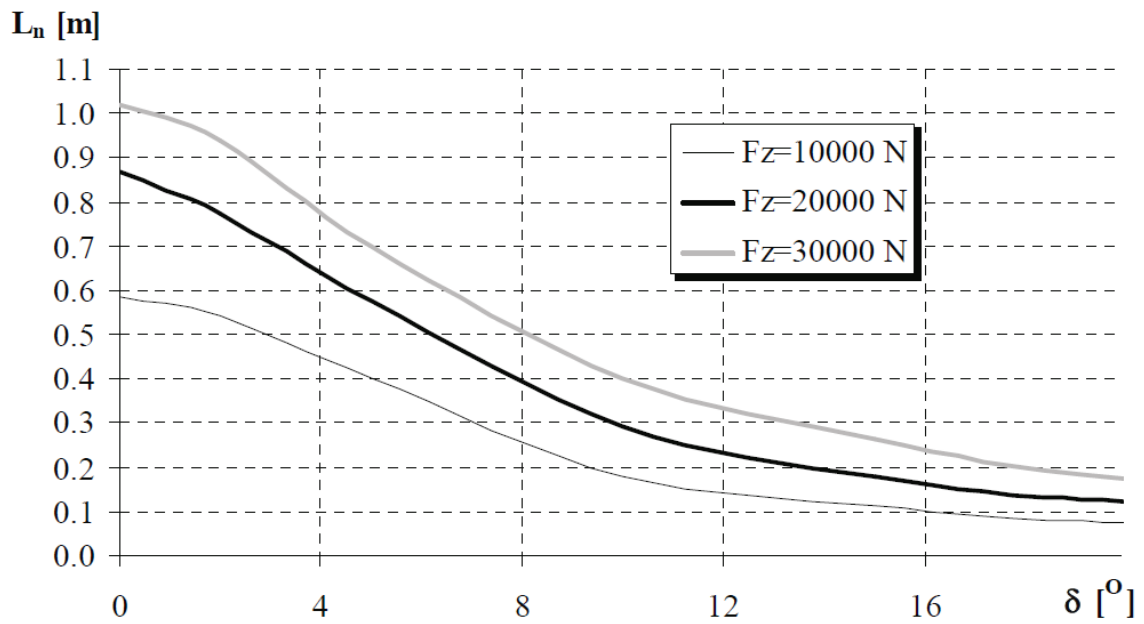


Figure 5.38 – Variations of the relaxation length value  $L_n$ , after forcing a cornering angle step  $\delta$  (all-steel 275/70R22.5 tire, normal load  $F_z=20000\text{N}$ ) ([67])

Following an approach identical to the one adopted in the previous section, the following expression is fitted to the data sets presented above (lateral force time histories depicted in Figure 5.31 to Figure 5.34 and steering angle time history displayed in Figure 5.26):

$$TF(s) = \frac{SF_y(s)}{sa(s)} = \frac{K}{s - p} \quad 5.4-14$$

Pole  $p$  is obtained for each load case and, by applying Equation 5.4–10, the corresponding time constant is calculated. Finally, the relaxation length associated with each vertical load is obtained by Equation 5.4–7. The quantities mentioned above are illustrated in the following table:

Table 5.12: Tyre first-order behaviour – Simulation results					
Vertical force variation tests					
Test	Vertical load	Pole	Time constant	Cut-off frequency	Relaxation length
2a	1000 N	-3.7014	0.2702 s	0.5890 Hz	0.8105 m
2b	1200 N	-3.6889	0.2711 s	0.5871 Hz	0.8132 m
2c	1400 N	-3.6041	0.2775 s	0.5735 Hz	0.8324 m
2d	1600 N	-3.5007	0.2857 s	0.5571 Hz	0.8570 m

The relaxation length trend presented in the above table is in accordance with Equation 5.4–13 and with experimental data presented in [67], see Figure 5.38. Therefore, it may be concluded that the trend between vertical load and delay in lateral force generation observed in a physical tyre is replicated by the proposed tyre modelling approach, as the effect of the main mechanism responsible for this behaviour, namely tyre deformation, is a fundamental part of the virtual tyre presented in Chapter 3.

## **5.5 Remarks on chapter 5**

Having developed the equations formulating the proposed tyre model in Chapter 3 and having obtained experimental data to populate these aforementioned equations in Chapter 4, the next step has been the validation of the tyre model, a process which is demonstrated in the preceding sections. The virtual tyre is mainly tested and validated in terms of vertical stiffness and relaxation length corresponding to lateral tyre slip.

Initially, the effect of model fidelity on tyre vertical stiffness is examined. The virtual tyre is loaded, by applying several different vertical forces, and for each vertical force the respective tyre vertical deformation is obtained. The outcome of this process is that, for the presented tyre model, tyre vertical stiffness depends on the level of modal reduction. In particular, it has been demonstrated that inclusion of additional modes results in a decrease of the observed tyre vertical stiffness, a conclusion which is in accordance with literature and also supported by the observation that – for a given load – the contribution of additional modes would increase tyre vertical deformation, hence decreasing tyre vertical stiffness. Moreover, this relation between modal reduction and tyre vertical stiffness is found to depend on the level of the applied vertical load.

The validation of the proposed tyre model in terms of vertical stiffness has been examined further and compared to experimental data obtained using an indoor tyre test rig and applying vertical force on the wheel centre against a stationary steel drum. The collected experimental data cover a broad range of vertical loading scenarios. In particular, data corresponding to the following cases have been obtained:

- Step transition,
- Pseudo – random transition, and
- Gradual transition.

The first two cases have been examined in relatively low levels of vertical force, while a considerably higher vertical force has been applied in the third case. The outcome of the comparison between the obtained experimental data and simulation results acquired for the exact same vertical force is that correlation has been achieved for the first two cases, where applied vertical load has been kept within a limited range.

On the contrary, comparison between experimental and simulation data corresponding to the third case reveals a fundamental limitation of the proposed modelling approach, which is associated with the limited number of structural modes included in the tyre model. This modal reduction leads to higher vertical stiffness values, compared to the measured ones, as the tyre appears to be stiffer since the contribution of the excluded modes is not taken into account. An additional limitation of the proposed model contributing to this phenomenon is that the experimentally acquired structural modes are linear and, consequently, the accuracy of the model decreases for cases of large deformations – for example, those corresponding to high vertical loads.

Moving the discussion to the response of the tyre to lateral slip variations, the following two test cases have been investigated:

- Relaxation length calculation as a function of forward speed, and
- Relaxation length calculation as a function of vertical load.

For each of the above test cases, the virtual tyre has been excited by steering angle variation, driven by a sinusoidal signal of increasing frequency. The relaxation lengths, corresponding to each simulation run, have been calculated by modelling the tyre as a single input (steering angle) – single output (lateral force) system and the poles of the respective transfer functions have been identified leading to the calculation of the associated time constant term. By taking into account the forward speed of the tyre, the relaxation length of each test scenario has been obtained. This process revealed that the relaxation length variation follows certain trends for both the above test scenarios. In particular, relaxation length increases with both longitudinal speed and vertical force, an observation which is in agreement with trends found in literature.



## **6. Conclusions, contribution to knowledge and suggestions for future work**

### **6.1 Conclusions**

In the first chapter of this work, a series of objectives has been defined. The fundamental criterion in setting these objectives has been the requirement to investigate the potential and limitations of developing a dynamic tyre model which exploits data derived directly from modal testing. To this end, these objectives reflect the phases of the research work required to develop the abovementioned model and have been set as follows:

- development of a high fidelity tyre model exploiting data obtained directly from performing modal testing on a physical tyre,
- three dimensional modal testing on a physical tyre adopting the free-free boundary condition,
- identification of eigenvalues and eigenvectors corresponding to a number of flexible tyre belt modes and
- validation of the abovementioned tyre model in cases where tyre response depends highly on tyre deformation.

The following sections describe each one of these objectives in detail. The main scope of this process is to examine how these challenges have been dealt with.

#### **6.1.1 Objective 1**

##### ***Development of a high-fidelity tyre model exploiting data obtained directly by performing modal testing on a physical tyre***

The dynamic tyre model presented in this work is based on a first principles approach, as demonstrated by Equation 3.3–1. The main assumption made in this expression is that the linear non-proportional viscous damping model is the most appropriate for simulating tyre belt damping – a modelling choice which is in accordance with the findings of Z. Geng et al. in [36] and A. A. Popov and Z. Geng in [87]. Starting from this first principles level, tyre motion has been divided into two distinct components; namely, the macroscopic motion of each belt node and the respective local deformation.

The next key point of this development process has been the expression of this nodal motion in terms of contribution of – rigid-body or elastic – tyre belt modes (see Equations 3.3–8 and 3.3–11), rather than spatial translation and deformation of tyre belt nodes. This approach had a dual contribution in developing further the presented tyre model (see Equation 3.3–22):

- this method allowed for expressing these equations of motion in terms of modal matrices instead of the inefficient – from a numerical and a parameterisation point of view – linear mass, stiffness and damping matrices, and
- the number of differential equations of motion representing the tyre is directly proportional to the respective fidelity, i.e. the number of tyre belt modes included in the corresponding matrices, rather than to the number of degrees of freedom, i.e. the number of nodes representing the tyre belt.

The first point listed above has been fundamental for this work, as the flexible component of the proposed tyre model is exclusively populated by a set of flexible belt modes, feasibly obtained by modal testing. To this end, Equation 3.3–15 may be considered as a cornerstone of this work as it allows the uncoupling of the equations of rigid body motion from those corresponding to local deformation and, in addition, eliminates all the system matrices associated with spatial coordinates and yields two systems of differential equations which are populated by modal or macroscopic inertial quantities (see Equation 3.3–23 for the rigid-body motion and Equation 3.3–24 for the local deformation).

The excitation of the first system of differential equations of motion, describing the rigid-body motion of the wheel, consists of user-defined inputs, of kinematic and dynamic nature, and the calculated contact forces. Given this excitation vector, the rigid-body motion of the wheel is calculated analytically. As the user-defined input quantities of the model are applied on the wheel centre, a point which is not represented by a node, the second system of differential equations of motion – corresponding to local deformation of the tyre belt – is excited by an equivalent force vector which introduces the same net effect in terms of wheel motion but is applied on circumferential tyre belt nodes rather than on the wheel centre. Moreover, this process is not required for the excitation component introduced by contact forces, as the respective calculation is performed at a nodal level which results in a distributed force vector. Finally, the total wheel response – as expressed by Equations 3.3–40 to 3.3–42 – is the superposition outcome of the analytically derived rigid-body motion, presented in Section 3.3.3, and the numerically calculated local deformation, Equations 3.3–25 and 3.3–26.

With reference to the implemented contact sub-model, an elastic boundary approach is adopted to accommodate for vertical contact phenomena and a distributed LuGre model is embedded. Initially, tyre belt nodes in proximity to the ground – within a user-defined spatial tolerance representing the radial length of the tyre tread – are identified as contact nodes. For each one of these nodes, the vertical component of the contact force is calculated based on nodal vertical position and vertical speed expressed in the inertial frame of reference. Having obtained the distribution of the vertical contact force along the contact patch, the next step is the calculation of the shear contact forces via the distributed LuGre model. Apart from the vertical force distribution, these contact forces also depend on the sliding speed of the wheel with respect to the ground, which in turn is a function of the following user imposed quantities:

- steering angle,
- wheel angular speed, and
- linear longitudinal speed

in addition to the calculated nodal deformation speed along the global longitudinal and lateral axes, see Equations 3.4–3 and 3.4–4.

### **6.1.2 Objective 2a**

#### ***Three-dimensional modal testing on a physical tyre adopting the free-free boundary condition***

This objective summarises the experimental work conducted for this project. The structural parameters required to populate the system matrices of the proposed tyre model have been defined in Chapter 3 of the present work, see Equation 3.3–25. Because of the nature of the proposed tyre model and specifically the way tyre motion is expressed, that is as the superposition of nodal translation and deformation, the structural parameters corresponding to tyre belt flexibility and found in the abovementioned equation have to derive from a mode set containing both rigid-body and flexible tyre belt modes. The above observation dictated the boundary condition of the performed modal testing, an attribute which represented one of the main challenges in terms of experimental design. Since the acquired data should reflect both rigid-body motion and tyre belt deformation, the free-free boundary condition has been adopted, see Figure 4.23 and Figure 4.24.

Populating the full frequency response function matrix, see Equation 4.2–1, could impose a significant challenge time-wise, a resource which is considered vital in the context of the present work. The efficiency of the above experimental procedure has been enhanced by adopting elements found in relevant literature. Initially, by exploiting the principle of reciprocity, the number of required frequency response functions is significantly reduced as only the upper or lower triangular frequency response function matrix has to be obtained. Furthermore, application of the modal constants consistency led to a further reduction in the required frequency response functions, as applying the excitation force on a single tyre belt node and measuring the resulting acceleration of all nodes – or vice versa – provides adequate information to identify the eigenvectors and the eigenvalues of the full tyre belt. Without any loss of information or any model simplification, these two steps reduced the total number of required frequency response functions from  $(3N)^2$  to  $9N$ , where  $N$  is the number of tyre belt nodes. The final step in this process has been the ad hoc assumption that there is no energy exchange between in-plane and out-of-plane tyre belt flexible modes. This assumption reduced the required frequency response functions further, from  $9N$  to  $5N$ .

The physical tyre has been discretised into 30 equi-spaced circumferential nodes along the tread centreline. Excitation force has been applied on the first node via an electromagnetic shaker driven by a white noise signal, along the radial, tangential, and lateral directions. In terms of data acquisition, both the excitation force and the resulting acceleration of each node have been acquired. For each combination of excitation and response, the above acquisition process has been repeated five times. The logged force and acceleration time histories have been analysed in the frequency domain, providing the respective spectra and ultimately the respective accelerance frequency response functions which yielded the receptance frequency response functions. By averaging these five transfer functions, the final frequency response function corresponding to each excitation-response combination and used to identify the structural properties of the tyre belt, is obtained. The outcome of this procedure is that Equation 4.2–9 is populated.

### **6.1.3 Objective 2b**

***Identification of eigenvalues and eigenvectors corresponding to a number of flexible tyre belt modes***

Having obtained the receptance frequency response functions corresponding to the in-plane and the out-of-plane modes of the tyre belt, a task described in Sections 4.2 and 4.3, Equation 4.2–9 has been populated. This has been a fundamental milestone of the present work, as it allowed for identifying the quantities found in Equation 3.3–24, namely the eigenvalues and the eigenvectors of a number of flexible modes of the tyre belt.

The identified receptance frequency response functions consisted of numerous tyre belt deformation modes, which introduced a substantial identification challenge – especially for cases where several modes were found within a limited frequency band – in the sense that the identified quantities used in Equation 3.3–24 had to correspond to a single mode each. The requirement to distinguish between the contribution of a particular mode and the contribution of neighbouring modes to the measured frequency response functions, dictated to a great extent the identification strategy presented in Section 4.4.1.

The first step has been the identification of eigenvalues corresponding to the modes of interest, which has been performed by fitting a series of fraction terms to measured data. The degrees of the numerator and the denominator polynomials of the fitted curve depend on the number of modes in the vicinity of the investigated mode and the respective eigenvalue is calculated based on the identified polynomial coefficients. In terms of residue identification, the fitted curve approach applied above would not generate reliable identified values, as the residue of each mode depends heavily on adjacent or out-of-band modes and consequently a more advanced identification process has been developed. In particular, every experimentally acquired frequency response function is examined around each observed resonance. For each resonance, the frequency response function is evaluated for the corresponding natural frequency, which has been identified in the previous step, and for a *fixing frequency* which is located relatively close to the identified natural frequency. Because of the relative position of these two frequency values along the frequency axis, it is assumed that out-of-band modes have an identical effect on the two abovementioned evaluations, an approach inspired by the work of B. J. Dobson in [27]. Correlation between the analytical, Equation 4.4–6, and the experimental, Equation 4.4–7, expressions yields the complex residues which ultimately form the eigenvectors of the tyre belt used in Equation 3.3–24.

The outcome of the tasks presented above, namely the damped natural frequency, the damping ratio and the residue of every investigated mode, is summarised in Section 4.4.2.

Moreover, a quantitative assessment of the identified natural frequencies is presented in the same section. As expected, the identified natural frequencies derived by radial, tangential and lateral response follow a specific pattern which is consistent between mode categories – that is radially, tangentially and laterally excited modes, see Figure 4.33. The maximum observed deviation in terms of identified natural frequency, expressed by function Delta in Equation 4.4–16, is equal to 3%, an error which is considered negligible in the context of the present work.

Section 4.4.3 has been dedicated to transforming the identified complex eigenvectors to real ones. At the early stages of this work, the motivation to complete this task has been to perform a qualitative visual assessment of the identified eigenvectors. Taking into account the experimental process followed to identify the complex eigenvectors, the transformation sequence proposed by Niedbal in [74] has been adopted. The core of this particular transformation method is Equation 4.4–32, which yielded the real mode shapes corresponding to the identified complex eigenvectors. Visual observation of the calculated real eigenvectors revealed agreement between the results presented in this work and previously conducted related research, for example the work of D. Guan et al. in [44]. Another – alarming – observation has been the apparent spatial noise observed in the real mode shapes, which would severely compromise the proposed tyre model.

To overcome this particular issue, a spatial digital filter has been applied to all mode shapes, as is demonstrated in Section 4.4.4. The calculated waveform representing each mode shape has been analysed in the spatial domain and the dominant spatial frequency component has been identified, see Figure 4.46. The next step has been the application of a spatial digital filter, so that the filtered waveform consists exclusively of the dominant component identified above, see Equations 4.4–39 and 4.4–40 and Figure 4.47. The process of reconstructing each mode shape based on the respective identified dominant component has been performed by applying the inverse Fast Fourier Transform and has offered a unique opportunity to enhance the proposed tyre model, by evaluating the mode shape for interpolated points other than the initial 30 nodes representing the tyre, a number which imposes a significant experimental workload in terms of acquisition of frequency response functions but could be found inadequate in terms of tyre modelling. Consequently, without any loss of fundamental information, this filtering process led to spatially noise-free mode shapes. The final necessary post-processing item has been the transformation of the identified eigenvectors from the

node-specific radial/tangential/lateral frame of reference, see Figure 4.21, to a frame of reference which axes are parallel to the wheel-fixed coordinate system presented in Section 3.2.2, so that the eigenvectors used for populating Equation 3.3–24 are expressed appropriately.

Visual examination of the identified real mode shapes reveals some anomalies in the form of repeated modes shapes corresponding to different natural frequencies, an observation which is not in accordance with relevant literature<sup>[44]</sup>. This phenomenon is investigated in Section 4.4.6, where it is presented that each set of repeated modes consists of modes demonstrating a different motion and deformation state of the tyre/wheel assembly. Moreover, every identified natural frequency is associated with two eigenvectors, due to tyre symmetry. The experimental procedure presented in Chapter 4 yields only one of these eigenvectors and consequently the second one is calculated analytically in Section 4.4.7 – by rotating the first eigenvector about the lateral axis of the tyre according to Equation 4.4–54. Having obtained these two eigenvectors, every possible nodal configuration corresponding to the respective tyre belt mode may be replicated by the tyre model, see Figure 4.60.

#### **6.1.4 Objective 3**

##### ***Validation of the presented tyre model in cases where tyre response depends highly on tyre deformation***

The validation of the proposed tyre model is performed on two distinct levels, namely tyre vertical stiffness and relaxation length. For the former case, tyre model response is investigated for cases of different tyre belt fidelity and, in addition, it is compared to data acquired using the experimental facility presented in Section 5.2. As presented in Section 5.3.2, four cases of tyre belt fidelity are examined, see Table 5.1. For each modal reduction case, the vertical deflection of the wheel centre is obtained by the proposed tyre model, see Table 5.2, as the result of the application of a varying vertical force, see Figure 5.3. The comparison between the four modal reduction test cases, in terms of vertical force versus vertical deflection, is illustrated in Figure 5.4 and in Figure 5.5. As expected<sup>[110]</sup>, the introduction of additional tyre belt modes resulted in increased overall tyre vertical compliance. This effect is quantified in Table 5.3.

With reference to data acquisition, the exploitation of the abovementioned dedicated tyre test facility has allowed for the application of a user-defined vertical force at the wheel centre, via a closed hydraulic circuit. Measurements have been acquired for three test cases of vertical force variation, namely:

- step variation,
- pseudo-random transient, and
- low rate transition between low and high vertical force values.

These vertical force data sets are displayed in Figure 5.6 to Figure 5.11. Simultaneously, the vertical position of the wheel centre has been obtained and the respective time histories are displayed in Figure 5.12 to Figure 5.15. The next step of this process has been the excitation of the tyre model using the experimentally acquired vertical force curves. Comparison between measured and simulated tyre vertical deflection reveals that correlation is achieved for the test cases where vertical force is kept below a certain level, see Figure 5.19 to Figure 5.21. In case the applied vertical force is increased further, deviation is observed between experimental data and simulation results. This phenomenon has been demonstrated by Equation 5.3–5.

The second validation level is performed by assessing relaxation length trends for two test scenarios, namely longitudinal speed variation and vertical force variation. Details on these test cases may be found in Table 5.6. The tyre is excited by a pre-specified sinusoidal steering angle profile of increasing frequency, see Figure 5.26. The steering angle time history and resulting lateral force time history of each test case are analysed in the frequency domain to calculate the transfer function of the tyre corresponding to a first-order system. As the forward speed of each test case is known, the corresponding transfer function is exploited to yield the respective relaxation length. This process is summarised in Table 5.10 and Table 5.12. For both test scenarios, the relaxation length trends are found to be in accordance with experimental findings from literature<sup>[12][67][68]</sup>.

## **6.2 Contribution to knowledge**

- A modal testing procedure, adopting the free-free boundary condition, has been developed to test a pneumatic tyre, in terms of both in-plane and out-of-plane modes. The boundary condition resulted in the identification of additional modes which have not been observed previously in similar experimental works.



- An efficient post-processing procedure has been developed to identify the mode shapes corresponding to the tyre belt structural modes. The novel element of this procedure is that out-of-band modes are taken into account and consequently the identified residues correspond exclusively to the investigated modes. In addition, a digital filter has been applied to the identified mode shapes which yielded waveforms free from spatial noise and optimal for introduction in a tyre modelling environment, without any loss of fundamental information.
- A fully operational three-dimensional tyre structural model has been formulated by exploiting properties derived directly by performing modal testing on a physical pneumatic tyre. Moreover, the presented tyre model includes non-linear kinematic effects, and the respective contribution in tyre response is coupled with tyre belt deformation.
- The presented tyre model has been partially validated. This validation process has been performed for two distinct scenarios, namely vertical stiffness and relaxation length. In terms of vertical stiffness, correlation to experimental data has been achieved for a limited range of vertical loads. As expected, when the applied vertical load reaches and exceeds a certain value, deviation is observed between a physical tyre and the tyre model. This vertical load value is a direct function of the performed modal reduction. Introduction of additional tyre belt structural modes would expand the valid vertical load range. With reference to the first-order behaviour of the tyre model, as expressed by the respective relaxation length, the model is in agreement with trends found in the literature for the cases of longitudinal speed and vertical load variation.

### **6.3 Suggestions for future work**

In the present work, a high-fidelity physical tyre model has been developed by exploiting data obtained directly from performing modal testing on a pneumatic tyre. The computational requirements of this tyre model depend on the number of included flexible modes of the tyre belt instead of the number of degrees of freedom. This has been achieved by solving the

equations of motion with respect to the contribution of each tyre belt mode on the total tyre motion and deformation rather than the calculation of the nodal spatial motion.

In terms of developing this model further, the first suggested action is the introduction of the wheel centre as an additional, centrally located, node. This feature would allow for the application of kinematic and dynamic inputs simply as another component of the excitation vector as opposed to the current formulation, where the equivalent force vector of Equation 3.3–52 has been introduced. As has been demonstrated in Chapter 3, the introduction of this central node, and the consequent requirement to perform modal testing on it, would alter the structural characteristics of the tyre/wheel assembly, but such a development would significantly simplify the model structure. In addition, with reference to the embedded contact model, real time capability could be achieved by adopting a lumped LuGre formulation instead of the current distributed one, along with modifying the elastic foundation of the tyre to a single Kelvin element from the currently implemented elastic layer. These actions would reduce the contact-associated number of equations to solve, from the current  $3N_{\text{cont}}$  to only 3 equations, where  $N_{\text{cont}}$  is the number of contact nodes.

Another suggestion, relevant to the one proposed above, is the introduction of a flexible wheel sub-model within the proposed tyre modelling approach. Relevant research, see the work of B. Kao et al. in [52] or the work of P. Kindt et al. in [59], suggests that the modal behaviour of typical passenger car wheels may influence to a great extent the tyre motion and deflection in the frequency band of interest. The effect of wheel motion and deflection has already been preliminary investigated in the context of the present work in Section 4.4.6. Such a sub-model could be introduced either by performing modal testing on the physical wheel, similarly to the approach adopted for the tyre belt sub-model, or by developing a separate finite element model, as wheel material properties are less laborious to identify.

Moreover, in order to capture camber-related phenomena, additional tyre belt nodes are required. In the present formulation, the tyre belt is represented by a series of nodes all located at the wheel-fixed XZ plane, see Figure 3.3. An introduction of two additional nodal series, one with a positive offset and one with a negative offset along the wheel-fixed Y axis, would allow for the camber angle of the wheel to have an effect on tyre vertical stiffness calculated by the model, as demonstrated in Section 5.3.1. The introduction of the additional series of nodes would be implemented in the present model by slightly modifying Equation

3.3–24 to accommodate of the additional equations of motion and the respective coupling with the already existing ones.

An additional enhancement of the proposed tyre model would be the capture of the effect that inflation pressure has on tyre belt eigenvectors and eigenvalues. These effects have been extensively investigated in the literature, see for example the work of Y. Guan et al. in [45] and the work of B. Kim et al. in [55]. In the first work it is suggested that eigenvectors are not affected by inflation pressure variations. On the other hand, both mentioned works produce data according to which natural frequencies and damping ratios depend heavily on inflation pressure. In particular, for the case of the freely suspended tyre, natural frequencies increase with inflation pressure, while damping ratios decrease. These dependencies could be implemented in the proposed tyre model by introducing two scaling factors in Equation 4.2–5, one for the pressure-dependent natural frequency  $\omega_r$  and one of the pressure-dependent damping ratio  $\xi_r$ . These, experimentally identified, scaling factors would then be directly reflected in the core of the tyre model by adjusting the eigenvalues  $s_i$ , found in Equation 3.3–24, based on the inflation pressure.

## References

- [1] **S. Adhikari, J. Woodhouse**, *Identification of damping: part 1, viscous damping*, Journal of Sound and Vibration, v. 243(1), pp. 43-61, 2001
- [2] **S. Adhikari, J. Woodhouse**, *Identification of damping: part 2, non-viscous damping*, Journal of Sound and Vibration, v. 243(1), pp. 63-88, 2001
- [3] **V. Alkana, S. M. Karamihas, G. Anlas**, *Experimental analysis of tyre-enveloping characteristics at low speed*, Vehicle System Dynamics, v. 47(5), pp. 575-587, 2009
- [4] **R. A. B. Almeida, A. P. V. Urgueira, N. M. M. Maia**, *Further developments on the estimation of rigid body properties from experimental data*, Mechanical System and Signal Processing, v. 24, pp. 1391-1408, 2010
- [5] **R. A. B. Almeida, N. M. M. Maia, A. P. V. Urgueira**, *Improved techniques for the identification of rigid body properties*, Conference proceedings of the Society for Experimental Mechanics Series, IMAC-XXII: Conference and Exposition on Structural Dynamics – Structural Health Monitoring, 2005
- [6] **P. Andersson, K. Larsson, F. Wullens, W. Kropp**, *High frequency dynamic behaviour of smooth and patterned passenger car tyres*, Acta Acustica United with Acustica, v. 90, pp. 445-456, 2004
- [7] **G. W. Asher**, *A method of normal mode excitation utilizing admittance measurements*, Proceedings of National Specialists Meeting in Dynamics and Aeroelasticity, Institute of Aeronautical Sciences, pp. 69-76, 1958
- [8] **M. Baecker, A. Gallrein, H. Haga**, *Simulating very large tire deformations with CDTire*, SAE International Journal of Passenger Cars – Mechanical Systems, v. 2(1), pp. 765-771, 2009
- [9] **E. Bakker, L. Nyborg, H. B. Pacejka**, *Tire modelling for use in vehicle dynamics studies*, SAE Paper, No. 870421, 1987
- [10] **E. Bakker, H. B. Pacejka, L. Lidner**, *A new tire model with an application in vehicle dynamics studies*, SAE Paper, No. 890087, 1989
- [11] **E. Balmes**, *New results on the identification of normal modes from experimental complex modes*, Mechanical Systems and Signal Processing, v. 11(2), pp. 229-243, 1997
- [12] **P. Bandel, C. di Bernardo**, *A test for measuring tyre characteristics of tires*, Tire Science and Technology, v. 17(2), pp. 126-137, 1989
- [13] **M. Berzeri, M. Campanelli, A. A. Shabana**, *Definition of the elastic forces in the finite-element absolute nodal coordinate formulation and the floating frame of reference formulation*, Multibody System Dynamics, v. 21, pp. 21-54, 2001

- [14] **M. Berzeri, A. A. Shabana**, *Development of simple models for the elastic forces in the absolute nodal co-ordinate formulation*, Journal of Sound and Vibration, v. 235(4), pp. 539-565, 2000
- [15] **I. J. M. Besselink, L. W. L. Houben, I. B. A. Op Het Veld, A. J. C. Schmeitz**, *Run-flat versus conventional tyres: an experimental and model based comparison*, VDI Berichte, v. 2014, pp. 185-202, 2007
- [16] **I. J. M. Besselink, A. J. C. Schmeitz, H. B. Pacejka**, *An improved Magic Formula / Swift tyre model that can handle inflation pressure changes*, Vehicle System Dynamics, v. 48(s1), pp. 337-352, 2010
- [17] **C. Canudas-de-Wit, P. Tsiotras, E. Velenis, M. Basset, G. Gissinger**, *Dynamic friction models for road/tire longitudinal interaction*, Vehicle System Dynamics, v. 39(3), pp. 189-226, 2003
- [18] **T. G. Carne, D. T. Griffith, M. E. Casias**, *Support conditions for experimental modal analysis*, Sound and Vibration, June 2007, pp. 10-15, 2007
- [19] **F. Chengjian, G. Dihua**, *Tire modelling for vertical properties including enveloping properties using experimental modal parameters*, Vehicle System Dynamics, v. 40(6), pp. 419-433, 2003
- [20] **F. Chengjian, G. Dihua**, *The quantitative analysis and experimental verification of the tire static enveloping model using experimental modal parameters*, Vehicle System Dynamics, v. 44(9), pp. 678-688, 2006
- [21] **J. R. Cho, K. W. Kim, W. S. Yoo, S. I. Hong**, *Mesh generation considering detailed tread blocks for reliable 3D tire analysis*, Advances in Engineering Software, v. 35, pp. 105-113, 2004
- [22] **J. R. Cho, H. S. Jeong, W. S. Yoo**, *Multi-objective optimization of tire carcass contours using a systematic aspiration-level adjustment procedure*, Computational Mechanics, v. 29, pp. 498-509, 2002
- [23] **A. K. Cline, I. S. Dhillon**, *Handbook of linear algebra*, Chapter 45, CRC Press, 2nd edition, London, 2006
- [24] **M. V. Cook**, *Flight dynamics principles*, Butterworth-Heinemann, 2<sup>nd</sup> edition, Oxford, 2007
- [25] **L. Cremer, M. Heckl, E. E. Ungar**, *Structure-borne sound*, Springer Verlag, 2<sup>nd</sup> edition, 1988
- [26] **J. Deur, V. Ivanovic, M. Troulis, C. Milano, D. Hrovat, J. Asgari**, *Extensions of the LuGre tyre friction model related to variable slip speed along the contact patch length*, Vehicle System Dynamics, v. 3(s1), pp. 508-524, 2011
- [27] **B. J. Dobson**, *A straight-line technique for extracting modal properties from frequency response data*, Mechanical Systems and Signal Processing, v. 1(1), pp. 29-40, 1987
- [28] **H. R. Dorfi**, *Tire cleat impact and force transmission: Modeling based on FTire and correlation to experimental data*, SAE Technical Papers, v. 41, pp. 734-743, 2004
- [29] **J. R. Ellis**, *Vehicle handling dynamics*, Mechanical Engineering Publications, London, 1994

- [30] **D. J. Ewins**, *Modal testing*, Research Studies Press LTD, 2<sup>nd</sup> edition, Baldock, 2000
- [31] **P. Fansher, J. Bernard, C. Clover, C. Winkler**, *Representing truck tire characteristics in simulations of braking and braking-in-a-turn manoeuvres*, *Vehicle System Dynamics*, vol. 27(s1), pp. 207-220, 1997
- [32] **A. M. Fareed, F. Wahl**, *Identification of rigid body parameters using experimental modal analysis data*, *Technische Mechanik*, v. 21(1), pp. 63-75, 2001
- [33] **U. Fuellekrug**, *Computation of real normal modes from complex eigenvectors*, *Mechanical Systems and Signal Processing*, v. 22, pp. 57-65, 2008
- [34] **A. Gallrein, M. Backer**, *CDTire: a tire model for comfort and durability applications*, *Vehicle System Dynamics*, v. 45(s1), pp. 69-77, 2007
- [35] **A. Gallrein, J. De Cuyper, W. Dehandschutter, M. Backer**, *Parameter identification for LMS CDTire*, *Vehicle System Dynamics*, v. 43(s1), pp. 444-456, 2005
- [36] **Z. Geng, A. A. Popov, D. J. Cole**, *Measurement, identification and modelling of damping in pneumatic tyres*, *International Journal of Mechanical Sciences*, v. 49, pp. 1077-1094, 2007
- [37] **M. Hamid Reza Ghoreishy**, *A numerical study on the non-linear finite element analysis of a tyre under axisymmetric loading*, *Iranian Polymer Journal (English Edition)*, v. 11(5), pp. 325-332, 2002
- [38] **G. Gim, Y. Choi, S. Kim**, *A semiphysical tyre model for vehicle dynamics analysis of handling and braking*, *Vehicle System Dynamics*, v. 43(s1), pp. 267-280, 2005
- [39] **M. Gipser**, *FTire: a physically based application-oriented tyre model for use with detailed MBS and finite-element suspension models*, *Vehicle System Dynamics*, vol. 43(s1), pp. 76-91, 2005
- [40] **M. Gipser**, *FTire – the tire simulation model for all application related to vehicle dynamics*, *Vehicle System Dynamics*, v. 45(s1), pp. 139-151, 2007
- [41] **P. Gruber, R. S. Sharp, A. D. Crocombe**, *Friction and camber influences on the static stiffness properties of a racing tyre*, *Proceedings of the Institution of Mechanical Engineers, Part D: Journal of Automobile Engineering*, v. 222, pp. 1965-1976, 2008
- [42] **P. Gruber, R. S. Sharp, A. D. Crocombe**, *Normal and shear forces in the contact patch of a braked racing tyre. Part 1: results from a finite-element model*, *Vehicle System Dynamics*, v. 50(2), pp. 323-337, 2012
- [43] **D. Guan, C. Fan, X. Xie**, *A dynamic tyre model of vertical performance rolling over cleats*, *Vehicle System Dynamics*, v. 43(s1), pp. 209-222, 2005
- [44] **D. Guan, L. H. Yam, M. P. Mignolet, Y. Y. Li**, *Techniques: Experimental modal analysis of tires*, *Experimental Techniques*, v. 24(6), pp. 39-45, 2000

- [45] **Y. Guan, G. Cheng, G. Zhao, H. Zhang**, *Investigation of the vibration characteristics of radial tires using experimental and numerical techniques*, Journal of Reinforced Plastics and Composites, v. 30(24), pp. 2035-2050, 2011
- [46] **K. Guo, D. Lu**, *UniTire: unified tire model for vehicle dynamic simulation*, Vehicle System Dynamics, v. 45(s), pp. 79-99, 2007
- [47] **K. K. Gupta, J. L. Meek**, *Finite element multidisciplinary analysis*, American Institute of Aeronautics and Astronautics, Reston, 2003
- [48] **H. Haga**, *Evaluation of tyre models for durability loads prediction using a suspension-on-a-drum environment*, Vehicle System Dynamics, v. 43(s1), pp. 281-296, 2005
- [49] **W. Hall, J. Mottram, D. Donnelly, R. Jones**, *Characterisation of the contact patch behaviour of an automobile tyre by physical testing*, International Journal of Vehicle Design, v. 31(3), pp. 354-376, 2003
- [50] **A. Higuchi, H. B. Pacejka**, *The relaxation length concept at large wheel slip and camber*, Vehicle System Dynamics, v. 27(s1), pp. 50-64, 1997
- [51] **S. Jansen, L. Verhoeff, R. Cremers, A. Schmeitz, and I. Besselink**, *MF-SWIFT simulation study using benchmark data*, Vehicle System Dynamics, v. 43(1), pp. 92-101, 2005
- [52] **B. Kao, M. Riesner, P. Surulinarayanasami**, *Modal Analysis of a Tire and Wheel and Its Application for Vehicle Ride Evaluation*, SAE Paper, No. 860826, 1986
- [53] **H. Kardestunver, D. H. Norrie**, *Finite element handbook*, McGraw-Hill, New York – London, 1987
- [54] **G. Kerschen, K. Worden, A. F. Vakakis, J. C. Golinval**, *Past, present and future of non-linear system identification in structural dynamics*, Mechanical Systems and Signal Processing, v. 20, pp. 505-592, 2006
- [55] **B. S. Kim, C. H. Chi, T. K Lee**, *A study on radial directional natural frequency and damping ratio in a vehicle tyre*, Applied Acoustics, v. 68, pp. 538-556, 2007
- [56] **S. Kim, K. Kondo, T. Akasaka**, *Contact pressure distribution of radial tire in motion with camber angle*, Tire Science and Technology, v. 28(1), pp. 2-32, 2000
- [57] **S. Kim, P. E. Nikravesh, G. Gim**, *A two-dimensional tire model on uneven roads for vehicle dynamic simulation*, Vehicle System Dynamics, v. 46(10), pp. 913-930, 2008
- [58] **P. Kindt, P. Sas, W. Desmet**, *Development and validation of a three-dimensional ring-based structural tyre model*, Journal of Sound and Vibration, v. 326, pp. 852-869, 2009
- [59] **P. Kindt, P. Sas, W. Desmet**, *Three-dimensional ring model for the prediction of the tyre structural dynamics behaviour*, Proceedings of ISMA 2008, pp. 4155-4170, 2008

- [60] **F. Kozhevnikov**, *The vibrations of a free and loaded tyre*, Journal of Applied Mathematics and Mechanics, v. 70, pp. 223-228, 2006
- [61] **C. Lecomte, W. R. Graham**, *A tyre belt model based on a 2D beam theory*, Technical Report CUED/-AERO/TR, No. 28, 2008
- [62] **C. Lecomte, W. R. Graham, D. J. O' Boy**, *Validation of a belt model for prediction of hub forces from a rolling tire*, Tire Science and Technology, v. 37(2), pp. 62-102, 2009
- [63] **I. Lopez, R. R. J. J. van Doorn, R. van der Steen, N. B. Roozen, H. Nijmeijer**, *Frequency loci veering due to deformation in rotating tyres*, Journal of Sound and Vibration, v. 324, pp. 622-639, 2009
- [64] **I. Lopez, R. E. A. Blom, N. B. Roozen, H. Nijmeijer**, *Modelling vibrations on deformed rolling tyres – a modal approach*, Journal of Sound and Vibration, v. 307, pp. 481-494, 2007
- [65] **A. E. H. Love**, *The small free vibrations and deformation of a thin elastic shell*, Philosophical Transactions of the Royal Society of London, v. 179, pp. 491-546, 1888
- [66] **P. Lugner, H. Pacejka, M. Plochl**, *Recent advances in tyre models and testing procedures*, Vehicle System Dynamics, v. 43(6 – 7), pp. 413-426, 2005
- [67] **W. Luty**, *An analysis of tire relaxation process during dynamic changes of cornering angle*, Journal of KONES Powertrain and Transport, v. 16(1), 2009
- [68] **W. Luty**, *An analysis of tire relaxation length in conditions of the wheel side cornering angle oscillations*, Journal of KONES Powertrain and Transport, v. 18(1), 2011
- [69] **N. M. M. Maia, J. M. M. Silva**, *Building a general model for damping: further contributions*, Proceedings of the International Modal Analysis Conference – IMAC, v. 1, pp. 591-594, 1998
- [70] **N. M. M. Maia, J. M. M. Silva et al**, *Theoretical and experimental modal analysis*, Research Studies Press LTD, Taunton, 1997
- [71] **J. P. Maurice, M. Berzeri, H. B. Pacejka**, *Pragmatic tyre model for short wavelength side slip variations*, Vehicle System Dynamics, v. 31(2), pp. 65-94, 1999
- [72] **J. P. Maurice, H. B. Pacejka**, *Relaxation Length Behaviour of Tyres*, Vehicle System Dynamics, v. 27(s1), pp. 339-342, 1997
- [73] **G. Mavros**, *Tyre models for vehicle handling analysis under steady-state and transient manoeuvres*, PhD Thesis, Loughborough University, 2005
- [74] **N. Niedbal**, *Analytical determination of real normal modes from measured complex responses*, Proceedings of 25th Structures, Structural Dynamics and Materials Conference, pp. 292-295, 1994
- [75] **C. Oertel and A. Fandre**, *Ride comfort situations and steps towards life time calculations: RMOD-K and ADAMS*, International ADAMS Users' Conference, Berlin, 1999



- [76] **M. Okuma, W. Heylen, P. Sas**, *Identification of rigid body properties of 3-D frame structure by MCK identification method*, Proceedings of the 25<sup>th</sup> International Conference on Noise and Vibration Engineering, ISMA, pp. 1239-1245, 2000
- [77] **M. Okuma, Q. Shi**, *Identification of principal rigid body modes under free-free boundary condition*, Journal of Vibration and Acoustics, v. 119, pp. 341-345, 1997
- [78] **H. B. Pacejka**, *Magic Formula tyre model with transient properties*, Vehicle System Dynamics, v. 27(s1), pp. 234-249, 1997
- [79] **H. B. Pacejka**, *Spin: camber and turning*, Vehicle System Dynamics, v. 43(1), pp. 3-17, 2005
- [80] **H. B. Pacejka**, *Tyre and Vehicle Dynamics*, Second edition, Butterworth-Heinemann, Oxford 2006
- [81] **H. B. Pacejka, E. Bakker**, *The Magic Formula tyre model*, Proceedings of 1<sup>st</sup> Colloquium on Tyre Models for Vehicle Analysis, Delft, 1991
- [82] **M. Pau, B. Leban, A. Baldi**, *Ultrasonic measurements of contact area and pressure distribution of a pneumatic tire on a rigid surface*, Tire Science and Technology, v. 36(1), pp. 43-62, 2008
- [83] **J. P. Pauwelussen, L. Gootjes, C. Schroder, K.-U. Kohne, S. Jansen, A. Schmeitz**, *Full vehicle ABS braking using the SWIFT rigid ring tyre model*, Control Engineering Practice, v. 11, pp. 199-207, 2003
- [84] **J. Perisse, J. M. Clairet, J. F. Hamet**, *Modal testing of a smooth tire in low and medium frequency – estimation of structural parameters*, SPIE proceedings series, pp. 960-967, 2000
- [85] **R. J. Pinnington**, *A wave model of a circular tyre. Part 1: belt modelling*, Journal of Sound and Vibration, v. 290, pp. 101-132, 2006
- [86] **R. J. Pinnington**, *A wave model of a circular tyre. Part 2: side-wall and force transmission modelling*, Journal of Sound and Vibration, v. 290, pp. 133-168, 2006
- [87] **A. A. Popov, Z. Geng**, *Modelling of vibration damping in pneumatic tyres*, Vehicle System Dynamics, v. 43(s1), pp. 145-155, 2005
- [88] **M. Prandina, J. E. Mottershead, E. Bonisoli**, *An assessment of damping identification methods*, Journal of Sound and Vibration, v. 323, pp. 662-676, 2009
- [89] **S. S. Rao**, *The finite element method in engineering*, Butterworth-Heinemann, 5<sup>th</sup> edition, Oxford, 2011
- [90] **K. Ramji, V. K. Goel, V. H. Saran**, *Stiffness properties for small-sized pneumatic tyres*, Proceedings of the Institution of Mechanical Engineers, Part D: Journal of Automobile Engineering, v. 216(2), pp. 107-114, 2002
- [91] **E. Sakai**, *Measurement and visualization of the contact pressure distribution of rubber disks and tires*, Tire Science and Technology, v. 23(4), pp. 238-255, 1995

- [92] **A. J. C. Schmeitz, W. D. Verstedden**, *Structure and parameterization of MF-Swift, a Magic Formula-based rigid ring tire model*, Tyre Science and Technology, v. 37(3), pp. 142-164, 2009
- [93] **A. J. C. Schmeitz, I. J. M. Besselink, S. T. H. Jansen**, *TNO MF-SWIFT*, Vehicle System Dynamics, v. 45(s), pp. 121-137, 2007
- [94] **A. A. Shabana**, *Definition of the slopes and the finite element absolute nodal coordinate formulation*, Multibody system dynamics, v. 1, pp. 339-348, 1997
- [95] **A. A. Shabana, R. Yakoub**, *Three-dimensional absolute nodal coordinate formulation for beam elements: theory*, Journal of Mechanical Design, v. 123, pp. 606-613, 2001.
- [96] **A. A. Shabana, R. Yakoub**, *Three-dimensional absolute nodal coordinate formulation for beam elements: implementation and applications*, Journal of Mechanical Design, v. 123, pp. 614-621, 2001
- [97] **J. Shang, D. Guan, L. H. Yam**, *Study on tire dynamic cornering properties using experimental modal parameters*, Vehicle System Dynamics, v. 37(2), pp. 129-144, 2002
- [98] **H. Shiobara, T. Akasaka, S. Kagami, S. Tsutsumi**, *One-dimensional contact pressure distribution of radial tires in motion*, Tire Science and Technology, v. 23(2), pp. 116-135, 1995
- [99] **H. Shiobara, T. Akasaka, S. Kagami**, *Two-dimensional contact pressure distribution of a radial tire in motion*, Tire Science and Technology, v. 24(4), pp. 294-320, 1996
- [100] **W. Soedel**, *Vibrations of shells and plates*, Marcel Dekker Inc, New York, 2004
- [101] **G. Strang**, *Linear algebra and its applications*, Academic Press, 2<sup>nd</sup> edition, New York, 1980
- [102] **H. Sugiyama, Y. Suda**, *A curved beam element in the analysis of flexible multi-body systems using the absolute nodal coordinates*, Proceedings of the Institution of Mechanical Engineers, Part K: Journal of Multi-body dynamics, v.221(2), pp. 219-231, 2007
- [103] **H. Sugiyama, J. Gerstmayr, A. A. Shabana**, *Deformation modes in the finite element absolute nodal coordinate formulation*, Journal of Sound and Vibration, v. 298, pp. 1129-1149, 2006
- [104] **H. Sugiyama, Y. Suda**, *Non-linear elastic ring tyre model using the absolute nodal coordinate formulation*, Proceedings of the Institution of Mechanical Engineers, Part K: Journal of Multi-body dynamics, v. 223(3), pp. 211-219, 2009
- [105] **R. K. Taylor, L. L. Bashford, M. D. Schrock**, *Methods for measuring vertical tire stiffness*, Transactions of the American Society of Agricultural Engineers, v. 43(6), pp. 1415-1419, 2000
- [106] **W. Tong, Z. Lingmi, T. K. Fah**, *Extraction of real modes and physical matrices from modal testing*, Earthquake Engineering and Engineering Vibration, v. 10, pp. 219-227, 2011
- [107] **P. Tsiotras, E. Velenis, M. Sorine**, *A LuGre tire friction model with exact aggregate dynamics*, Vehicle System Dynamics, v. 42(3), pp. 195-210, 2004

- [108] **A. Tsotras, G. Mavros**, *Frictional contact behaviour of the tyre: the effect of tread slip on the in-plane structural deformation and stress field development*, *Vehicle System Dynamics*, v. 48(8), pp. 891-921, 2009
- [109] **A. Tsotras, G. Mavros**, *A modal-based derivation of transient pressure distribution along the tyre-road contact*, *SAE International Journal of Passenger Cars – Mechanical Systems*, v. 2(1), pp. 680-692, 2009
- [110] **A. Tsotras**, *On the interaction between modal behaviour and contact force development of a pneumatic tyre*, PhD Thesis, Loughborough University, 2010
- [111] **A. Tsotras, G. Mavros**, *The simulation of in-plane tyre modal behaviour: a broad modal range comparison between analytical and discretised modelling approaches*, *Vehicle System Dynamics*, v. 47(11), pp. 1377-1400, 2009
- [112] **E. Velenis, P. Tsotras, C. Canudas-de-Wit and M. Sorine**, *Dynamic tyre friction models for combined longitudinal and lateral vehicle motion*, *Vehicle System Dynamics*, v. 43(1), pp. 3-29, 2005
- [113] **E. Velenis, P. Tsotras, C. Canudas-de-Wit**, *Extension of the LuGre dynamic tire friction model to 2D motion*, *Proceedings of the 10<sup>th</sup> IEEE Mediterranean Conference on Control and Automation – MED 2002*, Lisbon, Portugal, 9 – 12 July 2002
- [114] **P. D. Welch**, "The Use of Fast Fourier Transform for the Estimation of Power Spectra: A Method Based on Time Averaging Over Short, Modified Periodograms", *IEEE Transactions on Audio Electroacoustics*, v. 15(2), pp. 70–73, 1967
- [115] **J. Woodhouse**, *Linear damping models for structure vibration*, *Journal of Sound and Vibration*, v. 215(3), pp. 547-569, 1998
- [116] **L. H. Yam, D. H. Guan, A. Q. Zhang**, *Three-dimensional mode shapes of a tire using experimental modal analysis*, *Experimental Mechanics*, v. 40(4), pp. 369-375, 2000
- [117] **A. Zanten, R. Erhardt, A. Lutz**, *Measurement and Simulation of Transients in Longitudinal and Lateral Tire Forces*, *SAE Paper*, No. 900210, 1990
- [118] **P. W. A. Zegelaar, H. B. Pacejka**, *Dynamic tyre responses to brake torque variations*, *Vehicle System Dynamics*, v. 27(1), pp. 65-79, 1997
- [119] **J. Zhou, J. Y. Wong, R. S. Sharp**, *A multi-spoke, three plane tyre model for simulation of transient behaviour*, *Vehicle System Dynamics*, v. 31(1), pp. 35–45, 1999

## Appendix A – Table of Figures

Figure 1.1 – Tyre formulation (1: tyre tread, 2: rim, 3: tyre belt, sidewall and air cavity).....	14
Figure 2.1 – Magic Formula curves and influence of constant terms ([80]) .....	20
Figure 2.2 – The brush tyre model; view of the driven and side-slipping tyre ([80]) .....	21
Figure 2.3 – Vectorial form of total slip .....	24
Figure 2.4 – SWIFT model formulation ([93]) .....	27
Figure 2.5 – Frame of reference and velocities at the contact patch. Derivation of the distributed tire model ([107]) .....	33
Figure 2.6 – Some force elements between adjacent belt elements and rim ([40]) .....	35
Figure 2.7 – Force elements between single belt node and rim (only those in radial direction shown) ([40]) .....	35
Figure 2.8 – First unloaded vibration modes for use in FTire parameterization and validation ([39]) .....	37
Figure 2.9 – CDTire model family (Model 20) ([34]) .....	38
Figure 2.10 – CDTire model family (Model 30) ([34]) .....	38
Figure 2.11 – CDTire model family (Model 40) ([34]) .....	39
Figure 2.12 – Generic description of CDTire parameter identification procedure ([34]) .....	40
Figure 2.13 – Vertical force for a trapezoid cleat 20 mm high (without a suspension; drum surface speed, 40 km h <sup>-1</sup> ) ([48]) .....	41
Figure 2.14 – Longitudinal force for a variant cleat 36 mm high (drum surface speed, 40 km h <sup>-1</sup> ) ([48]) .....	41
Figure 2.15 – Longitudinal force for a variant cleat 36 mm high (drum surface speed, 20 km h <sup>-1</sup> ) ([48]) .....	42
Figure 2.16 – Illustration of flexible belt and rigid rim ([75]) .....	43
Figure 2.17 – Calculated mode shapes ([75]) .....	43
Figure 2.18 – Tire model: orthotropic thin plate under tension ([84]) .....	45
Figure 2.19 – Correlation between theoretical (pre-tensed orthotropic thin plate) and experimental results. (Left pair: model parameters updated within [20-400]Hz – Right pair: model parameters updated within [500-2000] Hz) ([84]) .....	46
Figure 2.20 – The first four mode shapes derived by equation 2.8–3 ([60]) .....	46
Figure 2.21 – Geometry of the infinite cylinder ([62]) .....	47
Figure 2.22 – Real part of input radial mobility as a function of speed ([85]) .....	48
Figure 2.23 – Ring model mode shapes ([110]) .....	49
Figure 2.24 – Flexible ring on elastic foundation with internal pressure ([58]) .....	50

Figure 2.25 – Identification of general viscous damping in the pneumatic tyre (7.5 bar): (a) modal coordinates; (b) physical coordinates ([36]) .....	52
Figure 3.1 – Graphical representation of the four user-defined input quantities of the proposed tyre model.....	60
Figure 3.2 – Indoor tyre testing facility (photograph courtesy of the Department of Aeronautical and Automotive Engineering, Loughborough University).....	61
Figure 3.3 – Tyre belt node position expressed in both the wheel-fixed and the upright-fixed frames of reference .....	62
Figure 3.4 – Transformation from upright-fixed and rig-fixed frames of reference.....	64
Figure 3.5 – Vertical translational degree of freedom; a) Configuration at the first time step; b) Configuration after the application of $F_z$ .....	66
Figure 3.6 – Nodal configuration of the belt – first rigid body mode .....	70
Figure 3.7 – Nodal configuration of the belt – second rigid body mode .....	71
Figure 3.8 – Nodal configuration of the belt – third rigid body mode.....	71
Figure 3.9 – Nodal configuration of the belt – fourth rigid body mode .....	72
Figure 3.10 – Nodal configuration of the belt – fifth rigid body mode.....	72
Figure 3.11 – Nodal configuration of the belt – sixth rigid body mode .....	73
Figure 3.12 – Expression of vertical acceleration vector in the inertial and the rig-fixed frame of reference.....	87
Figure 3.13 – Expression of vertical acceleration vector in the rig-fixed and the upright-fixed frame of reference .....	88
Figure 3.14 – Expression of vertical acceleration vector in the upright-fixed and the wheel-fixed frame of reference .....	89
Figure 3.15 – Illustration of the elastic boundary introduced between the tyre belt and the ground.....	96
Figure 3.16 – Distinction between nodes located within the elastic boundary (contact nodes) and nodes located above the elastic boundary (no contact nodes).....	97
Figure 3.17 – Frames of reference and velocities at the contact patch ([113]).....	100
Figure 3.18 – Illustration of the ‘tyre on a drum’ option offered by the proposed tyre model.....	102
Figure 4.1 – Linearity of the tyre structure under steady sinusoidal excitation with different amplitudes ([36]).....	106
Figure 4.2 – Real and imaginary parts of the frequency response functions ([36]) .....	107
Figure 4.3 – Measured and fitted frequency response functions; a) real and imaginary parts, b) amplitudes and phase angles ([36]) .....	108

Figure 4.4 – Identification of general viscous damping in the pneumatic tyre expressed in modal coordinates ([36]) .....	111
Figure 4.5 – Frequency response function for white noise excitation ([44]).....	112
Figure 4.6 – Frequency response function for sinusoidal sweep excitation ([44]) .....	112
Figure 4.7 – Calculation results of contact forces distributions under three static loads ([19]) .....	114
Figure 4.8 – The calculated static vertical force as function of the static deflection ([19]).....	114
Figure 4.9 – Vertical stiffness versus vertical load (300Hz) ([20]).....	115
Figure 4.10 – Footprint length versus vertical load (300Hz) ([20]) .....	116
Figure 4.11 – Vertical stiffness versus vertical load (700Hz) ([20]).....	116
Figure 4.12 – Footprint length versus vertical load (700Hz) ([20]) .....	116
Figure 4.13 – Vertical stiffness versus vertical load (non-linear sidewall) ([20]) .....	117
Figure 4.14 – Footprint length versus vertical load (non-linear sidewall) ([20]) .....	117
Figure 4.15 – Comparison between calculated and test results of transfer function of lateral force to yaw angle ([97]) .....	119
Figure 4.16 – Comparison between calculated and test results of transfer function of self-aligning moment to yaw angle ([97]) .....	119
Figure 4.17 – Transfer function of self-aligning moment to yaw angle for high frequency range at two velocities ([97]) .....	120
Figure 4.18 – Point mobility of the tyre measured at the centre of the belt ([84]).....	121
Figure 4.19 – Influence of driving force area on point mobility ([84]).....	121
Figure 4.20 – Corrective term due to local stiffness effect for several excitation circular areas ([84]).....	122
Figure 4.21 – Radial/lateral/tangential node-specific frame of reference .....	123
Figure 4.22 – Frequency response function (lateral response)/(radial excitation) .....	126
Figure 4.23 – Experimental layout for measurement of in-plane tyre belt modes .....	127
Figure 4.24 – experimental layout for measurement of out-of-plane tyre belt modes .....	128
Figure 4.25 – Changes in modal frequency as a function of the frequency ratio ([18]) .....	131
Figure 4.26 – Changes in modal damping as a function of the frequency ratio ([18]) .....	131
Figure 4.27 – User-defined band surrounding the investigated flexible mode of the tyre belt .....	134
Figure 4.28 – Variation of identified receptance frequency response function as a function of fixing frequency $\omega_f$ .....	137

Figure 4.29 – Selected receptance frequency response function based on the criterion introduced in equation 4.4–9 .....	137
Figure 4.30 – Frequency response function corresponding to a radially excited tyre belt mode .....	139
Figure 4.31 – Frequency response function corresponding to a tangentially excited tyre belt mode .....	140
Figure 4.32 – Frequency response function corresponding to a laterally excited tyre belt mode .....	141
Figure 4.33 – Comparison of the identified natural frequencies for all the tested combinations of excitation and response.....	142
Figure 4.34 – Identified residues: complex radial modes, radial response (top row: modes 1 to 5; bottom row: modes 6 to 10).....	143
Figure 4.35 – Identified residues: complex radial modes, tangential response (top row: modes 1 to 5; bottom row: modes 6 to 10).....	143
Figure 4.36 – Identified residues: complex tangential modes, radial response (top row: modes 1 to 7; bottom row: modes 8 to 13).....	144
Figure 4.37 – Identified residues: complex tangential modes, tangential response (top row: modes 1 to 7; bottom row: modes 8 to 13).....	144
Figure 4.38 – Identified residues: complex lateral modes, lateral response (top row: modes 1 to 6; bottom row: modes 7 to 13).....	145
Figure 4.39 – Complex eigenvector components demonstrating an “almost” real behaviour	146
Figure 4.40 – Complex eigenvector components demonstrating a heavily complex behaviour .....	146
Figure 4.41 – Real mode shapes; radial excitation radial response (top row: modes 1 to 5; bottom row: modes 6 to 10).....	150
Figure 4.42 – Real mode shapes; radial excitation, tangential response (top row: modes 1 to 5; bottom row: modes 6 to 10).....	150
Figure 4.43 – Real mode shapes; tangential excitation, radial response (top row: modes 1 to 7; bottom row: modes 8 to 13).....	151
Figure 4.44 – Real mode shapes; tangential excitation, tangential response (top row: modes 1 to 7; bottom row: modes 8 to 13).....	151
Figure 4.45 – Real mode shapes; lateral excitation, lateral response (top row: modes 1 to 6; bottom row: modes 7 to 11).....	151

Figure 4.46 – Waveform corresponding to a real mode shape analysed in the space domain.	152
Figure 4.47 – Application of equations 4.4–39 and 4.4–40 in the spatial frequency spectrum of Figure 4.46.	153
Figure 4.48 – Radial response of radially excited modes, comparison of original (dotted lines) and filtered (solid lines) waveforms (starting from the left, top row: modes 1 to 5, bottom row: modes 6 to 10)	154
Figure 4.49 – Radial response of radially excited modes (starting from the left, top row: modes 1 to 5, bottom row: modes 6 to 10)	154
Figure 4.50 – Tangential response of radially excited modes, comparison of original (dotted lines) and filtered (solid lines) waveforms (starting from the left, top row: modes 1 to 5, bottom row: modes 6 to 10)	154
Figure 4.51 – Tangential response of radially excited modes (starting from the left, top row: modes 1 to 5, bottom row: modes 6 to 10)	155
Figure 4.52 – Radial response of tangentially excited modes, comparison of original (dotted lines) and filtered (solid lines) waveforms (starting from the left, top row: modes 1 to 7, bottom row: modes 8 to 13)	155
Figure 4.53 – Radial response of tangentially excited modes (starting from the left, top row: modes 1 to 7, bottom row: modes 8 to 13)	155
Figure 4.54 – Tangential response of tangentially excited modes, comparison of original (dotted lines) and filtered (solid lines) waveforms (starting from the left, top row: modes 1 to 7, bottom row: modes 8 to 13)	156
Figure 4.55 – Tangential response of tangentially excited modes (starting from the left, top row: modes 1 to 7, bottom row: modes 8 to 13)	156
Figure 4.56 – Real lateral mode shapes, comparison of original (dotted lines) and filtered (solid lines) waveforms (starting from the left, top row: modes 1 to 6, bottom row: modes 7 to 11)	156
Figure 4.57 – Real lateral mode shapes (starting from the left, top row: modes 1 to 6, bottom row: modes 7 to 11)	157
Figure 4.58 – Flowchart describing the identification process of in-plane structural tyre belt modes.	158
Figure 4.59 – Illustration of the real mode shapes, corresponding to the first radial mode, calculated for a positive and a negative modal participation factor	166



Figure 4.60 – First radial mode: comparison between the experimentally identified real mode shape (term A) and the calculated orthogonal one (term B).....	168
Figure 5.1 – Indoor tyre testing facility (photograph courtesy of the Department of Aeronautical and Automotive Engineering, Loughborough University).....	171
Figure 5.2 – The total vertical load as a function of the imposed deformation for various degrees of reduction ([110]) .....	174
Figure 5.3 – Vertical force applied at the wheel centre.....	175
Figure 5.4 – Vertical load versus vertical deformation of the tyre belt for four cases of modal reduction.....	176
Figure 5.5 – Detail of Figure 5.4, area in the rectangle.....	176
Figure 5.6 – Vertical stiffness test, total vertical force applied at the wheel centre versus time .....	178
Figure 5.7 – Vertical stiffness test, total wheel centre vertical displacement versus time .....	178
Figure 5.8 – Vertical stiffness test, vertical force versus time (Area A) .....	179
Figure 5.9 – Vertical stiffness test, vertical force versus time (Area B) .....	179
Figure 5.10 – Vertical stiffness test, vertical force versus time (Area C) .....	179
Figure 5.11 – Vertical stiffness test, vertical force versus time (Area D) .....	180
Figure 5.12 – Vertical stiffness test, wheel centre vertical displacement versus time (Area A) .....	180
Figure 5.13 – Vertical stiffness test, wheel centre vertical displacement versus time (Area B) .....	180
Figure 5.14 – Vertical stiffness test, wheel centre vertical displacement versus time (Area C) .....	181
Figure 5.15 – Vertical stiffness test, wheel centre vertical displacement versus time (Area D) .....	181
Figure 5.16 – Vertical stiffness test, wheel vertical force versus wheel centre vertical displacement (Area D).....	182
Figure 5.17 – Vertical stiffness test, wheel vertical force versus wheel centre vertical displacement.....	182
Figure 5.18 – Vertical stiffness test, graphical representation of user-defined quantities .....	185
Figure 5.19 – Vertical stiffness test, comparison between experimental and simulation data in terms of wheel centre vertical displacement (Area A) .....	186
Figure 5.20 – Vertical stiffness test, comparison between experimental and simulation data in terms of wheel centre vertical displacement (Area B) .....	186

Figure 5.21 – Vertical stiffness test, comparison between experimental and simulation data in terms of wheel centre vertical displacement (Area C) .....	187
Figure 5.22 – Vertical stiffness test, comparison between experimental and simulation data in terms of wheel centre vertical displacement (Area D) .....	187
Figure 5.23 – Vertical stiffness test, virtual wheel vertical force versus wheel centre vertical displacement .....	189
Figure 5.24 – Changes of lateral reaction force $F_y$ , transmitted by wheel, as a response for the wheel cornering angle $\delta$ oscillatory changes ( $v=30\text{km/h}$ , $f=2\text{Hz}$ ); a) changes of the wheel cornering angle $\delta$ - input signal; b) changes of lateral force reaction $F_y$ , transmitted by wheel - output signal([68]) .....	191
Figure 5.25 - Time delay and frequency dependency of lateral force generation .....	192
Figure 5.26 – Steering angle variation, expressed in the time domain .....	193
Figure 5.27 – Lateral force, time domain ( $v_d=2\text{m/s}$ , $F_z=-1000\text{N}$ ) .....	195
Figure 5.28 – Lateral force, time domain ( $v_d=2.5\text{m/s}$ , $F_z=-1000\text{N}$ ) .....	196
Figure 5.29 – Lateral force, time domain ( $v_d=3\text{m/s}$ , $F_z=-1000\text{N}$ ) .....	196
Figure 5.30 – Amplitude characteristics, determined in frequency domain, for different wheel rolling speed, in conditions of the wheel cornering angle oscillatory changes([68]) .....	199
Figure 5.31 – Lateral force expressed in the time domain ( $v_d = 3\text{m/s}$ , $F_z = 1000\text{N}$ ).....	200
Figure 5.32 – Lateral force expressed in the time domain ( $v_d = 3\text{m/s}$ , $F_z = 1200\text{N}$ ).....	201
Figure 5.33 – Lateral force expressed in the time domain ( $v_d = 3\text{m/s}$ , $F_z = 1400\text{N}$ ).....	201
Figure 5.34 – Lateral force expressed in the time domain ( $v_d = 3\text{m/s}$ , $F_z = 1600\text{N}$ ).....	202
Figure 5.35 – Normalised lateral force time histories ( $v_d = 3\text{m/s}$ , $F_z: 1000\text{N} - 1600\text{N}$ ) .....	203
Figure 5.36 – Normalised lateral force time histories, close up of area A.....	203
Figure 5.37 – Cornering stiffness vs vertical load ([80]).....	204
Figure 5.38 – Variations of the relaxation length value $L_n$ , after forcing a cornering angle step $\delta$ (all-steel 275/70R22.5 tire, normal load $F_z=20000\text{N}$ ) ([67]).....	205

## **Appendix B – Tables**

### **Chapter 3**

Table 3.1: Contact parameters for the LuGre sub-model

Table 3.2: X and Z coordinates of drum key points

Table 3.3: Coefficients of drum quadratic expression

### **Chapter 4**

Table 4.1: Experimental equipment and parameters

Table 4.2: In-plane Radial Modes

Table 4.3: In-plane Tangential Modes

Table 4.4: Out-of-plane Modes

### **Chapter 5**

Table 5.1: Modal reduction scenarios

Table 5.2: Vertical deflection measured at the wheel centre

Table 5.3: Tyre vertical stiffness dependency as a function of tyre belt fidelity

Table 5.4: Vertical stiffness test – User defined input quantities

Table 5.5: Vertical stiffness test – Main simulation parameters

Table 5.6: Tyre hysteresis to slip angle variation – Virtual testing parameters

Table 5.7: Tyre first-order behaviour – Virtual testing parameters – Longitudinal velocity variation tests

Table 5.8: Tyre first-order behaviour – Simulation results – Longitudinal velocity variation tests (A)

Table 5.9: Tyre first-order behaviour – Simulation results – Longitudinal velocity variation tests (B)

Table 5.10: Tyre first-order behaviour – Simulation results – Longitudinal velocity variation tests (C)

Table 5.11: Tyre first-order behaviour – Virtual testing parameters – Vertical force variation tests

Table 5.12: Tyre first-order behaviour – Simulation results – Vertical force variation tests